AN ANALYTIC NODAL METHOD FOR SOLVING THE TWO-GROUP, MULTIDIMENSIONAL, STATIC AND TRANSIENT NEUTRON DIFFUSION EQUATIONS

by

Kord S. Smith

B.S., Kansas State University (1976)

SUBMITTED IN PARTIAL FULFILLMENT
OF THE REQUIREMENTS FOR THE
DEGREES OF

NUCLEAR ENGINEER
AND
MASTER OF SCIENCE

AT THE

 MASSACHUSETTS INSTITUTE OF TECHNOLOGY

MARCH 1979

Signature redacted

Signature of Author . . . . . .
Department of Nuclear Engineering, March 19, 1979

Signature redacted

Certified by . . . . . .
Thesis Supervisor

Signature redacted

Accepted by . . . . . .
Chairman, Nuclear Engineering Committee

AN ANALYTIC NODAL METHOD FOR SOLVING THE TWO-GROUP, MULTIDIMENSIONAL, STATIC AND TRANSIENT NEUTRON DIFFUSION EQUATIONS

by

Kord S. Smith

Submitted to the Department of Nuclear Engineering on March 9, 1979, in partial fulfillment of the requirements for the Degrees of Nuclear Engineer and Master of Science.

ABSTRACT

The objective of this research is to develop computationally efficient numerical methods for solving the two-group, multidimensional, static and transient neutron diffusion equations. In particular, refinements of the Analytic Nodal Method (which employs analytic solutions of the one-dimensional diffusion equations to determine spatial coupling) are investigated.

In the static case, the only approximation of the Analytic Nodal Method is that the spatial shape of the transverse leakages can be fit by quadratic polynomials. Numerical techniques for solving the nodal diffusion equations are investigated and optimized for LWR analysis with assembly-sized spatial mesh. The nodal method is extended to the time-dependent case by use of the Theta time-integration method.

Analysis of many two- and three-dimensional, static and transient LWR problems demonstrates that very accurate solutions can be obtained with assembly-sized spatial meshes (15-20 cm). The computational efficiency of the Analytic Nodal Method is also shown to be at least two orders of magnitude greater than that of conventional finite difference methods.

Thesis Supervisor: Allan F. Henry

Title: Professor of Nuclear Engineering

ACKNOWLEDGMENTS

The author extends his sincerest appreciation to his thesis supervisor, Professor Allan F. Henry, for his invaluable assistance and support during the course of this investigation. His unique ability to motivate and direct his students, while providing ample opportunity for development and exploration of his students' ideas, has made the author's association with him an extremely rewarding experience.

Thanks are also due to Professor Kent F. Hansen for his helpful comments on certain numerical considerations of this work.

The author also wishes to thank Mrs. Mary Bosco for her assistance in the preparation of this document. Her patience and technical skills, which are clearly demonstrated in this manuscript, are only exceeded by the apparent pride which she places in her work. The author is grateful for all her laborious efforts.

The financial support of this research by the Electric Power Research Institute is gratefully acknowledged.

TABLE OF CONTENTS

LIST OF FIGURES

LIST OF TABLES

Chapter 1

INTRODUCTION

1.1 OVERVIEW

An extensive knowledge of the spatial power distribution is required for the design and analysis of current-generation light water reactors. Efforts to answer safety questions which arise in conjunction with actual and hypothetical accident scenarios often require the knowledge of multi-dimensional transient power distributions. Accordingly, the nuclear reactor vendors and the nuclear utilities are under increasing pressure to develop techniques with which they can verify the safety of their reactors.

Several approaches to establishing that reactors are safely designed come to mind. It is possible to build experimental facilities for each reactor design and to perform a multitude of static and transient experiments designed to answer the pertinent safety questions. However, this option is frightfully expensive, of dubious value, and practically impossible. Another alternative is to adopt ever more stringent operating limits and ultraconservative design techniques. This course of action leads to a poor utilization of resources, to a degradation of plant efficiencies, and ultimately to prohibitively expensive nuclear electrical energy.

A more promising means of answering the safety questions appears to be the development of more sophisticated theoretical methods, which are capable of producing the required safety-related information. There are also economic incentives for pursuing this last course of action: It is possible that by increasing the accuracy of theoretical predictions and confidence in them, unnecessarily conservative design and operating margins may be relaxed.

Over the past two decades, finite difference methods have emerged as the standard computational technique used for calculation of the power distributions in nuclear reactors. Only in very recent years, since the development of the high speed digital computer, have finite difference techniques been capable of performing "relatively economic" three-dimensional calculations for light water reactors. To this date, three-dimensional transient calculations remain prohibitively expensive and a practical impossibility for use in "day-to-day" design and analysis of thermal reactors.

As a result, a large number of computational schemes have been proposed as alternatives to the computationally inefficient finite difference techniques (1). In particular, certain nodal methods have reached high levels of sophistication and have been demonstrated to be orders of magnitude more computationally efficient than finite difference schemes (2). Some of these methods, however, are subject to company confidentiality. Therefore, the need to develop new methods for multi-dimensional transient reactor analysis still exists. The primary objective of the author is to develop an efficient, economical, and accurate

method for the analysis of three-dimensional transient behavior of light water reactors.

1.2 SYNOPSIS OF THE PROBLEM

In most situations encountered in the analysis of light water reactors, it is sufficient to model the neutronic behavior of the reactor by a low order approximation to the formally exact neutron transport equation. The most widely used of these approximations is multigroup neutron diffusion theory. For this model, the set of time- and space-dependent coupled partial differential equations for which approximate solutions are sought can be written as

$$\underline{\nabla} \cdot D_g(\underline{r},t)\underline{\nabla}\phi_g(\underline{r},t) - \Sigma_{tg}(\underline{r},t)\phi_g(\underline{r},t) +$$

$$\sum_{g'=1}^{G} \left(\Sigma_{gg'}(\underline{r},t)+(1-\beta)\chi_{g_p}\frac{1}{\gamma}\nu\Sigma_{fg'}(\underline{r},t)\right)\phi_{g'}(\underline{r},t)$$

$$+ \sum_{d=1}^{D} \chi_{g_d}\lambda_d C_d(\underline{r},t) = \frac{1}{v_g}\frac{\partial}{\partial t}\phi_g(\underline{r},t) \quad ; \qquad g = 1,2,\ldots G \tag{1-1a}$$

$$\beta_d \sum_{g=1}^{G} \frac{\nu}{\gamma}\Sigma_{fg}(\underline{r},t)\phi_g(\underline{r},t) - \lambda_d C_d(\underline{r},t) = \frac{\partial}{\partial t} C_d(\underline{r},t) \quad ; \qquad d = 1,2,\ldots,D \tag{1-1b}$$

where

G ≡ total number of neutron energy groups

D ≡ total number of delayed neutron precursor families

ϕ_g ≡ scalar neutron flux in group g (cm^{-2} sec^{-1})

C_d ≡ density of delayed neutron precursors in family d (cm^{-3})

D_g ≡ diffusion coefficient for group g (cm)

Σ_{tg} ≡ macroscopic total cross section for group g (cm^{-1})

$\Sigma_{gg'}$ ≡ macroscopic transfer cross section from group g' to group g (cm^{-1})

χ_{g_p} ≡ prompt fission neutron spectrum to group g

ν ≡ mean number of neutrons emitted per fission

γ ≡ eigenvalue which makes all of the time derivatives identically zero

Σ_{fg} ≡ macroscopic fission cross section for group g (cm^{-1})

χ_{g_d} ≡ delayed neutron spectrum for family d in group g

λ_d ≡ decay constant for delayed neutron precursor family d (sec^{-1})

β_d ≡ fractional yield of decayed neutron precursors in family d per fission

β ≡ total fractional yield of delayed neutron precursors per fission, $\left(\beta = \sum_{d=1}^{D} \beta_d\right)$

v_g ≡ neutron velocity for group g (cm sec^{-1})

and the fission neutron spectrum is assumed to be that of the predominant fissioning isotope. If the distribution of material properties in space and time, the initial neutron flux distribution in space and energy, and the appropriate boundary conditions are specified, a unique solution to Eqs. 1-1 exists. The two most commonly used boundary conditions

applied to the outer surface of the reactor are, stated physically, that the neutron flux or the incoming neutron current for every energy group be identically zero. At any internal surfaces, continuity of neutron flux and the normal component of the neutron current are imposed for every energy group.

The solution to Eqs. 1-1 is usually obtained by first assuming that the reactor is in a "critical" configuration. That is, all of the properties of the reactor are independent of time and hence all of the time derivatives in Eqs. 1-1 are identically zero. The static solution to Eqs. 1-1 is obtained by varying the parameter γ (a critical eigenvalue) such that a nontrivial solution to the static multigroup equations exists. The static multigroup equations can be written as

$$\underline{\nabla} \cdot D_g(\underline{r})\underline{\nabla}\phi_g(\underline{r}) - \Sigma_{tg}(\underline{r})\,\phi_g(\underline{r}) + \sum_{g'=1}^{G} \left(\Sigma_{gg'}(\underline{r}) + \chi_g \frac{1}{\gamma} \nu\Sigma_{fg'}(\underline{r})\right) \phi_{g'}(\underline{r}) = 0 \; ;$$

$$g = 1,2,\ldots,G \qquad (1\text{-}2)$$

In principle, the spatial power distribution in a reactor can be determined by applying Eq. 1-2 and explicitly representing all of the geometrical detail which is present. The geometrical complexity of large current-generation light water reactors is so great that direct representation of full geometrical heterogeneity is precluded for reasons of practicality. The approach that is generally taken to alleviate this difficulty is to treat large spatial regions as homogenized. The actual spatial detail within each of the homogenized regions is treated in an auxiliary calculation, to obtain "equivalent homogenized diffusion theory

parameters" which are spatially constant within each region. The techniques used to perform this homogenization need not be limited to diffusion theory, and many such schemes have been devised over the years (3). This homogenization is commonly performed for regions which contain one or several fuel assemblies in a radial plane (typically a rectangular region with sides of approximately 20 cm) and have an axial length of similar extent. The full core reactor calculation is thus reduced to that of determining the spatial power distribution within a reactor containing several thousand homogenized regions. The author will not address the many problems associated with homogenization techniques, but rather, will approach the task of determining the spatial power distribution within a reactor which has been partitioned into "homogenized" regions. The equivalent homogenized diffusion theory parameters for each region are assumed to be known.

1.3 REVIEW OF SOLUTION METHODS

Many methods for solving the static multigroup diffusion equations are presently available to the nuclear reactor community. Complete descriptions of each of these methods are much too lengthy to be included in this review. Only the comparative advantages and disadvantages of several of the most widely used methods are summarized in this section.

In finite difference schemes, low order difference approximations are used to represent the leakage term of Eq. 1-2, $\underline{\nabla} \cdot D_g(\underline{r}) \underline{\nabla} \phi_g(\underline{r})$. These finite difference methods possess several advantages over most other schemes. For example, these methods are conceptually simple

and the resulting algebraic equations are such that only adjacent nodes are coupled by the spatial leakage terms. One very important property of finite difference techniques is that they can be shown to converge to the exact solution of the multigroup diffusion equations in the limit of infinitely fine mesh spacing (4). Also, as a consequence of the widespread use of finite difference methods, the associated numerical methods have also reached high levels of sophistication. The only real disadvantage of finite difference schemes is that very fine spatial meshes are required to achieve acceptable accuracy (5). This problem is particularly pronounced in regions near a water reflector in light water reactors, since the thermal neutron flux there is highly peaked. The need for fine mesh spacing translates into large numbers of unknowns, and hence, into excessive computational effort for multidimensional problems. Nevertheless, finite difference techniques are reliable means of generating solutions to the multigroup diffusion equations with which to compare the results of other methods, and despite their drawbacks for use with full core reactor calculations, they will probably continue to be the industry standard for quite some time to come.

In the past few years, many researchers have applied finite element techniques to solving the multigroup diffusion equations (6). In finite element methods, the spatial shapes of the multigroup fluxes are represented as polynomials over large homogeneous regions. Variational principles are generally used to determine the equations which specify the coefficients of the polynomials. It is possible to achieve a substantial reduction in the number of spatial unknowns, for a given degree of

accuracy, over finite difference methods (7). The finite element schemes also converge to the exact solution of the multigroup diffusion equations in the limit of infinitely fine mesh spacing. The major disadvantage is that the coupling of the finite element equations is much more extensive than with the finite difference equations. Hence, it is generally found that the reduction in the number of unknowns is offset by an increase in computational effort required to solve the resulting equations (8). Since any reduction in computational effort over the finite difference techniques is at best marginal, finite element methods will probably not replace finite difference methods as an industry standard.

If it is imperative that the full spatial heterogeneity within a reactor be modeled, spatial flux synthesis schemes offer the largest reduction in the number of spatial unknowns. In synthesis schemes, precomputed expansion functions are obtained over large regions of the reactor, perhaps by two-dimensional (x-y) finite difference calculations with full geometrical detail. These expansion functions are combined by coefficients which are determined by solving spatial equations of a lower dimensionality, such as one-dimensional (z-dependent) equations. The equations for the unknown "mixing coefficients" are derived by applying a variational principle and demanding that the approximate solution obey the multigroup diffusion equations in a weighted integral sense. A major reduction in the number of unknowns is routinely obtained by many synthesis schemes, and the resulting equations are not difficult to solve (9). The unfortunate drawback of synthesis methods is that there is no systematic procedure for choosing the expansion functions or the weighting

functions. Furthermore, rigorous error bounds on the synthesized solutions do not exist. This lack of error bounds has limited the widespread use of spatial flux synthesis. There are, however, many researchers who have used spatial flux synthesis with varying degrees of success (10).

Another class of techniques used to solve the multigroup diffusion equations are nodal methods. The quantities of interest in most nodal methods are the group-dependent neutron fluxes averaged over large spatial regions (nodes) and the neutron currents averaged over the faces of the nodes. No approximations to the formally exact neutron transport equation need to be made in the derivation of the nodal balance equations. The difficulty with the nodal methods is that relationships between the node-averaged fluxes and the face-averaged currents must be obtained. Many different schemes for determining these relationships have been proposed (11). Once the relationships between node-averaged fluxes and face-averaged currents are specified, equations with a structure similar to finite difference equations can be constructed. Thus, nodal methods possess much of the simple structure of finite difference methods, while offering a substantial reduction in the number of unknowns by utilizing node-averaged fluxes. Hence, if consistent, systematic schemes for determining the flux-current spatial coupling can be developed, nodal methods appear to offer considerable promise as accurate, efficient techniques for solving the multidimensional neutron diffusion equations.

1.4 MOTIVATION OF NODAL METHODS

Many researchers have recognized the potential accuracy and computational efficiency of consistently formulated nodal methods. Hence, many different schemes have been proposed to determine the flux-current coupling. Early nodal methods used crude approximations for the coupling terms and, consequently, had limited accuracy (12). Some attempts were made to circumvent the limited accuracy by imposition of ad hoc modifications ("refinements"). These modifications increased accuracy, but they relied on trial and error adjustment of artificially introduced parameters to match higher order calculations. These methods were applicable only to a limited range of reactor conditions, and thus, were not widely accepted as viable design tools.

In recent years, however, systematic, consistent methods to determine the flux-current coupling terms have been developed by several researchers. Methods which use polynomial expansions of the fluxes and currents have produced extremely accurate solutions to the multigroup diffusion equations (13-15). An "Analytic Nodal Method" which employs analytic solutions of the one-dimensional, two-group diffusion equations to determine the spatial coupling has also been notably successful and has undergone several stages of refinement (16-18).

1.5 OBJECTIVES AND SUMMARY

The objective of this paper is to extend the Analytic Nodal Method to three dimensions and to develop computationally efficient numerical methods for solving the time-dependent, multidimensional, 2-group

neutron diffusion equations. In Chapter 2, derivations of the static nodal diffusion equations and the Analytic Nodal Method are presented. Next, numerical techniques for solving the static nodal diffusion equations are discussed (Chapter 3), and results of several static benchmark problems are included (Chapter 4). The techniques employed to solve the time-dependent neutron diffusion equations are detailed in Chapter 5 and the solutions to a large number of two- and three-dimensional transient problems are presented (Chapter 6). Finally, a summary of the investigation, conclusions about the Analytic Nodal Method, and recommendations for future research are given in Chapter 7.

Chapter 2

DERIVATION OF THE ANALYTIC NODAL METHOD FOR SOLVING THE STATIC MULTIGROUP DIFFUSION EQUATIONS

2.1 INTRODUCTION

In a recent thesis, Cook demonstrated that many transients encountered in light water reactor (LWR) safety analysis can be successfully analyzed using assembly-sized thermal-hydraulic regions.(19). Cook also found that the LWR transient analysis code MEKIN (which uses a finite difference neutronic model) applied as much as 95 percent of its computational effort in certain problems to solving the neutronics equations (from which the average powers in the thermal-hydraulic regions were determined), and as little as 5 percent of the computational effort was expended in solving the thermal-hydraulic equations. Therefore, a neutronic model which had averaged fluxes in the thermal-hydraulic regions as the only unknowns could be very efficient, and still provide the necessary information to model successfully most LWR transients.

Several years ago, Antonopoulos developed a method for solving the one- and two-dimensional diffusion equations which used exact difference equations (20). Although Antonopoulos solved these exact difference equations by approximation, Shober later introduced an exact method for solving the difference equations (16). This method, which was exact

in one dimension for any mesh spacing (provided the cross sections were spatially constant within each region) and had region-averaged fluxes as the only unknowns, would seem to be ideally suited for use in coupled neutronic thermal-hydraulic problems in which assembly-sized thermal-hydraulic regions could be used.

In this chapter, the Analytic Nodal Method for solving the static multigroup diffusion equations will be derived, making use of Antonopoulos' exact difference equations. In more than one dimension, exact solutions will be shown to exist only for very simple problems, and thus, an approximation will be required for more complicated (realistic) problems. Several approximations have been developed by other researchers and will be presented in this chapter for completeness. Throughout the derivation of the Analytic Nodal Method, it will be assumed that equivalent homogenized diffusion theory parameters, which are spatially constant over large regions, can be used. Therefore, only regions which have constant material properties will be considered, and all derivations will be done in three-dimensional Cartesian geometry. It will be demonstrated that nodal diffusion equations can be derived, which have node-averaged fluxes as the primary unknowns and nearest neighbor spatial coupling in node-averaged fluxes.

2.2 DERIVATION OF THREE-DIMENSIONAL MULTIGROUP NODAL DIFFUSION EQUATIONS

The global reactor problem is treated in three-dimensional Cartesian geometry, where x, y, and z represent the three coordinate directions. A very general notation for the coordinate directions proves

quite useful; hence, u, v and w are used as generalized coordinate subscripts. The spatial domain is subdivided into a regular array of nucleearly homogeneous right rectangular parallelepipeds (nodes) with grid indices defined by u_ℓ, v_m, and w_n where

$$\ell,m,n \equiv \begin{cases} i = 1,2,\ldots I \; ; & u,v,w = x \\ j = 1,2,\ldots J \; ; & u,v,w = y \\ k = 1,2,\ldots K \; ; & u,v,w = z \; . \end{cases}$$

As an example of the future use of this generalized coordinate notation, the net currents on the faces of node (i,j,k) as a function of the two transverse directions are expressed as

$$\left[J_{u_{i,j,k}}(v,w) \right] = -[D_{i,j,k}] \frac{\partial}{\partial u} [\phi(u_\ell,v,w)] \; ; \qquad \begin{array}{l} u = x,y,z \\ v \neq u \\ w \neq u \neq v \; . \end{array}$$

This single equation actually expresses three equations:

1) The x-directed net current on the $x = x_i$ face, as a function of y and z ($u = x$, $v = y$, $w = z$)

2) The y-directed net current on the $y = y_j$ face, as a function of x and z ($u = y$, $v = x$, $w = z$)

3) The z-directed net current on the $z = z_k$ face, as a function of x and y ($u = z$, $v = x$, $w = y$) .

The node (i,j,k) is defined by

$$x \in [x_i, x_{i+1}]$$
$$y \in [y_j, y_{j+1}]$$
$$z \in [z_k, z_{k+1}] \; .$$

The node widths are then defined as

$$h_u^{\ell} \equiv u_{\ell+1} - u_{\ell} \; ; \qquad u = x,y,z \; ,$$

and the node volume is

$$V_{i,j,k} \equiv h_x^i h_y^j h_z^k \; .$$

For convenience, the static multigroup diffusion equation, Eq. 1-2, is cast in conventional matrix form:

$$-\underline{\nabla} \cdot [D(\underline{r})] \, \underline{\nabla} [\phi(\underline{r})] + [\Sigma_T(\underline{r})] \, [\phi(\underline{r})] = \frac{1}{\gamma} [\chi] [\nu\Sigma_f(\underline{r})]^T [\phi(\underline{r})] \qquad (2\text{-}1)$$

where

$[\phi(\underline{r})]$ is a column vector of length G containing neutron fluxes

$[D(\underline{r})]$ is a diagonal G × G matrix containing the diffusion coefficients

$[\Sigma_T(\underline{r})]$ is a G × G matrix containing the macroscopic total-minus-scattering cross section

$[\chi]$ is a column vector of length G containing the fission neutron spectrum

$[\nu\Sigma_f(\underline{r})]$ is a column vector of length G containing nu, the mean number of neutrons emitted per fission, times the macroscopic fission cross section

γ is a critical eigenvalue of the global static reactor problem.

The first step in the derivation of the nodal diffusion equations is to integrate Eq. 2-1 over the volume of an arbitrary node (i,j,k) to obtain:

$$h_y^j h_z^k([J_{x_{i+1,j,k}}] - [J_{x_{i,j,k}}]) + h_x^i h_z^k([J_{y_{i,j+1,k}}] - [J_{y_{i,j,k}}])$$

$$+ h_x^j h_y^k([J_{z_{j,j,k+1}}] - [J_{z_{i,j,k}}]) + V_{i,j,k}[\Sigma_{T_{i,j,k}}][\overline{\phi}_{i,j,k}]$$

$$= \frac{1}{\gamma} V_{i,j,k}[\chi][\nu\Sigma_{f_{i,j,k}}]^T[\overline{\phi}_{i,j,k}] \qquad (2\text{-}2)$$

where

$$[J_{u_{i,j,k}}] \equiv -\frac{1}{h_v^m h_w^n}[D_{i,j,k}]\frac{\partial}{\partial u}\int_{v_m}^{v_{m+1}} dv \int_{w_n}^{w_{n+1}} dw\,[\phi(u_\ell, v, w)]\,;$$

$$u = x,y,z$$

$$v \neq u$$

$$w \neq u \neq v$$

$$[\Sigma_{\alpha_{i,j,k}}] \equiv [\Sigma_\alpha(x,y,z)]\Big|_{\substack{x \in [x_i, x_{i+1}] \\ y \in [y_j, y_{j+1}] \\ z \in [z_k, z_{k+1}]}}\,; \qquad \alpha = T, f$$

$$[\overline{\phi}_{i,j,k}] \equiv \frac{1}{V_{i,j,k}} \int_{x_i}^{x_{i+1}} dx \int_{y_j}^{y_{j+1}} dy \int_{z_k}^{z_{k+1}} dz\,[\phi(x,y,z)]\,.$$

Equation 2-2 is a rigorous statement of neutron balance for any node (i,j,k). The utility of Eq. 2-2 is limited by the fact that without additional relationships between the face-averaged currents, $[J_{x_{i,j,k}}]$, $[J_{y_{i,j,k}}]$, $[J_{z_{i,j,k}}]$ and the node-averaged fluxes $[\overline{\phi}_{i,j,k}]$, the spatial flux distribution cannot be determined.

2.3 DERIVATION OF SPATIAL COUPLING EQUATIONS

One method of obtaining a differential equation from which the spatial coupling of Eq. 2-2 can be determined is to treat the directions one at a time and spatially integrate Eq. 2-1 over the two directions transverse to the direction of interest, to obtain for direction u and node (ℓ,m,n),

$$-h_v^m h_w^n [D_{\ell,m,n}] \frac{\partial^2}{\partial u^2} [\phi_{u_{\ell,m,n}}(u)] - [D_{\ell,m,n}] \int_{v_m}^{v_{m+1}} dv \int_{w_n}^{w_{n+1}} dw \frac{\partial^2}{\partial v^2}$$

$$\times [\phi(u,v,w)] - [D_{\ell,m,n}] \int_{v_m}^{v_{m+1}} dv \int_{w_n}^{w_{n+1}} dw \frac{\partial^2}{\partial w^2} [\phi(u,v,w)]$$

$$+ h_v^m h_w^n [\Sigma_{T_{\ell,m,n}}] [\phi_{u_{\ell,m,n}}(u)]$$

$$= \frac{1}{\gamma} h_v^m h_w^n [\chi][\nu\Sigma_{f_{\ell,m,n}}]^T [\phi_{u_{\ell,m,n}}(u)] ; \quad \begin{array}{l} u = x,y,z \\ v \neq u \\ w \neq u \neq v \end{array} \qquad (2\text{-}3)$$

where

$$[\phi_{u_{\ell,m,n}}(u)] \equiv \frac{1}{h_v^m h_w^n} \int_{v_m}^{v_{m+1}} dv \int_{w_n}^{w_{n+1}} dw \, [\phi(u,v,w)] .$$

Equation 2-3, when multiplied by du, is simply a statement of neutron balance within a slab contained in node (ℓ,m,n) which has the height and depth of the node, but which is of thickness du (in the u direction) about the point u. Hence, the two integrals represent the net rate at which neutrons leak out of the four surfaces of the slab which are transverse

to direction u. The following notation for the net leakages is convenient:

$$h_w^n[L_{v_{\ell,m,n}}(u)] \equiv -[D_{\ell,m,n}] \int_{v_m}^{v_{m+1}} dv \int_{w_n}^{w_{n+1}} dw \frac{\partial^2}{\partial v^2}[\phi(u,v,w)] ; \tag{2-4}$$

$$u = x,y,z$$
$$v = x,y,z ; \quad v \neq u$$
$$w = x,y,z ; \quad w \neq u \neq v .$$

Equation 2-4 possesses the property that when integrated over $[u_\ell, u_{\ell+1}]$ and divided by h_u^ℓ it yields

$$\frac{1}{h_u^\ell} \int_{u_\ell}^{u_{\ell+1}} du [L_{v_{\ell,m,n}}(u)] = [J_{v_{\ell+1,m,n}}] - [J_{v_{\ell,m,n}}] \equiv [\bar{L}_{v_{\ell,m,n}}] ; \tag{2-5}$$

$$u = x,y,z$$
$$v = x,y,z ; \quad v \neq u ,$$

which is the nodal face-averaged, v-directed, net leakage. By defining a sum of the two net leakages transverse to direction u, per unit u, divided by $h_v^m h_w^n$ as

$$[S_{u_{\ell,m,n}}(u)] \equiv \frac{1}{h_v^m}[L_{v_{\ell,m,n}}(u)] + \frac{1}{h_w^n}[L_{w_{\ell,m,n}}(u)] ; \tag{2-6}$$

$$u = x,y,z$$
$$v \neq u$$
$$w \neq u \neq v ,$$

Equation 2-3 can be cast in the form

$$-[D_{\ell,m,n}]\frac{\partial^2}{\partial u^2}[\phi_{u_{\ell,m,n}}(u)]+\left([\Sigma_{T_{\ell,m,n}}]-\frac{1}{\gamma}[\chi][\nu\Sigma_{f_{\ell,m,n}}]^T\right)$$

$$\times[\phi_{u_{\ell,m,n}}(u)]=-[S_{u_{\ell,m,n}}(u)]\;;\quad u=x,y,z. \tag{2-7}$$

To obtain relationships between the node-averaged fluxes and the face-averaged net leakages, one need only solve Eq. 2-7 for $[\phi_{u_{\ell,m,n}}(u)]$ and integrate this "one-dimensional" flux over the node. Unfortunately, the u-dependence of the transverse leakage source term on the right-hand side of Eq. 2-7 must be known or approximated if the solution of the equation is to be found. This circumstance makes necessary the first, and only, approximation of the Analytic Nodal Method.

2.3.1 The "Buckling" Approximation

The possibilities for the approximation of the transverse leakage shape in Eq. 2-7 appear to be unlimited. It does, however, seem reasonable to expect that the more complicated the assumed shape, the more difficult it will be to solve for the one-dimensional flux.

For this reason, Shober (16) initially assumed that the transverse leakages and the one-dimensional fluxes had the same shape. That is, the transverse leakages were assumed to obey the equation

$$[B_{u_{\ell,m,n}}][\phi_{u_{\ell,m,n}}(u)]=[S_{u_{\ell,m,n}}(u)]\;;\quad u=x,y,z\;. \tag{2-8}$$

The values of the diagonal matrix $[B_{u_{\ell,m,n}}]$ were assumed to be independent of u within node (ℓ,m,n) and were found by integrating Eq. 2-8 over $[u_\ell,u_{\ell+1}]$ and dividing by h_u^ℓ to obtain

$$[B_{u_{\ell,m,n}}][\overline{\phi}_{\ell,m,n}] = \frac{1}{h_v^m}[\overline{L}_{v_{\ell,m,n}}] + \frac{1}{h_w^n}[\overline{L}_{w_{\ell,m,n}}]$$

$$\equiv [\overline{S}_{u_{\ell,m,n}}] ; \qquad u = w,y,z . \tag{2-9}$$

This "buckling" approximation would be exact if the fluxes were spatially separable within node (i,j,k). The utility of this approximation was that it reduced Eq. 2-7 to an equation with $[\phi_{u_{\ell,m,n}}(u)]$ being the only unknown. Hence, Eq. 2-7 could be easily solved for $[\phi_{u_{\ell,m,n}}(u)]$, which in turn could be integrated to obtain the desired relationships between

$$[\overline{S}_{u_{\ell,m,n}}], [\overline{\phi}_{\ell-1,m,n}], [\overline{\phi}_{\ell,m,n}], \text{ and } [\overline{\phi}_{\ell+1,m,n}] .$$

However, Shober found that use of the buckling approximation led to large errors in highly nonseparable problems.

2.3.2 "Flat" Approximation

As an alternative to the buckling approximation, Shober (16) then approximated the transverse leakage shape as spatially flat across each node, that is,

$$[S_{u_{\ell,m,n}}(u)] = [\overline{S}_{u_{\ell,m,n}}] ; \qquad u = x,y,z . \tag{2-10}$$

Shober demonstrated the superiority of the "flat" approximation over the buckling approximation for several highly nonseparable problems. He has also implemented a "two-step" transverse leakage approximation in which the leakages were assumed to consist of two piecewise constant segments within each node (17). Results from Shober's work indicated

that, as expected, the two-step approximation was substantially more accurate than the flat leakage approximation.

Despite Shober's encouraging results with the two-step Analytic Nodal Method, other researchers had found that more accurate results could be obtained by expanding the transverse leakages in higher order polynomials (13-15). This led Greenman, by suggestion of Finneman (21), to incorporate a quadratic approximation for the shape of the transverse leakages into the Analytic Nodal Method (18).

2.3.3 Quadratic Approximation

The quadratic polynomials suggested by Finneman were chosen in such a way as to uniquely determine the shape of the transverse leakage in a node by utilizing the average transverse leakages in three adjacent nodes. This approximation leads to a functional form of the net leakage transverse to direction u given by

$$[S_{u_{\ell,m,n}}(u)] \cong [\bar{S}_{u_{\ell-1,m,n}}]\rho_{u_\ell}^{\ell-1}(u) + [\bar{S}_{u_{\ell,m,n}}]\rho_{u_\ell}^{\ell}(u) + [\bar{S}_{u_{\ell+1,m,n}}]\rho_{u_\ell}^{\ell+1}(u) \; ; \quad u = x,y,z \, , \tag{2-11}$$

where each of the ρ's is a quadratic polynomial in u. The constraints imposed on the expansion functions, stated physically, were that the integral of the transverse leakage approximation over each of the three adjacent nodes preserve the average transverse leakage of that node. In mathematical terms, these conditions imply the following constraints:

$$\frac{1}{h_u^{\ell+\ell'}} \int_{u_{\ell+\ell'}}^{u_{\ell+\ell'+1}} du\, \rho_{u_\ell}^{\ell+\ell''}(u) = \delta_{\ell'\ell''} \; ; \quad \begin{array}{l} u = x,y,z \\ \ell' = -1,0,1 \\ \ell'' = -1,0,1 \end{array} , \tag{2-12}$$

where $\delta_{\ell'\ell''}$ is the Kronecker delta defined by

$$\delta_{\ell'\ell''} \equiv \begin{cases} 1 \; ; & \ell' = \ell'' \\ 0 \; ; & \ell' \neq \ell'' \end{cases} . \tag{2-13}$$

The expansion functions of Eq. 2-12 are uniquely determined by the mesh spacing in direction u. It is important to note that the expansion for node (ℓ,m,n) is used only for that node, despite the fact that the expansion also preserves the average transverse leakages in nodes $(\ell-1,m,n)$ and $(\ell+1,m,n)$. This form of the transverse leakage is particularly useful since it involves only average transverse leakages which are already unknowns in the nodal balance equation, Eq. 2-2. However, although this transverse leakage expansion is unique, there is no a priori reason to believe that it is the "best" quadratic approximation to the transverse leakage within node (ℓ,m,n), for which it is used. This point will be discussed in detail in Chapter 4 after specific examples have been introduced. A complete derivation of the transverse leakage expansion functions for nonuniform mesh spacing is given in Appendix 1.

2.4 METHOD FOR SOLVING THE SPATIAL COUPLING EQUATIONS WITH QUADRATIC TRANSVERSE LEAKAGE

In principle, solving the spatial coupling equation to obtain relationships between node-averaged fluxes and face-averaged net leakages is quite simple. In the Analytic Nodal Method, the spatial coupling equation,

$$-[D_{\ell,m,n}]\frac{\partial^2}{\partial u^2}[\phi_{u_{\ell,m,n}}(u)]+\left([\Sigma_{T_{\ell,m,n}}]-\frac{1}{\gamma}[\chi][\nu\Sigma_{f_{\ell,m,n}}]^T\right)$$

$$\times[\phi_{u_{\ell,m,n}}(u)]=-[S_{u_{\ell,m,n}}(u)]\;;\qquad u=x,y,z\;, \tag{2-7}$$

is solved analytically. The transverse leakage expansion of Eq. 2-11 can be expressed in an alternate, but entirely equivalent form, as

$$[S_{u_{\ell,m,n}}(u)]\cong[\bar{S}_{u_{\ell,m,n}}]+\left([\bar{S}_{u_{\ell-1,m,n}}]-[\bar{S}_{u_{\ell,m,n}}]\right)\rho^{\ell-1}_{u_\ell}$$

$$+\left([\bar{S}_{u_{\ell+1,m,n}}]-[\bar{S}_{u_{\ell,m,n}}]\right)\rho^{\ell+1}_{u_\ell}\;;\qquad u=x,y,z\;. \tag{2-14}$$

The expansion functions can be expressed as

$$\rho^{\ell-1}_{u_\ell}(u)=a^-_{u_\ell}+b^-_{u_\ell}\left(\frac{u-u_\ell}{h^\ell_u}\right)+c^-_{u_\ell}\left(\frac{u-u_\ell}{h^\ell_u}\right)^2\;;$$

$$\rho^{\ell+1}_{u_\ell}(u)=a^+_{u_\ell}+b^+_{u_\ell}\left(\frac{u-u_\ell}{h^\ell_u}\right)+c^+_{u_\ell}\left(\frac{u-u_\ell}{h^\ell_u}\right)^2\;;\quad u=x,y,z\;. \tag{2-15}$$

Hence, Eq. 2-14 can be rewritten as

$$[S_{u_{\ell,m,n}}(u)]\cong\langle[\bar{S}_{u_{\ell,m,n}}]+([\bar{S}_{u_{\ell-1,m,n}}]-[\bar{S}_{u_{\ell,m,n}}])a^-_{u_\ell}$$

$$+([\bar{S}_{u_{\ell+1,m,n}}]-[\bar{S}_{u_{\ell,m,n}}])a^+_{u_\ell}\rangle+\left(\frac{u-u_\ell}{h^\ell_u}\right)$$

$$\times\langle([\bar{S}_{u_{\ell-1,m,n}}]-[\bar{S}_{u_{\ell,m,n}}])b^-_{u_\ell}$$

$$+([\bar{S}_{u_{\ell+1,m,n}}]-[\bar{S}_{u_{\ell,m,n}}])b^+_{u_\ell}\rangle+\left(\frac{u-u_\ell}{h^\ell_u}\right)^2$$

$$\times\langle([\bar{S}_{u_{\ell-1,m,n}}]-[\bar{S}_{u_{\ell,m,n}}])c^-_{u_\ell}+([\bar{S}_{u_{\ell+1,m,n}}]$$

$$-[\bar{S}_{u_{\ell,m,n}}])c^+_{u_\ell}\rangle\;;\quad u=x,y,z\;. \tag{2-16}$$

Substitution of the approximate form of the transverse leakage given by Eq. 2-16 allows Eq. 2-7 to be expressed in P1 form as

$$\frac{d}{dt_\ell}[\Phi_{u_{\ell,m,n}}(t_\ell)] + [N_{\ell,m,n}][\Phi_{u_{\ell,m,n}}(t_\ell)] = [S'_{u_{\ell,m,n}}(t_\ell)];$$

$$u = x,y,z\ , \qquad (2.17)$$

where

$$[\Phi_{u_{\ell,m,n}}(t_\ell)] \equiv \text{col}\{[\phi_{u_{\ell,m,n}}(t_\ell)],\ [J_{u_{\ell,m,n}}(t_\ell)]\}$$

$$[N_{\ell,m,n}] \equiv \begin{bmatrix} [0] & [D_{\ell,m,n}]^{-1} \\ [\Sigma_{T_{\ell,m,n}}] - \frac{1}{\gamma}[\chi][\nu\Sigma_{f_{\ell,m,n}}]^T & [0] \end{bmatrix}$$

$$[S'_{u_{\ell,m,n}}(t_\ell)] \equiv \text{col}\left\{[0],\ \left(-[S^f_{u_{\ell,m,n}}] - [S^\ell_{u_{\ell,m,n}}]\frac{t_\ell}{h^\ell_u} - [S^q_{u_{\ell,m,n}}]\left(\frac{t_\ell}{h^\ell_u}\right)^2\right)\right\}$$

$$t_\ell \equiv u - u_\ell\ ,$$

and the transverse leakage has been split into three pieces, a "flat," a "linear," and a "quadratic" defined by

$$[S^f_{u_{\ell,m,n}}] \equiv \langle [\bar{S}_{u_{\ell,m,n}}] + ([\bar{S}_{u_{\ell-1,m,n}}] - [\bar{S}_{u_{\ell,m,n}}])a^-_{u_\ell} + ([\bar{S}_{u_{\ell+1,m,n}}] - [\bar{S}_{u_{\ell,m,n}}])a^+_{u_\ell}\rangle\ ,$$

$$[S^\ell_{u_{\ell,m,n}}] \equiv \langle ([\bar{S}_{u_{\ell-1,m,n}}] - [\bar{S}_{u_{\ell,m,n}}])b^-_{u_\ell} + ([\bar{S}_{u_{\ell+1,m,n}}] - [\bar{S}_{u_{\ell,m,n}}])b^+_{u_\ell}\rangle\ ,$$

$$[S^{q}_{u_{\ell},m,n}] \equiv \langle ([\bar{S}_{u_{\ell-1},m,n}] - [\bar{S}_{u_{\ell},m,n}])\, c^{-}_{u_{\ell}} + ([\bar{S}_{u_{\ell+1},m,n}] - [\bar{S}_{u_{\ell},m,n}])\, c^{+}_{u_{\ell}} \rangle ; \quad u = x,y,z . \qquad (2\text{-}18)$$

The procedure for solving Eq. 2-17 for the relationships between face-averaged net leakages and node-averaged fluxes is now conceptually straightforward. For each node, and each direction u, the following seven steps are taken:

1) Three particular solutions to Eq. 2-17, on the interval $0 < t_{\ell} < h^{\ell}_{u}$, are determined for the flat, linear, and quadratic transverse leakage source terms, subject to the boundary condition

$$[\Phi^{p}(t_{\ell}=0)] = 0 .$$

2) The homogeneous solution to Eq. 2-17, on the interval $0 < t_{\ell} < h^{\ell}_{u}$, is obtained subject to the boundary condition

$$[\Phi^{h}(t_{\ell}=0)] = [\Phi(u_{\ell})] .$$

3) The particular and homogeneous solutions to Eq. 2-17 from Steps 1 and 2 are combined to obtain an analytic expression for $[\Phi(t_{\ell})]$ on the interval $0 < t_{\ell} < h^{\ell}_{u}$.

4) The analytic solution of Step 3 is integrated over the interval $[0, h^{\ell}_{u}]$ and a relationship between node-averaged fluxes and face-averaged net currents is obtained in terms of $[\Phi(u_{\ell})]$.

5) Steps 1-4 are repeated for the interval $0 < t_{\ell-1} < h^{\ell-1}_{u}$, but subject to the boundary conditions

$$[\Phi^{p}(t_{\ell-1} = h_u^{\ell-1})] = 0$$

$$[\Phi^{h}(t_{\ell-1} = h_u^{\ell-1})] = [\Phi(u_\ell)],$$

to obtain another equation relating node-averaged fluxes and face-averaged net currents in terms of $[\Phi(u_\ell)]$.

6) Since both solutions in Steps 4 and 5 are expressed in terms of $[\Phi(u_\ell)]$, the two equations are used to eliminate $[\phi_{u_{\ell,m,n}}(u_\ell)]$, as this surface flux is not an unknown in the nodal balance equation, Eq. 2-2. Thus, it is possible to find a relationship between node-averaged fluxes, face-averaged net leakages, and $[J_{u_{\ell,m,n}}(u_\ell)]$.

7) Steps 1-6 can be repeated to derive a relationship between node-averaged fluxes, face-averaged net leakages, and $[J_{u_{\ell+1,m,n}}(u_{\ell+1})]$. Taking the difference of these last two relationships finally allows one to obtain an equation relating node-averaged fluxes and face-averaged net leakages.

The actual application of the aforementioned procedure is quite long and tedious; it is presented in Appendix 2.

The final equations relating node-averaged fluxes and face-averaged net leakages can be expressed in the form

$$[\bar{L}_{u_{\ell,m,n}}] = [F^{\ell-1}_{u_{\ell,m,n}}][\bar{\phi}_{\ell-1,m,n}] + [F^{\ell}_{u_{\ell,m,n}}][\bar{\phi}_{\ell,m,n}]$$
$$+ [F^{\ell+1}_{u_{\ell,m,n}}][\bar{\phi}_{\ell+1,m,n}] + [G^{\ell-2}_{u_{\ell,m,n}}][\bar{S}_{u_{\ell-2,m,n}}]$$
$$+ [G^{\ell-1}_{u_{\ell,m,n}}][\bar{S}_{u_{\ell-1,m,n}}] + [G^{\ell}_{u_{\ell,m,n}}][\bar{S}_{u_{\ell,m,n}}]$$
$$+ [G^{\ell+1}_{u_{\ell,m,n}}][\bar{S}_{u_{\ell+1,m,n}}] + [G^{\ell+2}_{u_{\ell,m,n}}][\bar{S}_{u_{\ell+2,m,n}}];$$
$$u = x,y,z \,. \qquad (2\text{-}19)$$

Equation 2-19 reveals that the u-directed net leakage is coupled to node-averaged fluxes in three adjacent nodes in the u-direction, as well as to the transverse leakages in five adjacent nodes. The global reactor problem is much easier to visualize if Eq. 2-2 and Eq. 2-19 are cast in super-matrix form with the following definitions:

$[\bar{\phi}]$ ≡ a column vector of length G*I*J*K (≡ N) containing the node-averaged fluxes (ordered first by group, then x-direction, then y-direction, and finally z-direction).

$[\bar{L}_u]$ ≡ a column vector of length N containing the u-direction net leakage

$[F_u]$ ≡ a block tridiagonal matrix of order N × N containing the elements of $[F^{\ell'}_{u_{\ell,m,n}}]$

$[G_u]$ ≡ a block pentadiagonal matrix of order N × N containing the elements of $[G^{\ell'}_{u_{\ell,m,n}}]$

$[\Sigma_T]$ ≡ a block diagonal matrix of order N × N containing the elements of $V_{i,j,k}[\Sigma_{T_{i,j,k}}]$

$[M] \equiv$ a block diagonal matrix of order $N \times N$ containing the elements of $V_{i,j,k}[\chi][\nu\Sigma_{f_{i,j,k}}]^T$.

The resulting super-matrix equation can be written as

$$\begin{bmatrix} [\Sigma_t] & h_y^j h_z^k[I] & h_x^i h_z^k[I] & h_x^i h_y^j[I] \\ [F_x] & -[I] & \frac{1}{h_y^j}[G_x] & \frac{1}{h_z^k}[G_x] \\ [F_y] & \frac{1}{h_x^i}[G_y] & -[I] & \frac{1}{h_z^k}[G_y] \\ [F_z] & \frac{1}{h_x^i}[G_z] & \frac{1}{h_y^j}[G_z] & -[I] \end{bmatrix} \begin{bmatrix} [\bar{\phi}] \\ [\bar{L}_x] \\ [\bar{L}_y] \\ [\bar{L}_z] \end{bmatrix}$$

$$= \frac{1}{\gamma} \begin{bmatrix} [M] & [0] & [0] & [0] \\ [0] & [0] & [0] & [0] \\ [0] & [0] & [0] & [0] \\ [0] & [0] & [0] & [0] \end{bmatrix} \begin{bmatrix} [\bar{\phi}] \\ [\bar{L}_x] \\ [\bar{L}_y] \\ [\bar{L}_z] \end{bmatrix} \qquad (2\text{-}20)$$

The global reactor equation as expressed in Eq. 2-20 is of the form of a classical eigenvalue problem,

$$[A]^{-1}[B][X] = \gamma[X] \ ,$$

except for the fact that the elements of [A] depend on the eigenvalue γ.

Equations 2-2 and 2-19 form the basis of the Analytic Nodal Method with a quadratic transverse leakage approximation. These equations, along with the appropriate boundary conditions applied to the reactor

surface (Appendix 2), fully specify the global system of static nodal diffusion equations.

2.5 SUMMARY

In this chapter, and its related appendices, a complete set of nodal diffusion equations have been derived from multigroup diffusion theory. The only approximation that was found to be necessary (in addition to the original assumption of homogenized nodes) was that the spatial shape of the transverse leakage within a node could be fit to a specific quadratic polynomial. The resulting equations were written in terms of node-averaged fluxes and face-averaged net leakages. Nearest neighbor spatial coupling was obtained in node-averaged fluxes, but not in face-averaged net leakages.

In Chapter 3, the numerical methods used to solve the nodal diffusion equations will be discussed. In addition, the numerical properties of the equations will be examined and the consistency of the Analytic Nodal Method will be demonstrated. Applications of this nodal method to several two- and three-dimensional benchmark problems are presented in Chapter 4.

Chapter 3

NUMERICAL CONSIDERATIONS

3.1 INTRODUCTION

In Chapter 2, the spatially-discretized static nodal diffusion equations were derived for the solution of the multigroup diffusion equations. A method of determining the spatial coupling coefficients, subject only to the assumption that the transverse leakages could be fit by a quadratic polynomial, was derived for the two-group case in Appendix 2. In this chapter, the numerical techniques used to solve the two-group analytic nodal diffusion equations are presented. The consistency of the Analytic Nodal Method is also demonstrated for the case of infinitely fine mesh spacing. Results of optimizing several of the schemes used to accelerate the convergence rate of the iterative process are also presented. The solutions to many static reactor configurations are contained in Chapter 4.

3.2 NUMERICAL PROPERTIES OF THE ANALYTIC NODAL DIFFUSION EQUATIONS

The equation for which a solution is sought in the Analytic Nodal Method is given in Chapter 2, by Eq. 2-20. This super-matrix equation is a set of linear equations in the four vector unknowns, $[\bar{\phi}]$, $[\bar{L}_x]$, $[\bar{L}_y]$, and $[\bar{L}_z]$. In its present form, Eq. 2-20 has very little spatial

coupling in the node-averaged flux terms and most of the coupling in the face-averaged net leakage terms. It is known from physical principles that the net leakages will be small compared to the average fluxes in a large number of reactor configurations. Therefore, Eq. 2-20 has the undesirable characteristic that the spatial coupling is dominated by the net leakage equations. This situation is altered by substituting the last three blocks of equations into the first block of equations to obtain

$$[H][\psi] = \frac{1}{\gamma}[P][\psi] \ , \tag{3-1}$$

where

$$[H] \equiv \begin{bmatrix} [F]\left(h_z^k[G_y]+h_y^j[G_z]\right) & \left(h_z^k[G_x]+h_x^i[G_z]\right) & \left(h_y^j[G_x]+h_x^i[G_y]\right) \\ [F_x] & -[I] & \frac{1}{h_y^j}[G_x] & \frac{1}{h_z^k}[G_x] \\ [F_y] & \frac{1}{h_x^i}[G_y] & -[I] & \frac{1}{h_z^k}[G_y] \\ [F_z] & \frac{1}{h_x^i}[G_z] & \frac{1}{h_y^j}[G_z] & -[I] \end{bmatrix}$$

$$[F] \equiv \left([\Sigma_T] + h_y^j h_z^k[F_x] + h_x^i h_z^k[F_y] + h_x^i h_y^j[F_z]\right)$$

$$[P] \equiv \begin{bmatrix} [M] & [0] & [0] & [0] \\ [0] & [0] & [0] & [0] \\ [0] & [0] & [0] & [0] \\ [0] & [0] & [0] & [0] \end{bmatrix}$$

$$[\psi] \equiv \text{col}\{[\bar{\phi}], [\bar{L}_x], [\bar{L}_y], [\bar{L}_z]\} \ .$$

Since each of the matrices $[F_u]$ is block (2 × 2) tridiagonal, Eq. 3-1 has substantially more spatial coupling in node-averaged flux terms than does Eq. 2-20. Equation 3-1 is clearly an eigenvalue problem in which the elements of the matrix [H] depend on the eigenvalue.

Any iterative scheme that is used to solve Eq. 3-1 will require that the matrices [H] and [P] have certain properties in order to guarantee successful convergence. Therefore, it is very useful to examine the properties of the matrices in Eq. 3-1.

The matrix [P] is quite simple. The only non-zero submatrix of the matrix [P] is [M], and the matrix [M] is block diagonal with nonnegative components (all fission cross sections are nonnegative). Unfortunately, the matrix [H] is not nearly as simple. In the general case, the only property of the matrix [H] that can be guaranteed is that all of its components are real.

There is, however, at least one case in which the properties of the matrix [H] can be specified. This special case is in the limit of infinitely fine mesh spacing. As the mesh spacings, h_u^ℓ, go to zero, the basic spatial coupling matrices, as defined in Appendix 3, become

$$\left[A_{u_{\ell,m,n}}\right]_{12} \rightarrow \begin{bmatrix} 1/D_1 & 0 \\ 0 & 1/D_2 \end{bmatrix}_{\ell,m,n} \frac{h_u^\ell}{2}$$

$$\left[B_{u_{\ell,m,n}}\right]_{11} \rightarrow \begin{bmatrix} 1 & 0 \\ 0 & 1 \end{bmatrix}$$

$$\left[C^{\pm}_{u_{\ell,m,n}}\right]_{12} \rightarrow \left[\begin{matrix} 1/D_1 & 0 \\ 0 & 1/D_2 \end{matrix}\right]_{\ell,m,n} \frac{\left(h^{\ell}_{u}\right)^2}{6}$$

$$\left[D^{+}_{u_{\ell,m,n}}\right]_{12} \rightarrow \left[\begin{matrix} 1/D_1 & 0 \\ 0 & 1/D_2 \end{matrix}\right]_{\ell,m,n} \frac{\left(h^{\ell}_{u}\right)^2}{8}$$

$$\left[D^{-}_{u_{\ell,m,n}}\right]_{12} \rightarrow \left[\begin{matrix} 1/D_1 & 0 \\ 0 & 1/D_2 \end{matrix}\right]_{\ell,m,n} \frac{\left(h^{\ell}_{u}\right)^2}{24}$$

$$\left[E^{+}_{u_{\ell,m,n}}\right]_{12} \rightarrow \left[\begin{matrix} 1/D_1 & 0 \\ 0 & 1/D_2 \end{matrix}\right]_{\ell,m,n} \frac{\left(h^{\ell}_{u}\right)^2}{10}$$

$$\left[E^{-}_{u_{\ell,m,n}}\right]_{12} \rightarrow \left[\begin{matrix} 1/D_1 & 0 \\ 0 & 1/D_2 \end{matrix}\right]_{\ell,m,n} \frac{\left(h^{\ell}_{u}\right)^2}{60} \quad . \tag{3-2}$$

With these spatial coupling matrices, the flux coupling coefficients, as defined in Eq. A2-14, in the limit of infinitely fine mesh spacing become

$$-\left[F^{\ell-1}_{u_{\ell,m,n}}\right] = \left[\begin{matrix} \mathscr{D}^{1^-}_{u_{\ell,m,n}} & 0 \\ 0 & \mathscr{D}^{2^-}_{u_{\ell,m,n}} \end{matrix}\right]$$

$$\left[F^{\ell}_{u_{\ell,m,n}}\right] = \left[\begin{matrix} \mathscr{D}^{1^-}_{u_{\ell,m,n}} + \mathscr{D}^{1^+}_{u_{\ell,m,n}} & 0 \\ 0 & \mathscr{D}^{2^-}_{u_{\ell,m,n}} + \mathscr{D}^{2^+}_{u_{\ell,m,n}} \end{matrix}\right]$$

$$-\begin{bmatrix} F^{\ell+1} \\ u_{\ell,m,n} \end{bmatrix} = \begin{bmatrix} \mathcal{D}^{1^+}_{u_{\ell,m,n}} & 0 \\ 0 & \mathcal{D}^{2^+}_{u_{\ell,m,n}} \end{bmatrix} , \tag{3-3}$$

where

$$\mathcal{D}^{g^-}_{u_{\ell,m,n}} \equiv \left(\frac{2\, D_{g_{\ell,m,n}} D_{g_{\ell-1,m,n}}}{D_{g_{\ell,m,n}} h_u^{\ell-1} + D_{g_{\ell-1,m,n}} h_u^{\ell}} \right)$$

$$\mathcal{D}^{g^+}_{u_{\ell,m,n}} \equiv \left(\frac{2\, D_{g_{\ell,m,n}} D_{g_{\ell+1,m,n}}}{D_{g_{\ell,m,n}} h_u^{\ell+1} + D_{g_{\ell+1,m,n}} h_u^{\ell}} \right) \quad ; \; g = 1,2 \; .$$

Thus, all of the matrices, $[F_u]$, in Eq. 3-1 are block tridiagonal and diagonally dominant with components that are all of order 1/h. By examining the leakage coupling matrices of Eq. A2-14, one finds that all of the matrices, $[G_u]$, in Eq. 3-1 are of order h. Therefore, the first block of equations in Eq. 3-1 has coefficient matrices with terms of order h (flux terms) and terms of order h^2 (leakage terms). Hence, in the limit of infinitely fine mesh spacing, the order h^2 terms can be neglected and Eq. 3-1 becomes

$$[F][\bar{\phi}] = \frac{1}{\gamma}[M][\bar{\phi}] \; . \tag{3-4}$$

The net leakages of Eq. 3-1 do not enter directly into the nodal diffusion equations in the limit of infinitely fine mesh spacing. Close examination of the flux coupling matrices of Eq. 3-3 reveals that Eq. 3-4 is actually a finite difference approximation to the two-group diffusion

equations. The actual form of these difference equations is not that of the conventional finite difference equations with fluxes evaluated at the corner points of homogeneous volumes, but rather is that of a less frequently used formulation of finite differences with fluxes evaluated at the centers of the homogeneous volumes. Nevertheless, an important consequence of this reduction to the finite difference equations in the limit of infinitely fine mesh spacing is that the Analytic Nodal Method is guaranteed to converge to the exact solution of the two-group diffusion equations in this limit (23).

As a result of the elimination of net leakages in Eq. 3-1, the properties of matrices [F] and [M] suffice to determine completely the characteristics needed to guarantee convergence of the Analytic Nodal Method. Examination of Eq. 3-3 reveals that the matrices, $[F_u]$ are

1. Real
2. Irreducible
3. Symmetric
4. Diagonally dominant.

From these properties, it can be proved that Eq. 3-4 has the following properties (23):

1. There exists a unique positive real eigenvalue, γ_1, which is greater in modulus than all other eigenvalues.
2. The eigenvector corresponding to the eigenvalue γ_1 is unique and positive.

These properties and others derived from them will be used in Section

3.3 to demonstrate that the numerical schemes chosen to solve the Analytic Nodal Diffusion equations can be guaranteed to work in the limit of infinitely fine mesh spacing.

3.3 ITERATIVE STRATEGY FOR SOLVING THE STATIC NODAL DIFFUSION EQUATIONS

This section details the iterative strategy used to solve the static nodal diffusion equations, Eq. 3-1. Frequent use will be made of the properties of the matrices in Eq. 3-1, for the case of infinitely fine mesh spacing, despite the fact that these properties cannot be shown to exist (and perhaps do not exist) in the general case.

3.3.1 The General Iterative Scheme

The general scheme for solving Eq. 3-1 is as follows:

1. An initial guess for γ (usually $\gamma = 1.0$) is used to evaluate the components of the matrix [H].
2. An accelerated fission source (outer) iteration is employed to determine iteratively the maximum eigenvalue and corresponding eigenvector (γ and $[\psi]$).
3. After several outer iterations (usually 5-10), the latest estimate of γ is used to update the components of the matrix [H].

4. The matrix [H] is inverted at each outer iteration by a modified block (G*I*J*K × G*I*J*K) Gauss-Seidel (inner) iteration.

5. The matrix [F] is inverted at each inner iteration by an accelerated block (2 × 2) Gauss-Seidel (flux) iteration.

3.3.2 Eigenvalue Updating

The fact that the submatrices of matrix [H] depend on the eigenvalue of the global static reactor problem gives the outer iterations a nonlinear character. However, the effects of updating the matrices on the outer iterations are generally quite negligible, especially when a reasonable estimate of the eigenvalue is available. Another characteristic of the outer iterations which helps to mitigate nonlinear effects is that a very good estimate of the eigenvalue (accurate to about 0.5%) can be obtained in relatively few (3-5) outer iterations. In Section 3.2, it was shown that in the limit of infinitely fine mesh spacing, the nonlinearity disappears entirely, since the matrix components of [H] do not depend on the eigenvalue. Therefore, a general practice of updating the matrices every 5 to 10 outer iterations seems entirely appropriate. (In steady-state iterations for problems with feedback, more frequent updating may be required to account for changes in temperatures, densities, etc.) To date, no problem has failed to converge because of the nonlinear nature of the outer iterations.

3.3.3 Outer Iterations

The fission source iteration (23) is applied to Eq. 3-1 to determine the maximum eigenvalue and corresponding eigenvector. If p is used as the index of the outer iterations, Eq. 3-1 can be expressed as

$$[\psi]_{p+1} = \frac{1}{\gamma_{p+1}} [H]_p^{-1} [P][\psi]_p \; ; \quad p = 0, 1, \ldots, \infty \; , \tag{3-5}$$

where γ_{p+1} is an estimate of the global static eigenvalue and the matrix [H] is given a subscript p to indicate that its components are updated during the outer iterations. The maximum eigenvalue can be estimated by the ratio of the vector norms from successive solution vectors,

$$\gamma_{p+1} = \frac{\| [\psi]_{p+1} \|}{\| [\psi]_p \|} \; . \tag{3-6}$$

The fission source iteration is guaranteed to converge if the eigenvalue with the largest modulus is unique (22). This property exists in the case of infinitely fine mesh spacing, but cannot be demonstrated in the general case. Nevertheless, this property is assumed to exist in the general case, and no problem has failed to converge because of eigenvalues with degenerate maximum moduli.

The rate at which the outer iterations converge is determined by the ratio of the moduli of the two maximum eigenvalues, usually called the dominance ratio, defined by

$$d = \frac{|\gamma_2|}{|\gamma_1|} \; , \tag{3-7}$$

where γ_1 and γ_2 are the eigenvalues with the largest and second largest moduli, respectively. For a great many problems, the dominance ratio is very close to unity and convergence is very slow; hence, many methods have been developed to increase the convergence rate of the fission source iterations. One of the most direct methods of altering the convergence rate is "eigenvalue shifting" or Wielandt's fractional iteration (23). In Wielandt's method, Eq. 3-1 is modified to obtain

$$\left\{ [H] - \frac{1}{\gamma_s} [P] \right\} [\psi] = \left(\frac{1}{\gamma} - \frac{1}{\gamma_s} \right) [P][\psi] \ , \tag{3-8}$$

where γ_s is arbitrarily selected but subject to certain restrictions discussed below.

Equation 3-8 is a new eigenvalue problem with much different properties than Eq. 3-1. It is easily demonstrated that the eigenvector associated with the maximum value of $\left(\frac{1}{\gamma} - \frac{1}{\gamma_s} \right)^{-1}$ is identical to the eigenvector associated with the maximum value of γ in Eq. 3-1, provided γ_s is larger in modulus than γ (23). The dominance ratio of the new eigenvalue problem is (24)

$$d_s = \frac{1.0/\left(\frac{1}{\gamma_2} - \frac{1}{\gamma_s} \right)}{1.0/\left(\frac{1}{\gamma_1} - \frac{1}{\gamma_s} \right)} = \frac{\left(\frac{1}{\gamma_1} - \frac{1}{\gamma_s} \right)}{\left(\frac{1}{\gamma_2} - \frac{1}{\gamma_s} \right)} \ . \tag{3-9}$$

Since γ_s must be chosen such that the modulus of γ_s exceeds the modulus of γ_1, which in turn exceeds the modulus of γ_2, the dominance ratio, d_s, is less than unity and less than the unshifted dominance ratio, d. Naturally, the convergence rate of the outer iterations is maximized by

choosing the eigenvalue shift, γ_s, to be equal to the true static eigenvalue γ_1. Unfortunately, this choice makes the flux iteration matrix nearly singular, as is pointed out in Section 3.3.5. Nevertheless, an optimum value of γ_s may exist, and the problem of determining it is addressed in Section 3.4. Using the eigenvalue shift, the outer iteration is defined by

$$[\psi]_{p+1} = \left(\frac{1}{\gamma_{p+1}} - \frac{1}{\gamma_{s_p}}\right)\left\{[H]_p - \frac{1}{\gamma_{s_p}}[P]\right\}^{-1}[P][\psi]_p \; ;$$

$$p = 0, 1, 2, \ldots, \infty \qquad (3\text{-}10)$$

where $[\psi]_0$ is arbitrary (23). The new eigenvalue estimate can be determined using any vector norm. For simplicity, the ℓ_1 norm of the first block of the vector $[\psi]$ is chosen (23),

$$\left(\frac{1}{\gamma_{p+1}} - \frac{1}{\gamma_{s_p}}\right)^{-1} = \frac{\left\|[\bar{\phi}]_{p+1}\right\|_1}{\left\|[\bar{\phi}]_p\right\|_1} \; . \qquad (3\text{-}11)$$

It is recognized that if γ_{s_p} is fixed throughout the outer iteration process, most other conventional methods of accelerating the outer iteration convergence can also be applied. For reasons detailed in Section 3.4, there seems to be several advantages to altering the eigenvalue shift during the outer iterations. Also, the convergence rate of the outer iterations can be significantly increased by eigenvalue shifting, such that additional acceleration schemes are not required.

3.3.4 Inner Iterations

At each outer iteration, the matrix $\left\{[H]_p - \frac{1}{\gamma_{s_p}}[P]\right\}$ must be inverted. Since the matrix $[H]_p$ is in general quite complicated, an iterative scheme is also required to invert it. The method used to perform the inner iteration is a "modified" block Gauss-Seidel iteration, where each block is a square matrix whose order is the number of energy groups times the number of spatial mesh points. With q as the index of the inner iteration, this "modified" Gauss-Seidel iteration is defined by

$$[\bar{\phi}]_{p,q+1} = \left\{[F]_p - \frac{1}{\gamma_{s_p}}[M]\right\}^{-1} \left\langle \left(\frac{1}{\gamma_p} - \frac{1}{\gamma_{s_p}}\right)[M][\bar{\phi}]_p \right.$$
$$- \left(h_z^k[G_y]_p + h_y^j[G_z]_p\right)[\bar{L}_x]_{p,q} - \left(h_z^k[G_x]_p + h_x^i[G_z]_p\right)[\bar{L}_y]_{p,q}$$
$$\left. - \left(h_y^j[G_x]_p + h_x^i[G_y]_p\right)[\bar{L}_z]_{p,q} \right\rangle \qquad (3\text{-}12a)$$

$$[\bar{L}_u]_{p,q+1} = [F_x]_p[\bar{\phi}]_{p,q+1} + \frac{1}{h_v^m}[G_u]_p[\bar{L}_v]_{p,q} + \frac{1}{h_w^n}[G_y]_p[\bar{L}_w]_{p,q} ;$$

$$u = x,y,z$$

$$q = 0,1,2,\ldots,\infty . \qquad (3\text{-}12b)$$

This iterative scheme would be a true block Gauss-Seidel iteration if the latest values of the face-averaged net leakages were used.

This particular scheme is chosen for two reasons. First, it eliminates the need to calculate both $[G_u]_p[\bar{L}_v]_{p,q}$ and $[G_u]_p[\bar{L}_v]_{p,q+1}$, which saves computational effort. Second, this scheme does not "favor" any

one direction in the calculation of leakages. The inner iteration, defined by Eqs. 3-12, consists of two distinct steps. First, the new node-averaged fluxes are determined from the old fission source and the old net leakages. This step requires the inversion of the matrix $\left\{[F]_p - \frac{1}{\gamma_{s_p}}[M]\right\}$. The second step is the determination of the new net leakages ^{p} from the new fluxes and the old leakages. This step is not iterative, but requires a large number of matrix multiplications, since the matrices $[G_u]_p$ are block pentadiagonal.

In most cases, there is no reason to converge the fluxes and leakages completely at every inner iteration, since the fission source is computed from fluxes at the last outer iteration. In problems where the net leakages are small compared to the average fluxes, it seems reasonable to perform only one inner iteration per outer iteration and continue the outer iterations until the fluxes are converged. In some cases, however, the net leakages can be fairly large compared to the average fluxes, and it may be more efficient to perform additional inner iterations to converge the net leakages more rapidly than would otherwise be possible. This problem is discussed in detail in Chapter 4.

3.3.5 Flux Iterations

At each inner iteration, the matrix $\left\{[F]_p - \frac{1}{\gamma_{s_p}}[M]\right\}$ must be inverted. In the three-dimensional case, [F] is a block septadiagonal matrix, each block being 2 × 2 (i.e., G × G). Since primary consideration in this work is with two-group methods, both groups will be solved simultaneously. The method used to invert the flux coefficient matrix

is a variant of the block successive overrelaxation method, called the Cyclic Chebyshev Semi-Iterative (CCSI) method (22). If the matrix $\left\{[F] - \frac{1}{\gamma_{s_p}}[M]\right\}$ is split into a strictly lower block triangular matrix, a block diagonal matrix, and a strictly upper block triangular matrix such that

$$\left\{[F]_p - \frac{1}{\gamma_{s_p}}[M]\right\} \equiv [L]_p + [D]_p + [U]_p \ , \tag{3-13}$$

the CCSI method with iterative index r is defined by

$$[\bar{\phi}]_{p,q,r+1} = (1-\omega_{r+1})[\bar{\phi}]_{p,q,r} + \omega_{r+1}\{[D]_p+[L]_p\}^{-1}\{[S]_{p,q} - [U]_p[\bar{\phi}]_{p,q,r}\}, \tag{3-14}$$

where

$$[S]_{p,q} \equiv \left\{\left(\frac{1}{\gamma_p} - \frac{1}{\gamma_{s_p}}\right)[M][\bar{\phi}]_p - \left(h_z^k[G_y]_p + h_y^j[G_z]_p\right)[\bar{L}_x]_{p,q} - \left(h_z^k[G_x]_p + h_y^i[G_z]_p\right)[\bar{L}_y]_{p,q} - \left(h_y^j[G_x]_p + h_x^i[G_y]_p\right)[\bar{L}_z]_{p,q}\right\}$$

$$\omega_{r+1} \equiv \frac{1}{1 - \left(\frac{\rho^2\omega_r}{4}\right)} \ ; \quad r \geq 1 \qquad \equiv 1.0 \ ; \quad r = 0 \ ,$$

with ρ^2 defined below.

Strictly speaking, to guarantee that the CCSI method will converge, the flux iteration matrix must possess several properties. First, the flux iteration matrix must be an irreducible, consistently ordered, weakly cyclic matrix of order 2, which it is. The flux iteration matrix

must also be convergent, which can be guaranteed if the flux coefficient matrix is diagonally dominant – as in the case of infinitely fine mesh spacing. Lastly, it must be assumed that all eigenvalues of the flux iteration matrix are real (4). This is true for all real symmetric matrices; hence, real eigenvalues can be guaranteed only for infinitely fine mesh spacing.

The CCSI method is related to the block successive overrelaxation (SOR) methods and can be thought of as an SOR method in which the relaxation parameter is varied from iteration to iteration in such a way as to increase the average rate of convergence. For SOR methods, the optimum choice for the relaxation factor is defined to be the relaxation factor which gives the greatest asymptotic convergence rate and is given by (22)

$$\omega_b = \frac{2}{1 + \sqrt{1 - \rho^2}} , \tag{3-14}$$

where ρ is the spectral radius of the Jacobi iteration matrix. The relaxation factors in the CCSI method are chosen to give the greatest average convergence rate; hence, the relaxation factors change from iteration to iteration. Asymptotically, the CCSI relaxation factor must equal the SOR relaxation factor, and indeed

$$\omega_\infty = \frac{2}{1 + \sqrt{1 - \rho^2}} . \tag{3-15}$$

It is apparent from Eq. 3-13 that the spectral radius of the Jacobi flux iteration matrix must be known in order to actually use the CCSI

method. Since the flux coefficient matrix is to be inverted by the CCSI method, it would be useful to be able to obtain ρ^2 by using this same method. It is easily shown that ρ^2 is equal to the spectral radius of the Gauss-Seidel iteration matrix (22). Thus, ρ^2 can be determined by performing a series of flux iterations with ω_r equal to unity (i.e., Gauss-Seidel iterations) and estimating the spectral radius, ρ(G-S), by

$$\rho_{r+1}(\text{G-S}) = \frac{\left\| [\bar{\phi}]_{r+1} - [\bar{\phi}]_r \right\|_1}{\left\| [\bar{\phi}]_r - [\bar{\phi}]_{r-1} \right\|_1} = \rho^2 ; \quad r = 0,1,\ldots,\infty . \tag{3-16}$$

In an actual problem, the determination of ρ^2 is treated in the following manner:

1. At the start of the outer iterations, ω_r is set to unity.
2. When the eigenvalue is converged to within 0.5%, ρ^2 is estimated by the procedure outlined above.
3. The Gauss-Seidel flux iterations are performed until successive estimates of ρ^2 differ by less than 0.2%.
4. The latest estimate of ρ^2 is then used in Eq. 3-13 to determine ω_r for the duration of the static problem solution.

It is recognized that better estimates of ρ^2 are possible. However, the flux coefficient matrix is dependent on the true static eigenvalue which is not known at the point that ρ^2 is estimated; thus, there seems to be little value in obtaining the "exact" spectral radius of the "wrong" matrix.

In point of fact, the spatial mesh is not swept in the fashion indicated previously, but rather is swept in a three-dimensional checkerboard fashion. That is, one pass is made through the spatial mesh solving for the average fluxes in every second node. After the mesh is completely swept, the process is started again, this time solving for the average fluxes in all of the nodes that were skipped on the first pass through the mesh. By sweeping the mesh in this fashion, all of the fluxes in the first sweep are determined from "old" flux values, and all of the fluxes in the second sweep are determined from "new" flux values. One virtue of this checkerboard, two-pass sweeping is that no geometrical orientation is given any preferential treatment (as is the case in a direct line- or row-sweeping method).

Mathematically, this checkerboard iteration scheme is a permutation transformation (4) of the conventional Gauss-Seidel iteration. This transformation can be thought of as a reordering of equations and unknowns. The permutation transformation leaves the properties of the flux iteration matrix unchanged, and all of the properties required to guarantee convergence of the CCSI method, in the limit of infinitely fine mesh spacing, are guaranteed to exist.

3.4 ITERATION OPTIMIZATION

The iterative method for solving the static nodal diffusion equations, as detailed in Section 3.3, is largely complete. There remain, however, several items to be further developed before it will be completely specified. The two main items are the determination of the number of flux

iterations to be performed at each inner iteration and the selection of the eigenvalue shift to be used to accelerate the convergence of the outer iterations.

3.4.1 Flux Iteration Error Reduction

One quantity which is evaluated in the process of determining the relaxation parameters for use with the CCSI method in the flux iterations is the spectral radius of the Jacobi iteration matrix. This spectral radius also determines the optimum asymptotic relaxation factor,

$$\omega_b = \frac{2}{1 + \sqrt{1 - \rho^2}} \quad . \tag{3-15}$$

It can be shown that asymptotically, the error in the node-averaged flux vector is reduced by the factor $(\omega_b - 1)$ at each flux iteration (22). Thus, it is possible to estimate the number of flux iterations that are required to achieve some desired error reduction. If the error reduction, ε, is defined to be the ratio of the vector norm of the error in the average fluxes after n flux iterations to the vector norm of the error in the average fluxes prior to the first flux iteration, it can be shown that (22)

$$\varepsilon > \frac{2(\omega_b - 1)^n}{1 + (\omega_b - 1)^{2n}} \quad . \tag{3-17}$$

The error reduction can be thought of approximately as the average fractional decrease in the error of the node-averaged fluxes per inner iteration.

In order to determine a reasonable choice for the error reduction at each inner iteration, the BIBLIS 2-D checkerboard-loaded PWR problem (Problem 4.3) was solved with various error reductions. Table 3-1 illustrates the effects of the error reduction on the iterative solution. From this information, it can be seen that the choice of error reduction does not have a significant effect on the total iteration time required to converge the problem. The reason for this is quite simple: Once the fission source and leakages are converged to a certain point, it takes a certain number of flux iterations to converge the fluxes fully; it makes little difference whether fewer flux iterations are performed for more outer iterations or whether more flux iterations are performed for fewer outer iterations. As a result of these and other test results, the general practice of choosing the error reduction in the interval .1 to .4 has been adopted for static nodal diffusion problems.

3.4.2 Eigenvalue Shift Optimization

Trade-offs between two competing phenomena determine the optimum eigenvalue shift. The outer iteration convergence rate is maximized (the dominance ratio is zero) when the eigenvalue shift is equal to the true global eigenvalue and minimized when the eigenvalue shift is equal to infinity. The flux iteration convergence rate is minimized (the flux iteration matrix is singular in the case of infinitely fine mesh spacing) when the eigenvalue shift is equal to the true global eigenvalue and maximized when the eigenvalue shift is equal to infinity. Therefore, it seems that there is little additional insight to be gained from purely

Table 3-1

ERROR REDUCTION OPTIMIZATION

2-D BIBLIS (rods in configuration – Problem A4.3)

23.122 cm spatial mesh

$\gamma_s = \gamma + .05$

1 inner per outer iteration

Matrix updates every five iterations

Flux convergence criteria = 10^{-5}

Error Reduction ε	Total Iteration Time* (sec)	Number of Outer Iterations	Number of Flux Iterations
0.90	> 4.0	> 70	1
0.666	2.48	52	2
0.400	1.77	36	3
0.150	1.77	31	5
0.050	1.92	30	7
0.025	2.04	29	8

* Includes matrix update time.

theoretical considerations and numerical experiments are needed to provide additional insight into the problem of choosing the eigenvalue shift. The effects of the eigenvalue shift on the overall iteration process are summarized in Tables 3-2a - 3-2d, for two different reactor configurations and three different spatial mesh sizes. From this information, several general conclusions are drawn:

1. As the eigenvalue shift (γ_s) approaches the true eigenvalue (γ), the convergence rate of the outer iterations increases.

2. As γ_s approaches γ, the flux iteration convergence rate decreases.

3. The spectral radius of the Gauss-Seidel flux iteration matrix varies significantly with the spatial mesh size.

4. The spectral radius of the unshifted flux iteration matrix, for problems with assembly-sized meshes, is very small.

5. The overall iteration is optimized, with respect to total execution time, when an eigenvalue shift which exceeds the true eigenvalue by four to five percent is used.

6. The optimum eigenvalue shift is not significantly affected by the spatial mesh size, despite the fact that the spectral radius of the flux iteration matrix changes significantly.

Table 3-2a

EIGENVALUE SHIFT OPTIMIZATION

(Coarse Mesh BIBLIS)

2-D BIBLIS (rods in configuration – Problem A4.3)

23.122 cm spatial mesh

1 inner per outer iteration

Error reduction = .15**

Flux convergence criteria = 10^{-5}

Eigenvalue Shift γ_s	Total Iteration Time (sec)*	Number of Outer Iterations	Number of Flux Iterations	Gauss-Seidel Spectral Radius
$\gamma + .04$	1.24	28	7	0.957
$\gamma + .05$	1.16	29	5	0.923
$\gamma + .06$	1.34	35	5	0.885
$\gamma + .07$	1.31	43	3	0.727
$\gamma + .09$	1.52	48	3	0.683
∞†	> 2.0	> 50	2	0.08

* No matrix updating.

** Based on an alternate estimate of error reduction, not presently used.

† Unaccelerated outer iteration.

Table 3-2b

EIGENVALUE SHIFT OPTIMIZATION

(Coarse Mesh IAEA)

2-D IAEA (Problem A4.2)

20.0 cm spatial mesh

1 inner per outer iteration

Error reduction = .15**

Flux convergence criteria = 10^{-5}

Eigenvalue Shift γ_s	Total Iteration Time* (sec)	Number of Outer Iterations	Number of Flux Iterations	Gauss-Seidel Spectral Radius
$\gamma + .03$	.75	17	7	.950
$\gamma + .04$	.74	21	5	.898
$\gamma + .05$	.77	21	5	.883
$\gamma + .06$	.79	25	4	.804
$\gamma + .07$	.90	27	4	.761
∞	> 1.5	> 50	2	.030

* No matrix updating.

** Based on an alternate estimate of error reduction, not presently used.

Table 3-2c

EIGENVALUE SHIFT OPTIMIZATION

(Fine Mesh BIBLIS)

2-D BIBLIS (rods in configuration – Problem A4.3)

11.561 cm spatial mesh

1 inner per outer iteration

Error reduction = .15**

Flux convergence criteria = 10^{-5}

Eigenvalue Shift γ_s	Total Iteration Time (sec)*	Number of Outer Iterations	Number of Flux Iterations	Gauss-Seidel Spectral Radius
$\gamma + .04$	4.28	24	9	0.969
$\gamma + .05$	3.95	28	7	0.954
$\gamma + .06$	4.89	32	7	0.950
$\gamma + .07$	4.89	33	7	0.946
$\gamma + .10$	6.24	50	5	0.878
$\gamma + .15$	> 8.0	> 50	4	0.789
∞	> 10.0	> 50	4	0.300

*No matrix updating.

**Based on an alternate estimate of error reduction, not presently used.

Table 3-2d

EIGENVALUE SHIFT OPTIMIZATION

(Very Fine Mesh BIBLIS)

2-D BIBLIS (rods in configuration – Problem A4.3)

7.707 cm spatial mesh

1 inner per outer iteration

Error reduction = .15**

Flux convergence criteria = 10^{-5}

Eigenvalue Shift γ_s	Total Iteration* Time (sec)	Number of Outer Iterations	Number of Flux Iterations	Gauss-Seidel Spectral Radius
$\gamma + .03$	17.9	37	13	.985
$\gamma + .04$	13.9	30	12	.982
$\gamma + .05$	15.8	35	12	.982
$\gamma + .07$	16.2	38	10	.974
$\gamma + .10$	> 18.0	> 50	7	.949
∞	> 20.0	> 50	6	.548

*No matrix updating

**Based on an alternate estimate of error reduction, not presently used.

The reasons for the success of eigenvalue shifting in accelerating the overall iteration process seem particularly clear in the case of assembly-sized spatial meshes: The leakage computations at each inner iteration require so much computational effort (about five times that of a single flux iteration) that it is desirable to shift more of the computational burden to the flux iterations (which would only require one or two iterations if no shift was employed), to balance the computational effort between flux and leakage calculations. Thus, the eigenvalue shift succeeds in increasing the spectral radius of the flux iteration matrix and decreasing the dominance ratio of the outer iteration. The effect of the optimum eigenvalue shift on the dominance ratio is summarized in Table 3-3. For assembly-sized meshes, the dominance ratio is decreased from approximately 0.99 to 0.80 by the eigenvalue shift. This corresponds to a factor of 20 increase in the asymptotic convergence rate of the outer iterations. The computational burden on the flux iterations is increased by a factor of two to three, hence, the eigenvalue shift is very effective in accelerating the overall iteration process.

Application of the eigenvalue shifting method to a wide variety of problems has led to a general procedure for the implementation of the eigenvalue shift. At the start of the problem, since the true eigenvalue is generally unknown, an initial value of 1.50 is used for γ_s. Hence, there is no possibility of converging to the wrong eigenvector as long as the true eigenvalue is less than 1.50. After the global static eigenvalue is converged to about one percent (generally only 2 to 5 outer iterations),

Table 3-3

EIGENVALUE SHIFT EFFECT ON DOMINANCE RATIO

γ_s, eigenvalue shift = γ + .05

	γ_1	γ_2	d	d_s
2-D BIBLIS				
23.122 cm spatial mesh (Problem A4.3)	1.01972	1.01009	.991	.831
2-D IAEA				
20.0 cm spatial mesh (Problem A4.2)	1.02961	1.01736	.988	.794

γ_s is chosen to be equal to the estimated eigenvalue plus an arbitrary constant (generally 0.04 to 0.05). Thus, γ_s "follows" the eigenvalue estimate and ultimately is near the anticipated optimum when the true eigenvalue is determined. This general procedure has been used on a great many problems without any difficulties.

Following the implementation of eigenvalue shifting (Wielandt's method) into the Analytic Nodal Method in this thesis work, Shober has also implemented the method into his "two-step" Analytic Nodal Method (17). He found that eigenvalue shifting was much more effective in accelerating the outer iteration convergence than the Chebyshev Semi-Iterative method (not to be confused with CCSI) which he has used in the past. However, Shober chose to fix γ_s prior to the start of the outer iterations by using a value of 1.1 times the estimated eigenvalue.

This practice of fixing γ_s at the beginning of a problem seems to lack the flexibility required when a reliable estimate of the true eigenvalue is not available. Hence, the aforementioned method of altering the eigenvalue shift during the outer iterations seems to be better adapted for use in general problems.

3.5 SUMMARY

In this chapter, the properties of the nodal diffusion equations were examined and the Analytic Nodal Method was shown to reduce to the finite difference equations in the limit of infinitely fine spatial mesh. As a consequence, it was shown that the Analytic Nodal Method is guaranteed to give the exact solution to the differential diffusion equation in this limit.

The numerical methods used to solve the nodal diffusion equations were also detailed in this chapter. However, many of the properties which were required to guarantee that these numerical techniques will cause convergence to the solution to the nodal diffusion equations could be demonstrated only for the case of infinitely fine spatial mesh.

In Chapter 4, applications of the Analytic Nodal Method and the numerical methods described in the present chapter will be presented. The effectiveness of the numerical schemes and the implications of the quadratic transverse leakage approximation will also be discussed.

Chapter 4

STATIC APPLICATIONS

4.1 INTRODUCTION

In Chapter 2, the static nodal diffusion equations were derived, and the Analytic Nodal Method, based on the single assumption that the transverse leakages could be fit to quadratic polynomials, was derived. The flux and leakage coupling coefficients were obtained by solving analytic difference equations. A multi-level iterative scheme for solving the resulting analytic nodal diffusion equations was detailed in Chapter 3.

In this chapter, results from application of the Analytic Nodal Method to several two- and three-dimensional, two-group, static reactor benchmark problems are presented. The spatial convergence rate of the Analytic Nodal Method is also examined. Following the presentation of results from the benchmark problems, a detailed examination of the transverse leakage shapes is presented to identify possible deficiencies of the quadratic transverse leakage approximation. Throughout this chapter, the accuracy and computational efficiency of the Analytic Nodal Method are compared to those of conventional finite difference methods and other nodal methods of current interest.

4.2 FOREWORD TO STATIC RESULTS

4.2.1 Computer Codes

The methods developed in Chapter 2 and the numerical techniques detailed in Chapter 3 are incorporated into a computer code, hereafter referred to as QUANDRY (Quadratic Analytic Nodal Diffusion Theory). This computer code solves two- and three-dimensional, two-group diffusion theory problems.

QUANDRY is written in the IBM FORTRAN IV language, except for a few routines that perform the dynamic storage allocation, which are part of the ANL BPOINTER (27) package. The code was compiled under the IBM Level-H compiler with full optimization and in single precision. All computations reported in this research are performed on an IBM 370/168 computer.

There are actually two distinct versions of QUANDRY presently in existence. The primary difference between these two versions is in the treatment of the spatial coupling coefficients. Recall that in each direction, node-averaged fluxes in three adjacent nodes and face-averaged net leakages in five adjacent nodes are coupled to obtain net leakages. Thus, in three-dimensional, two-group problems, 96 coupling coefficients must be computed and stored for each node. Since one of the objectives of this work is to demonstrate the viability of the Analytic Nodal Method for large three-dimensional problems, a severe data handling and storage problem exists. One method of circumventing this problem is to determine only those coupling coefficients that

are unique. The reduction in the number of coupling coefficients which must be treated is substantial in most computational benchmark problems. For instance, the 3-D IAEA PWR benchmark problem (25) consists of approximately 1500 nodes (with assembly-sized mesh). But only 58 unique sets of coupling coefficients exist. The version of QUANDRY which utilizes only unique coupling coefficients has a routine which searches all three directions of the spatial mesh and determines the unique combinations of compositions and mesh spacings which occur in nodal quintuplets. Use of the unique coupling coefficients practically eliminates the computational effort required to perform matrix updates during the outer iterations.

The inherent advantages of using the unique coupling coefficients are not realized in the analyses of reactors with thermal-hydraulic feedback, since each node will be characterized by a unique temperature, moderator density, etc. Hence, a version of QUANDRY which constructs coupling coefficients for each node was used to perform most of the analyses in this research. The version with unique coupling coefficients was used mainly to generate fine mesh reference solutions to problems that would otherwise exceed the available storage capacity of the IBM 370/168.

QUANDRY is capable of handling nonuniform mesh spacing and irregular geometries (jagged boundaries). An option is also available to take advantage of diagonal symmetries, such as 2-D octants. The generalized albedo boundary conditions described in Appendix 2 are incorporated into QUANDRY, but no attempt has been made as yet to

utilize the albedos except to model zero flux and zero incoming current boundary conditions.

4.2.2 Vacuum Node Transverse Leakages

One detail of the quadratic transverse leakage expansion remains to be specified. Since the node-averaged transverse leakages in three adjacent nodes are required to determine the shape of the transverse leakage within each node, a problem exists for nodes located on the reactor surface. Since a surface node does not have the third adjacent node needed to perform the leakage expansion, a fictitious "vacuum node" is assumed to be present. The transverse leakage in the vacuum node is then arbitrarily related to the leakage in the surface node to complete the leakage expansion.

For problems with water reflectors, the spatial power distribution is almost totally insensitive to the leakage in the vacuum node, hence, the vacuum node transverse leakage is assumed to be zero. The only cases in which the vacuum node leakage is of any importance are problems without reflectors. In problems with fuel-bearing compositions on the surface of the reactor, the fluxes and leakages may be quite large near the surface, and thus, the power distribution may be somewhat sensitive to the shapes of the transverse leakages. For such problems, the vacuum node transverse leakages are set equal to the negative of the transverse leakages in the surface node. The rationale for this is that since the fluxes are generally assumed to be zero on the surface, so too are the transverse leakages. Hence, this assumption

provides a means of forcing the transverse leakage expansions to have a value near zero on the surface. This practice gives good results, but it should be emphasized that the power distributions remain quite insensitive to the vacuum node transverse leakages. Since realistic reactor configurations have reflectors, the assumption that the vacuum node transverse leakages be identically zero is completely sufficient.

4.2.3 Convergence Criteria

The convergence criterion on the node-averaged fluxes which is employed in QUANDRY is a slight variation of the usual point-wise flux convergence criterion. If the power density in the ith node at the qth outer iteration is expressed as P_i^q, convergence is defined to be achieved when

$$\underset{\text{all } i}{\text{maximum over}} \left\{ \frac{\left| P_i^q - P_i^{q-1} \right|}{\bar{P}} \right\} < \varepsilon ,$$

where $\bar{P}$ is the mean reactor power density and ε is the outer iteration convergence criterion. This convergence criterion has the characteristic that it places more emphasis on convergence in regions of high power density and less emphasis on convergence in regions of low power density. In most cases, little difference is observed between this convergence criterion and strict point-wise flux convergence.

Unless stated otherwise, all 2-D problems in this research use a convergence criterion of 10^{-5}. In 3-D problems, round-off errors become significant, since QUANDRY is compiled in single precision

(32 bit word). Thus, for large 3-D problems, it is not always possible to obtain convergence to 10^{-5}. Therefore, unless stated otherwise, all 3-D problems use an outer iteration convergence criterion of 10^{-4}.

These tight convergence criteria are used so that solutions can be compared to those of other codes without the ambiguities caused by loose convergence criteria. It is worth noting, however, that spatial power distributions are quite insensitive to the convergence criterion, for $\varepsilon < 10^{-3}$.

4.2.4 Errors in Power Distributions

The static solutions to problems presented in this chapter are compared to reference solutions which are spatially converged. The nodal power densities of the reference solutions and the errors in the nodal solutions are presented in Appendix 5. For purposes of summarizing the results of the approximate solutions, tables present the maximum and average errors in nodal power densities. With the power density in the ith node defined as P_i, and the reference power density represented as P_i^{ref}, the maximum error in nodal power density is defined to be

$$\varepsilon_{max} \equiv \underset{\text{all } i}{\text{maximum over}} \left\{ \frac{\left| P_i - P_i^{ref} \right|}{P_i^{ref}} \right\} ,$$

and the average error is

$$\bar{\varepsilon} \equiv \frac{1}{V_t} \sum_i \frac{\left| P_i - P_i^{ref} \right|}{P_i^{ref}} V_i ,$$

where V_i is the volume of the ith node and V_t is the total volume of the reactor core. All power densities are normalized such that the mean reactor power density is unity.

4.2.5 Execution Times

In making comparisons between different computational methods and different computer codes, many persons express interest in problem execution times. Direct comparisons between computer codes is often difficult because execution times vary depending upon the computer in use. In order to establish rough comparisons between computers, the following execution times are considered, in this work, to be equivalent in computational effort (for heavy floating-point calculations) to one second on an IBM 370/168:

IBM 370/168	–	1.0	
IBM 370/195	–	0.4	(35)
CDC CYBER 175	–	0.57	(35)
CDC 6600	–	1.43	(35)
IBM 360/91	–	~1.0	

It cannot be overemphasized how approximate these comparisons are. Short of actually performing identical calculations on each machine, no truly satisfactory method of comparison is available.

In two-dimensional nodal calculations, execution times are so small that care must be taken to include only the time associated with solving the actual problem and not performing input/output operations.

In this publication, the execution times reported are the total CPU time consumed from the point at which the input data have been read to the point at which solution editing begins. Execution times which are quoted in subsequent chapters are all for computations performed on an IBM 370/168. Unless stated otherwise, all execution times are for the version of QUANDRY which does not make use of the unique coupling coefficients. When available, the execution times for the version with unique coupling coefficients are given in parentheses, beside the other execution times.

4.3 STATIC 2-D RESULTS

In this section, results from several 2-D benchmark problems and a more realistic checkerboard-loaded reactor are presented. All of the problems are constructed with large homogenized regions, such that very coarse spatial meshes can be used. All of the geometries and cross sections are fully specified such that modeling ambiguities do not exist.

4.3.1 The 2-D LRA BWR Two-Group Benchmark Problem

The LRA BWR test problem is a highly simplified two- or three-dimensional, two-group kinetics benchmark problem, described in Section A4.1 of Appendix 4. The reactor has a two-zone core containing 312 fuel elements, each having a width of 15 cm. The core is reflected both radially and axially by 30 cm of pure water, and the active core height is 300 cm. Control rods are represented as smeared

absorbers in four adjacent fuel assemblies. Several control rods are modeled in their fully-removed positions, and hence, the flux distribution displays severe local perturbations. Although this problem is quite unlike a commercial BWR, the severe flux peaking makes this problem more difficult to solve, in many ways, than a real BWR.

In this section, only the results of the 2-D steady-state problem are presented. This problem was solved with a uniform 15 cm spatial mesh and with octal symmetry. Table 4-1 summarizes the results of the Analytic Nodal Method with quadratic transverse leakages. The normalized assembly power densities are displayed in Fig. A5-1 of Appendix 5. The reference solution is a 16 node per assembly calculation by Shober (17), which has been shown to be spatially converged.

TABLE 4-1

Summary of Results for the 2-D LRA BWR Static Benchmark Problem with Assembly-Size Mesh

# unknowns	396
# outer iterations	41
# flux iterations/inner[a]	3
Eigenvalue[b]	0.99641
ε_{max} (%)	0.19
$\bar{\varepsilon}$ (%)	0.07
Execution time (sec, IBM 370/168)	2.7 (2.3)

[a] 1 inner iteration/outer iteration

[b] Reference: 0.99636

The errors in this problem are so small as to be essentially negligible.

Sims reports that the finite difference code MEKIN requires a 2.5 cm spatial mesh to obtain a maximum error in assembly power of five percent for the 2-D LRA problem (15). The solution time for this problem, in quarter-core geometry, is about 333 seconds on an IBM 370/168. For the 2-D LRA problem, QUANDRY appears to be able to obtain superior accuracy with an order of magnitude fewer unknowns and two orders of magnitude less computational effort than MEKIN.

4.3.2 The 2-D IAEA PWR Two-Group Benchmark Problem

The IAEA PWR test problem is a highly simplified two- or three-dimensional, two-group static benchmark problem (25), as described in Section A4.2 of Appendix 4. The reactor consists of a two-zone core containing 177 fuel assemblies each having a width of 20 cm. The core is reflected radially and axially by 20 cm of water, and the active core height is 340 cm. Each of nine fully-inserted control rods are represented as smeared absorbers in a single fuel assembly. In the three-dimensional configuration, four partially inserted rods are also modeled. The existence of inserted control rods and a water reflector gives this problem severe local flux perturbations which make the problem quite challenging.

In this section, only the results of the 2-D IAEA problem are presented. The 2-D problem was solved with 20 cm and 10 cm spatial meshes, both solutions employing octal symmetry. Table 4-2 summarizes the QUANDRY results for these two cases. The normalized

TABLE 4-2

Summary of Results for the 2-D IAEA PWR Benchmark Problem

	Mesh Spacing	
	20 X 20 cm	10 X 10 cm
# unknowns	228	762
# outer iterations	23	35
# flux iterations/inner[a]	4	6
Eigenvalue[b]	1.02962	1.02960
ε_{max} (%)	0.94	0.32
$\bar{\varepsilon}$ (%)	0.27	0.11
Execution time (sec IBM 370/168)	1.24 (0.90)	6.7 (3.2)

[a] One inner iteration per outer iteration

[b] Reference: 1.02959

assembly power densities are displayed in Fig. A5-2 of Appendix 5. The reference solution is a 3-1/3 cm nodal calculation by Wagner (26), which is spatially converged. The maximum error in assembly powers is less than one percent with an assembly-size spatial mesh. Although these errors are larger than the errors obtained in the 2-D LRA problem, the errors remain quite small. The assembly with the largest percentage error in power density is one of the low power assemblies adjacent to the reflector.

Wagner reports that finite difference methods require a spatial mesh of less than 1.25 cm to achieve similar accuracy. The finite

TABLE 4-3

Summary of Results for the 2-D IAEA PWR Benchmark Problem Obtained by Nodal Codes with 20 cm Mesh

	QUANDRY	"TWO-STEP" (17)	IQSBOX (26)	NRMT (15)
Eigenvalue [a]	1.02962	1.02970	1.02966	1.02951
ε_{max} (%)	0.94	1.6	1.4	1.9
$\bar{\varepsilon}$ (%)	0.27	0.36	—	0.5
Execution time (sec IBM 370/168)	1.24 (0.90) [b]	1.41	1.50 [c]	4.1
(Symmetry)	($\frac{1}{8}$ core)	($\frac{1}{4}$ core)	($\frac{1}{8}$ core)	($\frac{1}{4}$ core)

[a] Reference: 1.02959

[b] $\frac{1}{4}$ core execution time 1.86 (1.35)

[c] Actual time 0.86 sec (CDC CYBER 175)

difference code VENTURE requires several minutes of computer time to solve this problem with a uniform 1.25 cm mesh.(25). Therefore, as in the LRA problem, the coarse mesh nodal method appears to attain superior accuracy with approximately two orders of magnitude less computation effort than finite difference methods.

A comparison of results from several nodal methods currently in the literature is presented in Table 4-3, for the 2-D IAEA problem with assembly-size mesh. These results indicate that the Analytic Nodal Method is at least as accurate as the other nodal methods and very competitive in execution time.

4.3.3 The 2-D BIBLIS PWR Problem

The BIBLIS reactor problem (28) is a 2-D, two-group PWR with a "checkerboard" core loading pattern. Fuel assemblies with widths of approximately 23 cm and nine different compositions are present in the core which is surrounded by a 23 cm water reflector with a smeared baffle. Control rods are also present, represented by smeared absorbers in single fuel assemblies. There are two configurations of the BIBLIS problem; a "rods in" configuration, and a "rods out" configuration in which eight control rods are removed from the core. This problem is particularly interesting because it is a model of an actual operating reactor with a multi-zone core. Confidentiality considerations prohibit general distribution of the problem specifications.

Summaries of the results for a series of mesh spacings are presented in Tables 4-4 and 4-5, for the "rods in" and "rods out" configurations, respectively. Normalized assembly power densities are displayed in Fig. A5-3 and A5-4 of Appendix 5. The reference solution for the rods-withdrawn case is a 16 node per assembly calculation by Shober (17), and for the rods-inserted case is a 16 node per assembly QUANDRY calculation.

The maximum errors in assembly powers are larger than in either the LRA or IAEA problems, but are still quite small. Refinement of the spatial mesh produces substantial reduction in errors. In fact, for the BIBLIS problems, the errors appear to be proportional to at least the cube of the mesh spacing.

TABLE 4-4

Summary of Results for the 2-D BIBLIS PWR Problem, Rods-Inserted Configuration

	Spatial Mesh		
	~23 × 23 cm	~11.5 × 11.5 cm	~7.75 × 7.75 cm
# unknowns	240	810	1872
# outer iterations	31	30	37
# flux iterations/ inner[a]	5	7	12
Eigenvalue[b]	1.01971	1.01955	1.01953
ε_{max} (%)	2.59	0.22	0.06
$\bar{\varepsilon}$ (%)	0.81	0.06	0.02
Execution time[c] (sec IBM 370/168)	1.77 (1.50)	5.3 (4.6)	18.9

[a] One inner iteration per outer iteration

[b] Reference: 1.01953

[c] Octal symmetry

TABLE 4-5

Summary of Results for the 2-D BIBLIS PWR Problem, Rods-Withdrawn Configuration

	Spatial Mesh	
	~23 × 23 cm	~11.5 × 11.5 cm
# unknowns	240	810
# outer iterations	33	34
# flux iterations/inner [a]	3	5
Eigenvalue [b]	1.02530	1.02511
ε_{max} (%)	1.91	0.19
$\bar{\varepsilon}$ (%)	0.56	0.04
Execution time [c] (sec IBM 370/168)	1.50 (1.20)	6.1

[a] One inner iteration per outer iteration

[b] Reference: 1.02512

[c] Octal symmetry

Results for the BIBLIS "rods out" configuration are available for five different nodal codes currently in the literature, and a summary of these results is displayed in Table 4-6. These results give additional information to support the previous statement that the Analytic Nodal Method with quadratic transverse leakage approximations is very competitive with other nodal methods, in both accuracy and execution time. An interesting result shown in Table 4-6 is that the maximum and average errors in assembly power densities for both IQSBOX and NRMT are smaller than for QUANDRY. The transverse leakage approximations are identical in all three of these codes. QUANDRY makes no additional assumptions, but both IQSBOX and NRMT make additional polynomial approximations to the shapes of the fluxes. We conjecture that there is a fortuitous cancellation of errors in the IQSBOX and NRMT solutions which accounts for the smaller errors.

4.3.4 Summary of the 2-D Static Results

The Analytic Nodal Method with a quadratic transverse leakage approximation is capable of producing very accurate solutions to two-dimensional light water reactor problems with assembly-sized spatial meshes. The execution times for these 2-D problems are so small as to be practically negligible. Comparisons of coarse mesh nodal solutions with finite difference solutions show that the nodal methods are about two orders of magnitude more computationally efficient than finite difference methods.

TABLE 4-6

Summary of Results from Five Nodal Codes for the 2-D BIBLIS Problem, Rods-Withdrawn Configuration

	QUANDRY	"TWO-STEP" (17)	IQSBOX (26)	NRMT (15)	CUBBOX (29)
Eigenvalue [a]	1.02530	1.02549	1.02528	1.02520	1.02508
ε_{max} (%)	1.91	4.0	1.25	1.0	3.03
$\bar{\varepsilon}$ (%)	0.56	1.24	0.49	0.30	0.65
Execution time (sec IBM 370/168)	1.50 (1.20) [b]	1.66	–	3.9	–
(Symmetry)	($\frac{1}{8}$ core)	($\frac{1}{4}$ core)	–	($\frac{1}{4}$ core)	–

[a] Reference: 1.02512

[b] $\frac{1}{4}$ core execution time 2.25 (1.80)

4.4 STATIC 3-D RESULTS

In this section, results from several 3-D benchmark problems are presented. As in the 2-D problems, the geometries are constructed with large homogenized regions, such that very coarse spatial meshes can be used.

4.4.1 The 3-D Model LWR Problem

An interesting problem with which to begin the three-dimensional analyses is the static version of a transient problem by Langenbuch et al. (30). This problem, hereafter referred to as the LMW (Langenbuch-Maurer-Werner) test problem, is a highly simplified LWR, described in Section A4.5 of Appendix 4. The reactor has a two-zone core containing 77 fuel elements with widths of 20 cm. The core is reflected both radially and axially by 20 cm of water, and the active core height is 160 cm. Five control rods are parked in the upper axial reflector, and four control rods are inserted from the upper reflector to the axial midplane of the core.

The solution to the 3-D LMW test problem with a uniform 20 cm mesh in both radial and axial directions and utilizing the octal symmetry is summarized in Table 4-7. The normalized assembly power densities are given in Fig. A5-5. The reference solution is a QUANDRY calculation with a 10 cm radial mesh and a 20 cm axial mesh except in the reflectors where 10 cm meshes are used. The maximum error in nodal power densities occurs in the upper axial reflector and is less than 1.0%. The maximum error in assembly power density is less

TABLE 4-7

Summary of Results for the 3-D LMW LWR Test Problem with Assembly-Size Mesh

# unknowns	1600
# outer iterations [a]	17
# flux iterations/inner [b]	5
Eigenvalue [c]	0.99974
ε_{max} (node, %)	0.98
ε_{max} (assembly, %)	0.28
$\bar{\varepsilon}$ (assembly, %)	0.12
Execution time (sec IBM 370/168)	11.2 (8.1)

[a] Outer iteration convergence criterion: 10^{-5}

[b] 2 inner iterations per outer iteration

[c] Reference: 0.99966

than 0.3%. The results of this 3-D test problem are very similar to those obtained for 2-D problems in Section 4.3.

4.4.2 The 3-D IAEA PWR Benchmark Problem

The 3-D IAEA PWR benchmark problem was introduced in 1971 by Michaelson (31) and has proven to be a very important standard by which progress in reactor calculational methods have been measured. Following the introduction of this problem, many solutions were obtained, but very large discrepancies in these early solutions indicated

TABLE 4-8

Summary of Results for the 3-D IAEA PWR Benchmark Problem

	Mesh	
	20 X 20 X 20 cm	10 X 10 X 20 (10) cm
# unknowns	5776	21,336
# outer iterations	29	50
# flux iterations/inner [a]	5	5
Eigenvalue [b]	1.02902	1.02899
ε_{max} (node, %)	1.6	0.80
ε_{max} (assembly, %)	0.69	0.71
$\bar{\varepsilon}$ (assembly, %)	0.24	0.13
Execution time (sec IBM 370/168)	29.0 (20.0)	(150)

[a] 1 inner iteration per outer iteration

[b] Reference: 1.02903

that deficiencies existed in most multidimensional calculational methods.

The results of QUANDRY solutions to the 3-D IAEA PWR problem are summarized in Table 4-8 for two different spatial mesh configurations. The coarse mesh solution employs a 20 cm spatial mesh in the radial and axial directions. The fine mesh solution uses a 10 cm radial mesh and 20 cm axial mesh spacing, except in the axial reflectors where a 10 cm mesh spacing is used. Both calculations make use of the octal symmetry which exists in this problem. The

TABLE 4-9

Comparison of 3-D IAEA PWR Benchmark Solutions

	QUANDRY	IQSBOX (25)	VENTURE (25)
# spatial mesh points	722	722	$\sim 1.2 \times 10^6$
ε_{max} (node, %)	1.6	1.37	-3.97
ε_{max} (assembly, %)	0.69	-0.90	-2.11
$\bar{\varepsilon}$ (assembly, %)	0.24	0.28	1.0
Execution time (sec IBM 370/168)	29.0 (20.0)	35.0[a]	5.4×10^4[b]

[a] Actual time: 50 sec, CDC-6600

[b] Actual time: 2.16×10^4 sec, IBM 370/195

normalized power densities are given in Fig. A5-6.

The reference case for the 3-D IAEA problem was taken to be a finite difference solution by Vondy et al., obtained by using VENTURE (25). Vondy actually performed a series of calculations with refined mesh spacings and applied a Richardson extrapolation to obtain his reference solution, assuming that the errors were reduced with the square of the mesh spacing. The finest mesh VENTURE solution involved a 1-2/3 cm radial mesh and contained approximately 1.2 million mesh points.

Table 4-9 presents a comparison between the coarse mesh nodal solutions by QUANDRY and IQSBOX (26) and the finest mesh VENTURE solution. It is interesting to note that both of the nodal solutions have smaller errors than the finest mesh finite difference solution. In fact,

an examination of the 10 X 10 X 20 (10) cm mesh solutions by both QUANDRY and IQSBOX reveals that there is much better agreement in assembly powers between the two nodal solutions than there is between either of the nodal solutions and the VENTURE solution. A comparison of the QUANDRY and IQSBOX assembly powers is presented in Fig. A5-7, with the IQSBOX solution taken to the the reference. In light of the better agreement in solutions by the two nodal codes, it seems likely that VENTURE reference solution should not be considered to be a true reference, if the intent is to isolate errors in assembly powers of less than one percent.

The execution times quoted for VENTURE are not representative of an optimized finite difference solution because of the tight convergence criterion, the uniform radial mesh, and the use of obsolete numerical procedures. Nevertheless, the dramatic difference in execution times between VENTURE and QUANDRY does reflect on the power of the Analytic Nodal Method.

4.4.3 The 3-D LRA BWR Benchmark Problem

The 3-D LRA BWR benchmark problem was introduced as a full-core kinetics problem and has proven to be extremely difficult. The static solutions for both rod-inserted and rod-withdrawn configurations are presented in this section.

4.4.3.1 3-D LRA BWR-Control Rod Fully Inserted

A summary of results from a coarse mesh QUANDRY solution to the 3-D LRA BWR problem with control rods inserted is presented in

TABLE 4-10

Summary of Results for the 3-D LRA BWR Benchmark Problem with Control Rods Inserted

	Mesh	
	15 X 15 X 25 (15) cm	7.5 X 7.5 X 25 (15) cm
# unknowns	4224	16,192
# outer iterations	35	56
# flux iterations/inner [a]	5	5
Eigenvalue	0.99644	0.99639
ε_{max} (node, %)	-0.38	Ref.
ε_{max} (assembly, %)	-0.24	Ref.
$\bar{\varepsilon}$ (assembly, %)	0.08	Ref.
Execution time (sec IBM 370/168)	(18.7)	(110.0)

[a] 1 inner iteration per outer iteration

Table 4-10. The coarse mesh solution uses a 15 cm radial mesh spacing and an axial mesh spacing of 25 cm except in the axial reflector where a 15 cm mesh spacing is used. The reference solution is a fine mesh QUANDRY calculation with a 7.5 cm radial mesh and an axial mesh identical to that of the coarse mesh solution. Both solutions are for an octant of the reactor core and take advantage of the symmetry about the diagonals of the x-y planes. The normalized assembly power densities are displayed in Fig. A5-8 of Appendix 5.

The errors in the coarse mesh solution with assembly-size nodes are very small and quite similar to the errors obtained in the 2-D LRA

problem. This is not entirely unexpected since this 3-D LRA problem is essentially a homogeneous core in the axial direction with added reflectors. The fine mesh nodal solution cannot be considered a true reference, since it has a relatively coarse axial mesh. Nevertheless, these results demonstrate the accuracy of the Analytic Nodal Method.

4.4.3.2 3-D LRA BWR-Quarter Core, Control Rod Withdrawn

The actual 3-D LRA BWR transient is initiated by the removal of one control rod associated with four asymmetric peripheral assemblies. As a preliminary 3-D transient test, the quarter-core version of this transient (i.e., four control rods are withdrawn) is used. Therefore, examination of the errors in the spatial power distribution of this alternate problem is of interest. A summary of results from this problem is presented in Table 4-11. The spatial meshes for both the coarse and fine mesh (reference) QUANDRY solutions are identical to those described in Section 4.4.3.1. The normalized assembly powers are given in Fig. A5-9.

The errors in the coarse mesh QUANDRY solution are quite small, well under 1%, but larger than in the rods-inserted configuration. This is to be expected, since the power distribution is much more peaked in the rods-withdrawn case. The peak-to-minimum assembly-averaged power density is approximately 5 when the rod is inserted and approximately 18 when the control rod is withdrawn. From these results, it seems reasonable to conclude that the errors in assembly-averaged power densities are not significantly increased

TABLE 4-11

Summary of Results for the Quarter-Core, 3-D LRA BWR Benchmark Problem with Control Rods Withdrawn

	Mesh	
	15 X 15 X 25 (15) cm	7.5 X 7.5 X 25 (15) cm
# unknowns	4224	16,192
# outer iterations	35	39
# flux iterations/inner [a]	5	8
Eigenvalue	1.01559	1.01549
ε_{max} (node, %)	+.50	Ref.
ε_{max} (assembly, %)	+.45	Ref.
$\bar{\varepsilon}$ (assembly, %)	0.23	Ref.
Execution time (sec IBM 370/168)	(29.0)	(170.0)

[a] 1 inner iteration per outer iteration

when modest flux tilts are introduced in the 3-D LRA problem.

4.4.3.3 3-D LRA BWR-Full Core, Control Rod Withdrawn

The full core 3-D LRA BWR, with the asymmetric peripheral control rod fully removed, is a very challenging problem because of the severe flux tilt which exists across the core. Examination of spatial errors is difficult in this problem, since no reference solution exists at this time. The possibility of generating a reference solution with QUANDRY is precluded because of restrictions on the amount of computer core that can be obtained on the MIT IBM 370/168. Despite

TABLE 4-12

Summary of Results for the Full-Core, 3-D LRA BWR Benchmark Problem with Control Rods Removed

	Mesh	
	30(15) × 30(15) × 33.3(30) cm	15 × 15 × 25(30) cm
# unknowns	8,112	30,976
# outer iterations	34	61
# flux iterations/inner[a]	5	5
Eigenvalue	1.01510	1.01494
ε_{max} (assembly, %)	+3.2	Ref.
$\bar{\varepsilon}$ (assembly, %)	0.76	Ref.
Execution time (sec IBM 370/168)	45.0 (29.0)	(198.0)

[a] 1 inner iteration per outer iteration

the unfortunate lack of a reference solution, an indication of the magnitude of spatial errors can be obtained by comparing a very coarse mesh solution to a solution with assembly-size mesh. A summary of results for the 3-D LRA problem with the control rods fully removed is presented in Table 4-12. The reference solution uses 15 cm radial mesh spacing and 25 cm axial mesh spacing except in the axial reflector where 15 cm mesh spacing is used. The very coarse mesh solution uses a 30 cm radial mesh in the interior of the core, a 15 cm mesh in the two outermost fuel assemblies, and 30 cm mesh spacing in the radial reflectors. The axial mesh spacing is 33-1/3 cm in the core and 30 cm in the axial reflector. Normalized assembly power densities are

displayed in Fig. A5-10.

The errors in the normalized assembly power densities for the very coarse mesh solution are less than 3.5% for all assemblies and the average error is 0.76%. These errors are significantly larger than those exhibited in the quarter-core version of the 3-D LRA problem.

There are two significant factors which cause the decrease in accuracy. The most significant of these is the much coarser spatial mesh that is used in the full-core version. Secondly, the full-core 3-D LRA BWR problem displays a much more severe flux tilt than does the quarter-core version. In fact, the peak-to-minimum assembly-averaged power densities are approximately 2700 and 28 in the full- and quarter-core versions of the 3-D LRA problem. In light of the magnitude of the errors in the very coarse mesh solution, it seems likely that the errors in the assembly-averaged power densities are less than one percent for the coarse mesh (reference) solution.

4.4.3.4 3-D LRA BWR-Control Rod Reactivities

The static solutions to the 3-D LRA problem provide some information about the accuracy of coarse mesh predictions for control rod reactivities. Table 4-13 summarizes this information for both the full- and quarter-core configurations. These results indicate that both the coarse and very coarse mesh solutions provide very accurate predictions for control rod reactivities. The errors in the eigenvalues are somewhat sensitive to the spatial mesh, but these errors tend to be

TABLE 4-13

Control Rod Reactivities in the 3-D LRA BWR Benchmark Problem

	1/4-Core 3-D LRA		Full-Core 3-D LRA	
	Mesh		Mesh	
	Coarse	Fine	Very coarse	Coarse
Initial eigenvalue	0.996437	0.996394	0.996571	0.996437
Final eigenvalue	1.015591	1.015492	1.015056	1.014940
$\frac{\gamma_{final} - \gamma_{initial}}{\gamma_{final}}$	0.01886	0.01881	0.01821	0.01823
Error in "reactivity" of control rod	0.27%	Ref.	0.11%	Ref.

the same in both the rod-inserted and rod-withdrawn configurations. Therefore, control rod reactivities are very accurately predicted by the coarse mesh nodal method. This does not imply, however, that control rod reactivities during transients can be predicted to this accuracy. The fact that the axial position of a control rod may not correspond to nodal boundaries necessitates additional approximations. Such problems are addressed in Chapter 6.

4.4.4 General Conclusions from 3-D Results

The accuracy of the Analytic Nodal Method for 3-D problems is very similar to that of 2-D problems. If reactors can be homogenized into assembly-sized regions, the Analytic Nodal Method can be expected to yield assembly-averaged powers accurate to within 2.5% for assembly-sized spatial meshes. Static reactor eigenvalues are generally accurate to .01%. The computational efficiency of the Analytic Nodal Method, as demonstrated by the code QUANDRY, is much greater than that of finite difference methods and at least as great as other nodal methods currently in the literature.

4.5 EXAMINATION OF THE QUADRATIC TRANSVERSE LEAKAGE APPROXIMATION

The results of the two- and three-dimensional test problems, presented in the preceding two sections, indicate that the Analytic Nodal Method with the quadratic transverse leakage approximation is quite accurate. Since the leakage approximation is the only

approximation made, all of the resulting errors in power distributions, eigenvalues, etc. must be due to the inadequacy of this approximation. In order to gain insight into the deficiencies of the transverse leakage approximation, it is interesting to examine some additional 2-D problems.

4.5.1 IAEA Benchmark Problem No. 2b

The IAEA benchmark problem No. 2b (32) is a one-group, two-dimensional model of a swimming pool reactor and is described in Section A4.6 of Appendix 4. This problem is very different from any commercial power reactor and is intended to be solved by transport methods. The reactor modeled consists of a rectangular "core" region surrounded by a water reflector. The "core" region contains four rectangular quadrants. The first and third quadrants contain fissionable material, and the second and fourth quadrants contain strong absorbers but no fissionable material. The resulting quadrant-averaged fluxes have ratios of approximately 1 : 10 : 500 : 4. The large differences in quadrant-averaged fluxes make this problem very difficult to solve.

A summary of QUANDRY results for the diffusion theory approximation to the IAEA problem is given in Table 4-14. These results indicate that the coarse mesh solutions are very accurate except for the fluxes in the first quadrant. In fact, the very coarse mesh solution contains negative fluxes in some regions of the first quadrant. This implies that the transverse leakage approximation must be erroneous in some nodes, leading to negative fluxes. In addition, the existence

TABLE 4-14

Summary of Results for the One-Group IAEA Benchmark Problem No. 2

Spatial Mesh	Eigenvalue	Quadrant-Averaged Fluxes			
		1	2	3	4
12 × 12	0.99276	-.0000025	0.000342	0.01688	0.000144
16 × 16	0.99236	0.000015	0.000343	0.01687	0.000146
20 × 20	0.99222	0.000031	0.000343	0.01686	0.000146
30 × 26	0.99222	0.000035	0.000343	0.01686	0.000146

of negative fluxes also indicates that some of the numerical properties (i.e., nonnegative matrices) which exist in the limit of infinitely fine mesh spacing, do not exist in this problem with very coarse meshes. Despite the nonexistence of properties which are required to guarantee convergence of a solution, convergence difficulties were not encountered with this problem. The negative fluxes are not overly disturbing, since the problem was designed to exhibit severe flux distortions quite unlike those in power reactors. In fact, the problem was designed to test transport theory codes.

A problem which also displays erroneous leakage shapes and is of more concern is described in the following section.

4.5.2 The 2-D Zion 1 PWR Problem (with Explicit Core Baffle)

The Zion 1 problem (33) is a two-group, two-dimensional, static reactor problem in which the core baffle is explicitly modeled, as described in Section A4.7. The Zion 1 core contains a high enrichment outer zone and an inner zone which is checkboard-loaded with two lower enrichment assemblies. The entire core is surrounded by a baffle (about 2.5 cm thick) and a pure water reflector. The core baffle proves to be a very important complication in this problem.

An attempt to solve the 2-D Zion 1 problem, in a manner similar to that used for all the aforementioned problems, failed to converge. Since this was the first configuration to be attempted in which the spatial mesh contained adjacent nodes with significantly different mesh spacings, the quadratic transverse leakage expansion was suspected of causing the

difficulty. Hence, a flat transverse leakage approximation was attempted. Very rapid convergence of the problem resulted. It was also discovered that a finer spatial mesh solution, using the quadratic leakage approximation, then converged without difficulty.

The convergence difficulty of the coarse mesh Zion 1 problem is believed to be caused by unrealistic transverse leakage shapes in nodes that are adjacent to nodes which have the same mesh spacing as the baffle. The ratio of the mesh spacing in adjacent nodes is as great as 7:1. This disparity in mesh spacings requires essentially that the transverse leakage expansion fit the transverse leakages on the surfaces of the larger nodes. Since the adjacent nodes may have significantly different transverse leakages, the leakage expansion may not resemble the actual transverse leakage shape of the larger node. A very graphic example of this phenomenon, for a node with a "baffle" node on each side, is given in Fig. 4-1. The average transverse leakages in the three nodes occur in the ratios 3.5:-1:42.1. This example is admittedly severe; nevertheless, it demonstrates that the particular quadratic leakage expansion being used is incorrect. The example also indicates that a different quadratic polynomial could fit the transverse leakage quite well.

In an attempt to understand further the problems encountered when a baffle is explicitly represented, an ad hoc modification of the transverse leakage approximation was investigated. The transverse leakages in all nodes were assumed to be of the form

Figure 4-1. Transverse leakage shape for a node located between two "baffle nodes" (Zion 1, node {9,6}).

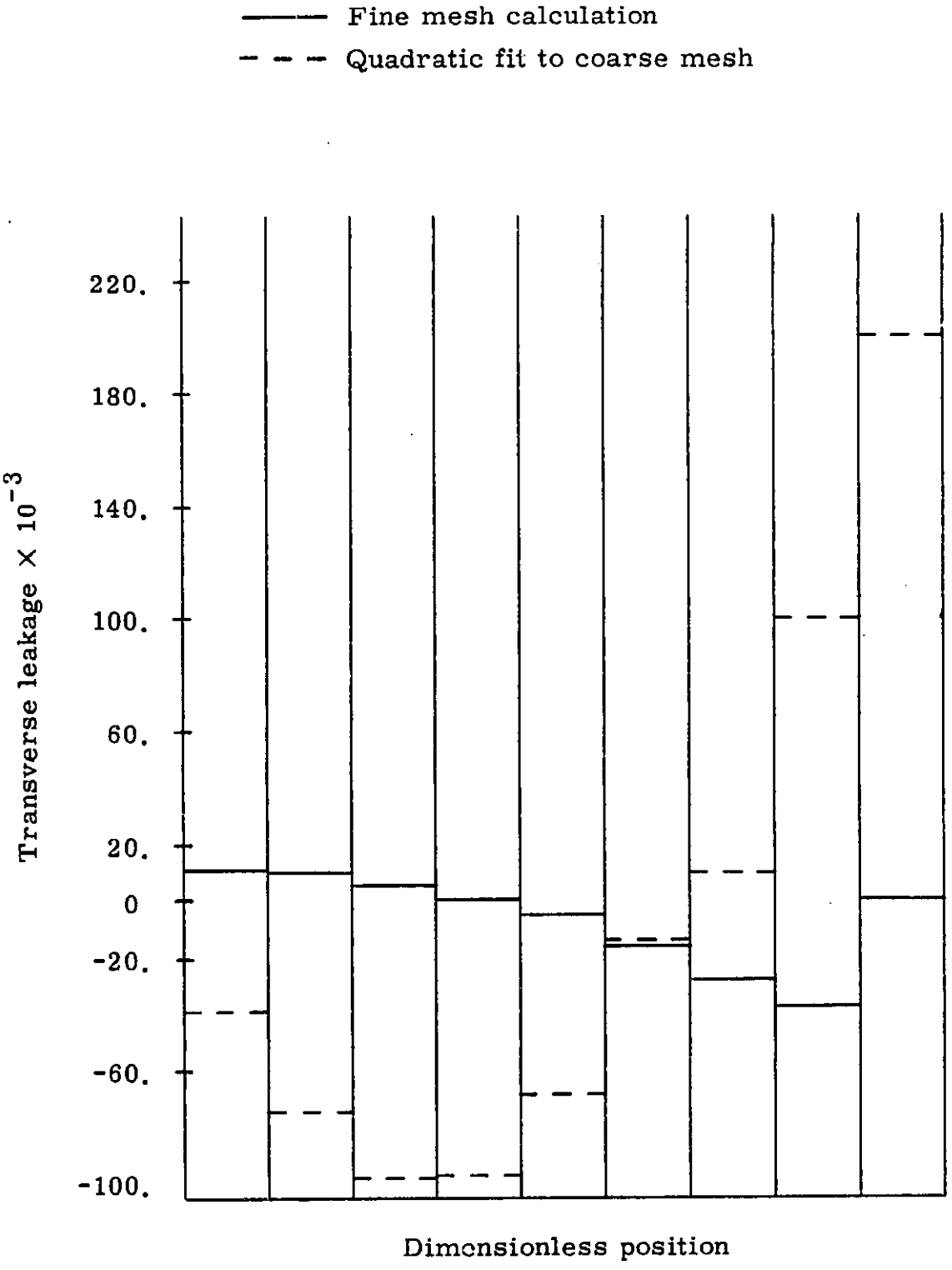

$$[S_{u_{\ell,m,n}}(u)] \cong [\bar{S}_{u_{\ell,m,n}}] + \left([\bar{S}_{u_{\ell-1,m,n}}] - [\bar{S}_{u_{\ell,m,n}}]\right) \rho^{\ell-1}_{u_\ell} \frac{h_u^{\ell-1}}{h_u^{\ell}}$$

$$+ \left([\bar{S}_{u_{\ell+1,m,n}}] - [\bar{S}_{u_{\ell,m,n}}]\right) \rho^{\ell+1}_{u_\ell} \frac{h_u^{\ell+1}}{h_u^{\ell}} \quad ; \quad u = x,y,z \,, \tag{4-1}$$

where the notation is that of Chapter 2. This approximation was chosen to reduce to the quadratic leakage approximation of Eq. 2-14, in the limit of uniform mesh spacing and to reduce to the flat leakage approximation for a node which is located between two infinitely narrow nodes.

A summary of results for the 2-D Zion 1 problem, using "modified quadratic," flat, and fine mesh quadratic transverse leakage approximations is presented in Table 4-14. The corresponding normalized power densities are displayed in Fig. A5-11. The reference solution is taken to be a 16 node per assembly QUANDRY calculation with the quadratic transverse leakage approximation of Eq. 2-14. The flat leakage solution is quite accurate, with a maximum error in assembly power density of 2.2%. The quadratic leakage solution with a 2×2 mesh per assembly is very accurate, with a maximum error in assembly power of 0.25%. The convergence difficulty encountered in the coarse mesh attempt with quadratic transverse leakages, is not exhibited when the "modified quadratic" leakage approximation is used. The accuracy of the "modified quadratic" approximation, as expected, is greater than that of the flat leakage approximation, but not as great as the fine mesh quadratic leakage approximation.

TABLE 4-15

Summary of Results for the 2-D Zion 1 PWR with Explicit Core Baffle

	Spatial Mesh		
	13 × 13	13 × 13	21 × 21
	Leakage Approximation		
	Flat	"Modified Quadratic"	Quadratic
# unknowns	546	546	1386
# outer iterations	22	22	40
# flux iterations/outer [a]	6	6	4
Eigenvalue	1.27505	1.27501	1.27489
ε_{max} (%)	2.22	1.96	0.25
$\bar{\varepsilon}$ (%)	0.79	0.59	0.06
Execution time (sec, IBM 370/168)	3.8	3.8	12.2

[a] 1 inner iteration per outer iteration

[b] Reference: 1.27489

Since explicit modeling of the core baffle significantly increases the number of unknowns in a problem, direct treatment of the baffle is probably not the approach to be favored in reactor calculations. The use of albedos to replace both the baffle and reflector is an appealing alternative to explicit modeling. Efforts to determine the appropriate albedos, compatible with the Analytical Nodal Method, are in progress at MIT (34).

4.5.3 Observations Regarding the Transverse Leakages

The inadequacy of the quadratic transverse leakage expansion in problems with explicit core baffles raises questions as to the accuracy of the approximation in general. Several very fine mesh solutions to general problems indicate that the quadratic fit to the transverse leakages is usually quite good. There are, however, some significant exceptions.

In reactor cores that have a checkerboard loading pattern with fuel assemblies of several enrichments (such as the BIBLIS and Zion 1 problems), the node-averaged transverse leakages in the interior of the core tend to be relatively constant in magnitude but oscillate in sign from node to node. Figure 4-2 shows the actual transverse leakage shape and the coarse mesh quadratic approximation to it, for a node in Zion 1. The quadratic fit is a reasonably good fit to the true shape, but it deviates by a fairly large amount near the surfaces of the node. Fortunately, the magnitude of the transverse leakage is smaller near the surface of the node than in the interior of the node. Hence, although the percentage deviations at the surfaces are large (~50%), the impact on the flux shape is thought to be relatively modest.

The transverse leakages in the reflector nodes present particularly difficult problems, since the leakages are large in magnitude and complicated in shape. Figure 4-3 illustrates the thermal transverse leakage shape and the corresponding quadratic expansion for a reflector node in the Zion 1 problem. Also plotted is the buckling approximation (see Eq. 2-8) to the transverse leakage. This figure shows quite clearly

Figure 4-2. Typical thermal transverse leakage in a checkerboard-loaded core (y-directed leakage from Zion 1, node {2,4}) with ~20 cm nodes.

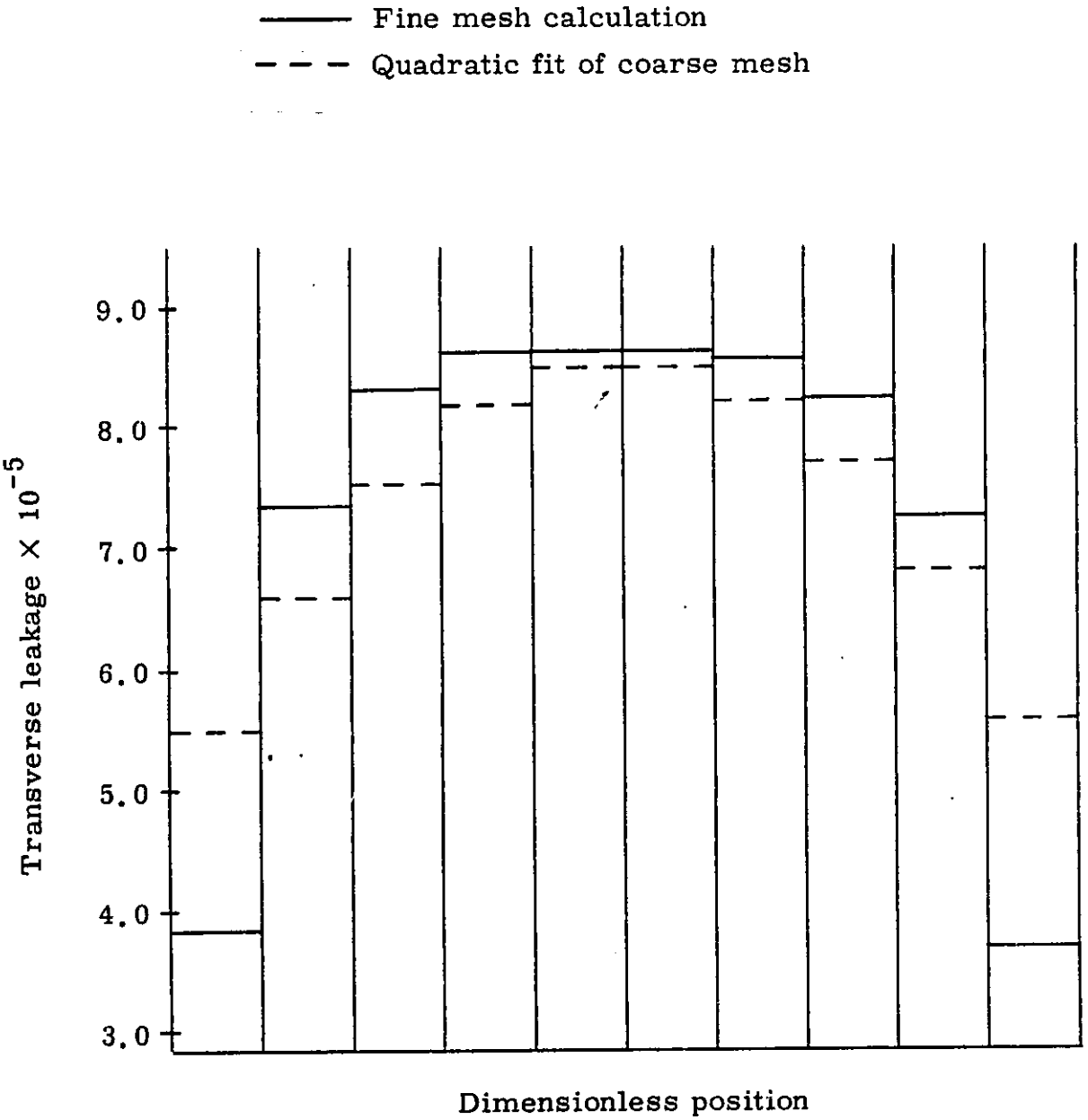

Figure 4-3. Typical thermal transverse leakage in the reflector nodes of Zion 1 (y-directed leakage, node $\{11,6\}$).

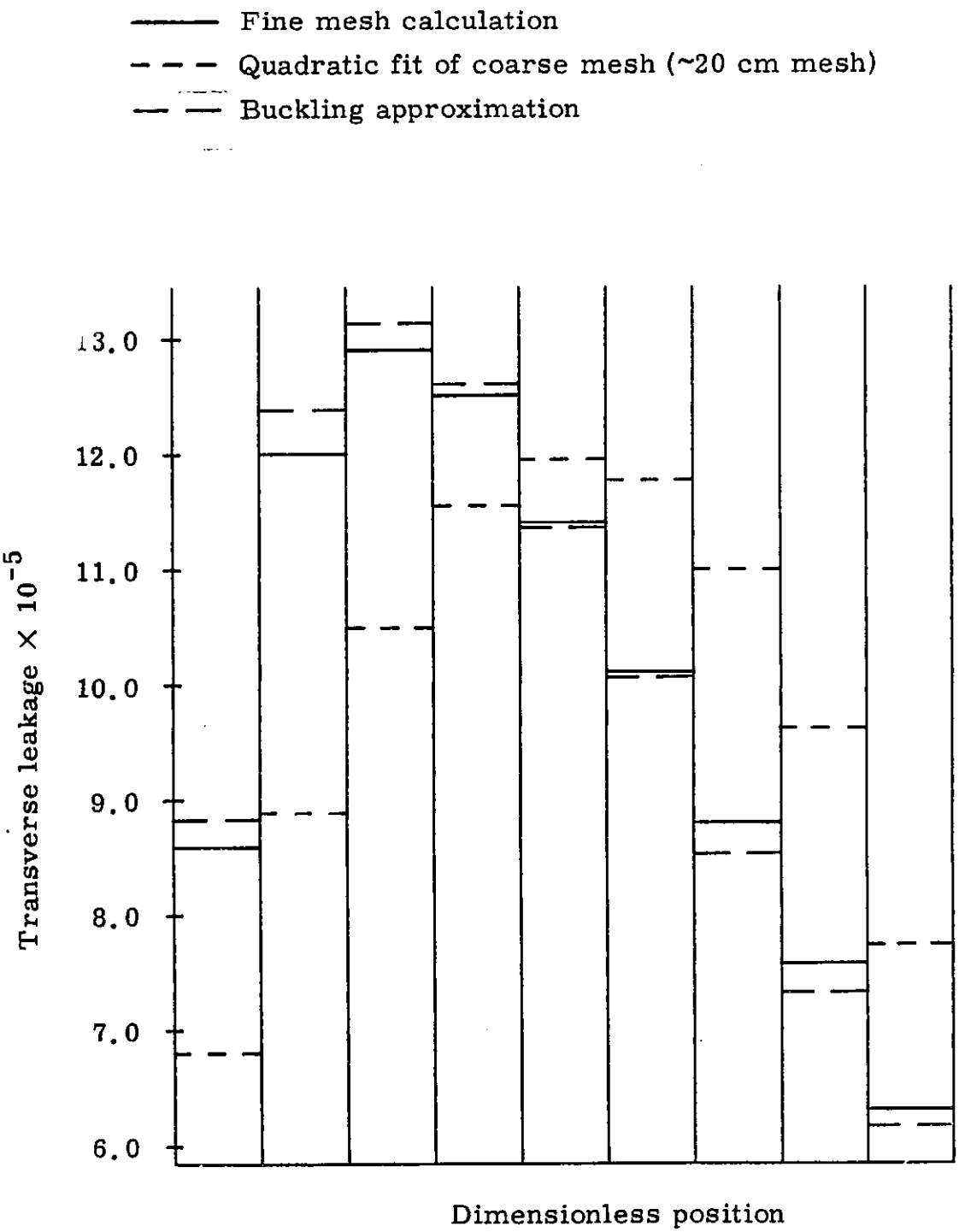

that the quadratic expansion is a poor fit to the true shape, having local errors as large as 30%. For this particular node, the buckling approximation is quite accurate, having a maximum local error of less than 3%. Figure 4-4 displays the transverse leakage approximations to the thermal transverse leakage in a reflector node of the 2-D IAEA problem. Hereto the buckling approximation is a much more accurate approximation (accurate to within 8%) than the quadratic expansion (accurate to within 50%). The thermal transverse leakage shapes depicted in Figs. 4-3 and 4-4 should not be thought to imply, however, that the buckling approximation is more accurate than the quadratic polynomial in all reflector nodes.

In the 2-D BIBLIS problem, the shapes of the thermal transverse leakages in the reflector nodes are well matched by the buckling approximation. The primary reason for this is that the reflector composition is that of a smeared baffle-reflector. Hence, the thermal neutron diffusion lengths are quite short and the thermal flux tends to be almost separable in space.

A QUANDRY calculation, employing the buckling approximation for the thermal leakage shapes in the reflector nodes and quadratic leakage approximations elsewhere, produces results very similar to those described in Section 4.3. The errors in assembly power densities near the reflector are reduced slightly (by about 0.1%) but not significantly. The primary reason for the small reduction in errors, despite the fact that the leakage fit is quite good in the reflector, is that the thermal neutron absorption rate is much larger than the thermal

Figure 4-4. Thermal transverse leakage in the reflector node $\{8,4\}$ of the 2-D IAEA PWR.

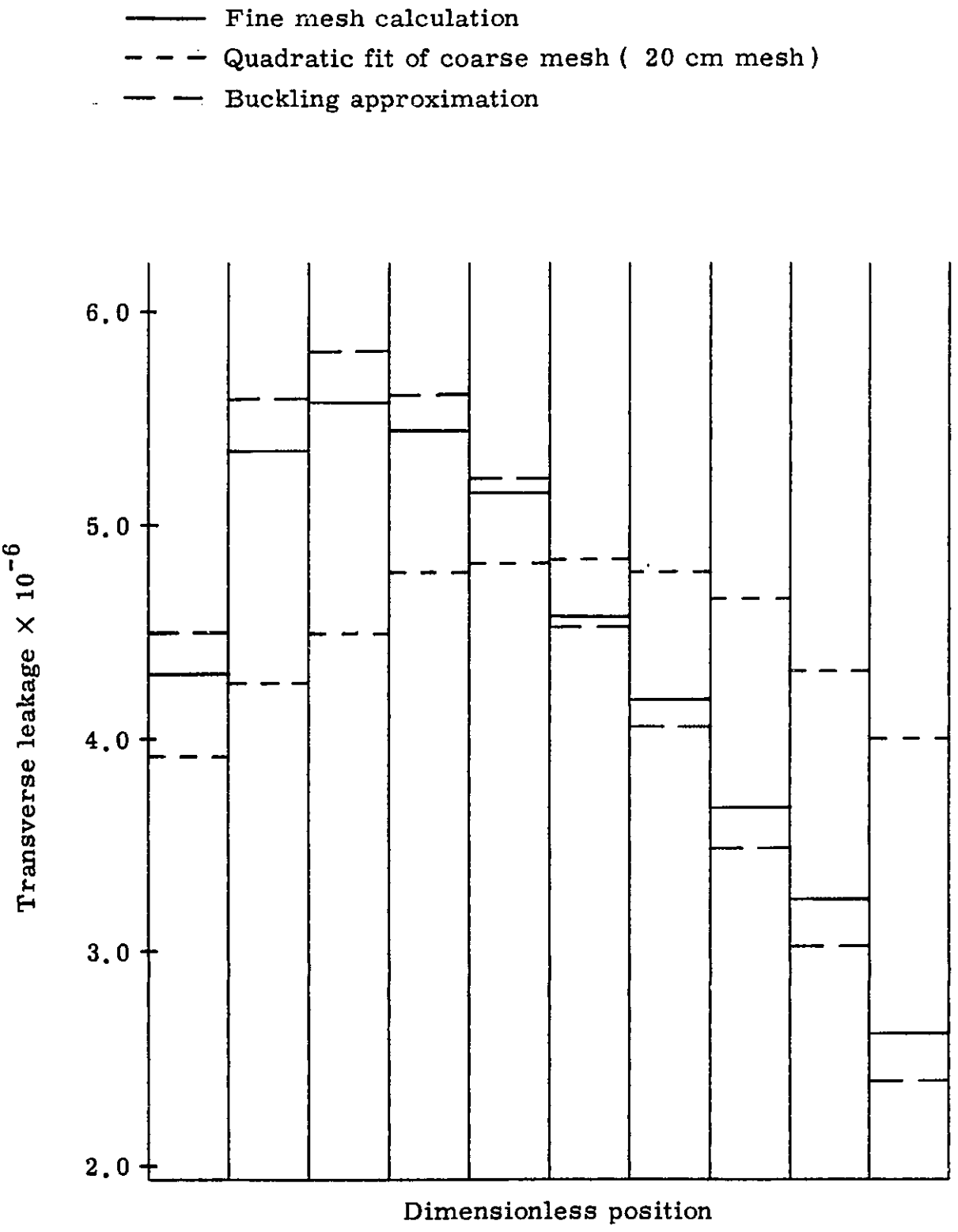

neutron leakage rate. Thus, errors in the leakage shape do not produce large changes in the thermal flux. It appears that errors in the thermal leakage shapes in smeared baffle-reflector nodes do not produce significant errors in the spatial power distributions.

In the Zion 1 problem, the buckling approximation is very accurate in the reflector nodes which have two sides bordering baffle nodes. Nevertheless, QUANDRY calculations with assembly-size mesh spacings and using the buckling approximation for the thermal transverse leakages in the aforementioned reflector nodes produce assembly powers which are only about 0.1% more accurate than those assembly powers predicted with a flat leakage approximation, even though use of the more accurate leakage approximations changes the average thermal leakages and thermal fluxes in the reflector nodes by as much as 9.% and 3.%, respectively. The presence of the highly-absorbing core baffle seems to minimize the propogation of the errors in thermal flux back into the core region.

The 2-D IAEA problem has only two nodes within which the buckling approximation is quite accurate. A QUANDRY calculation which uses the more accurate transverse leakage approximation in these two nodes changes the average thermal leakages and thermal fluxes by as much as 4.% and 2.%, respectively. The corresponding changes in core power densities are as large as 0.67%. The relatively large changes in core power densities which occur as a result of modifying the leakage approximation in only two of the reflector nodes, indicate that the 2-D IAEA solution is quite sensitive to errors in the thermal

leakage shapes in the reflector nodes.

The following generalizations about the transverse leakage approximation of Eq. 2-14 are based on detailed examination of leakages in several problems:

1. Errors in the leakage shapes generally produce small errors in the reactor power densities.

2. Cores with checkerboard loading patterns have transverse leakages which oscillate in sign from node to node, and the quadratic leakage expansion is only a moderately good fit.

3. The thermal transverse leakages in reflector nodes are not well approximated by the quadratic expansion.

4. Errors in power densities, which are due to inadequacies in reflector transverse leakages, are most pronounced in reactors with pure water reflectors and much less pronounced in reactors with explicit or smeared core baffles.

5. The largest errors in the quadratic transverse leakage shapes occur near nodal boundaries.

6. Most nodes in which the quadratic leakage shapes of Eq. 2-14 are seriously in error can nevertheless be fit quite well by <u>some</u> quadratic polynomial.

7. Information about local values of the transverse leakages <u>within a node</u> would be much more valuable in determining

the leakage shapes than out-of-node information about the transverse leakages.

Since there is no immediately obvious candidate for an improved transverse leakage approximation, the leakage expansion of Eq. 2-14 is used in the remainder of this work.

4.6 SUMMARY

In this chapter, the results of many two- and three-dimensional static reactor problems were presented. The Analytic Nodal Method with a quadratic transverse leakage approximation was shown to be a very accurate and highly efficient method for solving the multidimensional, two-group static diffusion equation, provided that reactors can be homogenized over large spatial regions (i.e., assemblies).

The Analytic Nodal Method was shown to require significantly fewer unknowns than finite difference methods to achieve equivalent accuracy. The nodal method was also demonstrated to be at least two orders of magnitude more computationally efficient than finite difference methods. The Analytic Nodal Method was also shown to be at least as computationally efficient as other nodal methods which are currently in the literature.

In the following two chapters, the Analytic Nodal Method will be extended to the time-dependent case.

Chapter 5

TRANSIENT APPLICATION OF THE ANALYTIC NODAL METHOD

5.1 INTRODUCTION

In the first four chapters, the Analytic Nodal Method was derived for the solution of the two-group, static diffusion equations for multi-dimensional reactors consisting of homogenized Cartesian nodes. The only approximation required in the derivation was that the transverse leakages could be fit by quadratic polynomials. Efficient numerical solution procedures were developed and a large number of two- and three-dimensional LWR test problems were solved. In all of the test cases, the Analytic Nodal Method was shown to have a very high degree of accuracy while employing assembly-sized spatial meshes. Comparison of solutions with finite difference and finite element methods revealed that the nodal method was at least two orders of magnitude more computationally efficient than the more conventional methods.

It is desirable to take advantage of the power of the Analytical Nodal Method to solve transient diffusion problems as well. In this chapter, the three-dimensional, temorally- and spatially-discretized Analytic Nodal diffusion equations are derived, and a simple thermal-hydraulic feedback model is introduced. An algorithm for solving these

neutronic and thermal-hydraulic equations in tandem is presented. Solutions to many two- and three-dimensional transients, with and without thermal-hydraulic feedback, are presented in Chapter 6.

5.2 FORMULATION OF TRANSIENT NODAL DIFFUSION EQUATIONS

The time- and space-dependent multigroup neutron diffusion equations, Eqs. 1-1, can be cast in matrix form as

$$\underline{\nabla}\cdot[D(\underline{r},t)]\underline{\nabla}[\phi(\underline{r},t)] - [\Sigma_T(\underline{r},t)][\phi(\underline{r},t)]$$
$$+ (1-\beta)[\chi_p]\frac{1}{\gamma}[\nu\Sigma_f(\underline{r},t)]^T[\phi(\underline{r},t)] + \sum_{d=1}^{D}\lambda_d[\chi_d]C_d(\underline{r},t)$$
$$= [v]^{-1}\frac{\partial}{\partial t}[\phi(\underline{r},t)] \ , \qquad (5\text{-}1a)$$

$$\beta_d\frac{1}{\gamma}[\nu\Sigma_f(\underline{r},t)]^T[\phi(\underline{r},t)] - \lambda_d C_d(\underline{r},t) = \frac{\partial}{\partial t}C_d(\underline{r},t) \ ; \quad d = 1,2,\ldots,D, \qquad (5\text{-}1b)$$

where

$$[\Sigma_T(\underline{r},t)] \equiv [\Sigma_t(\underline{r},t)] - [\Sigma_{gg'}(\underline{r},t)]$$

The time-dependent nodal balance equations are found by integrating Eqs. 5-1 over the volume of an arbitrary node (i, j, k) to obtain

$$-h_y^j h_z^k\left([J_{x_{i+1,j,k}}(t)] - [J_{x_{i,j,k}}(t)]\right) - h_x^i h_z^k\left([J_{y_{i,j+1,k}}(t)] - [J_{y_{i,j,k}}(t)]\right)$$

$$-h_x^i h_y^j\left([J_{z_{i,j,k+1}}(t)] - [J_{z_{i,j,k}}(t)]\right) - V_{i,j,k}[\Sigma_{T_{i,j,k}}(t)][\bar{\phi}_{i,j,k}(t)]$$

$$+(1-\beta)V_{i,j,k}[\chi_p]\frac{1}{\gamma}[\nu\Sigma_{f_{i,j,k}}(t)]^T[\bar{\phi}_{i,j,k}(t)] + \sum_{d=1}^{D}\lambda_d V_{i,j,k}[\chi_d]\bar{C}_{d_{i,j,k}}(t)$$

$$= V_{i,j,k}[v]^{-1}\frac{\partial}{\partial t}[\bar{\phi}_{i,j,k}(t)] \qquad (5\text{-}2a)$$

$$\beta_d\frac{1}{\gamma}[\nu\Sigma_{f_{i,j,k}}(t)]^T[\bar{\phi}_{i,j,k}(t)] - \lambda_d\bar{C}_{d_{i,j,k}}(t) = \frac{\partial}{\partial t}\bar{C}_{d_{i,j,k}}(t); \quad d=1,2,\ldots,D, \qquad (5\text{-}2b)$$

where

$$[J_{u_{i,j,k}}(t)] \equiv -\frac{1}{h_v^m h_w^n}[D_{i,j,k}(t)]\frac{\partial}{\partial u}\int_{v_m}^{v_{m+1}}dv\int_{w_n}^{w_{n+1}}dw\,[\phi(u_\ell,v,w,t)];$$

$$u = x,y,x$$

$$v \neq u$$

$$w \neq u \neq v$$

$$[\bar{\phi}_{i,j,k}(t)] \equiv \frac{1}{V_{i,j,k}}\int_{x_i}^{x_{i+1}}dx\int_{y_j}^{y_{j+1}}dy\int_{z_k}^{z_{k+1}}dz\,[\phi(x,y,x,t)]$$

$$\bar{C}_{d_{i,j,k}}(t) \equiv \frac{1}{V_{i,j,k}}\int_{x_i}^{x_{i+1}}dx\int_{y_j}^{y_{j+1}}dy\int_{z_k}^{z_{k+1}}dz\,C_d(x,y,z,t)\,.$$

A differential equation from which the spatial coupling of Eq. 5-2a can be determined is derived by integrating Eqs. 5-1

over the two directions transverse to direction u, to obtain for node (ℓ,m,n),

$$-[D_{\ell,m,n}(t)]\frac{\partial^2}{\partial u^2}[\phi_{u_{\ell,m,n}}(u,t)] - \frac{1}{h_v^m h_w^n}[D_{\ell,m,n}(t)]\int_{v_m}^{v_{m+1}} dv \int_{w_n}^{w_{n+1}} \times \frac{\partial^2}{\partial v^2}[\phi(u,v,w,t)] - \frac{1}{h_v^m h_w^n}[D_{\ell,m,n}(t)]\int_{v_m}^{v_{m+1}} dv \int_{w_n}^{w_{n+1}} dw \frac{\partial^2}{\partial w^2}[\phi(u,v,w,t)]$$

$$+\left\langle [\Sigma_{T_{\ell,m,n}}(t)] + [\omega_{p_{\ell,m,n}}(t)][v]^{-1} - \left\{ (1-\beta)[\chi_p] + \sum_{d=1}^{D} \frac{\lambda_d \beta_d}{(\omega_{d_{\ell,m,n}}(t)+\lambda_d)}[\chi_d] \right\} \frac{1}{\gamma}[\nu\Sigma_{f_{\ell,m,n}}(t)]^T \right\rangle [\phi_{u_{\ell,m,n}}(u,t)] = 0 \ , \tag{5-3}$$

where

$$[\phi_{u_{\ell,m,n}}(u,t)] \equiv \frac{1}{h_v^m h_w^n}\int_{v_m}^{v_{m+1}} dv \int_{w_n}^{w_{n+1}} dw\, [\phi(u,v,w,t)] \ ,$$

and the time derivatives have been replaced by

$$\frac{\partial}{\partial t}[\phi_{u_{\ell,m,n}}(u,t)] = [\omega_{p_{\ell,m,n}}(t)][\phi_{u_{\ell,m,n}}(u,t)]$$

$$\frac{\partial}{\partial t} C_{d_{\ell,m,n}}(u,t) = \omega_{d_{\ell,m,n}}(t) C_{d_{\ell,m,n}}(u,t) \ ,$$

where $[\omega_{p_{\ell,m,n}}(t)]$ is a diagonal G X G matrix.

Equation 5-3 is the transient counterpart to the static flux-leakage coupling equation, Eq. 2-7. Using the notation of Chapter 2 for the transverse leakages, Eq. 5-3 can be written as

$$-[D_{\ell,m,n}(t)]\frac{\partial^2}{\partial u^2}[\phi_{u_{\ell,m,n}}(u,t)]+\left\langle[\Sigma_{T_{\ell,m,n}}(t)]+[\omega_{p_{\ell,m,n}}(t)][v]^{-1}\right.$$

$$\left.-\left\{(1-\beta)[\chi_p]+\sum_{d=1}^{D}\frac{\lambda_d\beta_d}{(\omega_{d_{\ell,m,n}}(t)+\lambda_d)}[\chi_d]\right\}\frac{1}{\gamma}[\nu\Sigma_{f_{\ell,m,n}}(t)]^T\right\rangle[\phi_{u_{\ell,m,n}}(u,t)]$$

$$=-[S_{u_{\ell,m,n}}(u,t)]\ ;\qquad u=x,y,z\ . \tag{5-4}$$

For a fixed time, t, this equation can be solved analytically (provided the ω_p's and ω_d's are known) in the same manner as in Chapter 2, by expanding the transverse leakages in quadratic polynomials. Hence, the transient flux-leakage coupling equation is given by an equation analogous to Eq. 2-19,

$$\begin{aligned}[\bar{L}_{u_{\ell,m,n}}(t)] &= [F^{\ell-1}_{u_{\ell,m,n}}(t)][\bar{\phi}_{\ell-1,m,n}(t)]+[F^{\ell}_{u_{\ell,m,n}}(t)][\bar{\phi}_{\ell,m,n}(t)]\\ &+[F^{\ell+1}_{u_{\ell,m,n}}(t)][\bar{\phi}_{\ell+1,m,n}(t)]+[G^{\ell-2}_{u_{\ell,m,n}}(t)][\bar{S}_{u_{\ell-2,m,n}}(t)]\\ &+[G^{\ell-1}_{u_{\ell,m,n}}(t)][\bar{S}_{u_{\ell-1,m,n}}(t)]+[G^{\ell}_{u_{\ell,m,n}}(t)][\bar{S}_{u_{\ell,m,n}}(t)]\\ &+[G^{\ell+1}_{u_{\ell,m,n}}(t)][\bar{S}_{u_{\ell+1,m,n}}(t)]+[G^{\ell+2}_{u_{\ell,m,n}}(t)][\bar{S}_{u_{\ell+2,m,n}}(t)];\\ &\qquad u=x,y,z\ . \end{aligned}\tag{5-5}$$

The matrix elements of Eq. 5-5 are different from those in the static equation, Eq. 2-19, since these elements depend upon the kinetic distortion terms.

Using the notation of Chapter 2, Eq. 5-5 and Eqs. 5-2 can be combined to obtain the transient Analytic Nodal diffusion equations,

$$\begin{bmatrix} [V]^{-1} & [0] & [0] & [0] \\ [0] & [0] & [0] & [0] \\ [0] & [0] & [0] & [0] \\ [0] & [0] & [0] & [0] \end{bmatrix} \frac{d}{dt} \begin{bmatrix} [\bar{\phi}(t)] \\ [\bar{L}_x(t)] \\ [\bar{L}_y(t)] \\ [\bar{L}_z(t)] \end{bmatrix}$$

$$= \begin{bmatrix} [F(t)] - (h_z^k[G_y(t)] + h_y^j[G_z(t)]) & -(h_z^k[G_x(t)] + h_x^i[G_z(t)]) & -(h_y^j[G_x(t)] + h_x^i[G_y(t)]) \\ [F_x(t)] & -[I] & \frac{1}{h_y^j}[G_x(t)] \quad \frac{1}{h_z^k}[G_x(t)] \\ [F_y(t)] & \frac{1}{h_x^i}[G_y(t)] & -[I] \quad \frac{1}{h_z^k}[G_y(t)] \\ [F_z(t)] & \frac{1}{h_x^i}[G_z(t)] & \frac{1}{h_y^i}[G_z(t)] \quad -[I] \end{bmatrix}$$

$$\times \begin{bmatrix} [\bar{\phi}(t)] \\ [\bar{L}_x(t)] \\ [\bar{L}_y(t)] \\ [\bar{L}_z(t)] \end{bmatrix} + \sum_{d=1}^{D} \begin{bmatrix} [V_{i,j,k}[\chi_d]\lambda_d \bar{C}_{d_{i,j,k}}(t)] \\ [0] \\ [0] \\ [0] \end{bmatrix}, \qquad (5\text{-}6)$$

where

$$[F(t)] \equiv \left(-[\Sigma_T(t)] - h_y^j h_z^k [F_x(t)] - h_x^i h_z^k [F_y(t)] - h_x^i h_y^j [F_z(t)] + [M(t)]\right)$$

$$[M(t)] \equiv \left\{(1-\beta) V_{i,j,k} [\chi_p] \frac{1}{\gamma} [\nu\Sigma_{f_{i,j,k}}(t)]^T\right\}$$

$$[V]^{-1} \equiv \text{diag}\left\{V_{i,j,k}[v]^{-1}\right\}$$

Equations 5-6 and 5-2b represent the global system of equations which must be solved to obtain the time- and space-dependent reactor power distributions.

5.3 TIME INTEGRATION METHOD

Equations 5-6 represent a system of spatially-discretized, time-dependent ordinary differential equations. Of the four blocks of Eq. 5-6, only the first involves a temporal operator. The latter three blocks are simply expressions for the transverse leakages at time t and do not involve temporal operators. Hence, any time integration scheme which approximates the temporal derivatives of Eq. 5-2b and the first block of Eq. 5-6 can be employed to solve the time-dependent equations. If solutions to the transient nodal diffusion equations are desired only at discrete times, a finite difference approximation to the temporal derivatives can be used.

5.3.1 Theta Method for Time Integration

Let it be desired to approximate the solutions to the transient nodal diffusion equations at the times

$$t = t_0, t_1, t_2, \ldots ,$$

where time intervals are defined as

$$\Delta t_n \equiv t_{n+1} - t_n .$$

Equation 5-2b and the first block of Eq. 5-6 can be written in a much simpler form as

$$[V]^{-1} \frac{d}{dt} [\bar{\phi}(t)] = [F(t)][\bar{\phi}(t)] - [\mathcal{L}(t)] + \sum_{d=1}^{D} \lambda_d [\bar{C}_d(t)] \qquad (5\text{-}7a)$$

$$\frac{\partial}{\partial t} [\bar{C}_d(t)] = [M_d(t)][\bar{\phi}(t)] - \lambda_d [\bar{C}_d(t)] ; \quad d = 1, 2, \ldots, D , \qquad (5\text{-}7b)$$

where

$$[\mathcal{L}(t)] \equiv \left(h_z^k [G_y(t)] + h_y^j [G_z(t)] \right) [\bar{L}_x(t)]$$
$$+ \left(h_z^k [G_x(t)] + h_x^i [G_z(t)] \right) [\bar{L}_y(t)]$$
$$+ \left(h_y^j [G_x(t)] + h_x^i [G_y(t)] \right) [\bar{L}_z(t)]$$

$$[\bar{C}_d(t)] \equiv \text{col} \left\{ V_{i,j,k} [\chi_d] \bar{C}_{d_{i,j,k}}(t) \right\}$$

$$[M_d(t)] \equiv \left\{ V_{i,j,k} \beta_d [\chi_d] \frac{1}{\gamma} [\nu \Sigma_{f_{i,j,k}}(t)]^T \right\} .$$

Equations 5-7 can be differenced using the theta method (36) to obtain the approximations

$$[V]^{-1}\frac{1}{\Delta t_n}\{[\bar{\phi}]^{n+1}-[\bar{\phi}]^n\} = \theta_f[F]^{n+1}[\bar{\phi}]^{n+1}+(1-\theta_f)[F]^n[\bar{\phi}]^n$$
$$-\theta_f[\mathcal{L}]^{n+1}-(1-\theta_f)[\mathcal{L}]^n$$
$$+\sum_{d=1}^{D}\lambda_d\{\theta_p[\bar{C}_d]^{n+1}+(1-\theta_p)[\bar{C}_d]^n\} \qquad (5\text{-}8a)$$

$$\frac{1}{\Delta t_n}\{[\bar{C}_d]^{n+1}-[\bar{C}_d]^n\} = \theta_f[M_d]^{n+1}[\bar{\phi}]^{n+1}+(1-\theta_f)[M_d]^n[\bar{\phi}]^n$$
$$-\lambda_d\{\theta_p[\bar{C}_d]^{n+1}+(1-\theta_p)[\bar{C}_d]^n\}\ ;$$
$$d = 1,2,\ldots,D, \qquad (5\text{-}8b)$$

where two "thetas" have been employed, θ_f for the prompt source (flux) terms and θ_p for the delayed (precursor) terms. Equation 5-8b can be rearranged to obtain

$$[\bar{C}_d]^{n+1} = (1+\lambda_d\Delta t_n\theta_p)^{-1}\langle\{1-\lambda_d\Delta t_n(1-\theta_p)\}[\bar{C}_d]^n$$
$$+\Delta t_n\{\theta_f[M_d]^{n+1}[\bar{\phi}]^{n+1}+(1-\theta_f)[M_d]^n[\bar{\phi}]^n\}\rangle\ ;$$
$$d = 1,2,\ldots,D\ . \qquad (5\text{-}9)$$

Equation 5-9 can be substituted into Eq. 5-8a, and the resulting equation can be solved for $[\bar{\phi}]^{n+1}$. Performing the substitution and some subsequent rearrangement yields

$$\left\langle \left\{ \frac{1}{\Delta t_n \theta_f} [V]^{-1} - [F]^{n+1} - \sum_{d=1}^{D} \frac{\lambda_d \Delta t_n \theta_p}{(1+\lambda_d \Delta t_n \theta_p)} [M_d]^{n+1} \right\} \theta_f \right\rangle [\bar{\phi}]^{n+1}$$

$$= -\theta_f [\mathcal{L}]^{n+1} - (1-\theta_f)[\mathcal{L}]^n$$

$$+ \left\{ \frac{1}{\Delta t_n (1-\theta_f)} [V]^{-1} + [F]^n \right.$$

$$\left. + \sum_{d=1}^{D} \frac{\lambda_d \Delta t_n \theta_p}{(1+\lambda_d \Delta t_n \theta_p)} [M_d]^n \right\} (1-\theta_f)[\bar{\phi}]^n$$

$$+ \sum_{d=1}^{D} \frac{\lambda_d}{(1+\lambda_d \Delta t_n \theta_p)} [\bar{C}_d]^n . \qquad (5\text{-}10)$$

Equations 5-9 and 5-10 do not completely specify the temporal integration scheme. In order to advance the node-averaged fluxes from one time step to the next by use of Eq. 5-10, $[\mathcal{L}]^{n+1}$ must be known. Since $[\mathcal{L}]^{n+1}$ depends upon $[\bar{\phi}]^{n+1}$, it is not possible to solve directly for $[\bar{\phi}]^{n+1}$ in terms of quantities which are known from time step n. The overall transient iterative process is much easier to visualize if Eqs. 5-6, 5-9, and 5-10 are combined to obtain the full set of temporally- and spatially-discretized Analytic Nodal diffusion equations:

$$\begin{bmatrix} [P]^{n+1} - \theta_f\left(h_z^k[G_y]^{n+1} + h_y^j[G_z]^{n+1}\right) & -\theta_f\left(h_z^k[G_x]^{n+1} + h_x^i[G_z]^{n+1}\right) & -\theta_f\left(h_y^j[G_x]^{n+1} + h_x^i[G_y]^{n+1}\right) \\ [F_x]^{n+1} & -[I] & \frac{1}{h_y^j}[G_x]^{n+1} & \frac{1}{h_z^k}[G_x]^{n+1} \\ [F_y]^{n+1} & \frac{1}{h_x^i}[G_y]^{n+1} & -[I] & \frac{1}{h_z^k}[G_y]^{n+1} \\ [F_z]^{n+1} & \frac{1}{h_x^i}[G_z]^{n+1} & \frac{1}{h_y^j}[G_z]^{n+1} & -[I] \end{bmatrix} \begin{bmatrix} [\bar{\phi}]^{n+1} \\ [\bar{L}_x]^{n+1} \\ [\bar{L}_y]^{n+1} \\ [\bar{L}_z]^{n+1} \end{bmatrix}$$

$$= \begin{bmatrix} [Q]^n - (1-\theta_f)\left(h_z^k[G_y]^n + h_y^i[G_z]^n\right) & -(1-\theta_f)\left(h_z^k[G_x]^n + h_x^i[G_z]^n\right) & -(1-\theta_f)\left(h_y^j[G_x]^n + h_x^i[G_y]^n\right) \\ [0] & [0] & [0] & [0] \\ [0] & [0] & [0] & [0] \\ [0] & [0] & [0] & [0] \end{bmatrix} \begin{bmatrix} [\bar{\phi}]^n \\ [\bar{L}_x]^n \\ [\bar{L}_y]^n \\ [\bar{L}_z]^n \end{bmatrix}$$

$$+ \begin{bmatrix} \sum_{d=1}^{D} \left(\frac{\lambda_d}{(1+\lambda_d \Delta t_n \theta_p)} [\bar{C}_d]^n \right) \\ [0] \\ [0] \\ [0] \end{bmatrix}, \qquad (5\text{-}11)$$

$$[\bar{C}_d]^{n+1} = (1+\lambda_d \Delta t_n \theta_p)^{-1} \langle \{1 - \lambda_d \Delta t_n (1-\theta_p)\} [\bar{C}_d]^n$$

$$+ \Delta t_n \{\theta_f [M_d]^{n+1} [\bar{\phi}]^{n+1} + (1-\theta_f)[M_d]^n [\bar{\phi}]^n\} \rangle \; ;$$

$$d = 1, 2, \ldots, D, \qquad (5\text{-}9)$$

where

$$[P]^{n+1} \equiv \left\{ \frac{1}{\Delta t_n \theta_f} [V]^{-1} - [F]^{n+1} - \sum_{d=1}^{D} \frac{\lambda_d \Delta t_n \theta_p}{(1+\lambda_d \Delta t_n \theta_p)} [M_d]^{n+1} \right\} \theta_f$$

$$[Q]^n \equiv \left\{ \frac{1}{\Delta t_n (1-\theta_f)} [V]^{-1} + [F]^n + \sum_{d=1}^{D} \frac{\lambda_d \Delta t_n \theta_p}{(1+\lambda_d \Delta t_n \theta_p)} [M_d]^n \right\} (1-\theta_f) \; .$$

From Eq. 5-11, it is apparent that in order to advance from one time step to the next, a (4*G*N) × (4*G*N) matrix must (in principle) be inverted. The details of the iterative inversion process are provided in Section 5.6, following the description of feedback and control models.

5.4 THERMAL-HYDRAULIC FEEDBACK

Since the ultimate goal of this research is to develop a neutronics package which is capable of modeling successfully severe LWR accident scenarios, it is important that the neutronics solution method not be adversely affected by nonlinear reactor thermal-hydraulic feedback. The reactor safety analysis code, MEKIN, uses the COBRA thermal-hydraulic package as its feedback model (37). Our interest, at present, is not so much in accurate solutions to realistic coupled neutronic, thermal-hydraulic problems, but rather in accurate neutronic solutions to problems with feedback effects. The use of a complicated thermal-

hydraulic model (such as COBRA) to test the transient nodal method with feedback seems quite unnecessary. Therefore, the much simpler WIGL (36) lumped heat capacity model is used as the fundamental feedback mechanism for testing the neutronics solution methods.

5.4.1 The WIGL Model

The WIGL thermal-hydraulic model has three primary quantities of interest in each node: the average fuel temperature, the average coolant temperature, and the average coolant density. By performing time-dependent energy balances on the fuel and coolant in node (i, j, k) and by assuming that no boiling occurs, the following equations can be derived:

$$\frac{d\bar{T}^f_{i,j,k}}{dt} = \frac{1}{\rho^f C^f}\left\{(1-r)q'''_{i,j,k} - \frac{V^c_{i,j,k}}{V^f_{i,j,k}}\left[\frac{1}{A_h U} + \frac{1}{A_h h_0\left(\frac{W}{W_0}\right)^{.8}}\right]^{-1}\left(\bar{T}^f_{i,j,k} - \bar{T}^c_{i,j,k}\right)\right\}, \tag{5-12a}$$

$$\frac{d\bar{T}^c_{i,j,k}}{dt} = \left(\frac{\partial \rho^c H}{\partial \bar{T}^c}\right)^{-1}\left\{\left[\frac{1}{A_h U} + \frac{1}{A_h h_0\left(\frac{W}{W_0}\right)^{.8}}\right]^{-1}\left(\bar{T}^f_{i,j,k} - \bar{T}^c_{i,j,k}\right) + \frac{2W^r_{i,j,k}C^c}{V^c_{i,j,k}}\left(T^b_{i,j,k} - \bar{T}^c_{i,j,k}\right) + rq'''_{i,j,k}\frac{V^f_{i,j,k}}{V^c_{i,j,k}}\right\}, \tag{5-12b}$$

$$T^b_{i,j,k} = 2\bar{T}^c_{i,j,k-1} - T^b_{i,j,k-1} \quad , \tag{5-12c}$$

where

$\bar{T}^f_{i,j,k}$ ≡ average fuel temperature in node (i,j,k)

$\bar{T}^c_{i,j,k}$ ≡ average coolant temperature in node (i,j,k)

$T^b_{i,j,k}$ ≡ inlet (bottom) coolant temperature of node (i,j,k)

t ≡ time

ρ^f ≡ density of the fuel

ρ^c ≡ density of coolant

C^f ≡ specific heat of the fuel

C^c ≡ specific heat of the coolant

r ≡ fraction of fission power which is deposited directly into the coolant

$q'''_{i,j,k}$ ≡ volumetric energy generation rate in node (i,j,k)

$V^c_{i,j,k}$ ≡ volume of coolant in node (i,j,k)

$V^f_{i,j,k}$ ≡ volume of fuel in node (i,j,k)

A_h ≡ total heat transfer area/total coolant volume within a node

h_0 ≡ heat transfer coefficient at initial flow rate

W_0 ≡ total coolant mass flow rate into core at t = 0.0

W ≡ total coolant mass flow rate into core

$\left(\frac{\partial \rho^c H}{\partial \bar{T}^c}\right)$ ≡ energy required to raise the average temperature of a unit volume of coolant by one temperature unit

U ≡ conductivity/conduction lengths of the fuel, gap, and cladding (i.e., the inverse of the resistance to heat flow)

$W^r_{i,j,k}$ ≡ coolant mass flow rate through node (i,j,k).

For sake of simplicity, the thermal-hydraulic equations are solved using a fully-implicit temporal differencing scheme, with the same temporal mesh as the neutronic equations. Following evaluation of the core-wide fuel and coolant temperatures, the coolant density is evaluated using the STATE subroutine, taken from THERMIT (38), with uniform pressure assumed throughout the reactor core.

5.4.2 Cross Section Feedback

Feedback from the thermal-hydraulic equations to the neutronic equations is accomplished by assuming that all macroscopic cross sections (and inverse diffusion coefficients) are linear functions of the three thermal-hydraulic variables. That is, the cross sections are assumed to obey equations of the form

$$\Sigma_{\alpha_{i,j,k}} = \Sigma^*_{\alpha_{i,j,k}} + \left(\frac{\partial \Sigma_\alpha}{\partial \bar{T}^c}\right)\left(\bar{T}^c_{i,j,k} - \bar{T}^{c*}\right) + \left(\frac{\partial \Sigma_\alpha}{\partial \bar{T}^f}\right)\left(\bar{T}^f_{i,j,k} - \bar{T}^{f*}\right) + \left(\frac{\partial \Sigma_\alpha}{\partial \rho^c}\right)\left(\rho^c_{i,j,k} - \rho^*\right), \qquad (5\text{-}13)$$

where the starred quantities refer to reference conditions. It is

recognized that actual cross sections can be described accurately by Eq. 5-13, only over limited ranges of temperatures and densities. Since our objective is to provide feedback and not to accurately model the behavior of cross sections, the linear functional form of the cross sections is assumed to be valid over the entire range of thermal-hydraulic variables. Therefore, if the partial derivatives of the macroscopic cross sections are known, the thermal-hydraulic feedback model can be completely specified.

5.5 TRANSIENT CONTROL MECHANISMS

Since the reactor is assumed to be in a steady-state (critical) configuration prior to modeling subsequent transient behavior, some perturbation of the critical configuration must be made in order to initiate a transient. This perturbation can take any one of several forms.

Perhaps the simplest mechanism for inducing a transient in a critical reactor is to alter the positions of the control rods. In the Analytic Nodal Method, control rod motions are modeled as spatially-uniform changes in macroscopic cross sections within individual nodes. This restriction is necessary, since the spatial coupling equations of Chapter 2 are solved analytically only for the case of uniform material properties within a node. If true equivalent homogenized parameters are available, this restriction is inconsequential. However, if one is approximating the equivalent homogenized parameters, the use of spatially flat cross sections to model control rods which are partially

removed from a node may lead to inaccurate solutions.

For the sake of simplicity, the cross sections for a partially-rodded node can be assumed to be the volume-weighted average of the fully-rodded and fully-unrodded nodal cross sections. This approximation will be erroneous, unless the neutron flux is spatially flat within the node. In cases where the flux is not spatially flat, the transient solution may display a cusp-like behavior which results from over and under predictions of the differential control rod "worth" as control rods are removed from each node. Despite the shortcomings of this control rod model, it is incorporated into the transient neutronics model. The control rod cusping problem is discussed in some detail in Chapter 6.

The simple thermal-hydraulic model discussed in Section 5.4 permits two additicnal mechanisms for inducing transients. The reactor coolant inlet temperature can be varied as a function of time (to simulate such occurrences as the startup of a cold loop). Also, the coolant flow rate can be altered as a function of time (to model pump coast downs, etc.). Both of these control mechanisms alter the steady-state balance between neutronic and thermal-hydraulic conditions in the core, and hence a transient is induced.

5.6 TRANSIENT SOLUTION TECHNIQUES

The full set of temporally- and spatially-discretized Analytic Nodal diffusion equations are given by Eqs. 5-9 and 5-11. To advance the solution from one time step to the next requires that the (4*G*N)

× (4*G*N) coefficient matrix be inverted. The details of how this inversion is accomplished are very important to the computational efficiency of the method. Also, many of the elements of the coefficient matrix vary because of feedback effects. Hence, these matrix elements must (in principle) be recalculated at each time step, a procedure that requires considerable computational effort. This section provides the details of a transient solution technique aimed at minimizing the computational effort required to solve the transient equations.

5.6.1 Matrix Updating

The complicated matrices in Eq. 5.11 arise from the analytic solutions to the leakage equation, Eq. 5-4. Numerical experience indicates that approximately 0.0016 cpu seconds/node/direction (IBM-370/168) are required to update these matrices. If these matrices are updated at each time step, the computational effort expended in the updating process will dominate the total transient solution time. Since the matrices to be updated directly affect the leakages from a node and not the interaction rates within the node, it may be unnecessary to recompute matrices at each time step. In fact, in problems without feedback, the only dependencies of the matrices are on the local ω_p's, ω_d's, and the control rod motions. When feedback is present, the leakage matrices do depend on the feedback, but their impact on the transient solution is much less than that of the altered interaction rates which are also caused by the feedback. From these observations, the following general procedure has been developed for matrix updating:

1. The "rows" and "columns" in which a control rod is moved are updated at every time step to insure proper calculation of "reactivity" effects.

2. Complete matrix updating is performed every 3 to 10 time steps, depending on the type of feedback. (If there is no thermal-hydraulic feedback, the matrices can be updated very infrequently because they depend only on the ω_p's and ω_d's, which change quite slowly.)

Specific examples of the matrix updating effects are contained in Chapter 6.

5.6.2 Frequency Estimations

Since the leakage coupling matrices obtained by solving Eq. 5-4 depend on ω_p and ω_d, it is necessary to estimate these quantities. These frequencies are identical with those required in frequency transformation methods (39), and the same approximation used there can be applied to the case at hand. That is, at time step n, the frequencies are assumed to be given by the expressions

$$\omega^n_{p_{g_{i,j,k}}} \equiv \frac{1}{\Delta t_{n-1}} \ln\left(\frac{\bar{\phi}^n_{g_{i,j,k}}}{\bar{\phi}^{n-1}_{g_{i,j,k}}}\right),$$

$$\omega^n_{d_{i,j,k}} \equiv \frac{1}{\Delta t_{n-1}} \ln\left(\frac{\bar{C}^n_{d_{i,j,k}}}{\bar{C}^{n-1}_{d_{i,j,k}}}\right). \qquad (5\text{-}14)$$

In all but the most rapidly changing transients, the frequencies play a very minor role. This behavior is very different from that observed with frequency transform methods. However, this is to be expected since here the frequencies affect only the leakage rates and not the interaction rates.

5.6.3 Matrix Inversion

The matrix in Eq. 5-11 which must be inverted at each time step has a structure identical with that of the matrix inverted at each outer iteration in the steady-state problem (Eq. 3-12). Hence, the same strategy is employed to invert the coefficient matrix in the transient problem, and details are contained in Chapter 3.

In solving the steady-state problem, it was found that performing one inner iteration per outer iteration was adequate. In the transient case, it also appears possible to perform only one inner iteration per time step, provided that reasonable estimates of the leakages at the advanced time step are available. These estimates of the leakages are obtained by using the estimated space-dependent frequencies, given by Eq. 5-14, to extrapolate the leakages. That is, the leakages at time step $n+1$ are approximated by

$$[\bar{L}_{u_{i,j,k}}]^{n+1} = [\bar{L}_{u_{i,j,k}}]^{n} \cdot e^{[\omega_{p_{i,j,k}}]^{n} \cdot \Delta t_n} \quad ; \; u = x,y,z . \qquad (5\text{-}15)$$

Since the leakages terms in the nodal balance equations are generally small in magnitude compared to the flux terms, the errors introduced

when only one inner iteration is performed are generally quite acceptable. Numerical examples which verify this hypothesis are presented in Chapter 6.

The flux iterations performed at each inner iteration are identical with those of the steady-state problem. To facilitate rapid convergence of the node-averaged fluxes at each time step, the fluxes are extrapolated to the advanced time step in the same manner as the leakages,

$$[\bar{\phi}_{i,j,k}]^{n+1} = [\bar{\phi}_{i,j,k}]^{n} \cdot e^{[\omega_{p_{i,j,k}}]^{n} \cdot \Delta t_n} . \qquad (5\text{-}16)$$

In most transient problems, less than five flux iterations are required to achieve an error reduction of 10^{-3} in node-averaged fluxes. A larger number of flux iterations may be required when extrapolated fluxes are poor estimates of the actual fluxes. Such erroneous extrapolations can occur when sudden movements of control rods take place or in time domains near local power extrema. Nevertheless, the extrapolation procedure significantly reduces the computational effort required to solve the transient nodal diffusion equations.

The Cyclic Chebyshev Semi-Iterative flux iterations require knowledge of the spectral radius of the Gauss-Seidel flux iteration matrix. This spectral radius varies significantly with material properties and time step size. Hence, for effective use of this acceleration technique, the spectral radius of the Gauss-Seidel flux iteration matrix must be reestimated during the transient. To facilitate this

reestimation, the transient problem is split into time domains within which the time step size remains constant. At the beginning of each time domain, the spectral radius is estimated by the procedure described in Section 3.3.5. For most transient problems, the spectral radius of the Gauss-Seidel iteration matrix varies over the range of approximately 0.8 to 0.95.

At each inner iteration, it is desirable to achieve some user-specified, minimum acceptable convergence without performing an unnecessarily large number of iterations. For simplicity, convergence at each inner iteration is defined to be achieved when

$$\varepsilon > \frac{1}{N} \sum_{n} \left| \frac{P_n^r}{P_n^{r-1}} - 1 \right|, \qquad (5\text{-}16)$$

where

P_n^r is the power in node n at the rth flux iteration

N is the total number of power-producing nodes

ε is the user-specified convergence criteria.

The number of flux iterations required to achieve the desired degree of convergence could have been estimated by using the spectral radius information as was done in Section 3.4.1, but this procedure neglects the advantages of extrapolating the fluxes and leads to an over-estimate of the required number of flux iterations. Examining the actual error reduction at each inner iteration also minimizes the effects of off-optimum acceleration parameters, since the iterative process

continues until the desired degree of convergence is achieved. The leakage calculation at each inner iteration requires about as much computational effort as five flux iterations. Hence, a minimum of five flux iterations are performed at each inner iteration, to maintain a balance between the two.

5.6.4 Transient Solution Algorithm

A description of the transient solution algorithm is outlined below:

1. Choose the times (0, T_1, T_2, T_3, ..., T_I) which divide the transient problem into domains within which Δt, θ_f, θ_p, and ε are constants.
2. Assume $[\vec{\phi}]^n$, $[\overline{L}_u]^n$, $[\overline{C}_d]^n$, $[\omega_p]^n$, $[\omega_d]^n$, $[\overline{T}^c]^n$, $[\overline{T}^f]^n$, and $[\rho^c]^n$ are known at time t_n.
3. If $t_n = T_i$, change Δt, θ_f, θ_p, and ε to correspond to those of time domain i+1. Calculate new CCSI optimization parameters.
4. Alter cross sections to correspond to control rod positions at time t_{n+1}.
5. Calculate new matrix elements (full or partial update).
6. Obtain approximations for $[\vec{\phi}]^{n+1}$, $[\overline{L}_u]^{n+1}$ by extrapolating with Eqs. 5-15 and 5-16.
7. Solve Eq. 5-11 iteratively for $[\bar{\phi}]^{n+1}$ and $[\overline{L}_u]^{n+1}$.

8. Solve Eq. 5-9 for $[\overline{C}_d]^{n+1}$.

9. Calculate new frequencies, $[\omega_p]^{n+1}$, $[\omega_d]^{n+1}$, with Eq. 5-14.

10. Solve thermal-hydraulic equations, Eqs. 5-12, for $[\overline{T}^f]^{n+1}$, $[\overline{T}^c]^{n+1}$, and $[\rho]^{n+1}$.

11. Calculate new cross sections from Eq. 5-13.

12. Repeat steps 3-11 for each time step until the end of the last time domain.

5.7 SUMMARY

In this chapter, the three-dimensional, temporally- and spatially-discretized Analytic Nodal diffusion equations were derived by employing a Theta method time integration scheme. A simple lumped heat capacity thermal-hydraulic model with cross section feedback was also introduced. An efficient algorithm for solving the neutronic and thermal-hydraulic equations in tandem was detailed. This algorithm made use of many of the iterative procedures developed for the solution of the steady-state problem.

The methods described in this chapter are applied to several two- and three-dimensional transient problems in Chapter 6. Transients, both with and without thermal-hydraulic feedback, are examined. The effects of spatial, temporal, and iterative convergence are investigated, and conclusions about the accuracy and efficiency of the Analytic Nodal Method are presented. Comparisons of the Analytic Nodal Method with conventional finite difference methods and other nodal methods are also presented.

Chapter 6

TRANSIENT RESULTS

6.1 INTRODUCTION

In Chapter 5, the spatially- and temporally-discretized Analytic Nodal diffusion equations were derived. A method for solving these equations was detailed for the two-group case.

In this chapter, the transient Analytic Nodal Method is applied to several two- and three-dimensional LWR benchmark problems. A parametric study of transient variables is presented and "optimum" choices for the transient variables are determined. The problems of control rod "cusping" which were described in Chapter 5 are addressed, and a simple scheme for reducing the cusping errors is introduced. Results from several problems are presented, including the full-core LRA BWR transient benchmark problem.

6.2 THE TWIGL TWO-DIMENSIONAL SEED-BLANKET REACTOR PROBLEMS

This test problem is a two-dimensional model of a 160 cm square unreflected seed-blanket reactor. The problem is modeled with two neutron energy groups, one delayed precursor family, and eighth-core symmetry. A complete problem description is contained in Appendix A4.4. Transient solutions were originally obtained by Hageman and

Yasinsky (40) for step and ramp positive reactivity insertions in the corner seed assemblies. This test problem is sufficiently small to allow systematic examination of spatial, temporal, and numerical convergence, as well as other effects peculiar to the Analytic Nodal Method.

The static TWIGL configuration was solved with two different spatial meshes, denoted as "coarse" and "fine" meshes. The mesh structures are defined as follows:

Region	Coarse Mesh	Fine Mesh
$0 \leq x,y \leq 24$ cm	12 cm	8 cm
$24 \leq x,y \leq 56$ cm	16 cm	8 cm
$56 \leq x,y \leq 80$ cm	12 cm	8 cm

The static results for the two mesh structures are summarized in Table 6-1, where the maximum and average errors in assembly powers are identical to those defined in Chapter 4. These results indicate that the coarse mesh static solution is very accurate and the fine mesh solution is essentially spatially converged.

The TWIGL transient with ramp reactivity insertion (modeled by a change in the thermal absorption cross section in the corner seed assemblies) provides the basis for a parametric study of transient variables. The base case for the parametric study is a QUANDRY solution with the following choice of variables:

Spatial mesh – coarse

Flux theta (θ_f) – 1.0

Number of inner iterations per step – 1

Transient convergence criterion – 10^{-3}

Time step size – 5 ms

Number of steps per matrix update – 1

Precursor theta (θ_p) – 0.5

TABLE 6-1

Summary of Static Results for the TWIGL Two-Dimensional Seed-Blanket Test Problem

	Mesh	
	Coarse	Fine
# unknowns	126	330
# outer iterations	20	25
# flux iterations/inner[a]	5	10
Eigenvalue	0.91323	0.91321
ε_{max} (%)	0.11	Ref.
$\bar{\varepsilon}$ (%)	0.025	Ref.
Execution time (sec, IBM 370/168)	0.6	2.6

[a] 1 inner iteration per outer iteration.

Prior to examination of the actual transient solution accuracy, it is enlightening to investigate the sensitivity of the transient nodal solution to various parameters. In each of the calculations, the initial reactor power is normalized to unity, and one parameter at a time is altered from the base case.

6.2.1 TWIGL Sensitivity Study

The total reactor power as a function of time is displayed in Table 6-2 for flux thetas of 0.5, 0.75, and 1.0. Computing times are also reported. It is seen that the degree of implicitness alters the accuracy of the solution by as much as two percent. On the basis of temporal truncation error, one would expect that the solution with $\theta_f = 0.5$ (i.e., Crank-Nicolson) to be more accurate than the fully-implicit solution (22). This, however, is not the case. Also, one would expect the flux iteration matrix to have a smaller spectral radius for $\theta_f = 0.5$ than for $\theta_f = 1.0$ and hence a reduced execution time. This, also, is not the case.

TABLE 6-2

Total Power Versus Time for the 2-D TWIGL Seed-Blanket Reactor Problem (Ramp Perturbation): Sensitivity to Theta (θ_f)

	θ_f			
Time(s)	0.5	0.75	1.0	Ref.
0.0	1.0	1.0	1.0	1.0
0.1	1.288	1.307	1.306	1.307
0.2	1.920	1.949	1.948	1.957
0.3	2.049	2.066	2.056	2.074
0.4	2.058	2.082	2.093	2.092
0.5	2.078	2.101	2.110	2.109
Execution time(s)	13.5	11.6	10.8	

The reasons for this peculiar behavior are difficult to pinpoint, but they are thought to be related to stability problems. For conventional spatial finite difference methods, the Theta method time integration scheme can be shown to be unconditionally stable for $0.5 \leq \theta_f \leq 1.0$ (4). The proof of stability relies on the fact that the flux iteration matrix is positive definite (22). Recall from Chapter 3 that the flux iteration matrix in the Analytic Nodal Method may not be positive definite in the general case. A closer examination of the transient nodal solution with $\theta_f = 0.5$ reveals that the solution consists of small oscillations superimposed on the actual solution. The oscillations change sign at each time step, and hence, the extrapolation procedure is not effective in predicting fluxes and leakages at the advanced time steps. Consequently, more iterations are required to converge the fluxes, and the total execution time is longer than that of the fully-implicit solution which displays no oscillatory behavior.

In light of the stability problems in the TWIGL test case, it seems prudent to employ the fully-implicit approximation which avoids possible stability problems. The semi-implicit approximations may prove useful if one chooses the time step size sufficiently small to insure stability. All transient solutions in the remainder of this chapter make use of the fully-implicit time integration method.

The effects of performing multiple inner iterations per time step on the transient nodal solution are shown in Table 6-3. The advantages of additional inner iterations are quite negligible, and, in fact, the improvement in the transient power history is actually due to the increased

TABLE 6-3

Total Power Versus Time for the 2-D TWIGL Seed-Blanket Reactor Problem (Ramp Perturbation): Sensitivity to Number of Inner Iterations Per Step

	# Inner Iterations/Step		
Time(s)	1	2	3
0.1	1.306	1.306	1.306
0.2	1.948	1.953	1.953
0.3	2.056	2.073	2.071
0.4	2.093	2.091	2.088
0.5	2.110	2.109	2.106
Execution time(s)	10.8	11.4	13.4

numerical convergence obtained when multiple inner iterations are used. In light of these results (and similar results for more complicated transients), the general practice of performing one inner iteration per time step has been adopted.

The sensitivity of the transient nodal solution to the transient numerical convergence criterion is shown in Table 6-4 for convergence criteria of 10^{-2}, 10^{-3}, 10^{-4}, and 10^{-5}. The power history is seen to be quite insensitive to the transient convergence criteria. The results for a convergence criterion of 10^{-2} are somewhat deceptive, in that a minimum of five flux iterations have been performed, and convergence to 10^{-3} has been achieved at most time steps. From these results, it would appear that a convergence criterion of 10^{-3} will give better than one percent accuracy in total power throughout the transient.

TABLE 6-4

Total Power Versus Time for 2-D TWIGL Seed-Blanket Reactor Problem (Ramp Perturbation): Sensitivity to Transient Convergence Criterion

Time(s)	Convergence Criterion 10^{-2}	10^{-3}	10^{-4}	10^{-5}
0.0	1.0	1.0	1.0	1.0
0.1	1.306	1.306	1.305	1.308
0.2	1.948	1.948	1.954	1.959
0.3	2.056	2.056	2.075	2.075
0.4	2.093	2.093	2.092	2.092
0.5	2.110	2.110	2.109	2.109
Execution time(s)	9.5	10.8	10.8	12.1

Temporal truncation effects on the nodal solution are displayed in Table 6-5 for time steps sizes of 10, 5, and 2.5 ms. The 10 ms solution displays an oscillatory behavior, which results in a significantly inaccurate solution. The oscillatory behavior is caused by a combination of large time step size, loose convergence criterion, and use of the extrapolation procedure. If any one of these three factors is eliminated, the oscillations cease. Similar oscillations were encountered by Sims (15) with his polynomial nodal method. A simple solution to this problem is to decrease the convergence criterion when going to coarser temporal meshes.

TABLE 6-5

Total Power Versus Time for 2-D TWIGL Seed-Blanket Reactor Problem (Ramp Perturbation): Sensitivity to Time Step Size

Time(s)	Time Step Size 10 ms	5 ms	2.5 ms
0.1	1.314	1.306	1.308
0.2	1.905	1.948	1.956
0.3	2.113	2.056	2.075
0.4	2.069	2.093	2.092
0.5	2.119	2.110	2.109
Execution time(s)	5.5	10.8	21.0

Approximately 60% of the computational effort expended in the base case solution is spent updating the spatial coupling matrices. If the matrices are not recomputed at each time step, a significant reduction in computational effort is achieved. Table 6-6 displays the transient solution when the matrices are updated every 1, 3, 5, and 10 time steps. Note that there is a steady degradation of the solution with decreasing frequency of matrix updates. There is, however, a very substantial reduction in execution time for any reduction in updating frequency. Additional considerations in matrix updating are addressed in the following section.

The results of several fine spatial mesh solutions to the TWIGL problem are summarized in Table 6-7. The only result which appears unlike the results of the coarse mesh cases is that the solution with a

TABLE 6-6

Total Power Versus Time for 2-D TWIGL Seed-Blanket Reactor Problem (Ramp Perturbation): Sensitivity to Matrix Updating Frequency

	# Steps/Update			
Time(s)	10	5	3	1
0.1	1.160	1.260	1.284	1.306
0.2	1.660	1.862	1.899	1.948
0.3	2.070	2.059	2.057	2.056
0.4	2.089	2.093	2.093	2.093
0.5	2.106	2.109	2.109	2.110
Execution time(s)	4.1	4.5	5.6	10.8

time step size of 5 ms and a convergence criterion of 10^{-3} displays an oscillatory behavior. This can be attributed to the fact that the transverse leakages play a more significant role in the fine mesh solution than in the coarse mesh case. Thus, to obtain accurate leakages, the fluxes must be well-converged. Consequently, the case with decreased convergence criterion does not display the oscillation. The fine mesh TWIGL configuration has 8 cm node widths. In problems with assembly-size mesh (15 to 20 cm), this oscillation is not expected to be exhibited when a transient convergence criterion of 10^{-3} is employed.

TABLE 6-7

Total Power Versus Time for 2-D TWIGL Seed-Blanket Reactor Problem
(Ramp Perturbation, Fine Spatial Mesh)

Time(s)	Time Step Size: / Convergence: / # Inners/Step:	5 ms / 10^{-3} / 1	2.5 ms / 10^{-3} / 1	5 ms / 10^{-3} / 2	2.5 ms / 10^{-3} / 2	5 ms / 10^{-5} / 1	2.5 ms / 10^{-5} / 1
0.0		1.0	1.0	1.0	1.0	1.0	1.0
0.1		1.314	1.304	1.313	1.307	1.308	1.307
0.2		1.908	1.949	1.942	1.955	1.959	1.957
0.3		2.197	2.056	2.057	2.075	2.077	2.074
0.4		2.025	2.090	2.107	2.092	2.090	2.092
0.5		2.150	2.109	2.106	2.110	2.110	2.109
Execution time(s)		26.7	52.0	30.0	64.5	34.7	56.0[a]

[a] Reference

6.2.2 Optimized TWIGL Solutions

The information obtained in the sensitivity study permits one to make reasonable choices for the transient variables and to obtain solutions which do not waste computational effort. "Optimized" solutions for the TWIGL seed-blanket reactor problem for both step and ramp perturbations are obtained with the following choice of transient variables:

	Step	Ramp
Flux theta	1.0	1.0
Precursor theta	0.5	0.5
Time step size	10 ms	5 ms
Transient convergence criterion	10^{-3}	10^{-3}
Inner iterations/step	1	1
Steps/update ($t < .25$)	3	1
Steps/update ($t > .25$)	10	5
Mesh	Coarse	Coarse

Note that the matrix updating frequency is chosen to be less in the step perturbation case than in the ramp case because the reactor properties are not changing with time, and the matrices depend only on the spatial omegas (ω_p, ω_d).

A comparison of the solutions obtained with QUANDRY, CUBBOX (30), and by Shober (16) (2DTD) is contained in Table 6-8. These results indicate that the QUANDRY solution is consistently the most accurate of the solutions. The maximum errors in perturbed region

TABLE 6-8

Total Power Versus Time for 2-D TWIGL Seed-Blanket Reactor Problems (Coarse Mesh)

Ramp Perturbation, Δt = 5 ms

	Code			
Time(s)	2DTD	CUBBOX	QUANDRY	Ref.
0.0	1.000	1.000	1.000	1.000
0.1	1.305	1.321	1.305	1.307
0.2	1.951	1.985	1.954	1.957
0.3	2.064	2.074	2.074	2.074
0.4	2.081	2.092	2.092	2.096
0.5	2.098	2.109	2.109	2.109

Step Perturbation, Δt = 10 ms

	Code		
Time(s)	2DTD	QUANDRY	Ref.
0.0	1.000	1.000	1.000
0.1	2.051	2.064	2.061
0.2	2.068	2.076	2.078
0.3	2.085	2.095	2.095
0.4	2.102	2.112	2.113
0.5	2.119	2.130	2.131

power at t = 0.5 sec are less than 0.1% and 1.4% in the step perturbation case and 0.1% and 0.6% in the ramp perturbation case for QUANDRY and 2DTD, respectively. The results obtained with the TWIGL code are not readily comparable because they consist of pointwise powers only. Comparison with Sims' solutions is not possible, as he modeled the TWIGL problem with a zero incoming current boundary condition.

It is possible, however, to obtain comparisons of execution times for the two TWIGL problems. The TWIGL calculation is for a full-core model with 8 cm spatial mesh obtained on a CDC 6600 computer which is approximately 0.7 times slower than the IBM 370/168 computer. By dividing the TWIGL execution times (40) by 4 to approximate quarter-core times and normalizing to the IBM 370/168, a comparison of execution times can be made. This comparison is displayed in Table 6-9. The QUANDRY and 2DTD execution times are seen to be roughly comparable. Sims' (NRMT) solutions and the TWIGL solutions are seen to be much longer running than the others. The TWIGL solution, however, using an 8 cm mesh, should be much less accurate than the nodal solutions. In fact, the initial eigenvalues are 0.91419, 0.91368, and 0.91323, for TWIGL, 2DTD, and QUANDRY, respectively. In light of the error in the TWIGL eigenvalue, it seems very likely that the errors in the TWIGL powers are quite large.

The TWIGL seed-blanket reactor problem demonstrates that the transient Analytic Nodal Method can obtain accurate transient solutions with coarse spatial and temporal meshes. However, the TWIGL problem does not exhibit radical changes in spatial flux shapes, and hence,

TABLE 6-9

Execution Time Comparison for 2-D TWIGL Seed-Blanket Reactor Problems (Coarse Mesh)

Problem	Code	Time Step	Execution Time (sec)
Ramp	QUANDRY	.005	10.9[c]
Ramp	2DTD	.005	9.4
Ramp	NRMT	.005	43.0
Ramp	TWIGL[a]	.005	96.3[b]
Step	QUANDRY	.010	4.1[c]
Step	2DTD	.010	5.3
Step	NRMT	.010	~30.0
Step	TWIGL[a]	.010	61.0[b]

[a] TWIGL finite difference mesh corresponds to nodal fine mesh.

[b] Execution times adjusted for quarter-core calculations.

[c] Actual eighth-core computational time multiplied by 1.55 to obtain quarter-core times.

more difficult problems are required to test fully the nodal method.

6.3 THE 3-D LMW OPERATIONAL TRANSIENT

The 3-D LMW (Langenbuch-Maurer-Werner) test problem (30) is a highly simplified LWR, described in Section A4.5 of Appendix 4. The transient is initiated by withdrawing a bank of four partially-inserted control rods at a rate of 3 cm per second. Subsequently, a bank of five control rods (initially parked in the upper reflector) is inserted at a rate of 3 cm per second. The resulting transient is followed for 60 seconds.

The static solution to the 3-D LMW test problem with a uniform 20 cm spatial mesh in both radial and axial directions was found to have a maximum error in nodal power of less than 1% (Section 4.4.1). In light of the small errors in spatial power distribution, these errors should have little effect on the transient solutions. The 3-D LMW test problem has been solved both with and without thermal-hydraulic feedback.

6.3.1 The 3-D LMW Test Problem Without Feedback

Three QUANDRY solutions to the LMW test problem are displayed in Table 6-10. These calculations employed convergence criterion of 10^{-3}, matrix updating every fourth time step, and time step sizes of 2.0, 1.0, and 0.5 seconds. If the 0.5 s time step solution is taken as a reference, the maximum temporal truncation errors of the other two solutions appear to be less than 3%. However, if one compares the "reference" solution to the most accurate CUBBOX (30) solution, the maximum discrepancy is greater than 5.0%.

The reason for the apparent discrepancies is that the QUANDRY solution exhibits considerable control rod cusping effects. Recall from Chapter 5, that the Analytic Nodal Method requires that all cross sections be spatially uniform with each node, even if the node contains a partially-inserted control rod. Hence, the modeling of the cross sections in a partially-rodded node as the volume-weighted cross sections of the fully-rodded and -unrodded cross sections leads to errors in control rod "reactivities." CUBBOX (30), on the other hand, is not

TABLE 6-10

Power Versus Time for the 3-D LMW Test Problem (QUANDRY)

Time (s)	Mean Power Density (% Error)[a]		
	Δt = 2000 ms	Δt = 1000 ms	Δt = 500 ms
0.0	150.0	150.0	150.0
5.0	—	163.9 (-1.9)	167.1
10.0	193.2 (-1.9)	195.3 (-.8)	196.9
20.0	251.7 (+.6)	253.2 (+1.2)	250.3
30.0	207.0 (+3.0)	206.9 (+2.9)	201.0
40.0	122.3 (+2.8)	121.2 (+1.8)	119.0
50.0	74.7 (+.8)	74.3 (+.3)	74.1
60.0	56.9 (0.0)	57.5 (+1.1)	56.9

[a] Mean power density in w/cc; reference is the solution with a time step size of 500 ms.

constrained to spatially uniform cross sections and can model more accurately the partially-inserted control rods.

In order to correct some of the control rod cusping effects in QUANDRY, an alternate model can be used for nodes with partially-inserted control rods. To do so, the axial shapes of the fluxes in node (i, j, k) are approximated by the following quadratic polynomials:

$$[\phi_{z_{i,j,k}}(z,t)] = [\bar{\phi}_{i,j,k}(t)] + \{[\bar{\phi}_{i,j,k-1}(t)] - [\bar{\phi}_{i,j,k}(t)]\} \rho^{k-1}_{z_k}(z) + \{[\bar{\phi}_{i,j,k+1}(t)] - [\bar{\phi}_{i,j,k}(t)]\} \rho^{k+1}_{z_k}(z) , \quad (6-1)$$

where the expansion functions are identical with those utilized in the quadratic transverse leakage approximation of Section 2.3.3. This expansion possesses the property that the one-dimensional fluxes preserve the average fluxes in each of the three adjacent nodes. The "homogenized" cross sections, $[\Sigma^{h}_{i,j,k}(t)]$, are then determined by requiring that

$$h_z^k[\Sigma^{h}_{i,j,k}(t)][\bar{\phi}_{i,j,k}(t)] = \int_{z_k}^{z_{k+1}} dz\,[\Sigma_{i,j,k}(z,t)][\phi_{z_{i,j,k}}(z,t)], \tag{6-2}$$

where $[\Sigma_{i,j,k}(z,t)]$ is the true space-dependent cross section. The "homogenized" cross sections are then used as the spatially uniform cross sections for the transient calculation.

Results for the 3-D LMW test problem obtained by QUANDRY with the control rod cusping adjustment are displayed in Table 6-11. These solutions display a much more uniform temporal convergence rate than the solutions contained in Table 6-10. The finest temporal mesh solution is also in much better agreement with the CUBBOX solution than is the previous solution. Hence, the control rod cusping adjustment appears to be more successful in predicting control rod "reactivities" than the volume-weighted cross section procedure.

Comparisons of the temporal convergence of QUABOX (30), CUBBOX (30), and QUANDRY solutions to the 3-D LMW test problem are contained in Table 6-12. To eliminate any differences in spatial approximations, the reference case for each method is considered to be a finer temporal mesh solution generated by the same method.

TABLE 6-11

Power Versus Time for the 3-D LMW Test Problem With Control Rod Cusping Adjustment (QUANDRY)

Time (s)	Mean Power Density (% Error) [a]			
	$\Delta t = 2000$ ms	$\Delta t = 1000$ ms	$\Delta t = 500$ ms	$\Delta t = 250$ ms
0.0	150.0	150.0	150.0	150.0
5.0	—	164.3 (-2.3)	167.5 (-.4)	168.1
10.0	204.1 (2.3)	198.4 (-.6)	200.8 (0.6)	199.6
20.0	281.6 (9.6)	267.0 (3.9)	260.9 (1.5)	257.0
30.0	221.0 (7.7)	216.4 (5.5)	210.2 (2.4)	205.2
40.0	120.2 (-.7)	121.5 (+.5)	122.5 (1.3)	120.9
50.0	70.5 (-5.7)	73.1 (-2.3)	75.4 (0.8)	74.8
60.0	52.7 (-8.2)	55.9 (-2.6)	57.8 (0.7)	57.4

[a] Mean power density in w/cc; reference is the solution with a time step size of 250 ms.

TABLE 6-12

Power Versus Time for the 3-D LMW Test Problem: Comparison of Temporal Convergence of Transient Solutions With Time Step Size = 500 ms

Time (s)	Mean Power Density (% Error)[a]		
	QUABOX	CUBBOX	QUANDRY
0.0	150.0	150.0	150.0
5.0	167.1 (-0.5)	167.2 (-0.6)	167.5 (-0.4)
10.0	196.6 (-1.2)	198.2 (-1.0)	200.8 (+0.6)
20.0	255.6 (-1.6)	257.8 (-0.7)	260.9 (+1.5)
30.0	217.9 (+0.9)	214.2 (+0.8)	210.2 (+2.4)
40.0	133.3 (+2.9)	129.8 (+2.2)	122.5 (+1.3)
50.0	80.3 (+1.5)	78.8 (+1.5)	75.4 (+0.8)
60.0	61.0 (+0.7)	59.8 (+0.9)	57.8 (+0.7)

[a] The error is defined to be the difference between solutions with time step sizes of 500 ms and 250 ms.

These results indicate that the temporal truncation errors of the three methods are roughly comparable for this problem.

In order to compare the accuracy of the three nodal methods, it is necessary to have a reference solution. In light of the fact that even the 125 ms time step CUBBOX solution displays spatial errors of several percent and is not temporally converged, no truly satisfactory reference solution exists. Hence, for purposes of comparison, a Richardson extrapolation (41) of the CUBBOX solutions is considered to be a reference, although it is probably not accurate to better than one percent. Table 6-13 summarizes three nodal solutions to the LMW problem. The QUABOX and CUBBOX calculations use a time step size of 125. ms. The QUANDRY calculation employs a 10 cm axial mesh (to further eliminate cusping effects) and a time step size of 25 ms. These results indicate that QUANDRY and CUBBOX solutions have a maximum error in mean power density of about 1%, while the QUABOX solution exhibits a maximum error of approximately 3%. The execution times for QUANDRY, QUABOX, and CUBBOX are available only for the 1.0 second time step case, and they are 56.0, 70.0, and 45.0, respectively.

6.3.2 The 3-D LMW Test Problem with Feedback

The 3-D LMW test problem with thermal-hydraulic feedback provides a very interesting test for a neutronics model in a coupled neutronic thermal-hydraulic environment. The parameters for the thermal-hydraulic model are chosen to be fairly representative of an

TABLE 6-13

Power Versus Time for the 3-D LMW Test Problem: Comparison of the Most Accurate Solutions for Three Nodal Methods

Time (s)	Mean Power Density (% Error)			
	QUABOX[a]	CUBBOX[a]	QUANDRY[b]	Ref.[c]
0.0	150.0	150.0	150.0	150.0
5.0	168.7 (-0.4)	168.8 (-0.4)	169.1 (-0.2)	169.4
10.0	200.2 (-0.9)	201.1 (-0.5)	202.0 (0.0)	202.0
20.0	260.5 (0.0)	260.0 (-0.2)	262.2 (+0.6)	260.5
30.0	213.6 (+1.8)	211.3 (+0.7)	210.8 (+0.4)	209.9
40.0	127.5 (+2.9)	125.5 (+1.3)	123.0 (-.7)	123.9
50.0	78.6 (+2.7)	77.1 (+0.8)	75.7 (-1.0)	76.5
60.0	60.3 (+2.9)	58.9 (+0.5)	57.9 (-1.2)	58.6

[a] Time step size, 125 ms.

[b] Time step size, 250 ms, fine axial mesh (10 cm).

[c] Richardson extrapolation of CUBBOX solutions.

operating PWR; they are given in Section A4.5 of Appendix 5. With feedback, the LMW problem takes on the characteristics of an operational transient.

In converging the steady-state solution, QUANDRY requires the same number of outer iterations (17) as the nonfeedback problem. It is interesting to note that the zero power (hot standby) eigenvalue is 0.99974, while the full power (184.3 Mw) eigenvalue is 0.98355. Hence, the feedback accounts for approximately 2.50 dollars of

negative reactivity. Despite the large feedback effects, the steady-state iteration scheme appears to be very well suited to the feedback problem.

A summary of three QUANDRY solutions, employing time step sizes of 1000, 500, and 250 ms, is displayed in Table 6-14. A plot of the total reactor power as a function of time, for the 250 ms case, is shown in Figure 6-1. These calculations did not make use of the control rod cusping adjustment discussed in the previous section, and fairly significant cusping effects are present. The temporal truncation errors are smaller than in the nonfeedback case, which should be expected since the magnitude of the power excursion is limited by feedback effects. Cusping effects are more pronounced when feedback is present, and accurate equivalent homogenized parameters for partially-rodded nodes appear to be more important in these problems. No serious attempt has yet been made to permit spatially-dependent cross sections within nodes. Instead, efforts are being devoted to finding equivalent homogenized parameters (spatially uniform) which properly predict control rod effects in partially-rodded nodes (42).

Except for the enhancement of cusping effects, no additional difficulties in solving the neutronics equations with feedback have been encountered with the transient Analytic Nodal Method.

TABLE 6-14

Total Reactor Power Versus Time for 3-D LMW Problem with Thermal-Hydraulic Feedback

Time (s)	Total Reactor Power × 10^{-2} (Mw)		
	Δt = 1000 ms	Δt = 500 ms	Δt = 250 ms
0.0	1.848	1.848	1.848
2.5		1.899	1.892
5.0	1.945	1.914	1.917
7.5		1.945	1.937
10.0	1.924	1.935	1.943
12.5		1.965	1.957
15.0	1.967	1.951	1.948
17.5		1.932	1.939
20.0	1.953	1.938	1.934
22.5		1.888	1.891
25.0	1.863	1.867	1.867
27.5		1.840	1.841
30.0	1.779	1.780	1.790
32.5		1.755	1.753
35.0	1.723	1.711	1.716
37.5		1.665	1.672
40.0	1.617	1.631	1.632
42.5		1.595	1.600
45.0	1.568	1.566	1.568
47.5		1.534	1.537
50.0	1.581	1.576	1.563
52.5		1.544	1.563
55.0	1.557	1.569	1.563
57.5		1.557	1.561
60.0	1.561	1.561	1.560

Figure 6-1. Total reactor power versus time for the 3-D LMW problem with thermal-hydraulic feedback (no cusping adjustment).

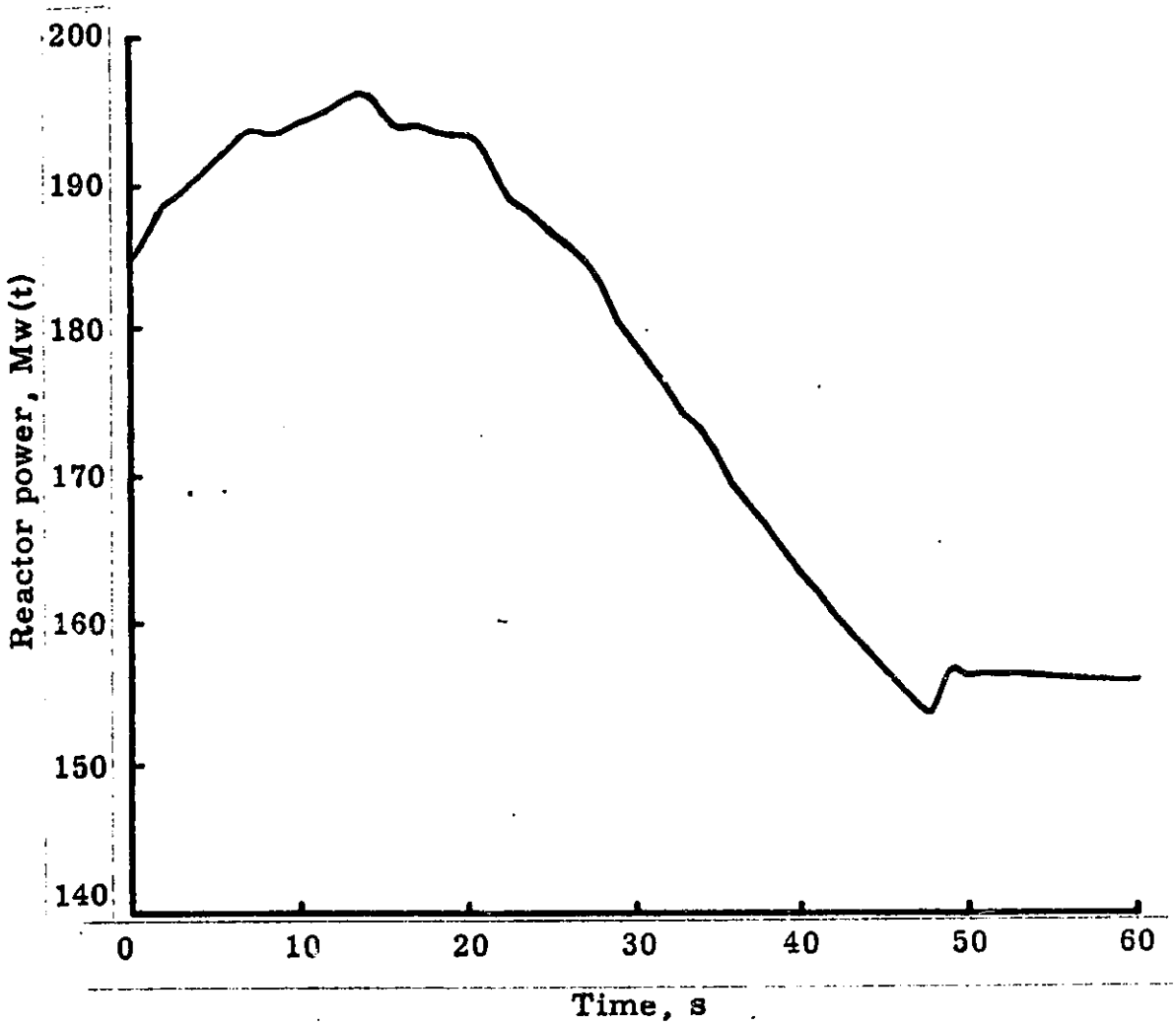

6.4 THE LRA BWR TRANSIENT BENCHMARK PROBLEM

The LRA benchmark problem (25) is a full-core BWR kinetics problem with two neutron energy groups and two delayed neutron precursor families. A superprompt critical transient from low power is induced by the rapid withdrawal of an asymmetric peripheral control rod. Feedback is modeled by adiabatic heatup and space-dependent Doppler feedback. The feedback model is specified fully by two relations:

$$\text{adiabatic heatup} - \quad \alpha\left[\Sigma_f(\underline{r},t)\right]\left[\phi(\underline{r},t)\right] = \frac{\partial}{\partial t}\, T(\underline{r},t)$$

$$\text{Doppler feedback} - \quad \Sigma_{a_1}(\underline{r},t) = \Sigma_{a_1}(\underline{r},0)\left\{1+\beta(\sqrt{T(\underline{r},t)} - \sqrt{T_0})\right\},$$

where $T(\underline{r},t)$ is the fuel temperature, and α, β, and T_0 are known constants. A complete problem description is contained in Section A4.1.

This problem has proven to be extremely difficult for two reasons. First, the severe flux tilts which occur during the transient require a highly accurate spatial neutronics model. Secondly, the reactor power during the transient spans approximately 10 orders of magnitude, thereby complicating the time integration processes.

The full-core LRA BWR problem is approached in several stages. Initially, the two-dimensional, quarter-core version of the LRA problem is considered. This problem permits examination of feedback and temporal truncation effects, without the complications of large radial and axial flux tilts. Subsequently, the quarter-core version of the 3-D

LRA problem is examined, in which axial power tilts play an important role. Finally, results are presented for the full-core LRA BWR problem.

Two spatial mesh configurations are considered for the nodal calculations. The "very coarse" and "coarse" mesh structures are defined as follows:

Region	Very Coarse Mesh	Coarse Mesh
$0 < x,y < 30$ cm	30 cm	15 cm
$30 < x,y < 60$ cm	15 cm	15 cm
$60 < x,y < 270$ cm	30 cm	15 cm
$270 < x,y < 300$ cm	15 cm	15 cm
$300 < x,y < 330$ cm	30 cm	15 cm

These mesh structures apply to both the two-dimensional problems and the x-y planes in three-dimensional problems.

6.4.1 The 2-D LRA BWR Transient Problem

The two-dimensional LRA problem is described in Section A4.1. Two temporal meshes have been employed to obtain solutions to this problem. The two temporal meshes are defined as follows:

329 Step		1000 Step	
Time Interval	Time Step Size	Time Interval	Time Step Size
$0 \leq t \leq 0.8$ s	25 ms	$0 \leq t \leq 1.0$ s	10 ms
$0.8 \leq t \leq 1.0$ s	10 ms	$1.0 \leq t \leq 1.3$ s	1 ms
$1.0 \leq t \leq 1.3$ s	3 ms	$1.3 \leq t \leq 1.5$ s	0.5 ms
$1.3 \leq t \leq 1.45$ s	1.5 ms	$1.5 \leq t \leq 2.0$ s	5 ms
$1.45 \leq t \leq 2.0$ s	15 ms	$2.0 \leq t \leq 3.0$ s	10 ms
$2.0 \leq t \leq 3.0$ s	25 ms		

A summary of results for the very coarse spatial mesh calculation and both temporal meshes is presented in the last two columns of Table 6-15. These results indicate that the 1000 step solution overpredicts peak powers and temperatures by as much as 8%, and the 329 step solution is even worse. There are two spatial effects which are responsible for most of the error. First, there is the inaccuracy in the neutronic model due to large mesh spacing. This effect is quite small and cannot account for the large errors. The fact that the temperature feedback is computed with the same spatial mesh as the neutronics is, however, quite important. Since some of the nodes in the temperature calculation are as large as 30 cm × 30 cm, the fluxes (and consequently the fuel temperatures) may display large changes within a node.

In order to examine the effects of the temperature shapes on the transient solutions, a very simple model for the temperature distribution within each node is employed. The fluxes in each quarter node are approximated by the mean of the node-averaged fluxes in the four nodes which are closest to the quarter node in question. Once the average fluxes in the four quarter nodes are determined, they are renormalized such that the average flux in each node is preserved. Average fuel temperatures in each quarter node at a given time step are then advanced to the next time step by using the quarter node-averaged fluxes. Hence, the new cross sections in each subnode can be approximated. The node-averaged cross sections to be used in the neutronics calculation for the next time step are obtained by flux-weighting the subnode cross sections. This procedure is admittedly crude; however, it suffices to demonstrate

TABLE 6-15

Summary of Results for the 2-D LRA Transient: QUANDRY Calculations with Very Coarse Mesh

	QUANDRY				
Number of steps	329	329	329	1000	
Steps per update	5	5, t < 1.4 2, t > 1.4	1	1	Ref.[a]
Temperature shape?	Yes	Yes	No	No	
Time to first peak (s)	1.424	1.425	1.423	1.430	1.436
Power at first peak (w/cc)	5897.	5913.	5967.	5749.	5411.
Power at second peak (w/cc)	1037.	1080.	1117.	861.	784.
Power at t = 3.0 sec (w/cc)	100.0	100.2	93.6	101.3	96.2
Average fuel temperature at t = 3.0 s(°K)	1142.	1125.	1141.	1132.	1087.
Peak fuel temperature at t = 3.0 s(°K)	3154.	3094.	3342.	3178.	2948.
CPU time (s) (IBM 370/168)	40.5	47.2	75.	258.	4154.

[a] Shober's fine temporal and spatial mesh calculation (17).

the significance of the temperature shape in the transient calculations.

A summary of results for the very coarse spatial mesh calculation is presented in the first two columns of Table 6-15. These results indicate that the errors in the final fuel temperatures are reduced from 14% to 5% for the 329 step solution. This significant increase in accuracy indicates that accurate solutions can be achieved with very coarse neutronic meshes, provided that spatial details of the feedback effects within each node can be computed. The results displayed in Table 6-15 also indicate that there is no significant loss of accuracy when the spatial coupling matrices are not computed at each time step.

The results of a more systematic examination of the errors introduced by infrequent updating of spatial coupling matrices are displayed in Table 6-16, for the coarse mesh 2-D LRA problem with 1000 time steps. These results clearly indicate that the computational efficiency of the transient Analytic Nodal Method can be increased by a factor of two by performing infrequent matrix updates, with less than a one percent degradation in accuracy of the quantities of interest.

The results of several QUANDRY solutions to the coarse mesh LRA problem with 329 time steps are summarized in Table 6-17. Several observations can be made from these results. The solution obtained by employing two inner iterations per time step indicates that the only quantity which is predicted with noticeably increased accuracy is the power at the first peak. Since the value of the power at the first peak has little to do with the overall transient solution, one inner iteration per time step appears adequate. The impact of tightening the

TABLE 6-16

Summary of Results for 2-D LRA Transient: QUANDRY Calculations with 1000 Time Steps, Coarse Mesh

	QUANDRY				
Number of steps per update	10; t < 1.4 4; t > 1.4	10	5	1	Ref. [a]
Time to first peak (s)	1.435	1.435	1.435	1.434	1.436
Power at first peak (w/cc)	5473.	5466.	5496.	5450.	5411.
Power at second peak (w/cc)	797.	855.	798.	800.	784.
Power at t = 3.0 sec (w/cc)	97.5	97.0	97.4	98.0	96.2
Average fuel temperature at t = 3.0 s (°K)	1108.	1126.	1111.	1101.	1087.
Peak fuel temperature at t = 3.0 s (°K)	3029.	3097.	3037.	3003.	2948.
Maximum error in nodal power at t = 3.0 s (%)	+0.4	+0.3	+0.4	+0.4	Ref.
CPU time (s) (IBM 370/168)	307.	327.	357.	595.	4150.

[a] Shober's fine temporal and spatial mesh calculation (17).

TABLE 6-17

Summary of Results for 2-D LRA Transient: QUANDRY Calculations with 329 Time Steps, Coarse Mesh

	QUANDRY				
Time steps per update	5[b]	5; t<1.4 2; t>1.4	5; t<1.4 2; t>1.4	5	Ref.[a]
Inners per outer	1	1	1	2	
Convergence criterion	10^{-3}	10^{-3}	10^{-3}; 10^{-4} near peak	10^{-3}	
Time to first peak (s)	1.427	1.429	1.429	1.426	1.436
Power at first peak (w/cc)	5699.	5610.	5538.	5447.	5411.
Power at second peak (w/cc)	792.	783.	796.	803.	784.
Power at t = 3.0 s (w/cc)	94.8	96.0	96.2	96.8	96.2
Average fuel temperature at t = 3.0 s (°K)	1152.	1116.	1116.	1114.	1087.
Peak fuel temperature at t = 3.0 s (°K)	3188.	3055.	3057.	3047.	2948.
Maximum error in nodal power shape at t = 3.0 s (%)	+0.4	+0.4	+0.4	+0.4	Ref.
CPU time (s) (IBM 370/168)	107.	113.	118.	154.	4150.

[a] Shober's fine temporal and spatial mesh calculation (17).

[b] No temperature shape computed.

convergence criterion near the first power peak is roughly the same as that of performing an additional inner iteration per time step. The impact of employing 329 rather than 1000 time steps appears to be a degradation of solution accuracy by about 1%, about the same as that of infrequent matrix recomputation.

A summary of transient results for several nodal methods is given in Table 6-18. Comparison of solutions indicates that QUANDRY calculations with very coarse temporal meshes and infrequent matrix updating are quite accurate and very computationally efficient. Power and temperature distributions for the 2-D LRA problem appear in Appendix A6.1 (coarse mesh, 1000 time steps QUANDRY calculation).

6.4.2 The 3-D Quarter-Core LRA BWR Transient Problem

The 3-D quarter-core LRA transient exhibits larger radial flux tilts than the 2-D transient and also displays significant axial shifts in power distribution. These effects make the 3-D LRA problem very difficult to solve and provide a very significant test for any transient neutronics model.

This problem was solved with the very coarse radial mesh and two different axial meshes. The static eigenvalues for the rod-in and rod-out configurations are

	10 Axial Planes (37.5 cm)	14 Axial Planes (25 cm)
Rod in	0.99652	0.99648
Rod out	1.01575	~1.01579

TABLE 6-18. Comparison of Nodal Solutions to the 2-D LRA BWR Transient Problem

	2 DTD (17) "Two-Step"	CUBBOX (25)	IQSBOX (25)	QUANDRY	QUANDRY	QUANDRY	Ref.[a]
Number of spatial mesh points	121	121	121	49	121	121	484
Initial eigenvalue	0.99655	0.99633	0.99631	0.99644	0.99641	0.99641	0.99636
Time to first peak (s)	1.426	1.421	1.445	1.425	1.429	1.435	1.436
Power at first peak (w/cc)	5552.	5734.	5451.	5913.	5538.	5473.	5411.
Power at second peak (w/cc)	815.	~830.	~800.	1080.	796.	797.	784.
Power at t = 3.0 s (w/cc)	97.0	~60.	~100.	100.2	96.2	97.5	96.2
Average fuel temperature at t = 3.0 s (°K)	1127.	1070.	1127.	1125.	1116.	1108.	1087.
Peak fuel temperature at t = 3.0 s (°K)	3112.	2925.	2989.	3094.	3057.	3029.	2948.
Maximum error in nodal power shape at t = 3.0 s (%)	+1.3	-5.	-1.2	-2.7	+0.4	+0.4	Ref.
Number of time steps	1000	1200	522	329	329	1000	2600
CPU time (s)	210.	180.	255.	47.2	118.	307.	1661.
(Computer)	(IBM 370/168)	(IBM 360/91)	(CYBER 175)	(IBM 370/168)	(IBM 370/168)	(IBM 370/168)	(IBM 370/195)

[a] Shober's fine temporal and spatial mesh calculation (17).

A comparison of control rod worths with the reference solution of Chapter 4 indicates that the static rod worths are predicted with an accuracy of +0.65% and +1.06% for the 10 and 14 plane configurations, respectively. A comparison of static power distributions with the reference case shows that the maximum errors in nodal powers are less than 1.6% and 3.15% for the rod-in and rod-out configurations, respectively. Since flux tilts are smaller (because of feedback) in the transient problem than in the static, rod-out configuration, the maximum errors in power distribution during the transient are expected to be less than 3.0%. Table 6-19 summarizes the results of the two QUANDRY calculations, which employ the following temporal mesh:

Time Interval	Time Step Size
$0 \leq t \leq 0.5$ s	25 ms
$0.5 \leq t \leq 0.6$ s	10 ms
$0.6 \leq t \leq 0.7$ s	2.5 ms
$0.7 \leq t \leq 0.8$ s	1.25 ms
$0.8 \leq t \leq 0.95$ s	1.0 ms
$0.95 \leq t \leq 1.0$ s	2.5 ms
$1.0 \leq t \leq 2.0$ s	20 ms
$2.0 \leq t \leq 3.0$ s	25 ms

These calculations make use of the x-y temperature shape model which was described in the previous section, and the spatial coupling matrices are recomputed every fifth time step until t = 1.05 and subsequently, every other time step. The control rod cusping adjustment is not used in these calculations.

TABLE 6-19

Summary of QUANDRY Results for the 3-D Quarter-Core LRA BWR Problem, Very Coarse Spatial Mesh

Number of Axial Planes	10	14	14
Number of Time Steps	410	410	820
Time to first peak (s)	0.907	0.900	0.903
Power at first peak (w/cc)	5739.	6549.	5781.
Time to first minimum (s)	0.988	0.980	0.989
Power at first minimum (w/cc)	109.0	93.8	114.7
Time to second peak (s)	1.44	1.54	—
Power at second peak (w/cc)	412.	408.	—
Power at t = 3.0 s (w/cc)	71.2	69.9	—
Peak/average assembly power at t = 3.0 s	3.64	3.63	—
Average fuel temperature at t = 3.0 s (°K)	1033.	1024.	—
Peak assembly fuel temperature at t = 3.0 s (°K)	2696.	2786.	—
Peak nodal fuel temperature at t = 3.0 s (°K)	4148.	4177.	—
Execution time (s) (IBM 370/168)	580.	831.	—

Control rod cusping effects in the 3-D LRA problem are not very pronounced, as evidenced by the close agreement between the solutions which used 10 and 14 axial planes. The partial solution with halved temporal mesh spacing indicates that the temporal truncation effects are larger than those observed in the two-dimensional problems.

The temporal truncation errors are fairly significant in the powers at the first peak and minimum, but evidence from the two-dimensional transients suggests that these errors do not affect substantially the subsequent powers and temperatures. Unfortunately, no reference solution exists for this problem. Assembly-averaged power densities, partial planar power densities, and temperatures at several times of interest are displayed in Appendix A6.2 for the 10 plane QUANDRY solution.

6.4.3 The 3-D Full-Core LRA BWR Transient Problem

The full-core LRA transient problem is very similar to the quarter-core transient problem, except that radial flux tilts are more severe. This problem is solved with the very coarse radial mesh and the same two axial meshes as the quarter-core problem. The static eigenvalues for the rod-in and rod-out configurations are

	10 Axial Planes	14 Axial Planes
Rod in	0.99657	0.99653
Rod out	1.01506	~1.01510

A comparison of control rod worths with the reference solution of Chapter 4 indicates that the static rod worths are predicted with an accuracy of -0.10% and +0.33% for the 10 and 14 plane configurations, respectively. A comparison of static power distributions shows that the maximum errors in nodal powers are less than 1.6% and 3.2% for the rod-in and rod-out configurations. Hence, as in the quarter-core problem, transient power distributions should have maximum errors

in power distribution of less than 3.0%.

The 3-D full-core LRA problem was solved with the same temporal mesh as the quarter-core problem. A summary of results for this problem is given in Table 6-20. The results are very similar to those of the quarter-core problem. That is, cusping effects are small and temporal truncation effects appear to be significant at the first peak and minimum. The errors in the powers at the peaks and minimum are larger than those observed in the quarter-core problem. This is due, in part, to the fact that the peaks occur later in the whole-core problem and the temporal mesh is too coarse near the first minimum. This poor choice for temporal mesh spacings could be eliminated if an automatic time step selector (which limits the maximum change in reactor power allowed per time step) is used. Nevertheless, the final powers and temperatures are predicted quite well, even with the coarse temporal mesh.

No reference solution is available for this problem, hence, it is difficult to measure, in any absolute sense, the errors in the QUANDRY solutions. The assembly-averaged power densities, partial planar power densities and temperatures at several times of interest are displayed in Appendix A6.3, for the 10 plane, fine temporal mesh QUANDRY solution. A plot of total reactor power density as a function of time, is shown in Figure 6-2.

It is interesting to compare the execution times of QUANDRY to those which would be required to solve the 3-D LRA problem with a finite difference method. Supposing that a finite difference mesh of

TABLE 6-20

Summary of QUANDRY Results for the 3-D Whole-Core LRA BWR Problem, Very Coarse Spatial Mesh

Number of Axial Planes	10	14	10
Number of Time Steps	410	410	820
Time to first peak (s)	0.946	0.949	0.950
Power at first peak (w/cc)	1534.	1600.	1435.
Time to first minimum (s)	1.11	1.11	1.08
Power at first minimum (w/cc)	11.4	11.2	20.7
Time to second peak (s)	1.52	1.54	1.57
Power at second peak (w/cc)	240.	301.	141.
Power at t = 3.0 s (w/cc)	22.1	21.3	22.6
Peak/average assembly power at t = 3.0 s	11.29	11.20	11.33
Average fuel temperature at t = 3.0 s (°K)	508.	508.	503.
Peak assembly fuel temperature at t = 3.0 s (°K)	2692.	2682.	2630.
Peak nodal fuel temperature at t = 3.0 s (°K)	3979.	4069.	3877.
Execution time (s) (IBM 370/168)	2150.	3000.	4300.

Figure 6-2. Total reactor power versus time for the 3-D LRA BWR (full-core) transient problem.

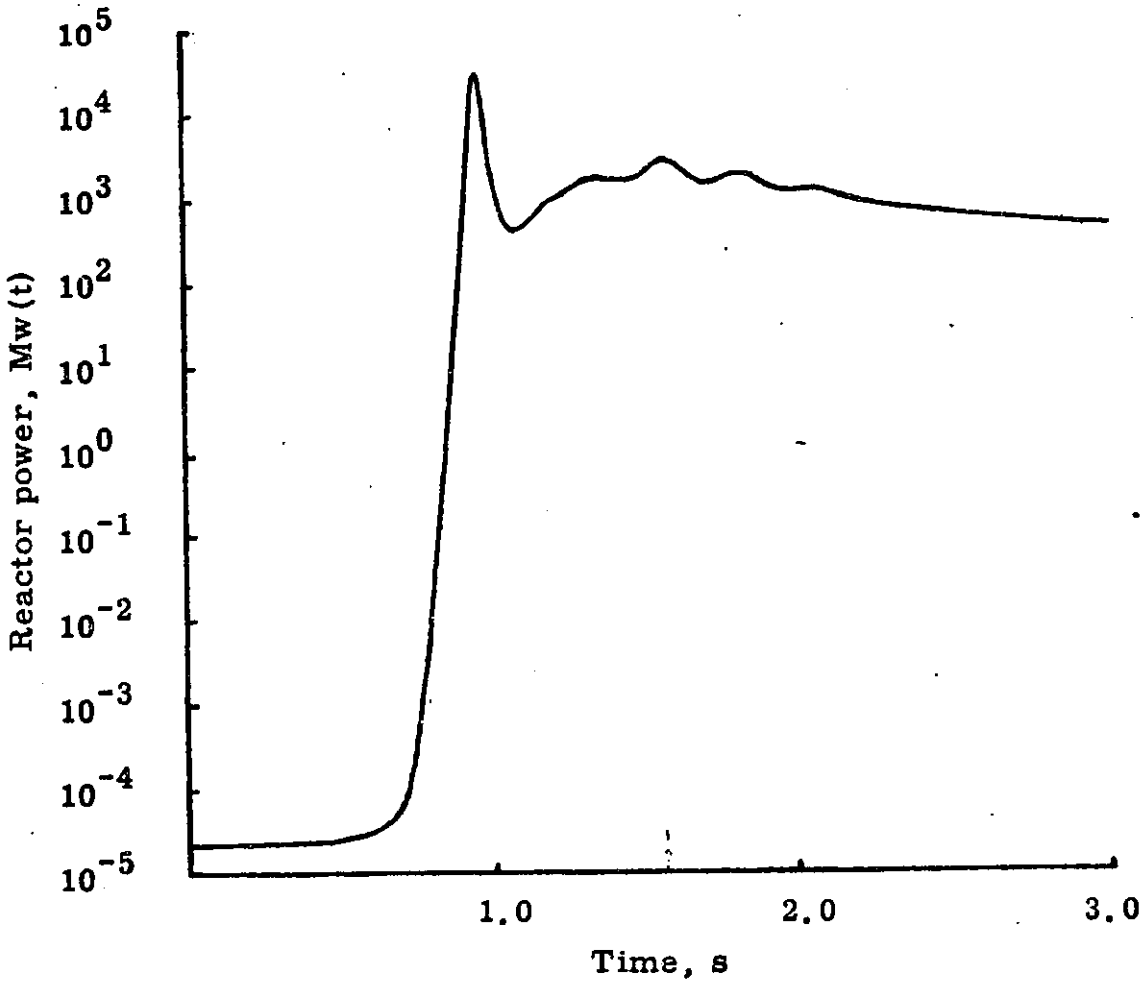

4 cm would yield an acceptably accurate spatial solution (evidence suggests that a mesh spacing of less than 2.5 cm is required to obtain errors in nodal powers of less than 5%), the full-core LRA problem would require approximately 600,000 mesh points. The finite difference core, MEKIN, requires 0.00078 seconds per time step per mesh point on an IBM 370/168 (43). Thus, 468 seconds per time step would be required to solve the full-core LRA problem with MEKIN. This compares with approximately 5.0 seconds per time step required for QUANDRY. Also, MEKIN uses an explicit time integration method which typically requires a much smaller time step size than the fully-implicit time integration method which is used in the QUANDRY calculation. Hence, the computational advantage of the transient Analytic Nodal Method over MEKIN is probably much larger than the conservative factor of 100 computed above.

In summary, the Analytic Nodal Method has been demonstrated to be very accurate for transient applications in which assembly-size nodes can be used. The temporal integration scheme allows use of large time steps and requires very little iterative effort at each time step. The transient Analytic Nodal Method is at least two orders of magnitude more computationally efficient than finite difference methods and is very competitive with other state-of-the-art nodal diffusion methods.

6.5 SUMMARY

In this chapter, the transient Analytic Nodal Method has been applied to several two- and three-dimensional, two-group reactor benchmark problems. Results demonstrate that accurate time-dependent solutions can be obtained with coarse spatial and temporal meshes. The computing times required to solve the transient problems were demonstrated to be very small and at least two orders of magnitude smaller than those required by finite difference methods.

The computational effort involved in solving the Analytic Nodal diffusion equations at each time step can be split into three separate tasks which require roughly the same computational effort: iterative convergence of node-averaged fluxes, noniterative computation of nodal face-averaged net leakages, and recomputation of spatial coupling matrices. Results indicate that recomputing the spatial coupling matrices at every time step would lead to longer transient solution times (which would be dominated by time spent recomputing matrices). Hence, the practice of updating matrices every 2 to 10 time steps is adopted and has been demonstrated to produce only a very small degradation of solution accuracy in problems with and without thermal-hydraulic feedback. A good estimate of the time required to solve transient problems with QUANDRY is 10^{-3} seconds per node per dimension per time step on an IBM 370/168.

Chapter 7

SUMMARY

7.1 OVERVIEW OF THE INVESTIGATION

The objective of this research effort was to extend the Analytic Nodal Method to three dimensions and to develop computationally efficient numerical methods for solving the time-dependent, multi-dimensional, two-group Analytic Nodal diffusion equations.

In Chapter 2, the Analytic Nodal diffusion equations, subject to the single approximation that the transverse leakages could be fit to quadratic polynomials, were derived for Cartesian geometry with homogenized nodes. These equations were written in terms of node-averaged fluxes and face-averaged net leakages. The resulting spatial coupling was three-node in fluxes and five-node in net leakages, in each direction.

The properties of the static nodal diffusion equations were examined in Chapter 3 and the Analytic Nodal diffusion equations were shown to reduce to the finite difference equations in the limit of infinitely fine spatial mesh. As a consequence, it was shown that the Analytic Nodal Method is guaranteed to give the exact solution to the differential diffusion equations in this limit. Iterative solution techniques were developed for the solution of the nodal diffusion equations,

and it was shown that these numerical techniques are guaranteed to cause convergence to the exact solution of the diffusion equations in the limit of infinitely fine spatial mesh.

The results of many two- and three-dimensional static reactor problems were presented in Chapter 4. The Analytic Nodal Method was shown to be a very accurate and highly efficient method for solving the multidimensional, two-group static diffusion equations. It was found that if LWRs can be homogenized into assembly-sized regions, the Analytic Nodal Method can be expected to yield assembly-averaged powers accurate to within approximately two percent and static reactor eigenvalues accurate to within about 0.01 percent. The Analytic Nodal Method was shown to be at least two orders of magnitude more computationally efficient than finite difference methods and at least as computationally efficient as other nodal methods of current interest.

In Chapter 5, the time-dependent Analytic Nodal diffusion equations were derived. From these equations, the multidimensional temporally- and spatially-discretized Analytic Nodal diffusion equations were derived by employing the Theta method time integration scheme. An algorithm, which made use of many of the steady-state iterative procedures, was detailed for solving the transient neutronic and thermal-hydraulic equations in tandem.

Results from several two- and three-dimensional transient problems were presented in Chapter 6. These results demonstrated that accurate transient solutions can be obtained with coarse (i.e.,

assembly-size) spatial meshes. Comparisons with several finite difference methods indicated that the Analytic Nodal Method is approximately two orders of magnitude more computationally efficient in transient applications.

Thus, the Analytic Nodal Method (as embodied in the computer code QUANDRY) has been demonstrated to be very accurate and highly efficient for multidimensional, two-group, static and transient LWR analysis. Hence, this method is an appealing alternative to the finite difference methods currently used in design and analysis of LWRs.

7.2 RECOMMENDATIONS FOR FUTURE RESEARCH

During the course of this investigation, several items of potential interest have been left unresolved or untouched. Many of these items warrant additional investigation. This section contains a description of these potential research areas.

7.2.1 The Transverse Leakage Approximation

Since the only approximation in the static Analytic Nodal Method is that the transverse leakage can be fit by a quadratic polynomial, improvements in this approximation would lead to increased accuracy. In particular, it would be very fruitful if a more accurate quadratic polynomial could be found. Examinations of the transverse leakage shapes have shown that a quadratic polynomial would be more accurate if it were based on leakage information from within the node. Use of additional "out-of-node" leakage information appears virtually useless.

7.2.2 Albedos

A generalized albedo boundary condition is incorporated into the Analytic Nodal Method. No attempt has been made as yet to utilize this albedo. If one were able to determine accurately the albedos, it would be much easier to model portions of a reactor (e.g., a few assemblies) than by use of alternate boundary conditions. Also, replacing the baffle and reflector by an albedo could lead to significant savings in terms of required spatial unknowns. Methods for finding these albedos need to be investigated.

7.2.3 INPUT/OUTPUT Considerations

If the Analytic Nodal Method is to be used to solve large LWR configurations, serious consideration must be given to I/O problems. Recall that in three-dimensional problems, there are 96 "coupling coefficients" per node. If a reactor is analyzed with a 20 cm mesh, approximately 5000 nodes will be required. Hence, even if a code is written in IBM single precision, approximately 2M-bytes of core storage would be required to contain only the coupling coefficients. Because of these storage requirements, considerable shuffling of data into and out of the computer core will be required. Therefore, I/O schemes and perhaps alternate iteration schemes will be required to handle these problems efficiently.

7.2.4 Alternate Time-Integration Methods

The Theta method time integration scheme has been investigated in this work. In light of the stability problems encountered with the semi-implicit approximations, all analysis was performed with the fully-implicit approximation. It seems unlikely that a much more computationally efficient temporal finite difference method can be found. The reason for this is simple: two-thirds of the computational effort required at each time step is spent computing matrices and solving for new leakages, which will be required regardless of the temporal finite difference approximation.

If a more efficient time integration scheme is to be found, it is necessary that the time-integration scheme be able to take large time steps between flux shape calculations. Hence, the quasi-static and related methods seem to be the most likely candidates for improved transient computational efficiency.

7.2.5 The Control Rod Cusping Problem

The control rod cusping problem, discussed in Chapters 5 and 6, requires additional investigation. The approximation suggested in Section 6.3 is a crude fix-up, at best. Two approaches to this problem seem possible. One approach is to allow cross sections to be space-dependent. This approach requires significant modification of the Analytic Nodal Method, since the analytic solution to the flux-leakage coupling equations becomes very difficult to find. One could represent the spatial dependence of the cross sections as source terms in the

one-dimensional flux equations, Eq. 5-4, by expanding the fluxes in polynomials.

However, representing the space dependence of cross sections within a node seems overly complicated and unnecessary. If one could devise rigorous methods for determining spatially constant equivalent homogenized parameters, the rod cusping problem could be solved without resorting to space-dependent cross sections. This approach appears to be the most promising.

7.2.6 Feedback Models

The thermal-hydraulic feedback model used in this investigation was quite simple. Hence, it was not possible to evaluate the effectiveness of the numerical techniques in certain feedback environments (e.g., boiling regimes). In particular, it is not known if the steady-state iterative process will be convergent when coupled to BWR thermal-hydraulic models. At present, there is no reason to believe that the methods are not applicable to BWRs, but numerical experience is more reassuring than conjecture. The effects of coupling the Analytic Nodal Method to realistic BWR (and PWR) feedback models should be investigated.

REFERENCES

1. D.R. Ferguson, "Multidimensional Reactor Dynamics Today: An Overview," Proc. Conf. on Computational Methods in Nuclear Engineering, CONF-750413, Vol. 2, p. VI-49 (1975).

2. M.R. Wagner, H. Finnemann, K. Koebke, and H.J. Winter, "Validation of the Nodal Expansion Method and the Depletion Program MEDIUM-2 by Benchmark Calculations and Direct Comparison with Experiment," Atomkernenergie (ATKE) Bd. 30 (1977), Lfg. 2.

3. A.F. Henry, Nuclear Reactor Analysis, M.I.T. Press, Cambridge, Mass. (1975).

4. M. Clark, Jr. and K.F. Hansen, Numerical Methods of Reactor Analysis, Academic Press, New York, N.Y. (1964).

5. R. Roechlich, "Current Problems in Multidimensional Reactor Calculations," Proc. Conf. Mathematical Models and Computational Techniques for Analysis of Nuclear Systems, CONF-730414, Vol. 2, p. VII-1 (1973).

6. C.M. Kang and K.F. Hansen, "Finite Element Methods for Reactor Analysis," Nucl. Sci. Eng. 51, 456 (1973).

7. G. Strang and G.J. Fix, An Analysis of the Finite Element Method, Prentice-Hall, Englewood Cliffs, N.J. (1973).

8. M.R. Wagner, "Current Trends in Multidimensional Static Reactor Calculations," Proc. Conf. on Computational Methods in Nuclear Engineering, CONF-750413, Vol. 2, p. VI-49 (1975).

9. W.M. Stacey, Jr., Variational Methods in Nuclear Reactor Physics, Academic Press, New York, N.Y. (1974).

10. S. Kaplan, "Synthesis Methods in Reactor Analysis," Advan. Nucl. Sci. Technology 3, 233 (1965).

11. A. Ancona, M. Becker, D.R. Harris, A. DaC. Menezes, M.A. Robinson, and D.M. Ver Plank, "Unified Analysis of Nodal Methods," Trans. Am. Nucl. Soc. 24, 444 (1976).

12. D.L. Delp, D.L. Fischer, J.M. Harriman, M.J. Stedwell, "FLARE – A Three-Dimensional Boiling Water Reactor Simulator," GEAP-4592, General Electric Corporation (July 1964).

13. W. Werner, H. Finneman, and S. Langenbuch, "Two- and Three-Dimensional BWR Kinetics Problem," Trans. Am. Nucl. Soc. 23, 215-217 (1976).

14. H. Finnemann and M.R. Wagner, "A New Computational Technique for the Solution of Multidimensional Neutron Diffusion Problems," Presented at the International Meeting of Specialists on "Methods of Neutron Transport Theory in Reactor Calculations," Bologna, Italy, November 3-5, 1975.

15. A.F. Henry and R.N. Sims, "A Coarse Mesh Nodal Diffusion Method Based on Response Matrix Considerations," Ph.D. Thesis, Department of Nuclear Engineering, M.I.T., Cambridge, Mass., March 1977.

16. R.A. Shober and A.F. Henry, "Nonlinear Methods for Solving the Diffusion Equation," M.I.T. Report MITNE-196 (November 1976).

17. R.A. Shober, "A Nodal Method for Solving Transient Few-Group Neutron Diffusion Equations," ANL-78-51, Argonne National Laboratory (June 1978).

18. G. Greenman, personal communication (1977).

19. A. Cook, "Light Water Reactor Kinetics Analysis with Feedback," Ph.D. thesis, Department of Nuclear Engineering, M.I.T., Cambridge, Mass. (June 1978).

20. P. Antonopoulos, "Large Mesh Model Development Study," Sc.D. thesis, Department of Nuclear Engineering, M.I.T., Cambridge, Mass. (1972).

21. F. Bennewitz, H. Finnemann, and M.R. Wagner, "Higher Order Corrections in Nodal Reactor Calculations," Trans. Am. Nucl. Soc. 22, 250 (1975).

22. R.S. Varga, Matrix Iterative Analysis, Prentice-Hall, Englewood Cliffs, N.J. (1962).

23. E.L. Wachspress, Iterative Solution to Elliptic Systems and Applications to the Neutron Diffusion Equations of Reactor Physics, Prentice-Hall, Englewood Cliffs, N.J. (1966).

24. S.A. Orszag, Class Notes on Numerical Methods, Course 18.326, M.I.T. (Spring 1977).

25. Argonne Code Center: Benchmark Problem Book, ANL-7416, Supplement 2 (1977).

26. M.R. Wagner, H. Finnemann, K. Koebke, and H.J. Winter, "Validation of the Nodal Expansion Method and the Depletion Program MEDIUM-2 by Benchmark Calculations and Direct Comparison with Experiment," Atomkernenergie (ATKE) Bd. 30 (1977), Lfg. 2.

27. H. Henryson II, B.J. Toppel, and C.G. Stenberg, "MC^2-2: A Code to Calculate Fast Neutron Spectra and Multigroup Cross Sections," ANL-8144, Argonne National Laboratory (June 1976).

28. W. Werner, private communication (1976).

29. Ibid.

30. S. Langenbuch, W. Maurer, and W. Werner, "Coarse-Mesh Nodal Diffusion Method for the Analysis of Space-Time Effects in Large Light Water Reactors," Nucl. Sci. Eng. 63, 437-456 (1977).

31. B. Micheelson, H. Neltrup, "The 3-D IAEA Benchmark Problem," RISO-M-1572 (1973).

32. C. Maeder, personal communication (1978).

33. F.A. Kautz and L.O. Deppe, "CHD: A Two-Dimensional, Multigroup, Rectangular Geometry, Cubic Hermite, Finite Element Diffusion Code," COO-2262-10, MITNE-181 (June 1975).

34. A.F. Henry, personal communication (1979).

35. R.A. Shober, personal communication (1979).

36. A.V. Vota, N.J. Curlee, Jr., and A.F. Henry, "WIGL3 – A Program for the Steady-State and Transient Solution of the One-Dimensional, Two-Group, Space-Time Diffusion Equations Accounting for Temperature, Xenon, and Control Feedback," WAPD-TM-788 (February 1969).

37. D.S. Rowe, "COBRA III C: A Digital Computer Program for Steady-State and Transient Thermal-Hydraulic Analysis of Rod Bundle Nuclear Fuel Elements," BNWL-1695 (March 1973).

38. H.B. Stewart, personal communication (1978).

39. D.R. Ferguson, "Solution of the Space-Dependent Reactor Kinetics Equation in Three Dimensions," MITNE-132, M.I.T. Department of Nuclear Engineering, Cambridge, Mass. (August 1971).

40. L.A. Hageman and J.B. Yasinsky, "Comparison of Alternating-Direction Time-Differencing Methods and Other Implicit Methods for the Solution of the Neutron Group Diffusion Equations," Nucl. Sci. Eng. 38, 8 (1969).

41. F.B. Hildebrand, Introduction to Numerical Analysis, McGraw-Hill, New York, N.Y. (1974).

42. A.F. Henry, personal communication (1979).

43. R.W. Bowring, J.W. Stewart, R.A. Shober, and R.N. Sims, "MEKIN: MIT-EPRI Nuclear Reactor Core Kinetics Code," CCM-1, Electric Power Research Institute RP 227 (1975).

Appendix 1

DERIVATION OF EXPANSION FUNCTIONS FOR THE QUADRATIC TRANSVERSE LEAKAGES

The particular form of the approximation to the shape of the transverse leakages is given by Eq. 2-14,

$$[S_{u_{\ell,m,n}}(u)] \cong [\bar{S}_{u_{\ell,m,n}}] + \left([\bar{S}_{u_{\ell-1,m,n}}] - [\bar{S}_{u_{\ell,m,n}}]\right) \rho_{u_\ell}^{\ell-1}(u)$$

$$+ \left([\bar{S}_{u_{\ell+1,m,n}}] - [\bar{S}_{u_{\ell,m,n}}]\right) \rho_{u_\ell}^{\ell+1}(u) \; ; \quad u = x,y,z \; , \qquad \text{(A1-1)}$$

where $[\bar{S}_{u_{\ell,m,n}}] h_u^\ell h_v^m h_w^n$ is the average net rate at which neutrons leave node (ℓ,m,n) through the faces transverse to direction u, and the ρ's are quadratic expansion functions. The physical conditions which are imposed on the leakage expansion is that it preserve the average transverse leakage in each of the three adjacent nodes. These conditions uniquely determine the expansion functions. Mathematically, the conditions impose the following constraints upon the expansion functions:

$$\frac{1}{h_u^{\ell+\ell'}} \int_{u_{\ell+\ell'}}^{u_{\ell+\ell'+1}} du \, \rho_{u_\ell}^{\ell+\ell''}(u) = \delta_{\ell'\ell''} \; ; \quad u = x,y,z$$

$$\ell' = -1,0,1$$

$$\ell'' = -1,1 \; , \qquad \text{(A1-2)}$$

where the Kronecker delta is defined by

$$\delta_{\ell'\ell''} = \begin{cases} 1 \; ; & \ell' = \ell'' \\ 0 \; ; & \ell' \neq \ell'' \end{cases} .$$

If a spatial variable is defined,

$$t_\ell = u - u_\ell \; ,$$

the expansion functions can be expressed as

$$\begin{aligned} \rho^{\ell-1}_{u_\ell}(u) &= a^-_{u_\ell} + b^-_{u_\ell}\left(\frac{t_\ell}{h^\ell_u}\right) + c^-_{u_\ell}\left(\frac{t_\ell}{h^\ell_u}\right)^2 \\ \rho^{\ell+1}_{u_\ell}(u) &= a^+_{u_\ell} + b^+_{u_\ell}\left(\frac{t_\ell}{h^\ell_u}\right) + c^+_{u_\ell}\left(\frac{t_\ell}{h^\ell_u}\right)^2 . \end{aligned} \tag{A1-3}$$

Using the notation of Sims (15), alternate mesh spacings are defined to be

$$\begin{aligned} h_m &\equiv h^{\ell-1}_u \\ h &\equiv h^\ell_u \\ h_p &\equiv h^{\ell+1}_u \end{aligned} \; , \tag{A1-4}$$

and another useful quantity, d_{u_ℓ}, can be defined as

$$\begin{aligned} d_{u_\ell} \equiv\; & h^4\left(\tfrac{1}{6} h_m h_p\right) + h^3\left(\tfrac{1}{3} h_m^2 h_p + \tfrac{1}{3} h_m h_p^2\right) \\ & + h^2\left(\tfrac{1}{6} h_m^3 h_p + \tfrac{1}{2} h_m^2 h_p^2 + \tfrac{1}{6} h_m h_p^3\right) + h\left(\tfrac{1}{6} h_m^3 h_p^2 + \tfrac{1}{6} h_m^2 h_p^3\right) . \end{aligned} \tag{A1-5}$$

Application of Eqs. A1-2 to the expansion functions in Eqs. A1-3 produces the following values for the expansion coefficients:

$$
\begin{aligned}
d_{u_\ell} a^-_{u_\ell} &= h^4\left(\tfrac{1}{6} h_m h_p\right) + h^3\left(\tfrac{1}{3} h_m h_p^2\right) + h^2\left(\tfrac{1}{6} h_m h_p^3\right) \\
d_{u_\ell} b^-_{u_\ell} &= h^4\left(-\tfrac{2}{3} h_m h_p\right) + h^3\left(- h_m h_p^2\right) + h^2\left(-\tfrac{1}{3} h_m h_p^3\right) \\
d_{u_\ell} c^-_{u_\ell} &= h^4\left(\tfrac{1}{2} h_m h_p\right) + h^3\left(\tfrac{1}{2} h_m h_p^2\right) \\
d_{u_\ell} a^+_{u_\ell} &= h^3\left(-\tfrac{1}{6} h_m^2 h_p\right) + h^2\left(-\tfrac{1}{6} h_m^3 h_p\right) \\
d_{u_\ell} b^+_{u_\ell} &= h^4\left(-\tfrac{1}{3} h_m h_p\right) + h^2\left(\tfrac{1}{3} h_m^3 h_p\right) \\
d_{u_\ell} c^+_{u_\ell} &= h^4\left(\tfrac{1}{2} h_m h_p\right) + h^3\left(\tfrac{1}{2} h_m^2 h_p\right) \quad .
\end{aligned}
\tag{A1-6}
$$

Equation A1-6 demonstrates that the desired expansion functions are uniquely determined by the mesh spacing in the u direction. For the case of uniform mesh spacing, the expansion coefficients are given by

$$
\begin{aligned}
a^-_u &= \tfrac{1}{3} \\
b^-_u &= -1 \\
c^-_u &= \tfrac{1}{2} \\
a^+_u &= -\tfrac{1}{6} \\
b^+_u &= 0 \\
c^+_u &= \tfrac{1}{2} \quad .
\end{aligned}
\tag{A1-7}
$$

Appendix 2

DERIVATION OF SPATIAL COUPLING EQUATIONS

The differential equation which specifies the relationship between node-averaged fluxes and face-averaged net currents for the quadratic transverse leakage approximation is given by Eq. 2-17,

$$\frac{d}{dt_\ell}\left[\Phi_{u_{\ell,m,n}}(t_\ell)\right] + \left[N_{\ell,m,n}\right]\left[\Phi_{u_{\ell,m,n}}(t_\ell)\right] = \left[S'_{u_{\ell,m,n}}(t_\ell)\right] ; \quad u = x,y,z , \qquad \text{(A2-1)}$$

where

$$\left[\Phi_{u_{\ell,m,n}}(t_\ell)\right] \equiv \text{col}\left\{\left[\phi_{u_{\ell,m,n}}(t_\ell)\right], \left[J_{u_{\ell,m,n}}(t_\ell)\right]\right\}$$

$$\left[N_{\ell,m,n}\right] \equiv \begin{bmatrix} [0] & [D_{\ell,m,n}]^{-1} \\ [\Sigma_{T_{\ell,m,n}}] - \frac{1}{\gamma}[\chi][\nu\Sigma_{f_{\ell,m,n}}]^T & [0] \end{bmatrix}$$

$$\left[S'_{u_{\ell,m,n}}(t_\ell)\right] \equiv \text{col}\left\{ [0], \left(-[S^f_{u_{\ell,m,n}}] - [S^\ell_{u_{\ell,m,n}}] \frac{t_\ell}{h^\ell_u} - [S^q_{u_{\ell,m,n}}]\left(\frac{t_\ell}{h^\ell_u}\right)^2\right)\right\}$$

$$t_\ell \equiv u - u_\ell ,$$

and the transverse leakage source term has been split into "flat,"

"linear," and "quadratic" componen , defined by Eq. 2-18.

The general solution to Eq. A2-1 is determined by finding particular solutions, $[\Phi^{p}_{u_{\ell,m,n}}(t_\ell)]$, corresponding to each of the three components of the transverse leakage source term and superimposing the particular solutions on the homogeneous solution, $[\Phi^{h}_{u_{\ell,m,n}}(t_\ell)]$. The three particular solutions to Eq. A2-1, on the interval $0 < t_\ell < h^{\ell}_{u}$, subject to the boundary condition $[\Phi^{p}_{u_{\ell,m,n}}(t_\ell=0)] = 0$ are

$$[\Phi^{f}_{u_{\ell,m,n}}(t_\ell)] = [N_{\ell,m,n}]^{-1}\left\{[I]-e^{-[N_{\ell,m,n}]t_\ell}\right\}[S^{f}_{u_{\ell,m,n}}] \tag{A2-2a}$$

$$[\Phi^{\ell}_{u_{\ell,m,n}}(t_\ell)] = \frac{1}{h^{\ell}_{u}}[N_{\ell,m,n}]^{-1}\left\{t_\ell[I]-[N_{\ell,m,n}]^{-1}\times\left\langle[I]-e^{-[N_{\ell,m,n}]t_\ell}\right\rangle\right\}[S^{\ell}_{u_{\ell,m,n}}] \tag{A2-2b}$$

$$[\Phi^{q}_{u_{\ell,m,n}}(t_\ell)] = \frac{1}{\left(h^{\ell}_{u}\right)^2}[N_{\ell,m,n}]^{-1}\left\{t^2_\ell[I]-2[N_{\ell,m,n}]^{-1}\left\langle t_\ell[I]-[N_{\ell,m,n}]^{-1}\left([I]-e^{-[N_{\ell,m,n}]t_\ell}\right)\right\rangle\right\}[S^{q}_{u_{\ell,m,n}}]\,. \tag{A2-2c}$$

The homogeneous solution to Eq. A2-1, on the interval $0 < t_\ell < h^{\ell}_{u}$, subject to the boundary condition $[\Phi^{h}_{u_{\ell,m,n}}(t_\ell=0)] = [\Phi(u_\ell)]$, is

$$[\Phi^{h}_{u_{\ell,m,n}}(t_\ell)] = e^{-[N_{\ell,m,n}]t_\ell}[\Phi(u_\ell)]\,. \tag{A2-3}$$

Combining the particular solutions from Eqs. A2-2 and the homogeneous solution from Eq. A2-3, yields an expression for $[\Phi_{u_{\ell,m,n}}(t_\ell)]$:

$$[\Phi_{u_{\ell,m,n}}(t_\ell)] = e^{-[N_{\ell,m,n}]t_\ell}[\Phi(u_\ell)] + [N_{\ell,m,n}]^{-1}\left\{[I]-e^{-[N_{\ell,m,n}]t_\ell}\right\}$$
$$\times [S^f_{u_{\ell,m,n}}] + \frac{1}{h^\ell_u}[N_{\ell,m,n}]^{-1}\left\{t_\ell[I]-[N_{\ell,m,n}]^{-1}\right.$$
$$\left.\times\langle[I]-e^{-[N_{\ell,m,n}]t_\ell}\rangle\right\}[S^\ell_{u_{\ell,m,n}}]$$
$$+\frac{1}{\left(h^\ell_u\right)^2}[N_{\ell,m,n}]^{-1}\left\{t^2_\ell[I]-2[N_{\ell,m,n}]^{-1}\langle t_\ell[I]\right.$$
$$\left.-[N_{\ell,m,n}]^{-1}([I]-e^{-[N_{\ell,m,n}]t_\ell})\rangle\right\}[S^q_{u_{\ell,m,n}}]. \qquad \text{(A2-4)}$$

Likewise, the three particular solutions to Eq. A2-1, on the interval $0 < t_{\ell-1} < h^{\ell-1}_u$, subject to the boundary condition $[\Phi^p_{u_{\ell-1,m,n}}(t_{\ell-1} = h^{\ell-1}_u)] = 0$, are

$$[\Phi^f_{u_{\ell-1,m,n}}(t_{\ell-1})] = [N_{\ell-1,m,n}]^{-1}\left\{[I]-e^{-[N_{\ell-1,m,n}](t_{\ell-1}-h^{\ell-1}_u)}\right\}$$
$$\times [S^f_{u_{\ell-1,m,n}}] \qquad \text{(A2-5a)}$$

$$[\Phi^\ell_{u_{\ell-1,m,n}}(t_{\ell-1})] = \frac{1}{h^{\ell-1}_u}[N_{\ell-1,m,n}]^{-1}\left\{t_{\ell-1}[I]\right.$$
$$-h^{\ell-1}_u e^{-[N_{\ell-1,m,n}](t_{\ell-1}-h^{\ell-1}_u)}-[N_{\ell-1,m,n}]^{-1}$$
$$\left.\times\langle[I]-e^{-[N_{\ell-1,m,n}](t_{\ell-1}-h^{\ell-1}_u)}\rangle\right\}[S^\ell_{u_{\ell-1,m,n}}]$$
$$\text{(A2-5b)}$$

Combining the particular solutions from Eqs. A2-2 and the homogeneous solution from Eq. A2-3, yields an expression for $[\Phi_{u_{\ell,m,n}}(t_\ell)]$:

$$[\Phi_{u_{\ell,m,n}}(t_\ell)] = e^{-[N_{\ell,m,n}]t_\ell}[\Phi(u_\ell)] + [N_{\ell,m,n}]^{-1}\left\{[I] - e^{-[N_{\ell,m,n}]t_\ell}\right\}$$
$$\times [S^f_{u_{\ell,m,n}}] + \frac{1}{h_u^\ell}[N_{\ell,m,n}]^{-1}\left\{t_\ell[I] - [N_{\ell,m,n}]^{-1}\right.$$
$$\left.\times\langle [I] - e^{-[N_{\ell,m,n}]t_\ell}\rangle\right\}[S^\ell_{u_{\ell,m,n}}]$$
$$+ \frac{1}{\left(h_u^\ell\right)^2}[N_{\ell,m,n}]^{-1}\left\{t_\ell^2[I] - 2[N_{\ell,m,n}]^{-1}\langle t_\ell[I]\right.$$
$$\left. - [N_{\ell,m,n}]^{-1}([I] - e^{-[N_{\ell,m,n}]t_\ell})\rangle\right\}[S^q_{u_{\ell,m,n}}]. \qquad \text{(A2-4)}$$

Likewise, the three particular solutions to Eq. A2-1, on the interval $0 < t_{\ell-1} < h_u^{\ell-1}$, subject to the boundary condition $[\Phi^p_{u_{\ell-1,m,n}}(t_{\ell-1} = h_u^{\ell-1})] = 0$, are

$$[\Phi^f_{u_{\ell-1,m,n}}(t_{\ell-1})] = [N_{\ell-1,m,n}]^{-1}\left\{[I] - e^{-[N_{\ell-1,m,n}](t_{\ell-1} - h_u^{\ell-1})}\right\}$$
$$\times [S^f_{u_{\ell-1,m,n}}] \qquad \text{(A2-5a)}$$

$$[\Phi^\ell_{u_{\ell-1,m,n}}(t_{\ell-1})] = \frac{1}{h_u^{\ell-1}}[N_{\ell-1,m,n}]^{-1}\left\{t_{\ell-1}[I]\right.$$
$$- h_u^{\ell-1}\, e^{-[N_{\ell-1,m,n}](t_{\ell-1} - h_u^{\ell-1})} - [N_{\ell-1,m,n}]^{-1}$$
$$\left.\times\langle [I] - e^{-[N_{\ell-1,m,n}](t_{\ell-1} - h_u^{\ell-1})}\rangle\right\}[S^\ell_{u_{\ell-1,m,n}}] \qquad \text{(A2-5b)}$$

$$[\Phi^{q}_{u_{\ell-1,m,n}}(t_{\ell-1})] = \frac{1}{\left(h_u^{\ell-1}\right)^2}[N_{\ell-1,m,n}]^{-1}\Big\{(t_{\ell-1})^2[I]$$

$$-\left(h_u^{\ell-1}\right)^2 e^{-[N_{\ell-1,m,n}](t_{\ell-1}-h_u^{\ell-1})} - 2[N_{\ell-1,m,n}]^{-1}$$

$$\times \langle t_{\ell-1}[I] - h_u^{\ell-1} e^{-[N_{\ell-1,m,n}](t_{\ell-1}-h_u^{\ell-1})}$$

$$- [N_{\ell-1,m,n}]^{-1}([I] - e^{-[N_{\ell-1,m,n}](t_{\ell-1}-h_u^{\ell-1})})\rangle\Big\}$$

$$\times [S^{q}_{u_{\ell-1,m,n}}] . \qquad \text{(A2-5c)}$$

The homogeneous solution to Eq. A2-1, on the interval $0 < t_{\ell-1} < h_u^{\ell-1}$, subject to the boundary condition $[\Phi^{h}_{u_{\ell-1,m,n}}(t_{\ell-1}=h_u^{\ell-1})] = [\Phi(u_\ell)]$ is

$$[\Phi^{h}_{\ell-1,m,n}(t_{\ell-1})] = e^{-[N_{\ell-1,m,n}](t_{\ell-1}-h_u^{\ell-1})}[\Phi(u_\ell)] . \qquad \text{(A2-6)}$$

Combining the particular solutions from Eqs. A2-5 and the homogeneous solution from Eq. A2-6 leads to an expression for $[\Phi_{u_{\ell-1,m,n}}(t_{\ell-1})]$:

$$[\Phi_{u_{\ell-1,m,n}}(t_{\ell-1})] = e^{-[N_{\ell-1,m,n}](t_{\ell-1}-h_u^{\ell-1})}[\Phi(u_\ell)]$$

$$+ [N_{\ell-1,m,n}]^{-1}\Big\{[I] - e^{-[N_{\ell-1,m,n}](t_{\ell-1}-h_u^{\ell-1})}\Big\}$$

$$\times [S^{f}_{u_{\ell-1,m,n}}] + \frac{1}{h_u^{\ell-1}}[N_{\ell-1,m,n}]^{-1}\Big\{t_{\ell-1}[I]$$

$$- h_u^{\ell-1} e^{-[N_{\ell-1,m,n}](t_{\ell-1}-h_u^{\ell-1})} - [N_{\ell-1,m,n}]^{-1} \times$$

$$\times \left\langle [I] - e^{-[N_{\ell-1,m,n}](t_{\ell-1}-h_u^{\ell-1})} \right\rangle \Bigg\} [S^{\ell}_{u_{\ell-1,m,n}}]$$

$$+ \frac{1}{\left(h_u^{\ell-1}\right)^2} [N_{\ell-1,m,n}]^{-1} \Bigg\{ t_{\ell-1}^2 [I]$$

$$- \left(h_u^{\ell-1}\right)^2 e^{-[N_{\ell-1,m,n}](t_{\ell-1}-h_u^{\ell-1})}$$

$$- 2[N_{\ell-1,m,n}]^{-1} \left\langle t_{\ell-1}[I] - h_u^{\ell-1} e^{-[N_{\ell-1,m,n}](t_{\ell-1}-h_u^{\ell-1})} \right.$$

$$\left. - [N_{\ell-1,m,n}]^{-1} \left([I] - e^{-[N_{\ell-1,m,n}](t_{\ell-1}-h_u^{\ell-1})} \right) \right\rangle \Bigg\} [S^{q}_{u_{\ell-1,m,n}}] . \quad \text{(A2-7)}$$

Integrating Eq. A2-4 over the interval $[0, h_\ell^u]$ and dividing by h_u^ℓ gives the result

$$[\bar{\Phi}_{u_{\ell,m,n}}] = \frac{1}{h_u^\ell} [N_{\ell,m,n}]^{-1} \left\{ [I] - e^{-[N_{\ell,m,n}]h_u^\ell} \right\} [\Phi(u_\ell)]$$

$$+ \frac{1}{h_u^\ell} [N_{\ell,m,n}]^{-1} \left\{ h_u^\ell [I] - [N_{\ell,m,n}]^{-1} \left\langle [I] - e^{-[N_{\ell,m,n}]h_u^\ell} \right\rangle \right\}$$

$$\times [S^{f}_{u_{\ell,m,n}}] + \frac{1}{\left(h_u^\ell\right)^2} [N_{\ell,m,n}]^{-1} \left\{ \frac{\left(h_u^\ell\right)^2}{2} [I] \right.$$

$$- [N_{\ell,m,n}]^{-1} \left\langle h_u^\ell [I] - [N_{\ell,m,n}]^{-1} ([I] \right.$$

$$\left. \left. - e^{-[N_{\ell,m,n}]h_u^\ell} \right\rangle \right\} [S^{\ell}_{u_{\ell,m,n}}] + \frac{1}{\left(h_u^\ell\right)^3} [N_{\ell,m,n}]^{-1} \left\{ \frac{\left(h_u^\ell\right)^3}{3} [I] \right.$$

$$- 2[N_{\ell,m,n}]^{-1} \left\langle \frac{\left(h_u^\ell\right)^2}{2} [I] - [N_{\ell,m,n}]^{-1} (h_u^\ell [I] \right.$$

$$\left. \left. - [N_{\ell,m,n}]^{-1} [[I] - e^{-[N_{\ell,m,n}]h_u^\ell}] \right) \right\rangle \Bigg\} [S^{q}_{u_{\ell,m,n}}] . \quad \text{(A2-8)}$$

Likewise, integrating Eq. A2-7 over the interval $[0, h_u^{\ell-1}]$ and dividing by $h_u^{\ell-1}$ produces the result

$$
\begin{aligned}
[\bar{\Phi}_{u_{\ell-1,m,n}}] = & -\frac{1}{h_u^{\ell-1}} [N_{\ell-1,m,n}]^{-1} \left\{ [I] - e^{[N_{\ell-1,m,n}] h_u^{\ell-1}} \right\} [\Phi(u_\ell)] \\
& + \frac{1}{h_u^{\ell-1}} [N_{\ell-1,m,n}]^{-1} \left\{ h_u^{\ell-1} [I] + [N_{\ell-1,m,n}]^{-1} \langle [I] \right. \\
& \left. - e^{[N_{\ell-1,m,n}] h_u^{\ell-1}} \rangle \right\} [S^f_{u_{\ell-1,m,n}}] \\
& + \frac{1}{\left(h_u^{\ell-1}\right)^2} [N_{\ell-1,m,n}]^{-1} \left\{ \frac{\left(h_u^{\ell-1}\right)^2}{2} [I] \right. \\
& + h_u^{\ell-1} [N_{\ell-1,m,n}]^{-1} \langle [I] - e^{[N_{\ell-1,m,n}] h_u^{\ell-1}} \rangle \\
& - [N_{\ell-1,m,n}]^{-1} \left(h_u^{\ell-1} [I] + [N_{\ell-1,m,n}]^{-1} \langle [I] \right. \\
& \left. \left. - e^{[N_{\ell-1,m,n}] h_u^{\ell-1}} \rangle \right) \right\} [S^\ell_{u_{\ell-1,m,n}}] \\
& + \frac{1}{\left(h_u^{\ell-1}\right)^3} [N_{\ell-1,m,n}]^{-1} \left\{ \frac{\left(h_u^{\ell-1}\right)^3}{3} [I] \right. \\
& + \left(h_u^{\ell-1}\right)^2 [N_{\ell-1,m,n}]^{-1} \langle [I] - e^{[N_{\ell-1,m,n}] h_u^{\ell-1}} \rangle \\
& - 2[N_{\ell-1,m,n}]^{-1} \left(\frac{\left(h_u^{\ell-1}\right)^2}{2} [I] + h_u^{\ell-1} [N_{\ell-1,m,n}]^{-1} \langle [I] \right. \\
& - e^{[N_{\ell-1,m,n}] h_u^{\ell-1}} \rangle - [N_{\ell-1,m,n}]^{-1} \left[h_u^{\ell-1} [I] \right. \\
& \left. \left. \left. + [N_{\ell-1,m,n}]^{-1} \langle [I] + e^{[N_{\ell-1,m,n}] h_u^{\ell-1}} \rangle \right] \right) \right\} [S^q_{u_{\ell-1,m,n}}] \, .
\end{aligned}
\tag{A2-9}
$$

Using the definitions of the hyperbolic functions and the identity

$$\{\sinh[N]\}^{-1}\{[I]-\cosh[N]\} = -\{\tanh[N/2]\},$$

multiplying Eq. A2-8 by $\{\sinh[N_{\ell,m,n}]\}^{-1}$, and adding the result to Eq. A2-9 multiplied by $\{\sinh[N_{\ell-1,m,n}]\}^{-1}$ yields

$$\left\{-\tanh[N_{\ell,m,n}]\frac{h_u^{\ell}}{2}-\tanh[N_{\ell-1,m,n}]\frac{h_u^{\ell-1}}{2}\right\}[\Phi(u_\ell)]$$

$$=\left(\sinh[N_{\ell,m,n}]h_u^{\ell}\right)^{-1}[N_{\ell,m,n}]h_u^{\ell}[\bar{\Phi}u_{\ell,m,n}]$$

$$-\left(\sinh[N_{\ell-1,m,n}]h_u^{\ell-1}\right)^{-1}[N_{\ell-1,m,n}]h_u^{\ell-1}[\bar{\Phi}u_{\ell-1,m,n}]$$

$$-\left(\sinh[N_{\ell,m,n}]h_u^{\ell}\right)^{-1}\left\{h_u^{\ell}[I]-[N_{\ell,m,n}]^{-1}\langle[I]-e^{-[N_{\ell,m,n}]h_u^{\ell}}\rangle\right\}$$

$$\times[S^f_{\ell,m,n}]+\left(\sinh[N_{\ell-1,m,n}]h_u^{\ell-1}\right)^{-1}\left\{h_u^{\ell-1}[I]\right.$$

$$\left.+[N_{\ell-1,m,n}]^{-1}\langle[I]-e^{[N_{\ell-1,m,n}]h_u^{\ell-1}}\rangle\right\}[S^f_{\ell-1,m,n}]$$

$$-\frac{1}{h_u^{\ell}}\left(\sinh[N_{\ell,m,n}]h_u^{\ell}\right)^{-1}\left\{\frac{\left(h_u^{\ell}\right)^2}{2}[I]-[N_{\ell,m,n}]^{-1}\langle h_u^{\ell}[I]\right.$$

$$\left.-[N_{\ell,m,n}]^{-1}\langle[I]-e^{-[N_{\ell,m,n}]h_u^{\ell}}\rangle\rangle\right\}[S^{\ell}_{u_{\ell,m,n}}]$$

$$+\frac{1}{h_u^{\ell-1}}\left(\sinh[N_{\ell-1,m,n}]h_u^{\ell-1}\right)^{-1}\left\{\frac{\left(h_u^{\ell-1}\right)^2}{2}[I]+h_u^{\ell-1}[N_{\ell-1,m,n}]^{-1}\right.$$

$$\times\langle[I]-e^{[N_{\ell-1,m,n}]h_u^{\ell-1}}\rangle-[N_{\ell-1,m,n}]^{-1}\langle h_u^{\ell-1}[I]$$

$$\left.+[N_{\ell-1,m,n}]^{-1}([I]-e^{[N_{\ell-1,m,n}]h_u^{\ell-1}}\rangle\rangle\right\}[S^{\ell}_{u_{\ell-1,m,n}}]-$$

$$
- \frac{1}{\left(h_u^{\ell}\right)^2}\left(\sinh[N_{\ell,m,n}]h_u^{\ell}\right)^{-1}\left\{\frac{\left(h_u^{\ell}\right)^3}{3}[I] - 2[N_{\ell,m,n}]^{-1}\left\langle \frac{\left(h_u^{\ell}\right)^2}{2}[I]\right.\right.
$$

$$
\left.\left. - [N_{\ell,m,n}]^{-1}\left(h_u^{\ell}[I] - [N_{\ell,m,n}]^{-1}\left[[I] - e^{-[N_{\ell,m,n}]h_u^{\ell}}\right]\right)\right\rangle\right\}[S^q_{u_{\ell,m,n}}]
$$

$$
+ \frac{1}{\left(h_u^{\ell-1}\right)^2}\left(\sinh[N_{\ell-1,m,n}]h_u^{\ell-1}\right)^{-1}\left\{\frac{\left(h_u^{\ell-1}\right)^3}{3}[I]\right.
$$

$$
+ \left(h_u^{\ell-1}\right)^2[N_{\ell-1,m,n}]^{-1}\left\langle [I] - e^{[N_{\ell-1,m,n}]h_u^{\ell-1}}\right\rangle
$$

$$
- 2[N_{\ell-1,m,n}]^{-1}\left\langle \frac{\left(h^u_{\ell-1}\right)^2}{2}[I] + h_u^{\ell-1}[N_{\ell-1,m,n}]^{-1}\left([I]\right.\right.
$$

$$
\left. - e^{[N_{\ell-1,m,n}]h_u^{\ell-1}}\right) - [N_{\ell-1,m,n}]^{-1}\left(h_u^{\ell-1}[I] + [N_{\ell-1,m,n}]^{-1}\right.
$$

$$
\left.\left.\times\left[[I] - e^{[N_{\ell-1,m,n}]h_u^{\ell-1}}\right]\right)\right\rangle\left.\right\}[S^q_{u_{\ell-1,m,n}}]\,. \qquad \text{(A2-10)}
$$

Equation A2-10 can be cast in a simpler form, as

$$
-[A_{u_{\ell-1,m,n}} + A_{u_{\ell,m,n}}][\Phi(u_{\ell})] = [B_{u_{\ell,m,n}}][\bar{\Phi}_{u_{\ell,m,n}}]
$$

$$
- [B_{u_{\ell-1,m,n}}][\bar{\Phi}_{u_{\ell-1,m,n}}] + [C^-_{u_{\ell,m,n}}][S^f_{u_{\ell,m,n}}]
$$

$$
- [C^+_{u_{\ell-1,m,n}}][S^f_{u_{\ell-1,m,n}}] + [D^-_{u_{\ell,m,n}}][S^f_{u_{\ell,m,n}}]
$$

$$
- [D^+_{u_{\ell-1,m,n}}][S^{\ell}_{u_{\ell-1,m,n}}] + [E^-_{u_{\ell,m,n}}][S^q_{u_{\ell,m,n}}]
$$

$$
- [E^+_{u_{\ell-1,m,n}}][S^q_{u_{\ell-1,m,n}}]\,, \qquad \text{(A2-11)}
$$

where

$$[A_{u_{\ell,m,n}}] \equiv \left(\tanh[N_{\ell,m,n}]\,\frac{h_u^\ell}{2}\right)$$

$$[B_{u_{\ell,m,n}}] \equiv \left(\sinh[N_{\ell,m,n}]h_u^\ell\right)^{-1}[N_{\ell,m,n}]h_u^\ell$$

$$[C^{\pm}_{u_{\ell,m,n}}] \equiv -\left(\sinh[N_{\ell,m,n}]h_u^\ell\right)^{-1}\left\{h_u^\ell[I]\pm[N_{\ell,m,n}]^{-1}\langle[I] - e^{\pm[N_{\ell,m,n}]h_u^\ell}\rangle\right\}$$

$$[D^{-}_{u_{\ell,m,n}}] \equiv -\frac{1}{h_u^\ell}\left\{\left(\sinh[N_{\ell,m,n}]h_u^\ell\right)^{-1}\frac{\left(h_u^\ell\right)^2}{2}[I] + [N_{\ell,m,n}]^{-1}[C^{-}_{u_{\ell,m,n}}]\right\}$$

$$[D^{+}_{u_{\ell,m,n}}] \equiv -\frac{1}{h_u^\ell}\left\{\left(\sinh[N_{\ell,m,n}]h_u^\ell\right)^{-1}\langle\frac{\left(h_u^\ell\right)^2}{2}[I]+h_u^\ell[N_{\ell,m,n}]^{-1}\left([I] - e^{[N_{\ell,m,n}]h_u^\ell}\right)\rangle + [N_{\ell,m,n}]^{-1}[C^{+}_{u_{\ell,m,n}}]\right\}$$

$$[E^{-}_{u_{\ell,m,n}}] \equiv -\frac{1}{\left(h_u^\ell\right)^2}\left\{\left(\sinh[N_{\ell,m,n}]h_u^\ell\right)^{-1}\frac{\left(h_u^\ell\right)^3}{3}[I] + 2h_u^\ell[N_{\ell,m,n}]^{-1}[D^{-}_{u_{\ell,m,n}}]\right\}$$

$$[E^{+}_{u_{\ell,m,n}}] \equiv -\frac{1}{\left(h_u^\ell\right)^2}\left\{\left(\sinh[N_{\ell,m,n}]h_u^\ell\right)^{-1}\langle\frac{\left(h_u^\ell\right)^3}{3}[I]+\left(h_u^\ell\right)^2[N_{\ell,m,n}]^{-1}\langle[I] - e^{[N_{\ell,m,n}]h_u^\ell}\rangle\rangle + 2h_u^\ell[N_{\ell,m,n}]^{-1}[D^{+}_{u_{\ell,m,n}}]\right\}.$$

If the matrices of Eq. A2-11 are partitioned into four G×G blocks, and if one notes that $[A_{u_{\ell,m,n}}]$ is block anti-diagonal and $[B_{u_{\ell,m,n}}]$ is block diagonal (see Appendix 3), the top equation of Eq. A2-11 can be expressed as

$$
\begin{aligned}
[J_{u_{\ell,m,n}}] = &-[A_{u_{\ell-1,m,n}} + A_{u_{\ell,m,n}}]_{12}^{-1} [B_{u_{\ell,m,n}}]_{11} [\bar{\phi}_{\ell,m,n}] \\
&+[A_{u_{\ell-1,m,n}} + A_{u_{\ell,m,n}}]_{12}^{-1} [B_{u_{\ell-1,m,n}}]_{11} [\bar{\phi}_{\ell-1,m,n}] \\
&+ [A_{u_{\ell-1,m,n}} + A_{u_{\ell,m,n}}]_{12}^{-1} [C^{-}_{u_{\ell,m,n}}]_{12} [S^{f}_{u_{\ell,m,n}}] \\
&- [A_{u_{\ell-1,m,n}} + A_{u_{\ell,m,n}}]_{12}^{-1} [C^{+}_{u_{\ell-1,m,n}}]_{12} [S^{f}_{u_{\ell-1,m,n}}] \\
&+ [A_{u_{\ell-1,m,n}} + A_{u_{\ell,m,n}}]_{12}^{-1} [D^{-}_{u_{\ell,m,n}}]_{12} [S^{\ell}_{u_{\ell,m,n}}] \\
&- [A_{u_{\ell-1,m,n}} + A_{u_{\ell,m,n}}]_{12}^{-1} [D^{+}_{u_{\ell-1,m,n}}]_{12} [S^{\ell}_{u_{\ell-1,m,n}}] \\
&+ [A_{u_{\ell-1,m,n}} + A_{u_{\ell,m,n}}]_{12}^{-1} [E^{-}_{u_{\ell,m,n}}]_{12} [S^{q}_{u_{\ell,m,n}}] \\
&- [A_{u_{\ell-1,m,n}} + A_{u_{\ell,m,n}}]_{12}^{-1} [E^{+}_{u_{\ell-1,m,n}}]_{12} [S^{q}_{u_{\ell-1,m,n}}] \, .
\end{aligned}
\tag{A2-12}
$$

An analogous expression can be written for $[J_{u_{\ell+1,m,n}}]$, and Eq. A2-12 can be subtracted from it to give an expression for the face-averaged net leakages,

$$
\begin{aligned}
[\bar{L}_{u_{\ell,m,n}}] = &- [A_{u_{\ell-1,m,n}} + A_{u_{\ell,m,n}}]_{12}^{-1} [B_{u_{\ell-1,m,n}}]_{11} [\bar{\phi}_{\ell-1,m,n}] \\
&+ \left\{ [A_{u_{\ell-1,m,n}} + A_{u_{\ell,m,n}}]_{12}^{-1} + [A_{u_{\ell,m,n}} + A_{u_{\ell+1,m,n}}]_{12}^{-1} \right\} \times
\end{aligned}
$$

$$\times [B_{u_{\ell,m,n}}]_{11} [\bar{\phi}_{\ell,m,n}]$$

$$- [A_{u_{\ell,m,n}} + A_{u_{\ell+1,m,n}}]^{-1}_{12} [B_{u_{\ell+1,m,n}}]_{11} [\bar{\phi}_{\ell+1,m,n}]$$

$$+ [A_{u_{\ell-1,m,n}} + A_{u_{\ell,m,n}}]^{-1}_{12} [C^{+}_{u_{\ell-1,m,n}}]_{12} [S^{f}_{u_{\ell-1,m,n}}]$$

$$- \Big\{ [A_{u_{\ell-1,m,n}} + A_{u_{\ell,m,n}}]^{-1}_{12} [C^{-}_{u_{\ell,m,n}}]_{12}$$

$$+ [A_{u_{\ell,m,n}} + A_{u_{\ell+1,m,n}}]^{-1}_{12} [C^{+}_{u_{\ell,m,n}}]_{12} \Big\} [S^{f}_{u_{\ell,m,n}}]$$

$$+ [A_{u_{\ell,m,n}} + A_{u_{\ell+1,m,n}}]^{-1}_{12} [C^{-}_{u_{\ell+1,m,n}}]_{12} [S^{f}_{u_{\ell+1,m,n}}]$$

$$+ [A_{u_{\ell-1,m,n}} + A_{u_{\ell,m,n}}]^{-1}_{12} [D^{+}_{u_{\ell-1,m,n}}]_{12} [S^{\ell}_{u_{\ell-1,m,n}}]$$

$$- \Big\{ [A_{u_{\ell-1,m,n}} + A_{u_{\ell,m,n}}]^{-1}_{12} [D^{-}_{u_{\ell,m,n}}]_{12}$$

$$+ [A_{u_{\ell,m,n}} + A_{u_{\ell+1,m,n}}]^{-1}_{12} [D^{+}_{u_{\ell,m,n}}]_{12} \Big\} [S^{\ell}_{u_{\ell,m,n}}]$$

$$+ [A_{u_{\ell,m,n}} + A_{u_{\ell+1,m,n}}]^{-1}_{12} [D^{-}_{u_{\ell+1,m,n}}]_{12} [S^{\ell}_{u_{\ell+1,m,n}}]$$

$$+ [A_{u_{\ell-1,m,n}} + A_{u_{\ell,m,n}}]^{-1}_{12} [E^{+}_{u_{\ell-1,m,n}}]_{12} [S^{q}_{u_{\ell-1,m,n}}]$$

$$- \Big\{ [A_{u_{\ell-1,m,n}} + A_{u_{\ell,m,n}}]^{-1}_{12} [E^{-}_{u_{\ell,m,n}}]_{12}$$

$$+ [A_{u_{\ell,m,n}} + A_{u_{\ell+1,m,n}}]^{-1}_{12} [E^{+}_{u_{\ell,m,n}}]_{12} \Big\} [S^{q}_{u_{\ell,m,n}}]$$

$$+ [A_{u_{\ell,m,n}} + A_{u_{\ell+1,m,n}}]^{-1}_{12} [E^{-}_{u_{\ell+1,m,n}}]_{12} [S^{q}_{u_{\ell+1,m,n}}].$$

(A2-13)

Since each of the $[S^{p}_{u_{\ell,m,n}}]$ vectors contain specified combinations of face-averaged net leakages, Eq. A2-13 is an expression relating node-averaged fluxes and face-averaged net leakages. By substituting the definitions of $[S^{p}_{u_{\ell,m,n}}]$ from Eq. 2-18, Eq. A2-13 can be manipulated to obtain a much more useful expression,

$$
\begin{aligned}
[\bar{L}_{u_{\ell,m,n}}] = {} & [F^{\ell-1}_{u_{\ell,m,n}}][\bar{\phi}_{\ell-1,m,n}] + [F^{\ell}_{u_{\ell,m,n}}][\bar{\phi}_{\ell,m,n}] \\
& + [F^{\ell+1}_{u_{\ell,m,n}}][\bar{\phi}_{\ell+1,m,n}] + [G^{\ell-2}_{u_{\ell,m,n}}][\bar{S}_{u_{\ell-2,m,n}}] \\
& + [G^{\ell-1}_{u_{\ell,m,n}}][\bar{S}_{u_{\ell-1,m,n}}] + [G^{\ell}_{u_{\ell,m,n}}][\bar{S}_{u_{\ell,m,n}}] \\
& + [G^{\ell+1}_{u_{\ell,m,n}}][\bar{S}_{u_{\ell-1,m,n}}] + [G^{\ell+2}_{u_{\ell,m,n}}][\bar{S}_{u_{\ell+2,m,n}}] ,
\end{aligned}
\qquad \text{(A2-14)}
$$

where

$$
[F^{\ell-1}_{u_{\ell,m,n}}] \equiv -[A_{u_{\ell-1,m,n}} + A_{u_{\ell,m,n}}]^{-1}_{12} [B_{u_{\ell-1,m,n}}]_{11}
$$

$$
\begin{aligned}
[F^{\ell}_{u_{\ell,m,n}}] \equiv + \Big\{ & [A_{u_{\ell-1,m,n}} + A_{u_{\ell,m,n}}]^{-1}_{12} \\
& + [A_{u_{\ell,m,n}} + A_{u_{\ell+1,m,n}}]^{-1}_{12} \Big\} [B_{u_{\ell,m,n}}]_{11}
\end{aligned}
$$

$$
[F^{\ell+1}_{u_{\ell,m,n}}] \equiv -[A_{u_{\ell,m,n}} + A_{u_{\ell+1,m,n}}]^{-1}_{12} [B_{u_{\ell+1,m,n}}]_{11}
$$

$$
\begin{aligned}
[G^{\ell-2}_{u_{\ell,m,n}}] \equiv \Big\{ & [A_{u_{\ell-1,m,n}} + A_{u_{\ell,m,n}}]^{-1}_{12} \langle [C^{+}_{u_{\ell-1,m,n}}]_{12} \bar{a}_{u_{\ell-1}} \\
& + [D^{+}_{u_{\ell-1,m,n}}]_{12} \bar{b}_{u_{\ell-1}} + [E^{+}_{u_{\ell-1,m,n}}]_{12} \bar{c}_{u_{\ell-1}} \rangle \Big\}
\end{aligned}
$$

$$[G^{\ell-1}_{u_{\ell,m,n}}] \equiv \Big\{ [A_{u_{\ell-1,m,n}} + A_{u_{\ell,m,n}}]^{-1}_{12} \langle [C^{+}_{u_{\ell-1,m,n}}]_{12} (1 - a^{-}_{u_{\ell-1}} - a^{+}_{u_{\ell-1}})$$

$$+ [D^{+}_{u_{\ell-1,m,n}}]_{12} (-b^{-}_{u_{\ell-1}} - b^{+}_{u_{\ell-1}}) + [E^{+}_{u_{\ell-1,m,n}}]_{12} (-c^{-}_{u_{\ell-1}}$$

$$- c^{+}_{u_{\ell-1}}) \rangle - \langle [A_{u_{\ell-1,m,n}} + A_{u_{\ell,m,n}}]^{-1}_{12} [C^{-}_{u_{\ell,m,n}}]_{12}$$

$$+ [A_{u_{\ell,m,n}} + A_{u_{\ell+1,m,n}}]^{-1}_{12} [C^{+}_{u_{\ell,m,n}}]_{12} \rangle \; a^{-}_{u_{\ell}}$$

$$- \langle [A_{u_{\ell-1,m,n}} + A_{u_{\ell,m,n}}]^{-1}_{12} [D^{-}_{u_{\ell,m,n}}]_{12}$$

$$+ [A_{u_{\ell,m,n}} + A_{u_{\ell+1,m,n}}]^{-1}_{12} [D^{+}_{u_{\ell,m,n}}]_{12} \rangle \; b^{-}_{u_{\ell}}$$

$$- \langle [A_{u_{\ell-1,m,n}} + A_{u_{\ell,m,n}}]^{-1}_{12} [E^{-}_{u_{\ell,m,n}}]_{12}$$

$$+ [A_{u_{\ell,m,n}} + A_{u_{\ell+1,m,n}}]^{-1}_{12} [E^{+}_{u_{\ell,m,n}}]_{12} \rangle \; c^{-}_{u_{\ell}} \Big\}$$

$$[G^{\ell}_{u_{\ell,m,n}}] \equiv \Big\{ [A_{u_{\ell-1,m,n}} + A_{u_{\ell,m,n}}]^{-1}_{12} \langle [C^{+}_{u_{\ell-1,m,n}}]_{12} \; a^{+}_{u_{\ell-1}}$$

$$+ [D^{+}_{u_{\ell-1,m,n}}]_{12} \; b^{+}_{u_{\ell-1}} + [E^{+}_{u_{\ell-1,m,n}}]_{12} \; c^{+}_{u_{\ell-1}} \rangle$$

$$+ [A_{u_{\ell-1,m,n}} + A_{u_{\ell,m,n}}]^{-1}_{12} \langle [C^{-}_{u_{\ell+1,m,n}}]_{12} \; a^{-}_{u_{\ell+1}}$$

$$+ [D^{-}_{u_{\ell+1,m,n}}]_{12} \; b^{-}_{u_{\ell+1}} + [E^{-}_{u_{\ell+1,m,n}}]_{12} \; c^{-}_{u_{\ell+1}} \rangle$$

$$- \langle [A_{u_{\ell-1,m,n}} + A_{u_{\ell,m,n}}]^{-1}_{12} [C^{-}_{u_{\ell,m,n}}]_{12}$$

$$+ [A_{u_{\ell,m,n}} + A_{u_{\ell+1,m,n}}]^{-1}_{12} [C^{+}_{u_{\ell,m,n}}]_{12} \rangle (1 - a^{-}_{u_{\ell}} - a^{+}_{u_{\ell}}) -$$

$$
\begin{aligned}
&- \langle [A_{u_{\ell-1,m,n}} + A_{u_{\ell,m,n}}]_{12}^{-1} [D^-_{u_{\ell,m,n}}]_{12} \\
&+ [A_{u_{\ell,m,n}} + A_{u_{\ell+1,m,n}}]_{12}^{-1} [D^+_{u_{\ell,m,n}}]_{12} \rangle (-b^-_{u_\ell} - b^+_{u_\ell}) \\
&- \langle [A_{u_{\ell-1,m,n}} + A_{u_{\ell,m,n}}]_{12}^{-1} [E^-_{u_{\ell,m,n}}]_{12} \\
&+ [A_{u_{\ell,m,n}} + A_{u_{\ell+1,m,n}}]_{12}^{-1} [E^+_{u_{\ell,m,n}}]_{12} \rangle (-c^-_{u_\ell} - c^+_{u_\ell}) \Big\}
\end{aligned}
$$

$$
\begin{aligned}
[G^{\ell+1}_{u_{\ell,m,n}}] \equiv \Big\{ & [A_{u_{\ell,m,n}} + A_{u_{\ell+1,m,n}}]_{12}^{-1} \langle [C^-_{u_{\ell+1,m,n}}]_{12} (1 - a^-_{u_{\ell+1}} - a^+_{u_{\ell+1}}) \\
&+ [D^-_{u_{\ell+1,m,n}}]_{12} (-b^-_{u_{\ell+1}} - b^+_{u_{\ell+1}}) + [E^-_{u_{\ell+1,m,n}}]_{12} (-c^-_{u_{\ell+1}} \\
&- c^+_{u_{\ell+1}}) - \langle [A_{u_{\ell-1,m,n}} + A_{u_{\ell,m,n}}]_{12}^{-1} [C^-_{u_{\ell,m,n}}]_{12} \\
&+ [A_{u_{\ell,m,n}} + A_{u_{\ell+1,m,n}}]_{12}^{-1} [C^+_{u_{\ell,m,n}}]_{12} \rangle a^+_{u_\ell} \\
&- \langle [A_{u_{\ell-1,m,n}} + A_{u_{\ell,m,n}}]_{12}^{-1} [D^-_{u_{\ell,m,n}}]_{12} \\
&+ [A_{u_{\ell,m,n}} + A_{u_{\ell+1,m,n}}]_{12}^{-1} [D^+_{u_{\ell,m,n}}]_{12} \rangle b^+_{u_\ell} \\
&- \langle [A_{u_{\ell-1,m,n}} + A_{u_{\ell,m,n}}]_{12}^{-1} [E^-_{u_{\ell,m,n}}]_{12} \\
&+ [A_{u_{\ell,m,n}} + A_{u_{\ell+1,m,n}}]_{12}^{-1} [E^+_{u_{\ell,m,n}}]_{12} \rangle c^+_{u_\ell} \Big\}
\end{aligned}
$$

$$
\begin{aligned}
[G^{\ell+2}_{u_{\ell,m,n}}] \equiv \Big\{ & [A_{u_{\ell,m,n}} + A_{u_{\ell+1,m,n}}]_{12}^{-1} \langle [C^-_{u_{\ell+1,m,n}}]_{12} a^+_{u_{\ell+1}} \\
&+ [D^-_{u_{\ell+1,m,n}}]_{12} b^+_{u_{\ell+1}} + [E^-_{u_{\ell+1,m,n}}]_{12} c^+_{u_{\ell+1}} \rangle \Big\} .
\end{aligned}
$$

Also recall that

$$[\bar{S}_{u_{\ell,m,n}}] \equiv \left\{ \frac{1}{h_v^m} [\bar{L}_{v_{\ell,m,n}}] + \frac{1}{h_w^n} [\bar{L}_{w_{\ell,m,n}}] \right\} ;$$

$$u = x,y,z$$

$$v \neq u$$

$$w \neq u \neq v .$$

Equation A2-14 is identical to Eq. 2-19 which was simply stated in Chapter 2. These relationships between node-averaged fluxes and face-averaged net leakages are true for any group structure, but the matrices in Eq. A2-11 remain to be determined. The methods employed to evaluate these matrices are contained in Appendix 3.

The application of boundary conditions on the surfaces of the reactor slightly alters the form of Eq. A2-14. Application of a zero current boundary condition on the $t_\ell = 0$ surface of node (ℓ,m,n) implies that the analogous equation to Eq. A2-13 is obtained without subtracting $[J_{u_{\ell,m,n}}]$, that is,

$$[\bar{L}_{u_{\ell,m,n}}] = [J_{u_{\ell+1,m,n}}] .$$

The effect of this zero current boundary condition on the "coupling coefficients" of node (ℓ,m,n) in Eq. A2-14 is equivalent to replacing $[A_{u_{\ell-1,m,n}} + A_{u_{\ell,m,n}}]^{-1}_{12}$ by the null matrix.

Albedo boundary conditions are also permitted. The particular form of the albedo is

$$[\phi_{u_{\ell,m,n}}(t_\ell = h_u^\ell)] = [\alpha][J_{u_{\ell,m,n}}(t_\ell = h_u^\ell)] \qquad \text{(A2-15)}$$

where $[\alpha]$ is a full G×G matrix. To derive the equation analogous to Eq. A2-14, the albedo is substituted into Eq. A2-9 to obtain, for an albedo applied on the $t_\ell = h_u^\ell$ surface of node (ℓ,m,n)

$$-\left\{\left[A_{u_{\ell,m,n}}\right]_{12}^{-1} + [\alpha]\right\}\left[J_{u_{\ell+1,m,n}}\right]$$

$$= -\left[B_{u_{\ell,m,n}}\right]_{11}\left[\bar{\phi}_{\ell,m,n}\right] + \left[C^+_{u_{\ell,m,n}}\right]_{12}\left[S^f_{u_{\ell,m,n}}\right]$$

$$+ \left[D^+_{u_{\ell,m,n}}\right]_{12}\left[S^\ell_{u_{\ell,m,n}}\right] + \left[E^+_{u_{\ell,m,n}}\right]_{12}\left[S^q_{u_{\ell,m,n}}\right]. \quad \text{(A2-16)}$$

The net effect of the albedo, applied on the $t_\ell = h_u^\ell$ surface of node (ℓ,m,n), on the coupling coefficients of node (ℓ,m,n) in Eq. A2-14 is the same as replacing $\left[A_{u_{\ell+1,m,n}}\right]$ by $[\alpha]$ and all other matrices for node $(\ell+1,m,n)$ by the null matrix.

From the form of the albedo in Eq. A2-15, it is easy to see that the zero flux boundary condition is applied by setting $[\alpha]$ equal to the null matrix. An extrapolated flux (logarithmic derivative) approximation to a zero incoming current boundary condition is achieved by setting

$$[\alpha] = \begin{bmatrix} 3d\,\Sigma_{tr_1} & 0 & \cdots & 0 \\ 0 & \ddots & & \\ \vdots & & \ddots & \\ 0 & & & 3d\,\Sigma_{tr_G} \end{bmatrix},$$

where d is the extrapolation distance and Σ_{tr_g} is the macroscopic transport cross section of group g. Equation A2-14 and the matrices of Eq. A2-11 completely specify the spatial coupling of the node-averaged fluxes and the face-averaged net leakages in the Analytic Nodal Method.

Appendix 3

EVALUATION OF SPATIAL COUPLING MATRICES

Actual application of the Analytic Nodal Method requires evaluation of the matrices defined in Eq. A2-11. Each of these matrices is a $2G \times 2G$ matrix whose elements depend only on the properties of a single node. The essential difficulty in evaluating these matrices stems from the fact that the exponential of $[N_{\ell,m,n}]$, as defined in Eq. A2-1, must be evaluated. $[N_{\ell,m,n}]$ is block antidiagonal with its lower block being partially comprised of the $G \times G$ group-to-group scattering matrix. In the general multigroup case, it is not apparent how to obtain this exponential. If the matrix $[N_{\ell,m,n}]$ could be diagonalized in some fashion, the exponential of $[N_{\ell,m,n}]$ would, of course, be readily obtainable.

If the number of neutron energy groups is restricted to a small number, direct evaluation of the matrices becomes feasible. Since this paper is primarily concerned with light water reactor analysis, in which two-group diffusion theory is commonly used, the matrices will be evaluated directly for the two-group case.

The one-dimensional, source-free, two-group, diffusion equation for a nuclearly homogeneous region ($u_\ell < u < u_{\ell+1}$) can be expressed as

$$\begin{bmatrix} D_1 \frac{d^2}{du^2} - \Sigma_1 & \frac{1}{\gamma}\nu\Sigma_{f_2} \\ \Sigma_{21} & D_2 \frac{d^2}{du^2} - \Sigma_2 \end{bmatrix} \begin{bmatrix} \phi_1(u) \\ \phi_2(u) \end{bmatrix} = [0] \qquad \text{(A3-1)}$$

where

$D_g \equiv$ group g diffusion coefficient (cm)

$\Sigma_2 \equiv$ group 2 macroscopic absorption cross section (cm^{-1})

$\nu\Sigma_{f_g} \equiv$ group g macroscopic fission cross section times nu, the mean number of neutrons emitted per fission (cm^{-1})

$\Sigma_1 \equiv$ group 1 macroscopic removal (absorption plus outscatter) cross section minus $\frac{1}{\gamma}\nu\Sigma_{f_1}$ (cm^{-1})

$\Sigma_{21} \equiv$ macroscopic transfer cross section from group 1 to group 2 (cm^{-1})

$\phi_g \equiv$ group g scalar neutron flux (cm^{-2} sec^{-1})

$\gamma \equiv$ critical eigenvalue of global static reactor problem,

and it has been assumed that there exists no upscatter and all fission neutrons are born in group 1 (i.e., $\Sigma_{12} = 0$, $\chi_1 = 1$, $\chi_2 = 0$). If a particular solution to Eq. A3-1 exists such that

$$\begin{bmatrix} \frac{d^2}{du^2} & 0 \\ 0 & \frac{d^2}{du^2} \end{bmatrix} \begin{bmatrix} \phi_1(u) \\ \phi_2(u) \end{bmatrix} = \begin{bmatrix} -B^2 & 0 \\ 0 & -B^2 \end{bmatrix} \begin{bmatrix} \phi_1(u) \\ \phi_2(u) \end{bmatrix} \qquad \text{(A3-2)}$$

then B^2 must satisfy the equation

$$\begin{bmatrix} -D_1B^2 - \Sigma_1 & \frac{1}{\gamma}\nu\Sigma_{f_2} \\ \Sigma_{21} & -D_2B^2 - \Sigma_2 \end{bmatrix} \begin{bmatrix} \phi_1(u) \\ \phi_\ell(u) \end{bmatrix} = [0] \ . \tag{A3-3}$$

For a nontrivial solution to exist to Eq. A3-3, the determinant of the coefficient matrix must be identically zero. This implies that B^2 must have very special values. If the two values of B^2 which satisfy Eq. A3-2 are designated κ^2 and $-\mu^2$, their values are given by

$$\kappa^2 = -\frac{1}{2}\left(\frac{\Sigma_1}{D_1} + \frac{\Sigma_2}{D_2}\right) + \left\langle \left(\frac{\Sigma_2}{2D_2} - \frac{\Sigma_1}{2D_1}\right)^2 + \frac{\nu\Sigma_{f_2}\Sigma_{21}}{\gamma D_1 D_2} \right\rangle^{1/2}$$

$$\mu^2 = \frac{1}{2}\left(\frac{\Sigma_1}{D_1} + \frac{\Sigma_2}{D_2}\right) + \left\langle \left(\frac{\Sigma_2}{2D_2} - \frac{\Sigma_1}{2D_1}\right)^2 + \frac{\nu\Sigma_{f_2}\Sigma_{21}}{\gamma D_1 D_2} \right\rangle^{1/2} . \tag{A3-4}$$

μ^2 has been chosen such that it will always be positive, and κ^2 can be either positive or negative. With two "slow-to-fast flux ratios" defined to be

$$r \equiv \frac{\Sigma_{21}}{D_2\kappa^2 + \Sigma_2}$$

$$s \equiv \frac{\Sigma_{21}}{-D_2\mu^2 + \Sigma_2} , \tag{A3-5}$$

the general solution to Eq. A3-3 is then given by

$$\begin{bmatrix} \phi_1(u) \\ \phi_2(u) \end{bmatrix} = \begin{bmatrix} 1 & 1 \\ r & s \end{bmatrix} \begin{bmatrix} a_1 \sin \kappa u + a_2 \cos \kappa u \\ a_3 \sinh \mu u + a_4 \cosh \mu u \end{bmatrix} . \tag{A3-6}$$

Likewise, the current vector is given by

$$\begin{bmatrix} J_1(u) \\ J_2(u) \end{bmatrix} = \begin{bmatrix} -D_1 & -D_1 \\ -rD_2 & -sD_2 \end{bmatrix} \begin{bmatrix} a_1\kappa \cos \kappa u - a_2\kappa \sin \kappa u \\ a_3\mu \cosh \mu u + a_4\mu \sinh \mu u \end{bmatrix}. \quad \text{(A3-7)}$$

With the definitions

$$[\Phi(u)] \equiv \begin{bmatrix} \phi_1(u) \\ \phi_2(u) \\ J_1(u) \\ J_2(u) \end{bmatrix}$$

$$[P] \equiv \begin{bmatrix} 1 & 1 & 0 & 0 \\ r & s & 0 & 0 \\ 0 & 0 & -D_1 & -D_1 \\ 0 & 0 & -rD_2 & -sD_2 \end{bmatrix} \quad \text{(A3-8)}$$

$$[Q(u)] \equiv \begin{bmatrix} \sin \kappa u & \cos \kappa u & 0 & 0 \\ 0 & 0 & \sinh \mu u & \cosh \mu u \\ \kappa \cos \kappa u & -\kappa \sin \kappa u & 0 & 0 \\ 0 & 0 & \mu \cosh \mu u & \mu \sinh \mu u \end{bmatrix}$$

$$[R] \equiv \begin{bmatrix} a_1 \\ a_2 \\ a_3 \\ a_4 \end{bmatrix},$$

Equations A3-6 and A3-7 can be expressed as

$$[\Phi(u)] = [P][Q(u)][R] \ . \tag{A3-9}$$

The inverses of $[P]$ and $[Q]$ both exist and are given by

$$[P]^{-1} = \begin{bmatrix} s & -1 & 0 & 0 \\ -r & 1 & 0 & 0 \\ 0 & 0 & -\frac{s}{D_1} & \frac{1}{D_2} \\ 0 & 0 & \frac{r}{D_1} & -\frac{1}{D_2} \end{bmatrix} \frac{1}{s - r} \tag{A3-10}$$

and

$$[Q(u)]^{-1} = \begin{bmatrix} \sin \kappa u & 0 & \frac{1}{\kappa} \cos \kappa u & 0 \\ \cos \kappa u & 0 & -\frac{1}{\kappa} \sin \kappa u & 0 \\ 0 & -\sinh \mu u & 0 & \frac{1}{\mu} \cosh \mu u \\ 0 & \cosh \mu u & 0 & \frac{1}{\mu} \sinh \mu u \end{bmatrix} . \tag{A3-11}$$

Hence, the unknown coefficients of the general solution are

$$[R] = [Q(u)]^{-1}[P]^{-1}[\Phi(u)] \ . \tag{A3-12}$$

For a homogeneous region which extends from u_ℓ to $u_{\ell+1}$, $[\Phi(u_\ell)]$ can be expressed in terms of $[\Phi(u_{\ell+1})]$ by applying Eq. A3-9 at $u = u_\ell$ and Eq. A3-12 at $u = u_{\ell+1}$ and eliminating $[R]$ to obtain

$$[\Phi(u_\ell)] = [P][Q(u_\ell)][Q(u_{\ell+1})]^{-1}[P]^{-1}[\Phi(u_{\ell+1})] \ . \tag{A3-13}$$

With the further definitions, $h \equiv u_{\ell+1} - u_\ell$ and $[Q] \equiv [Q(u_\ell)][Q(u_{\ell+1})]^{-1}$, $[Q]$ can be expressed as

$$[Q] = \begin{bmatrix} \cos \kappa h & 0 & -\frac{1}{\kappa} \sin \kappa h & 0 \\ 0 & \cosh \mu h & 0 & -\frac{1}{\mu} \sinh \mu h \\ \kappa \sin \kappa h & 0 & \cos \kappa h & 0 \\ 0 & -\mu \sinh \mu h & 0 & \cosh \mu h \end{bmatrix}, \quad \text{(A3-14)}$$

and Eq. A3-13 becomes

$$[\Phi(u_\ell)] = [P][Q][P]^{-1}[\Phi(u_{\ell+1})] \ . \quad \text{(A3-15)}$$

In Appendix 2, an expression was derived which also related $[\Phi(u_\ell)]$ to $[\Phi(u_{\ell+1})]$. This expression, from Eq. A2-6, is

$$[\Phi_{\ell,m,n}(u_\ell)] = e^{+[N_{\ell,m,n}]h_u^\ell}[\Phi_{\ell,m,n}(u_{\ell+1})] \ ,$$

which (with the node subscripts dropped since each node is treated separately) becomes

$$[\Phi(u_\ell)] = e^{[N]h}[\Phi(u_{\ell+1})] \ . \quad \text{(A3-16)}$$

Comparison of Eqs. A3-15 and A3-16 indicates that

$$e^{[N]h} = [P][Q][P]^{-1} \ . \quad \text{(A3-17)}$$

The matrices $[P]$ and $[Q]$ depend only on the nuclear properties and mesh spacing of each node; hence, the exponential of $[N]h$ is completely specified by Eq. A3-17. With this expression for $e^{[N]h}$,

identities for each of the spatial coupling matrices of Eq. A2-11 can be derived. Making use of the definitions of the hyperbolic functions, one finds that

$$(\sinh [N]h)^{-1} = [P] \begin{bmatrix} 0 & 0 & \frac{1}{\kappa} \csc \kappa h & 0 \\ 0 & 0 & 0 & -\frac{1}{\mu} \operatorname{csch} \mu h \\ -\kappa \csc \kappa h & 0 & 0 & 0 \\ 0 & -\mu \operatorname{csch} \mu h & 0 & 0 \end{bmatrix} [P]^{-1} \tag{A3-18a}$$

$$[I] - \cosh [N]h = [P] \begin{bmatrix} 1 - \cos \kappa h & 0 & 0 & 0 \\ 0 & 1 - \cosh \mu h & 0 & 0 \\ 0 & 0 & 1 - \cos \kappa h & 0 \\ 0 & 0 & 0 & 1 - \cosh \mu h \end{bmatrix} [P]^{-1} . \tag{A3-18b}$$

The matrices defined in Eq. A2-11 involve only certain blocks of the full (4 × 4) matrices; hence, only certain blocks need to be evaluated. Several identities which prove very useful in simplifying the matrices are

$$[N]_{12}^{-1} = h^2 \begin{bmatrix} \frac{1}{\kappa^2 h^2} & -\frac{1}{\mu^2 h^2} \\ \frac{r}{\kappa^2 h^2} & -\frac{s}{\mu^2 h^2} \end{bmatrix} [P]_{22}^{-1} \tag{A3-19a}$$

$$(\sinh [N]h)^{-1}_{12} [N]^{-1}_{21} (\sinh [N]h)_{12} = [N]^{-1}_{12} \qquad \text{(A3-19b)}$$

$$(\sinh [N]h)^{-1}_{21} [N]^{-1}_{12} ([I] - \cosh [N]h)_{22} = -(\tanh [N]\tfrac{h}{2})_{21} [N^{-1}]_{12} \; . \qquad \text{(A3-19c)}$$

The latter two identities are easily proven from the fact that

$$f([N])g([N]) = g([N])f([N])$$

for any functions f and g which can be expressed as series involving powers of [N].

Evaluation of the matrices in Eq. A2-11 is by no means a trivial exercise, but once the algebra has been performed, the following simple expressions are obtained:

$$[A]_{12} = \begin{bmatrix} -\alpha & -\beta \\ -r\alpha & -s\beta \end{bmatrix} [P]^{-1}_{22} h$$

$$[B]_{11} = \begin{bmatrix} \gamma & \delta \\ r\gamma & s\delta \end{bmatrix} \begin{bmatrix} s & -1 \\ -r & 1 \end{bmatrix} \frac{1}{s-r}$$

$$[C^{\pm}]_{12} = \begin{bmatrix} -\varepsilon & \zeta \\ -r\varepsilon & s\zeta \end{bmatrix} [P]^{-1}_{22} h^2$$

$$[D^{+}]_{12} = \begin{bmatrix} -\xi & o \\ -r\xi & so \end{bmatrix} [P]^{-1}_{22} h^2$$

$$[D^{-}]_{12} = \begin{bmatrix} -\eta & \theta \\ -r\eta & s\theta \end{bmatrix} [P]^{-1}_{22} h^2$$

$$[E^+]_{12} = \begin{bmatrix} -\sigma & \tau \\ -r\sigma & s\tau \end{bmatrix} [P]_{22}^{-1} h^2$$

$$[E^-]_{12} = \begin{bmatrix} -\pi & \rho \\ -r\pi & s\rho \end{bmatrix} [P]_{22}^{-1} h^2 \qquad \text{(A3-20)}$$

where

$$\alpha \equiv \frac{1}{\kappa h} \tan(\kappa h/2); \quad \kappa^2 > 0 \quad \equiv \frac{1}{\sqrt{|\kappa^2|}\, h} \tanh\left(\sqrt{|\kappa^2|}\, h/2\right); \quad \kappa^2 < 0$$

$$\beta \equiv \frac{1}{\mu h} \tanh(\mu h/2)$$

$$\gamma \equiv \kappa h \csc(\kappa h); \quad \kappa^2 > 0 \quad \equiv \sqrt{|\kappa^2|}\, h \operatorname{csch}\left(\sqrt{|\kappa^2|}\, h\right); \quad \kappa^2 < 0$$

$$\delta \equiv \mu h \operatorname{csch}(\mu h)$$

$$\varepsilon \equiv \frac{1}{\kappa^2 h^2} (\gamma - 1)$$

$$\zeta \equiv \frac{1}{\mu^2 h^2} (\delta - 1)$$

$$\eta \equiv \frac{1}{\kappa^2 h^2} \left(\frac{\gamma}{2} - \alpha\right)$$

$$\theta \equiv \frac{1}{\mu^2 h^2} \left(\frac{\delta}{2} - \beta\right)$$

$$\xi \equiv \frac{1}{\kappa^2 h^2} \left(\frac{\gamma}{2} + \alpha - 1\right)$$

$$o \equiv \frac{1}{\mu^2 h^2} \left(\frac{\delta}{2} + \beta - 1\right)$$

$$\pi \equiv \frac{1}{\kappa^2 h^2} \left(\frac{\gamma}{3} - 2\varepsilon\right)$$

$$\rho \equiv \frac{1}{\mu^2 h^2}\left(\frac{\delta}{3}+2\zeta\right)$$

$$\sigma \equiv \pi + \frac{1}{\kappa^2 h^2}(2\alpha - 1)$$

$$\tau \equiv \rho + \frac{1}{\mu^2 h^2}(2\beta - 1) \quad . \tag{A3-21}$$

When $\nu\Sigma_{f_2}$ is identically zero, s is infinite, and l'Hospitol's rule must be used to obtain,

$$[A]_{12} = \begin{bmatrix} \frac{\alpha}{D_1} & 0 \\ \frac{r}{D_1}(\alpha-\beta) & \frac{\beta}{D_2} \end{bmatrix} h$$

$$[B]_{11} = \begin{bmatrix} \gamma & 0 \\ r(\gamma-\delta) & \delta \end{bmatrix}$$

$$[C^{\pm}]_{12} = \begin{bmatrix} \frac{\varepsilon}{D_1} & 0 \\ \frac{r}{D_1}(\varepsilon+\zeta) & -\frac{\zeta}{D_2} \end{bmatrix} h^2$$

$$[D^{+}]_{12} = \begin{bmatrix} \frac{\xi}{D_1} & 0 \\ \frac{r}{D_1}(\xi+o) & -\frac{o}{D_2} \end{bmatrix} h^2$$

$$[D^-]_{12} = \begin{bmatrix} \frac{\eta}{D_1} & 0 \\ \frac{r}{D_1}(\eta+\theta) & -\frac{\theta}{D_2} \end{bmatrix} h^2$$

$$[E^+]_{12} = \begin{bmatrix} \frac{\sigma}{D_1} & 0 \\ \frac{r}{D_1}(\sigma+\tau) & -\frac{\tau}{D_2} \end{bmatrix} h^2$$

$$[E^-]_{12} = \begin{bmatrix} \frac{\pi}{D_1} & 0 \\ \frac{r}{D_1}(\pi+\rho) & -\frac{\rho}{D_2} \end{bmatrix} h^2 \quad , \qquad \text{(A3-22a)}$$

and κ^2, μ^2 are given by the simple expressions

$$\kappa^2 = \max\left[-\frac{\Sigma_1}{D_1}, -\frac{\Sigma_2}{D_2}\right]$$

$$\mu^2 = \max\left[\frac{\Sigma_1}{D_1}, \frac{\Sigma_2}{D_2}\right] . \qquad \text{(A3-22b)}$$

When $\kappa^2 h^2$ or $\mu^2 h^2$ approach zero, many of the leading terms in the Taylor's series expansions of α, β, . . . τ cancel, and it becomes important to use the expansions rather than Eq. A2-21. The expansions for small κh and μh are

$$\alpha = \left(\frac{1}{2} + \frac{(\kappa h)^2}{24} + \frac{(\kappa h)^4}{240} + \ldots\right)$$

$$\beta = \left(\frac{1}{2} - \frac{(\mu h)^2}{24} + \frac{(\mu h)^4}{240} + \ldots\right)$$

$$\gamma = \left(1 + \frac{(\kappa h)^2}{6} + \frac{7(\kappa h)^4}{360} + \ldots\right)$$

$$\delta = \left(1 - \frac{(\mu h)^2}{6} + \frac{7(\mu h)^4}{360} + \ldots\right)$$

$$\varepsilon = \left(\frac{1}{6} + \frac{7(\kappa h)^2}{360} + \frac{31(\kappa h)^4}{15120} + \ldots\right)$$

$$\zeta = \left(-\frac{1}{6} + \frac{7(\mu h)^2}{360} - \frac{31(\mu h)^4}{15120} + \ldots\right)$$

$$\eta = \left(\frac{1}{24} + \frac{4(\kappa h)^2}{720} + \frac{73(\kappa h)^4}{120960} + \ldots\right)$$

$$\theta = \left(-\frac{1}{24} + \frac{4(\mu h)^2}{720} - \frac{73(\mu h)^4}{120960} + \ldots\right)$$

$$\xi = \left(\frac{1}{8} + \frac{(\kappa h)^2}{72} + \frac{175(\kappa h)^4}{120960} + \ldots\right)$$

$$o = \left(-\frac{1}{8} + \frac{(\mu h)^2}{72} - \frac{175(\mu h)^4}{120960} + \ldots\right)$$

$$\pi = \left(\frac{1}{60} + \frac{36(\kappa h)^2}{15120} + \frac{478(\kappa h)^4}{1814400} + \ldots\right)$$

$$\rho = \left(-\frac{1}{60} + \frac{36(\mu h)^2}{15120} - \frac{478(\mu h)^4}{1814400} + \ldots\right)$$

$$\sigma = \left(\frac{1}{10} + \frac{162(\kappa h)^2}{15120} + \frac{2008(\kappa h)^4}{1814400} + \ldots\right)$$

$$\tau = \left(-\frac{1}{10} + \frac{162(\mu h)^2}{15120} - \frac{2008(\mu h)^4}{1814400} + \ldots\right) \quad . \qquad \text{(A3-23)}$$

Equations A3-20 - A3-23 completely specify the spatial coupling matrices. From the definitions of κ^2 and μ^2 in Eq. A3-4, it is apparent that all of the matrices depend on the eigenvalue of the global static reactor problem.

The matrices required for a one-group model are equal to the (1, 1) elements of the matrices in Eq. A3-22a, with $D_1 = D$.

Appendix 4

DESCRIPTION OF TEST PROBLEMS

A4.1 The LRA BWR Kinetics Benchmark Problem

A4.2 The IAEA PWR Static Benchmark Problem

A4.3 The BIBLIS PWR Problem

A4.4 The TWIGL Seed-Blanket Reactor Problem

A4.5 The LMW LWR Test Problem

A4.6 The IAEA Benchmark Problem No. 2b (One-Group)

A4.7 The Zion 1 PWR Problem

A4.1 THE LRA BWR KINETICS BENCHMARK PROBLEM

Geometry:

Quadrant of Reactor Horizontal Cross Section

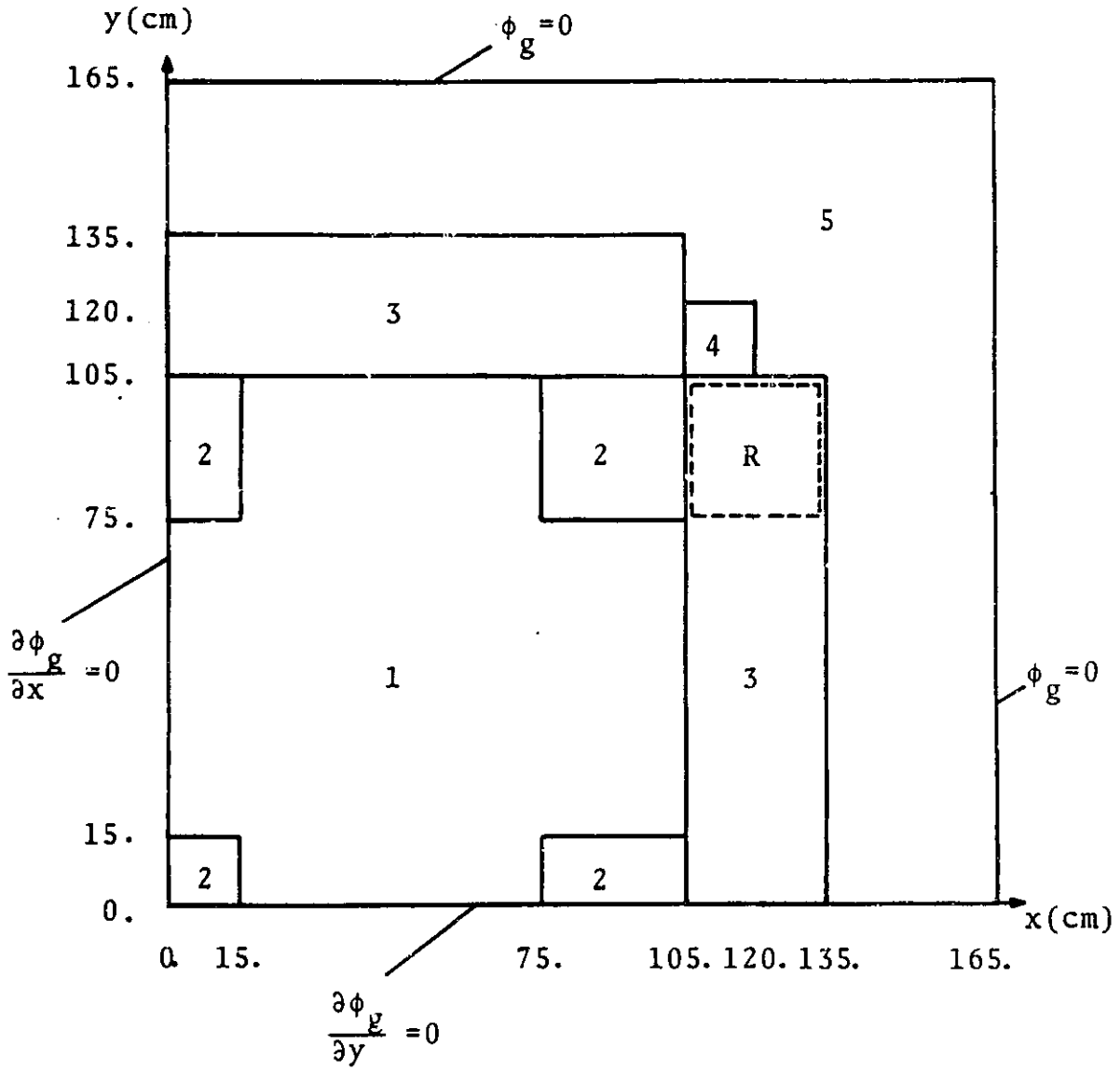

Vertical Cross Section, y = 0

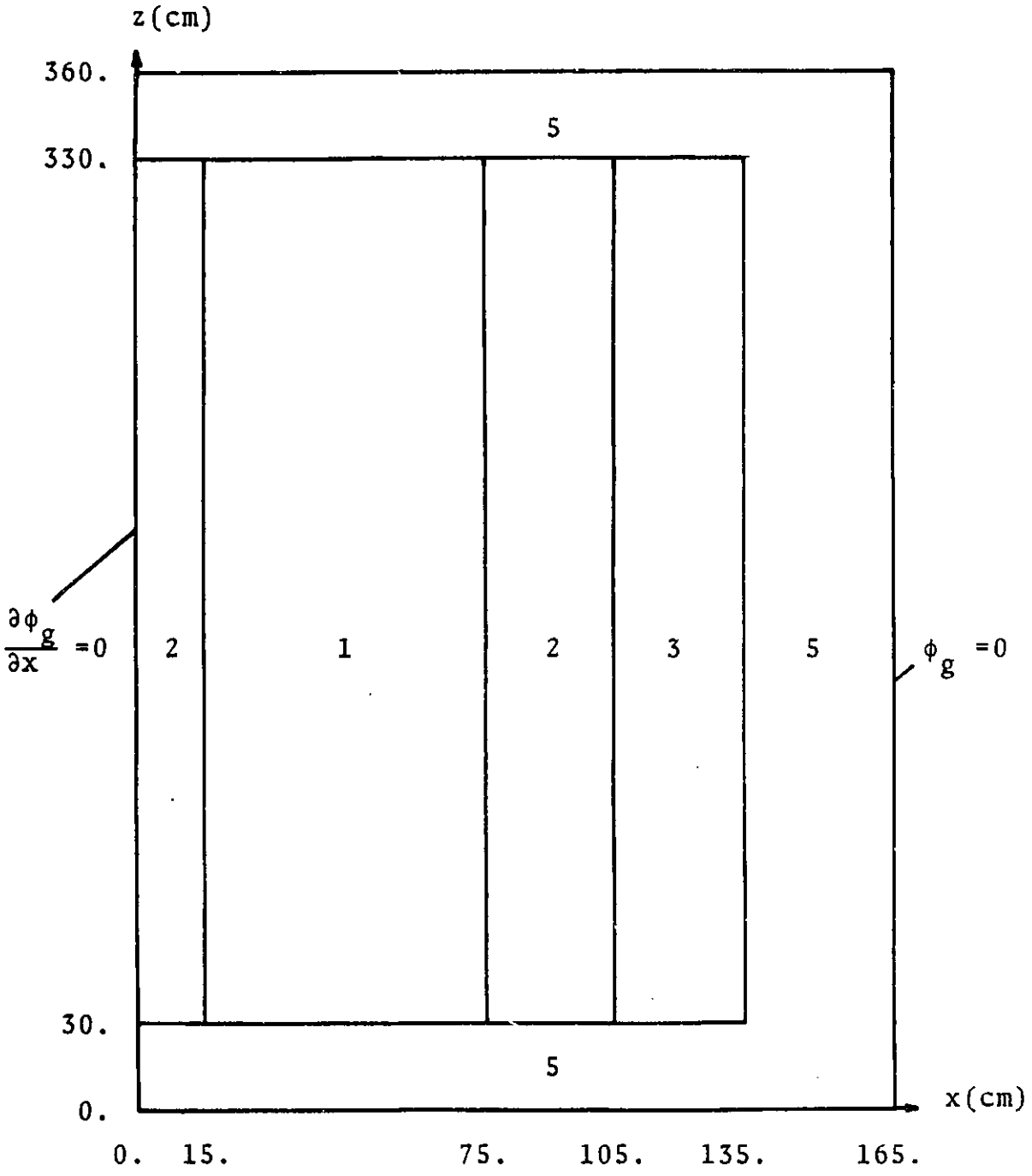

Material Properties

Composition*	Group, g	D_g (cm)	Σ_{a_g} (cm^{-1})	$\nu\Sigma_{f_g}$ (cm^{-1})	Σ_{21} (cm^{-1})
1	1	1.255	0.008252	0.004602	0.02533
	2	0.211	0.1003	0.1091	
2	1	1.268	0.007181	0.004609	0.02767
	2	0.1902	0.07047	0.08675	
3	1	1.259	0.008002	0.004663	0.02617
	2	0.2091	0.08344	0.1021	
4	1	1.259	0.008002	0.004663	0.02617
	2	0.2091	0.073324	0.1021	
5	1	1.257	0.0006034	0.0	0.04754
	2	0.1592	0.01911	0.0	

*Axial buckling of 10^{-4} cm^{-2} for all compositions in 2-D problem

$\chi_1 = 1.0$, $\chi_2 = 0.0$

$\nu = 2.43$

$v_1 = 3.0 \times 10^7$ cm/sec

$v_2 = 3.0 \times 10^5$ cm/sec

Delayed Neutron Data:

Family, d	β_d	$\lambda_d\ (s^{-1})$
1	0.0054	0.0654
2	0.001087	1.35

Adiabatic Feedback Data:

$$\alpha_1[\Sigma_f(\underline{r},t)][\phi(\underline{r},t)] = \frac{\partial}{\partial t} T(\underline{r},t)\ ; \quad \alpha_1 = 3.83 \times 10^{-11}\ ^\circ K\ cm^3$$

$$\Sigma_{a_1}(\underline{r},t) = \Sigma_{a_1}(\underline{r},0)\{1 + \alpha_2(\sqrt{T(\underline{r},t)} - \sqrt{T_0})\};$$

$$\alpha_2 = 2.034 \times 10^{-3}\ ^\circ K^{-\frac{1}{2}}$$

$$T_0 = 300^\circ K$$

Energy Conversion Factor:

$$\text{Power} = \varepsilon \int_{V_{core}} [\Sigma_f(\underline{r},t)][\phi(\underline{r},t)]\,d\underline{r}\ ;$$

$$\varepsilon = 3.204 \times 10^{-11}\ \text{Ws/fission}$$

Transient Initial Conditions:

Mean power density at t = 0, 10^{-6} W/cc

Fuel temperature at t = 0, 300°K

Perturbation:

3-D: Control rod (R) removed with velocity of 150 cm/s

2-D: Control rod composition (R) is given by

$$\Sigma_{a_2}(t) = \begin{cases} \Sigma_{a_2}(0)(1 - 0.0606184 \cdot t)\ ; & t < 2.0\ s \\ \Sigma_{a_2}(0)(0.8787631) & ;\ t > 2.0\ s \end{cases}$$

A4.2 THE IAEA PWR BENCHMARK PROBLEM

Geometry:

Quadrant of Reactor Horizontal Cross Section, Axial Midplane

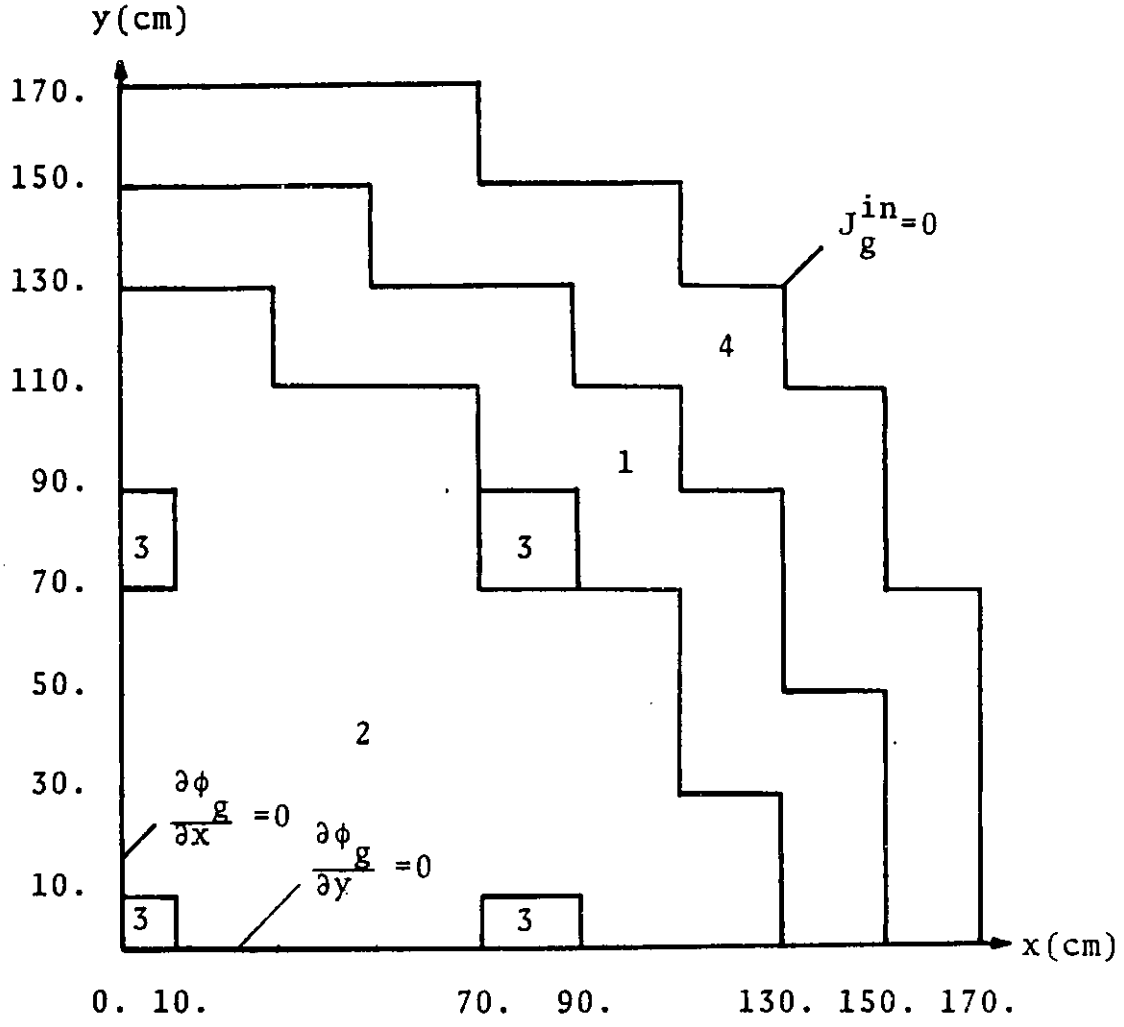

Vertical Reactor Cross Section, y = 0

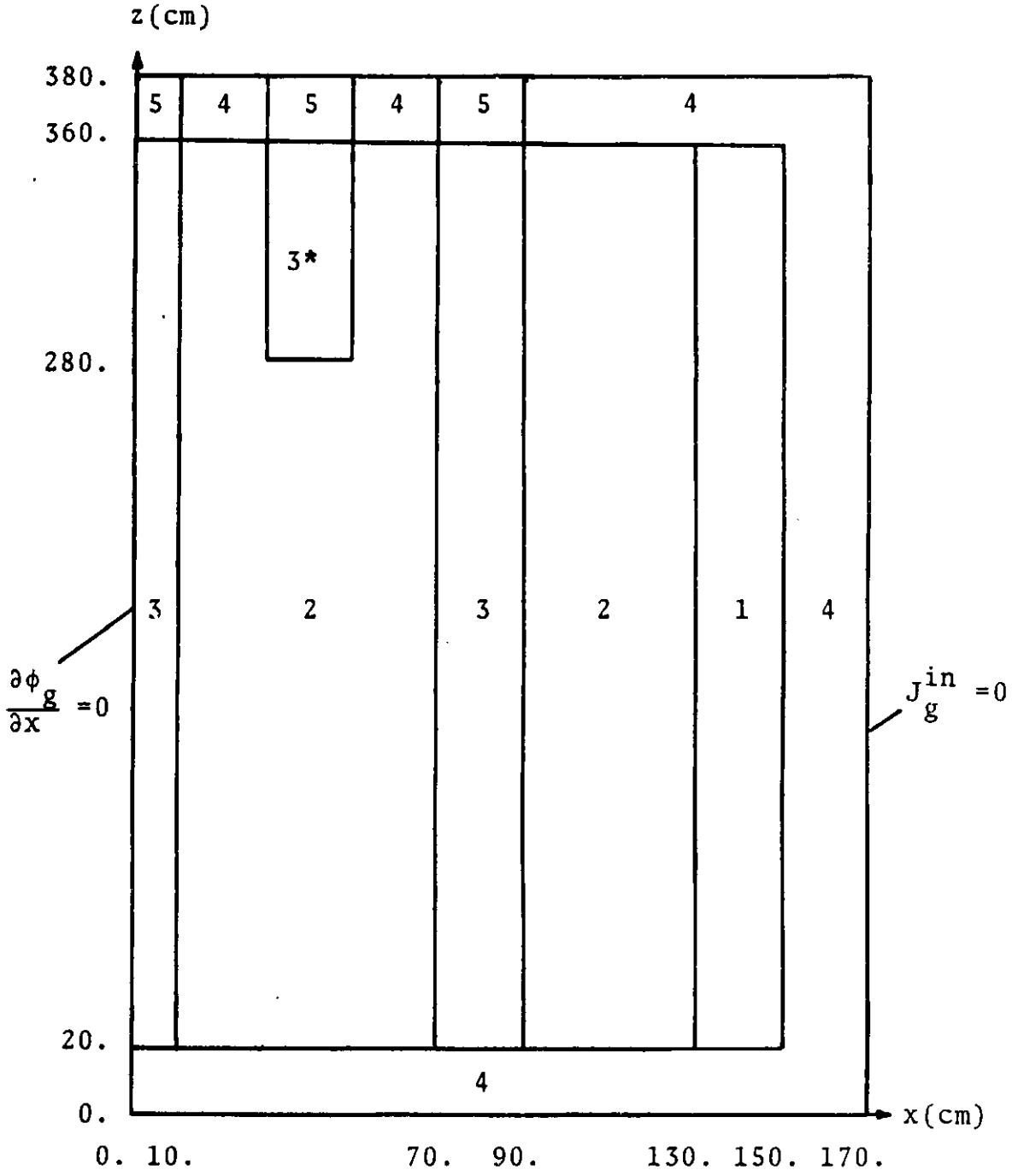

*Position of partially-inserted rod:

30.<x<50., 30.<y<50.

Material Properties:

Composition*	Group, g	D_g (cm)	Σ_{a_g} (cm^{-1})	$\nu\Sigma_{f_g}$ (cm^{-1})	Σ_{21} (cm^{-1})
1	1	1.5	0.01	0.0	0.02
	2	0.4	0.08	0.135	
2	1	1.5	0.01	0.0	0.02
	2	0.4	0.085	0.135	
3	1	1.5	0.01	0.0	0.02
	2	0.4	0.13	0.135	
4	1	2.0	0.0	0.0	0.04
	2	0.3	0.01	0.0	
5	1	2.0	0.0	0.0	0.04
	2	0.3	0.055	0.0	

* Axial buckling of 0.8×10^{-4} cm^{-2} for all compositions in 2-D problem.

$\chi_1 = 1.0$, $\chi_2 = 0$

A4.3 THE 2-D BIBLIS PWR PROBLEM

Confidentiality considerations prohibit general distribution of the BIBLIS problem specifications.

A4.4 THE TWIGL TWO-DIMENSIONAL SEED-BLANKET REACTOR KINETICS PROBLEM

Geometry:

Quadrant of TWIGL Reactor

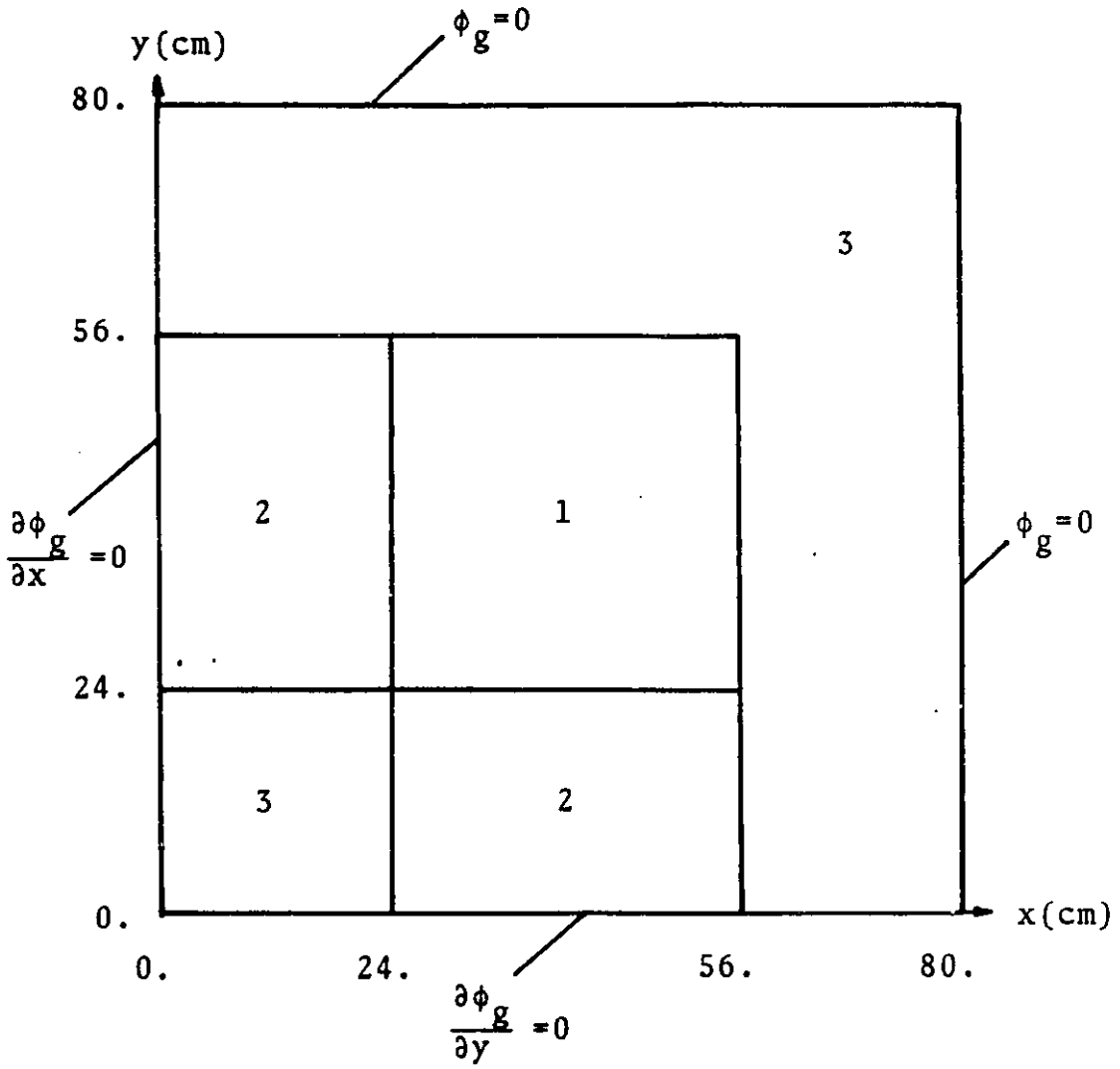

Material Properties:

Composition	Group, g	D_g (cm)	Σ_{a_g} (cm^{-1})	$\nu\Sigma_{f_g}$ (cm^{-1})	Σ_{21} (cm^{-1})
1	1	1.4	0.01	0.007	0.01
	2	0.4	0.15	0.2	
2	1	1.4	0.01	0.007	0.01
	2	0.4	0.15	0.2	
3	1	1.3	0.008	0.003	0.01
	2	0.5	0.05	0.06	

$\chi_1 = 1.0$, $\chi_2 = 0.0$

$\nu = 2.43$

$v_1 = 10^7$ cm/s

$v_2 = 2 \times 10^5$ cm/s

Delayed Neutron Data:

Family, d	β_d	λ_d (s^{-1})
1	0.0075	0.08

Perturbations: In composition 1,

Step: $\Delta\Sigma_{a_2} = -.0035\ cm^{-1}$; $t = 0$

Ramp: $$\Sigma_{a_2}(t) = \begin{cases} \Sigma_{a_2}(0)\{1 - 0.11667\ t\}; & t \leq .2 \\ \Sigma_{a_2}(0)(0.97666)\ ; & t \geq .2 \end{cases}$$

A4.5 THE LMW LWR TRANSIENT PROBLEM

Geometry:

Quadrant of Reactor Horizontal Cross Section

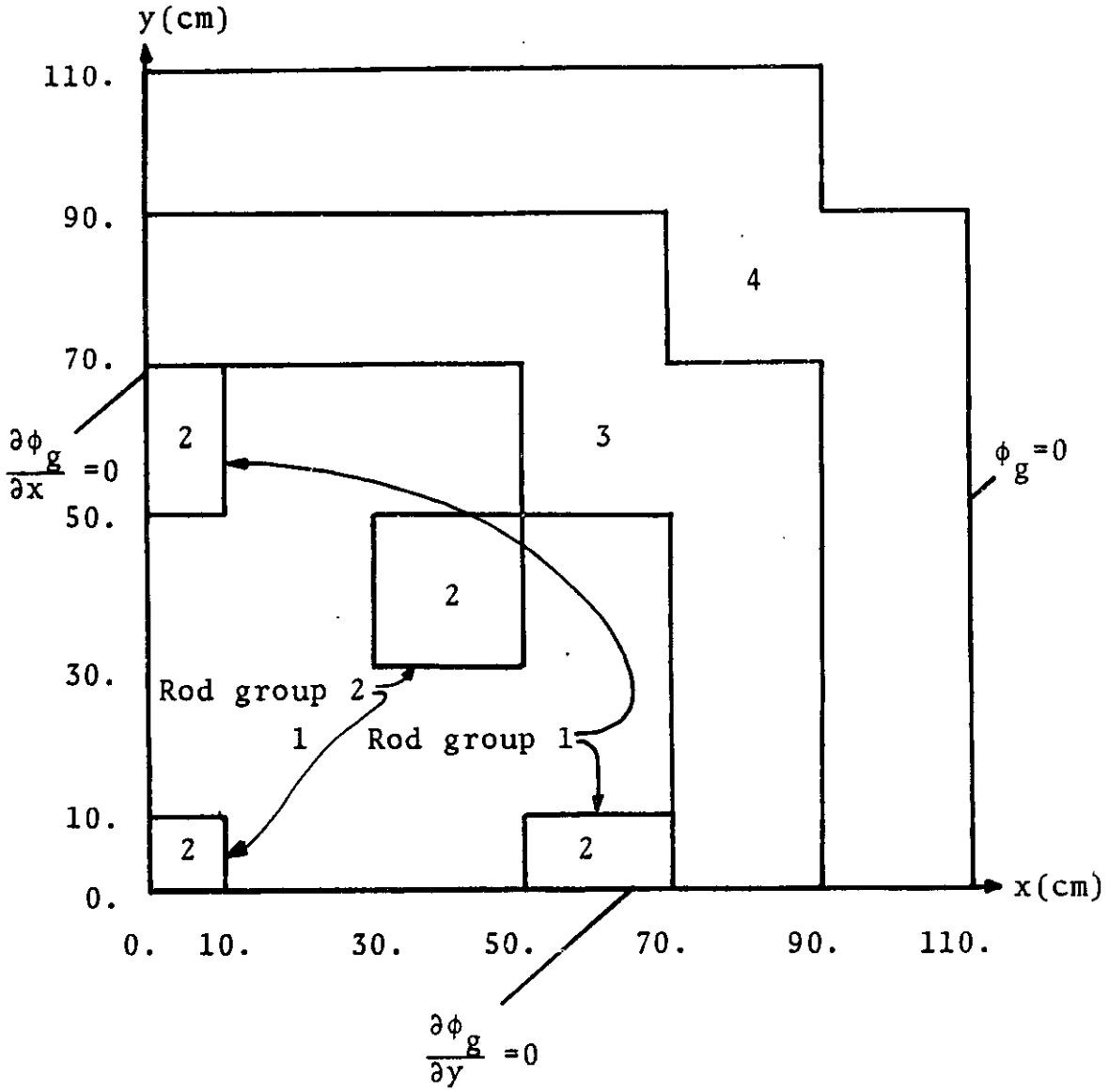

Vertical Cross Section

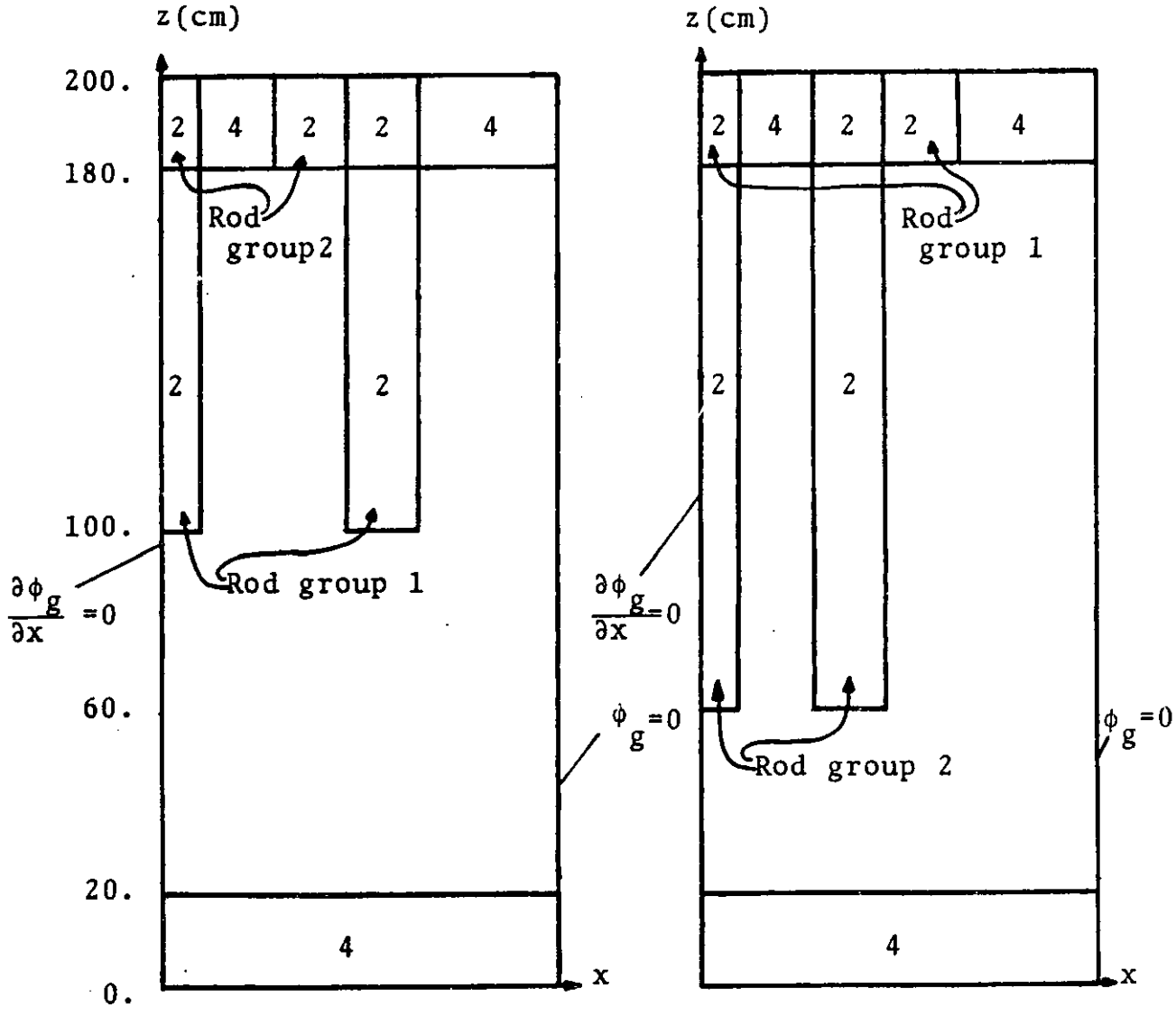

Initial rod positions

Final rod positions

Material Properties:

Composition	Group, g	D_g (cm)	Σ_{a_g} (cm^{-1})	$\nu\Sigma_{f_g}$ (cm^{-1})	Σ_{21} (cm^{-1})
1	1	1.423913	0.01040206	0.006477691	0.0175555
	2	0.356306	0.08766217	0.1127328	
2	1	1.423913	0.01095206	0.00647769	0.0175555
	2	0.356306	0.09146217	0.1127328	
3	1	1.425611	0.01099263	0.007503284	0.01717768
	2	0.350574	0.09925634	0.1378004	
4	1	1.634227	0.002660573	0.0	0.02759693
	2	0.264002	0.04936351	0.0	

$\chi_1 = 1.0$, $\chi_2 = 0.0$

$\nu = 2.5$

$v_1 = 1.25 \times 10^7$ cm/s

$v_2 = 2.5 \times 10^5$ cm/s

Delayed Neutron Data:

Family, d	β_d	λ_d (s^{-1})
1	0.000247	0.0127
2	0.0013845	0.0317
3	0.001222	0.115
4	0.0026455	0.311
5	0.000832	1.40
6	0.000169	3.87

Energy Conversion Factor:

3.204×10^{-11} Ws/fission

Perturbation.

Rod group 1 removed at 3.0 cm/s, $0 \leq t \leq 26.666$ s

Rod group 2 inserted at 3.0 cm/s, $7.5 \leq t \leq 47.5$ s

WIGL Thermal Hydraulic Parameters:

$C^f = 2.46 \times 10^6$ ergs gm^{-1} $°K^{-1}$

$C^c = 5.43 \times 10^7$ ergs gm^{-1} $°K^{-1}$

$\rho^f = 10.3$ gm cm^{-3}

$W_o = 2.2 \times 10^6$ gm s^{-1}

$h_o = 2.71 \times 10^7$ ergs cm^{-2} s^{-1} $°K^{-1}$

$A_h = 2.95$ cm^{-1}

$U = 2.2 \times 10^6$ ergs cm^{-2} s^{-1} $°K^{-1}$

$V^c/(V^c+V^f) = .559$

$r = 0.0$

$\left(\frac{\partial \rho^c H}{\partial \bar{T}^c}\right) = 1.60 \times 10^7$ ergs cm^{-3} $°K^{-1}$

Pressure = 1.53×10^7 pascals

Coolant inlet temperature = 533°K

Initial power = 184.8 Mw(t) (quarter-core)

Macroscopic Cross Section Derivatives:

Parameter, Σ	$\frac{\partial \Sigma}{\partial \rho^c}$	$\frac{\partial \Sigma}{\partial \bar{T}^c}$	$\frac{\partial \Sigma}{\partial \bar{T}^f}$
D_1^{-1}	+0.41	-8.0×10^{-5}	-6.6×10^{-6}
D_2^{-1}	+2.7	-1.3×10^{-3}	-2.6×10^{-6}
Σ_{c_1}	$+2.83 \times 10^{-3}$	$+3.0 \times 10^{-6}$	$+3.3 \times 10^{-7}$
Σ_{c_2}	$+1.4 \times 10^{-2}$	-8.2×10^{-6}	-3.8×10^{-7}
$\nu\Sigma_{f_1}$	0.0	0.0	0.0
$\nu\Sigma_{f_2}$	$+4.132 \times 10^{-2}$	-2.017×10^{-5}	-2.43×10^{-6}
Σ_{f_1}	0.0	0.0	0.0
Σ_{f_2}	$+1.7 \times 10^{-2}$	-8.3×10^{-6}	-1.0×10^{-6}
Σ_{21}	$+2.4 \times 10^{-2}$	-1.5×10^{-6}	$+8.5 \times 10^{-8}$

$\rho^* = .7961 \text{ g cm}^{-3}$

$\bar{T}^{c*} = 533°K$

$\bar{T}^{f*} = 533°K$

A4.6 THE IAEA TWO-DIMENSIONAL BENCHMARK PROBLEM NO. 2b (ONE-GROUP)

Geometry:

Reactor Cross Section

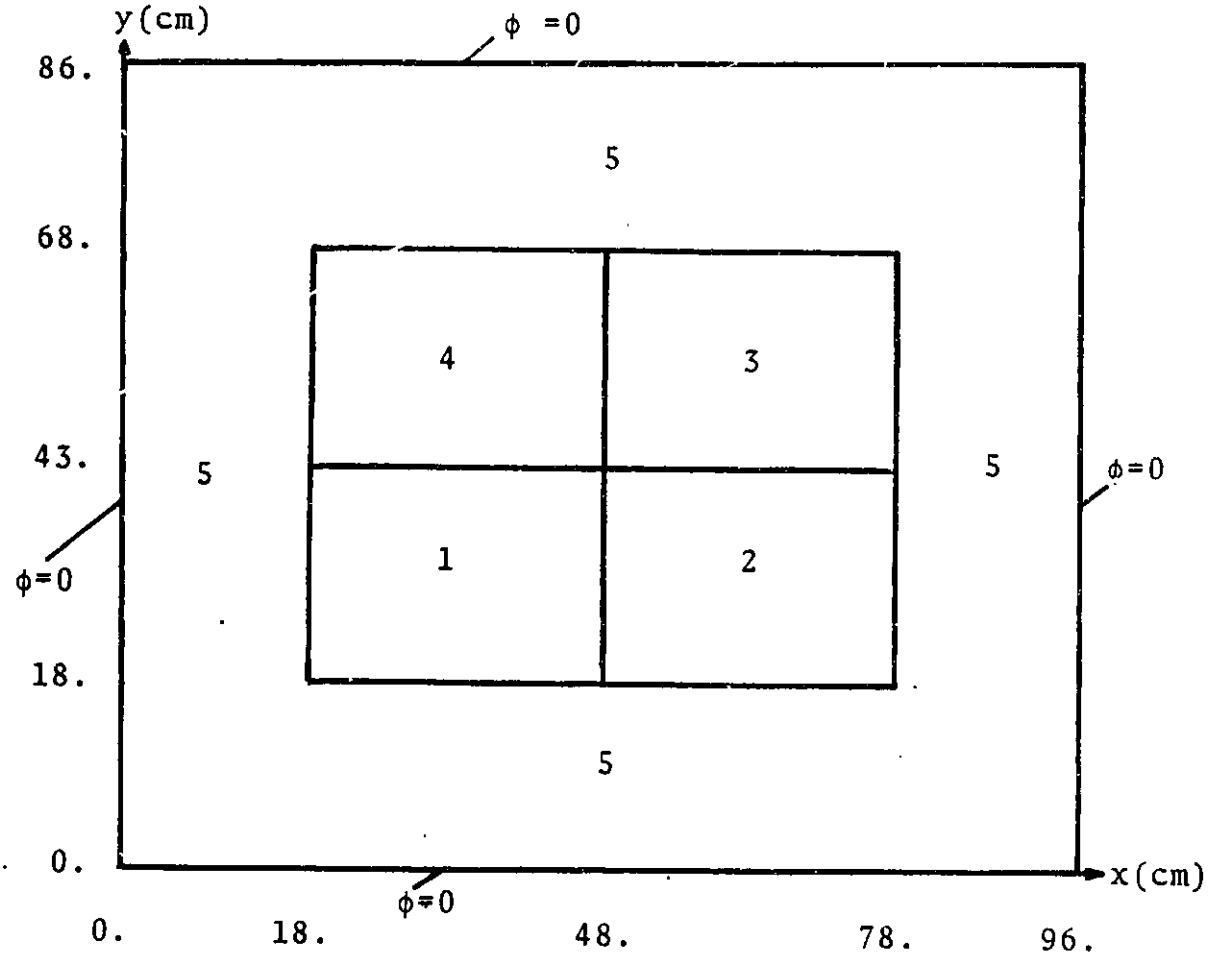

Material Properties:

Composition	D(cm)	Σ_a (cm^{-1})	$\nu\Sigma_f$ (cm^{-1})
1	0.6536	0.07	0.079
2	0.7042	0.28	0.0
3	0.55556	0.04	0.043
4	0.55556	0.15	0.0
5	0.43478	0.01	0.0

ν = 2.43

A4.7 THE ZION 1 PWR PROBLEM

Geometry:

Quadrant of Zion 1 Reactor

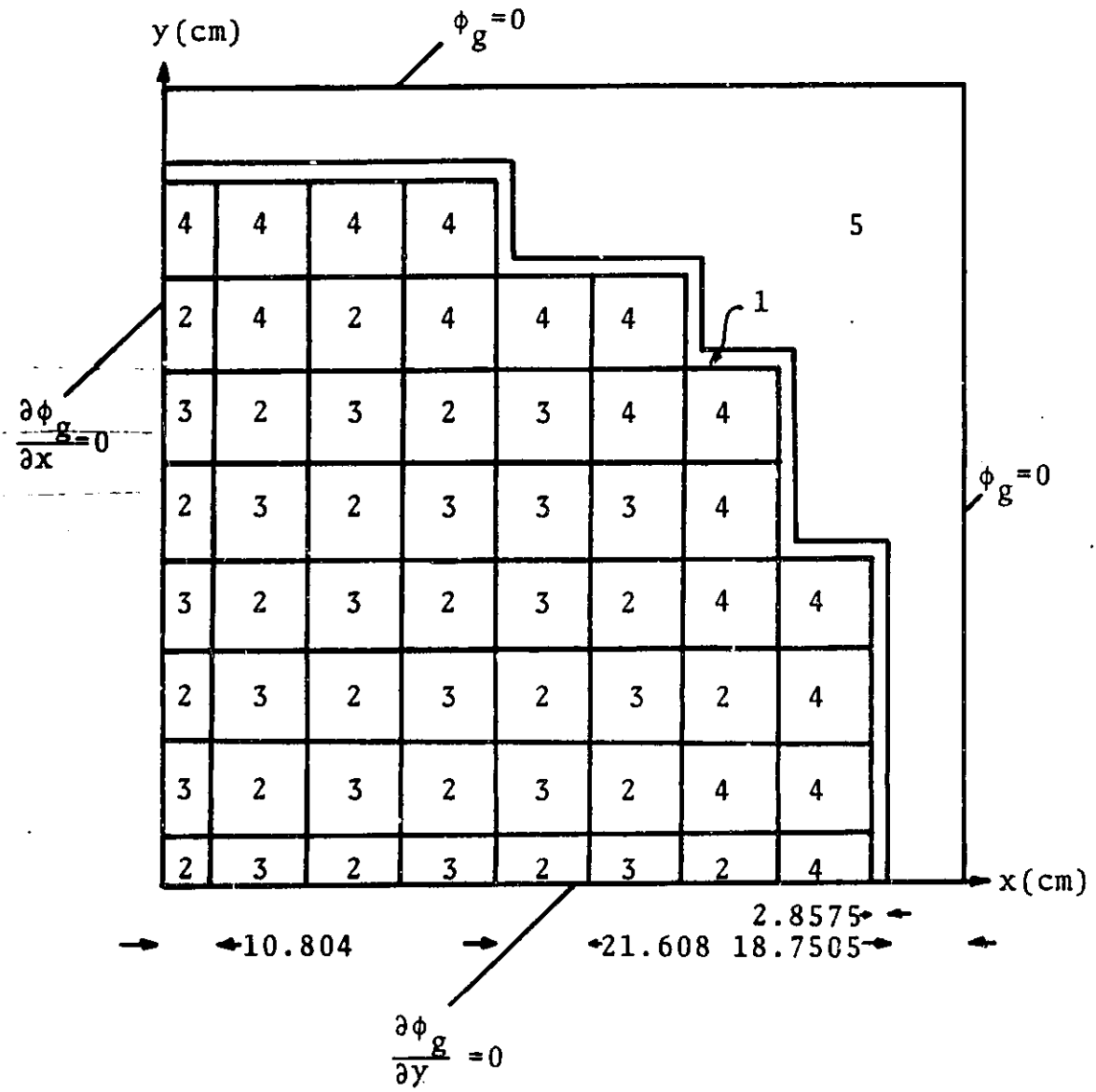

Material Properties:

Composition	Group, g	D_g(cm)	Σ_{a_g} (cm^{-1})	$\nu\Sigma_{f_g}$ (cm^{-1})	Σ_{21} (cm^{-1})
1	1	1.02130	0.00322	0.0	0.0
	2	0.33548	0.14596	0.0	
2	1	1.4176	0.00855	0.00536	0.01742
	2	0.37335	0.06669	0.10433	
3	1	1.4192	0.00882	0.00601	0.01694
	2	0.37370	0.07606	0.12472	
4	1	1.4265	0.00902	0.00653	0.01658
	2	0.37424	0.08359	0.1412	
5	1	1.4554	0.00047	0.0	0.02903
	2	0.28994	0.00949	0.0	

$\chi_1 = 1.0$, $\chi_2 = 0.0$

$\nu = 2.43$

Appendix 5

NORMALIZED STATIC POWER DISTRIBUTIONS

A5.1 2-D LRA BWR

A5.2 2-D IAEA PWR

A5.3 2-D BIBLIS PWR ("Rods In")

A5.4 2-D BIBLIS PWR ("Rods Out")

A5.5 3-D LMW LWR

A5.6 3-D IAEA PWR (VENTURE Reference)

A5.7 3-D IAEA PWR (IQSBOX Reference)

A5.8 3-D LRA BWR ("Rods In")

A5.9 3-D LRA BWR (Quarter-Core, "Rods Out")

A5.10 3-D LRA BWR (Full-Core, "Rods Out")

A5.11 2-D Zion 1 PWR

Figure A5-1. Normalized assembly power densities and errors for the 2-D LRA BWR (Problem A4.1). "Rods in" configuration.

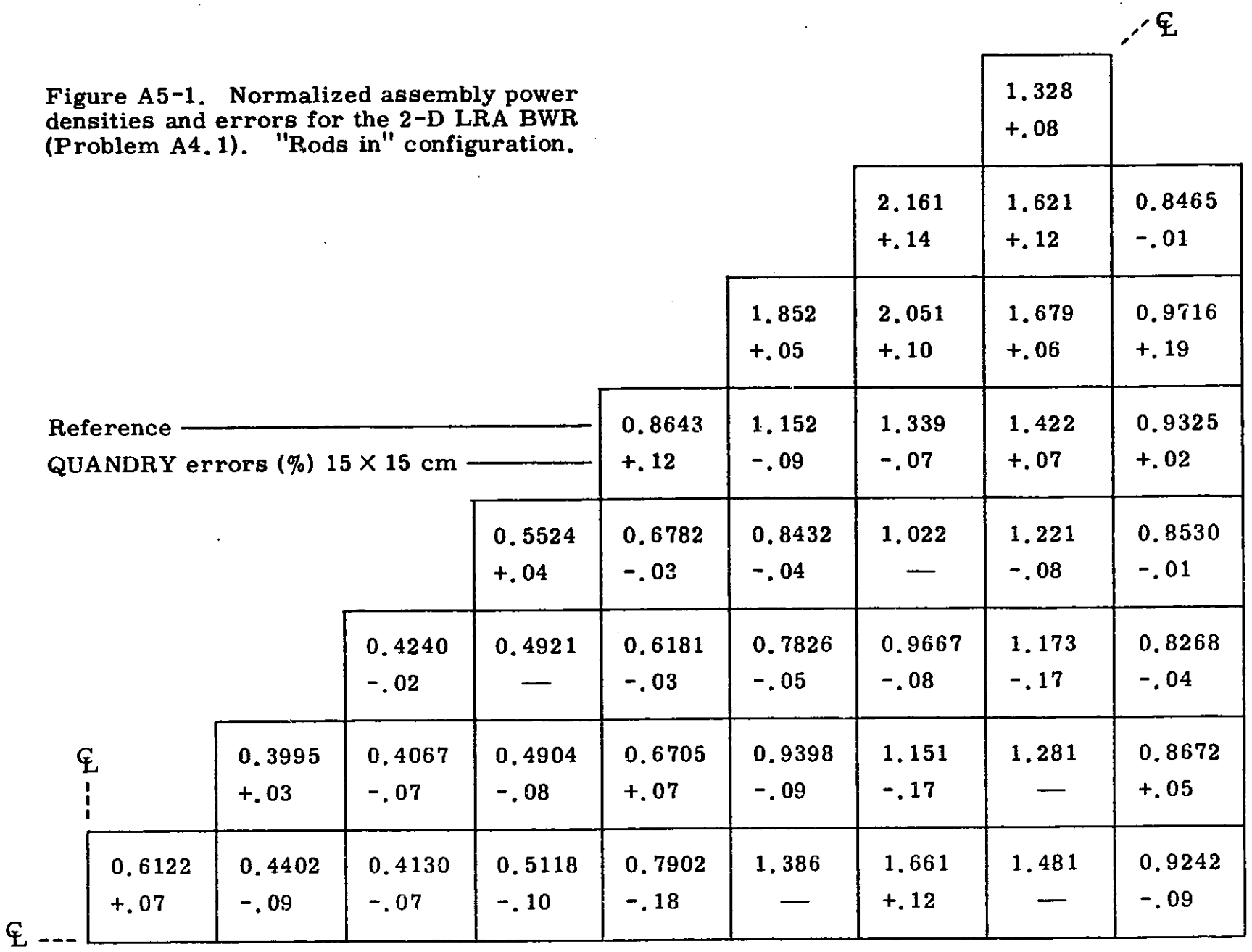

Figure A5-2. Normalized assembly power densities and errors for the 2-D IAEA PWR (Problem A4.2).

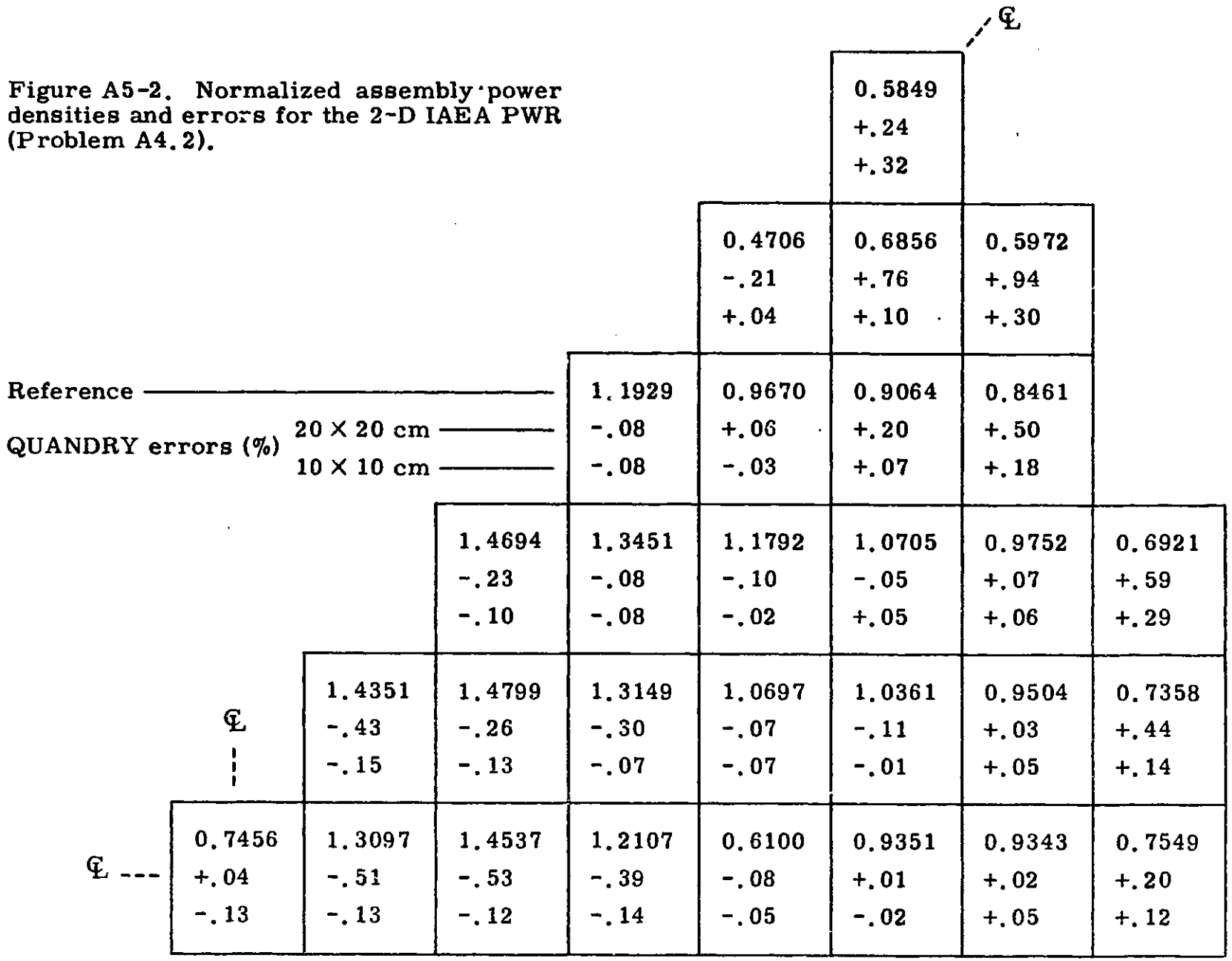

Figure A5-3. Normalized assembly power densities and errors for the 2-D BIBLIS PWR (Problem A4.3). "Rods in" configuration.

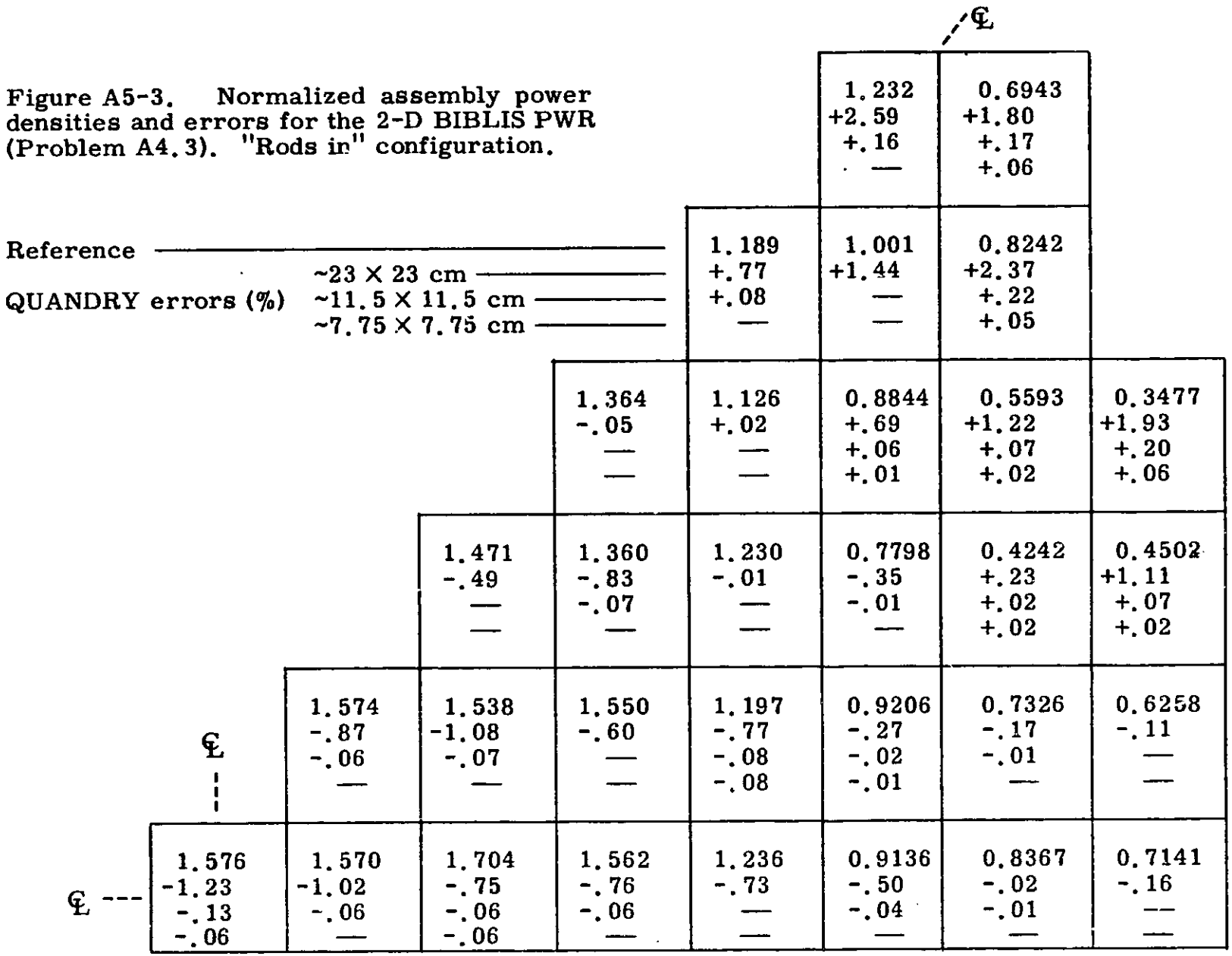

Figure A5-4. Normalized assembly power densities and errors for the 2-D BIBLIS PWR (Problem A4.3). "Rods out" configuration.

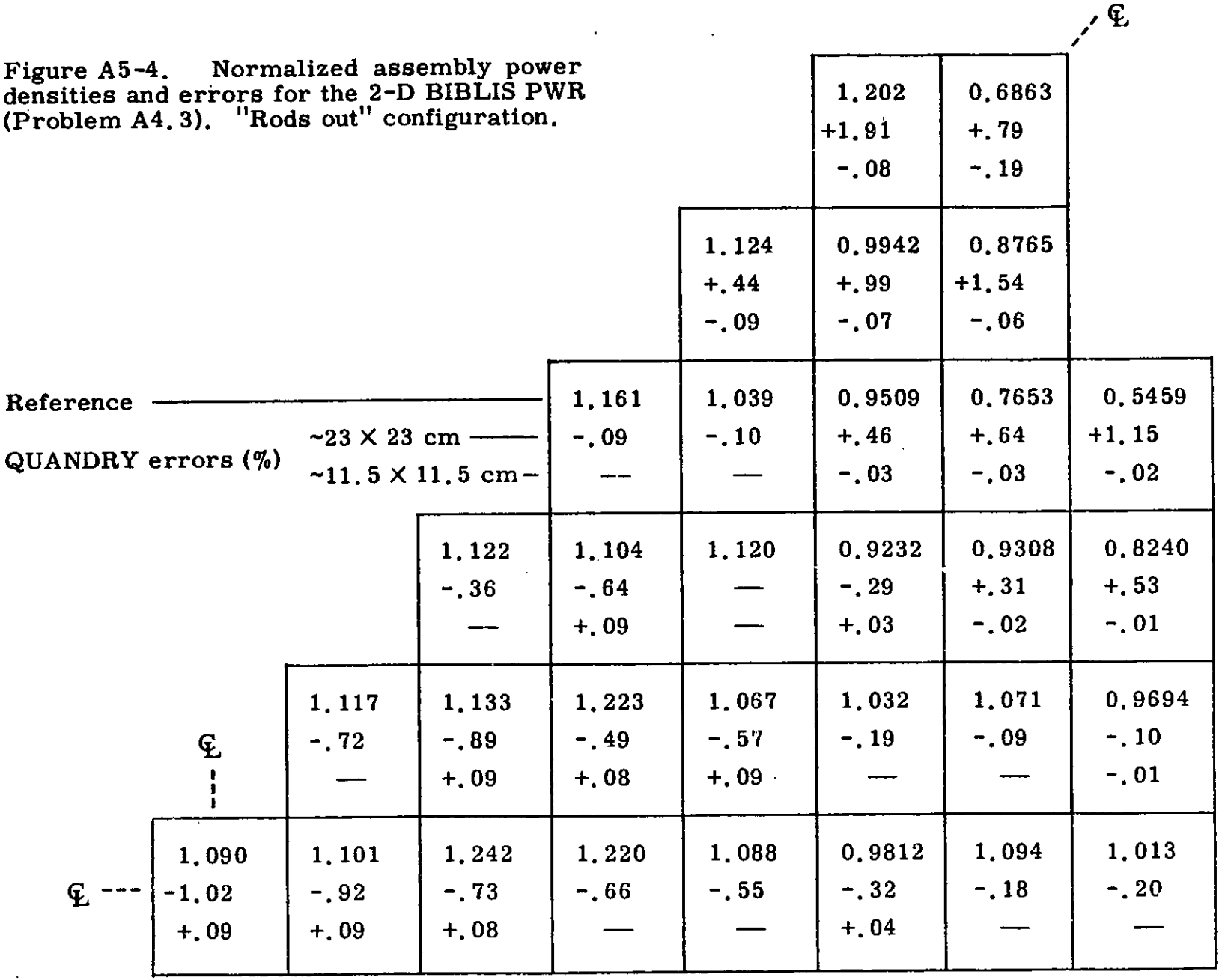

Figure A5-5. Normalized assembly power densities and errors for the 3-D LMW LWR problem (Problem A4.5).

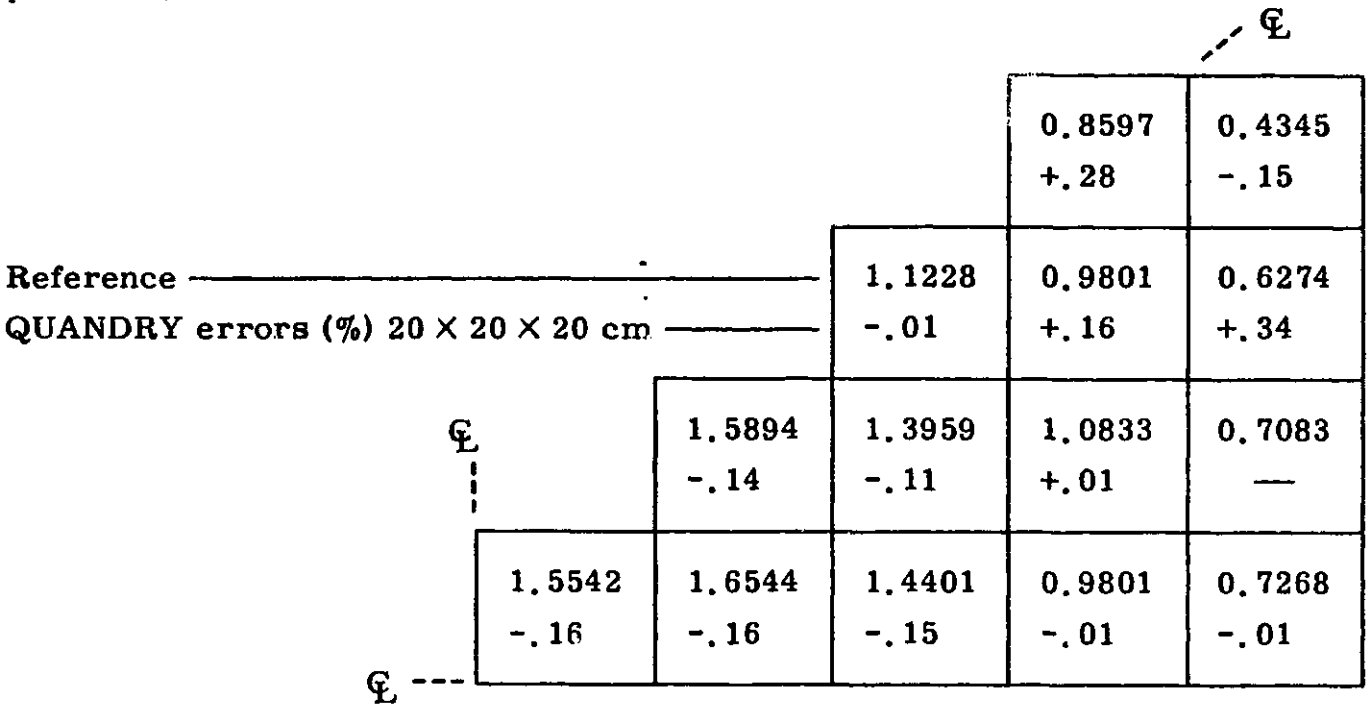

Figure A5-6. Normalized assembly power densities and errors for the 3-D IAEA PWR (Problem A4.2). (VENTURE reference.)

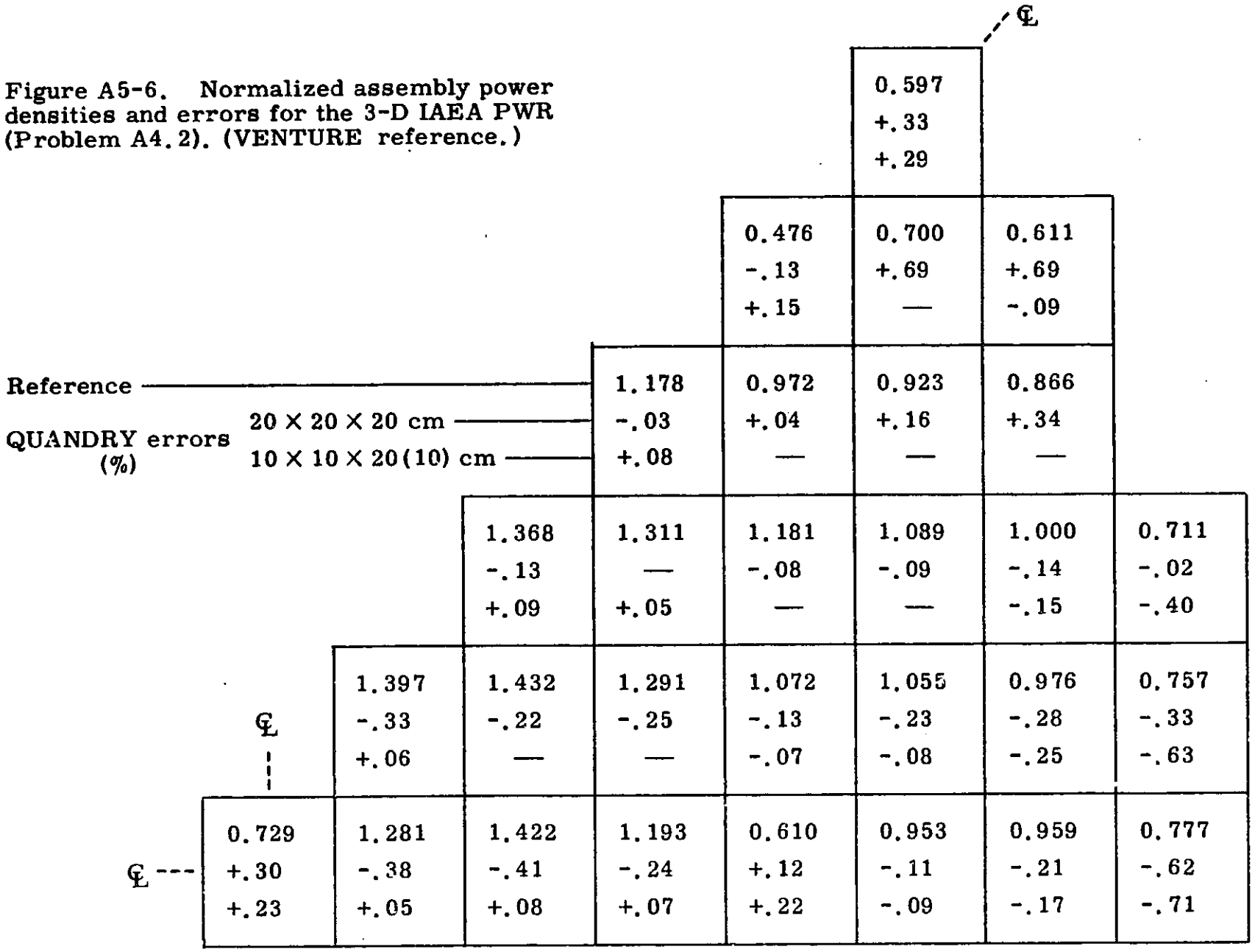

Figure A5-7. Normalized assembly power densities and errors for the 3-D IAEA PWR (Problem A4.2). (IQSBOX reference.)

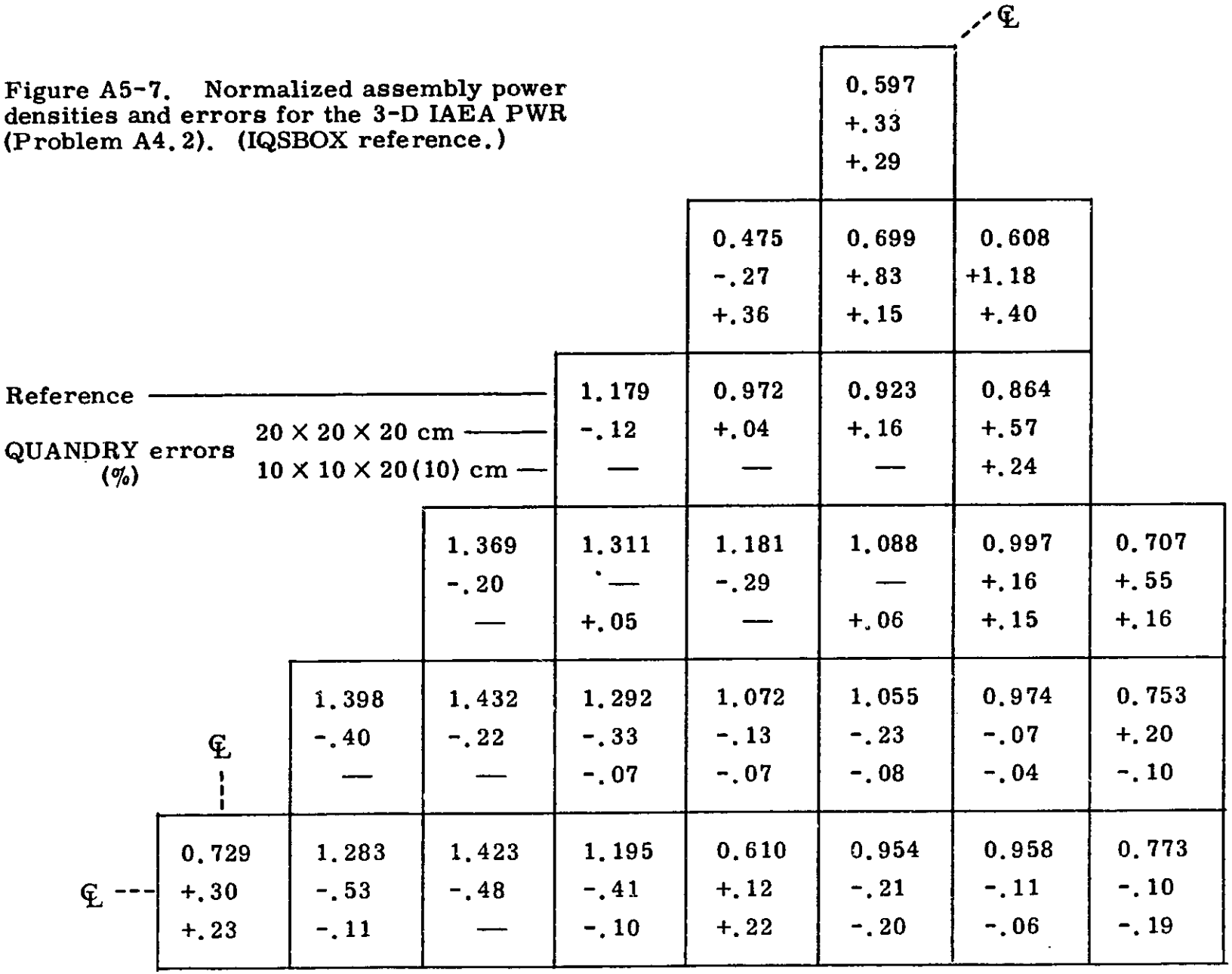

Figure A5-8. Normalized assembly power densities and errors for the 3-D LRA BWR (Problem A4.1). "Rods in" configuration.

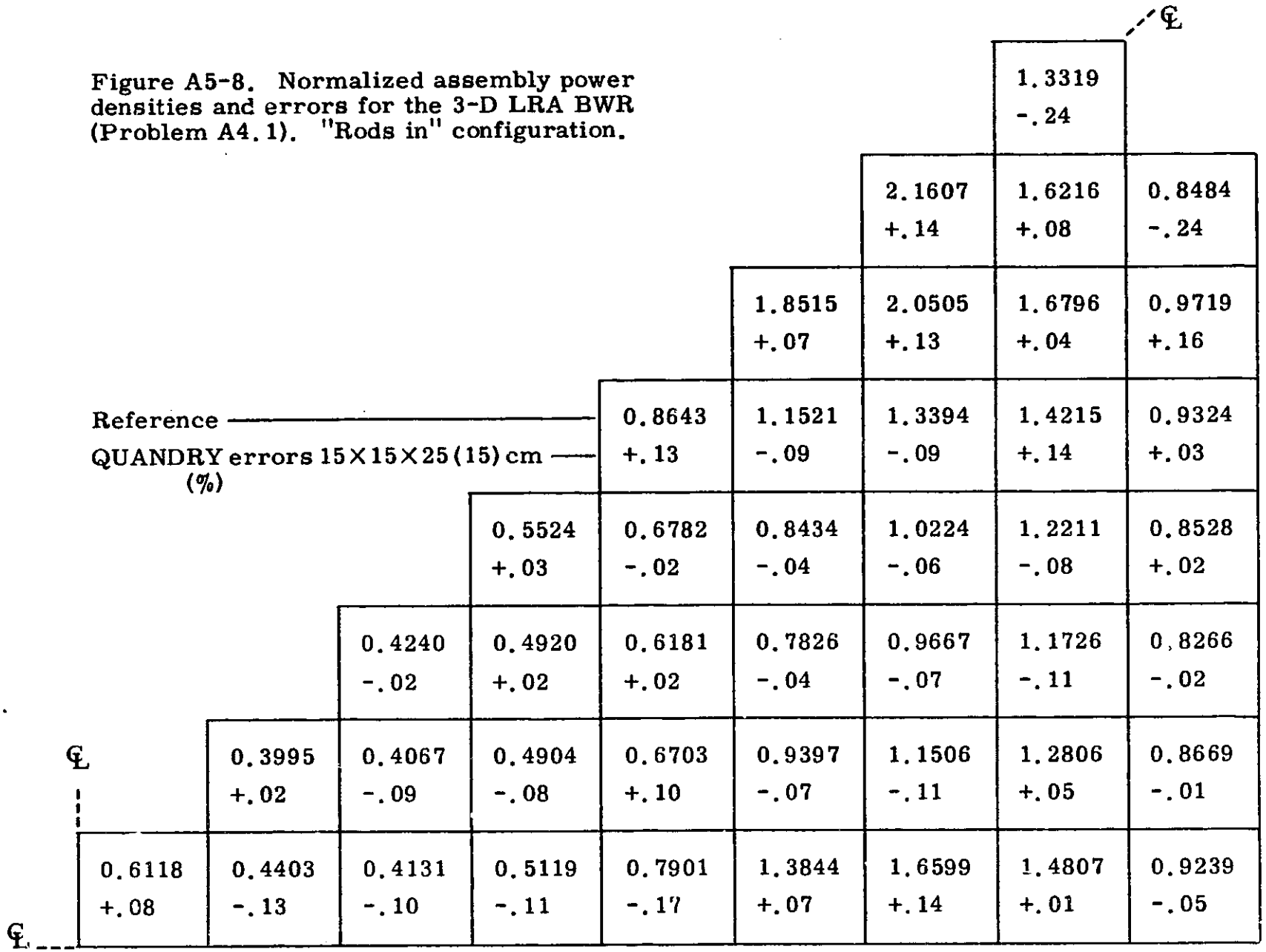

Figure A5.9. Normalized assembly power densities and errors for the 3-D LRA BWR (1/4-core). "Rod out" configuration.

0.3589 -.41	0.3851 -.33	0.4701 -.24	0.6425 -.06	0.8968 +.06	1.1358 +.40	1.1805 -.21			
0.5686 -.36	0.5631 -.30	0.6702 -.34	0.9427 -.20	1.4256 +.14	2.0807 +.10	2.4821 +.22	2.5842 -.28		
0.6290 -.21	0.4984 -.34	0.5571 -.23	0.8155 -.16	1.4146 -.19	2.6809 +.04	3.6004 +.19	4.0389 +.42	2.6072 +.04	
0.5222 -.25	0.4053 -.29	0.4524 -.16	0.6795 -.11	1.2292 -.18	2.4359 -.02	3.4237 +.16	4.1094 +.39	2.8021 +.45	
0.2996 -.44	0.2911 -.15	0.3515 -.20	0.5230 -.11	0.8620 +.14	1.4071 -.02	1.9793 —	2.4908 +.10	1.7871 +.14	
0.1923 -.36	0.2093 -.29	0.2645 -.17	0.3824 -.04	0.5807 -.03	0.8522 +.02	1.1774 -.07	1.5305 -.23	1.1188 -.07	
0.1478 -.41	0.1630 -.32	0.2060 -.23	0.2908 -.13	0.4252 -.13	0.6016 -.12	0.8101 -.19	1.0397 -.29	0.7568 -.21	
0.1458 -.44	0.1465 -.27	0.1767 -.34	0.2490 -.30	0.3762 -.12	0.5587 -.25	0.7219 -.32	0.8448 -.27	0.5899 -.31	
0.1928 -.32	0.1517 -.43	0.1675 -.42	0.2390 -.35	0.4008 -.42	0.7307 -.21	0.9064 -.16	0.8378 -.32	0.5363 -.35	

Reference
QUANDRY errors (%)
15×15×25(15) cm

℄

℄

Figure A5-10. Normalized assembly power densities and errors for the 3-D LRA BWR (full core). "Rod out" configuration.

		0.0819 +.49	0.1565 -.50	0.3479 +.85	0.7091 -.86	1.340 -3.08	2.877 -1.02	4.468 +.33	
	0.0886 +.59	0.1392 +1.53	0.2229 -1.19	0.5124 +.19	1.122 +.62	1.918 -3.20	4.437 -.95	8.817 +.89	9.979 +.66	
0.0515 +.75	0.1009 +1.47	0.1545 +1.27	0.1677 +.02	0.4098 -.54	1.130 +.38	1.463 -.32	3.873 -1.28	11.698 +.32	15.797 +1.28	10.473 +.50
0.0414 +.33	0.0657 +.52	0.0698 -.41	0.0940 +.96	0.2118 +.49	0.4632 -1.48	0.8368 +.22	2.127 +.82	5.082 -.46	7.583 -.67	5.488 -.84
0.0264 -.51	0.0398 -.80	0.0386 +.10	0.0509 +.21	0.1055 -.16	0.2222 -.49	0.4330 -.28	0.998 +.88	2.069 -.65	2.982 -2.93	2.156 -2.67
0.0196 +.48	0.0329 +1.32	0.0400 +1.12	0.0338 -.49	0.0732 -1.19	0.1988 +.61	0.2538 -.28	0.6171 -1.87	1.625 +.24	1.666 +1.32	1.067 +.40
0.0123 +1.04	0.0188 +.34	0.0177 -.19	0.0193 +.09	0.0382 +.35	0.0793 -1.07	0.1305 -.37	0.2918 +.38	0.5900 -.36	0.7490 +.74	0.5110 +1.52
0.0078 -.36	0.0116 +.24	0.0108 -.32	0.0119 +.71	0.0214 +.35	0.0406 -.66	0.0666 +.16	0.1314 +1.11	0.2410 +.30	0.3230 -.71	0.2274 +.08
0.0059 +.06	0.0107 +1.67	0.0144 +1.49	0.0118 -.20	0.0216 -.61	0.0511 +1.23	0.0520 +.24	0.0986 -.23	0.2213 +1.62	0.2002 +2.01	0.1181 +.90
	0.0081 +.79	0.0111 +1.39	0.0132 -.30	0.0233 +.76	0.0427 +1.56	0.0543 -.88	0.0928 +.84	0.1443 +1.78	0.1271 +.97	
		0.0062 +.01	0.0089 -.04	0.0153 +1.47	0.0256 +.56	0.0361 -.50	0.0584 +.72	0.0736 +1.01		

Fig. A5-11. Normalized assembly power densities and errors for the 2-D Zion 1 PWR (Problem A4.7).

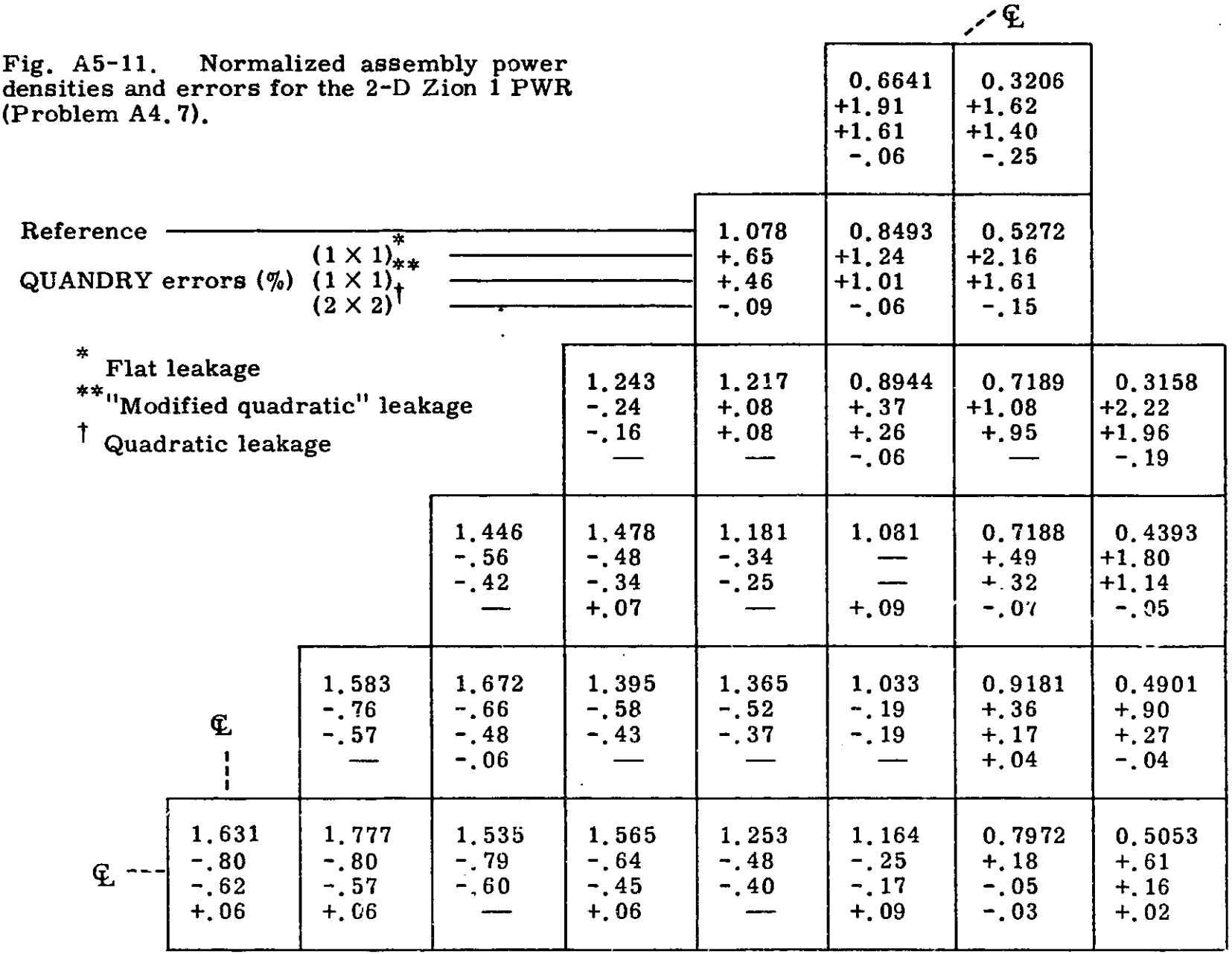

					0.6641 +1.91 +1.61 -.06	0.3206 +1.62 +1.40 -.25	
				1.078 +.65 +.46 -.09	0.8493 +1.24 +1.01 -.06	0.5272 +2.16 +1.61 -.15	
			1.243 -.24 -.16 —	1.217 +.08 +.08 —	0.8944 +.37 +.26 -.06	0.7189 +1.08 +.95 —	0.3158 +2.22 +1.96 -.19
		1.446 -.56 -.42 —	1.478 -.48 -.34 +.07	1.181 -.34 -.25 —	1.081 — — +.09	0.7188 +.49 +.32 -.07	0.4393 +1.80 +1.14 -.05
	1.583 -.76 -.57 —	1.672 -.66 -.48 -.06	1.395 -.58 -.43 —	1.365 -.52 -.37 —	1.033 -.19 -.19 —	0.9181 +.36 +.17 +.04	0.4901 +.90 +.27 -.04
1.631 -.80 -.62 +.06	1.777 -.80 -.57 +.06	1.535 -.79 -.60 —	1.565 -.64 -.45 +.06	1.253 -.48 -.40 —	1.164 -.25 -.17 +.09	0.7972 +.18 -.05 -.03	0.5053 +.61 +.16 +.02

Appendix 6

LRA BWR TRANSIENT RESULTS

A6.1 2-D LRA BWR

A6.2 3-D LRA BWR (Quarter-Core)

A6.3 3-D LRA BWR (Full-Core)

Figure A6-1a. 2-D LRA BWR transient problem.

NORMALIZED NODAL POWER DENSITIES AT T = 0.0
MEAN POWER DENSITY = 0.999999E-06

Y = 9	9.234E-01	8.668E-01	8.264E-01	8.529E-01	9.327E-01	9.734E-01	8.464E-01	0.0	0.0
Y = 8	1.481E+00	1.281E+00	1.171E+00	1.220E+00	1.423E+00	1.680E+00	1.623E+00	1.329E+00	0.0
Y = 7	1.663E+00	1.149E+00	9.659E-01	1.022E+00	1.338E+00	2.053E+00	2.164E+00	1.623E+00	8.464E-01
Y = 6	1.386E+00	9.390E-01	7.822E-01	8.429E-01	1.151E+00	1.853E+00	2.053E+00	1.680E+00	9.734E-01
Y = 5	7.888E-01	6.710E-01	6.179E-01	6.780E-01	8.653E-01	1.151E+00	1.338E+00	1.423E+00	9.327E-01
Y = 4	5.113E-01	4.900E-01	4.921E-01	5.526E-01	6.780E-01	8.429E-01	1.022E+00	1.220E+00	8.529E-01
Y = 3	4.127E-01	4.064E-01	4.239E-01	4.921E-01	6.179E-01	7.822E-01	9.659E-01	1.171E+00	8.264E-01
Y = 2	4.398E-01	3.996E-01	4.064E-01	4.900E-01	6.710E-01	9.390E-01	1.149E+00	1.281E+00	8.668E-01
Y = 1	6.126E-01	4.398E-01	4.127E-01	5.113E-01	7.888E-01	1.386E+00	1.663E+00	1.481E+00	9.234E-01
X =	1	2	3	4	5	6	7	8	9

Figure A6-1a. 2-D LRA BWR transient problem.

NORMALIZED NODAL POWER DENSITIES AT T = 0.400000E+00
MEAN POWER DENSITY = 0.138231E-05

Y = 9	8.459E-01	8.024E-01	7.821E-01	8.320E-01	9.381E-01	1.006E+00	8.959E-01	0.0	0.0
Y = 8	1.355E+00	1.185E+00	1.109E+00	1.193E+00	1.439E+00	1.749E+00	1.741E+00	1.480E+00	0.0
Y = 7	1.520E+00	1.062E+00	9.149E-01	1.002E+00	1.361E+00	2.153E+00	2.352E+00	1.890E+00	1.024E+00
Y = 6	1.267E+00	8.669E-01	7.410E-01	8.278E-01	1.172E+00	1.943E+00	2.231E+00	1.949E+00	1.163E+00
Y = 5	7.213E-01	6.199E-01	5.844E-01	6.624E-01	8.729E-01	1.193E+00	1.424E+00	1.554E+00	1.032E+00
Y = 4	4.672E-01	4.521E-01	4.631E-01	5.335E-01	6.707E-01	8.506E-01	1.048E+00	1.264E+00	8.885E-01
Y = 3	3.758E-01	3.732E-01	3.955E-01	4.677E-01	5.964E-01	7.638E-01	9.515E-01	1.161E+00	8.216E-01
Y = 2	3.983E-01	3.646E-01	3.758E-01	4.596E-01	6.354E-01	8.940E-01	1.099E+00	1.231E+00	8.353E-01
Y = 1	5.528E-01	3.995E-01	3.797E-01	4.764E-01	7.407E-01	1.306E+00	1.571E+00	1.404E+00	8.774E-01
X =	1	2	3	4	5	6	7	8	9

Figure A6-1a. 2-D LRA BWR transient problem.

NORMALIZED NODAL POWER DENSITIES AT T = 0.799999E+00
MEAN POWER DENSITY = 0.304568E-05

Y = 9	7.357E-01	7.108E-01	7.190E-01	8.023E-01	9.456E-01	1.051E+00	9.661E-01	0.0	0.0
Y = 8	1.177E+00	1.048E+00	1.020E+00	1.155E+00	1.461E+00	1.846E+00	1.910E+00	1.695E+00	0.0
Y = 7	1.317E+00	9.368E-01	8.422E-01	9.752E-01	1.394E+00	2.293E+00	2.617E+00	2.272E+00	1.283E+00
Y = 6	1.097E+00	7.643E-01	6.823E-01	8.061E-01	1.202E+00	2.070E+00	2.481E+00	2.332E+00	1.436E+00
Y = 5	6.252E-01	5.471E-01	5.366E-01	6.401E-01	8.834E-01	1.253E+00	1.546E+00	1.738E+00	1.173E+00
Y = 4	4.046E-01	3.981E-01	4.218E-01	5.062E-01	6.602E-01	8.614E-01	1.084E+00	1.326E+00	9.395E-01
Y = 3	3.232E-01	3.259E-01	3.551E-01	4.330E-01	5.658E-01	7.376E-01	9.310E-01	1.146E+00	8.148E-01
Y = 2	3.392E-01	3.147E-01	3.324E-01	4.162E-01	5.847E-01	8.299E-01	1.029E+00	1.160E+00	7.908E-01
Y = 1	4.678E-01	3.422E-01	3.328E-01	4.268E-01	6.723E-01	1.193E+00	1.442E+00	1.295E+00	8.120E-01
	X = 1	2	3	4	5	6	7	8	9

Figure A6-1a. 2-D LRA BWR transient problem.

NORMALIZED NODAL POWER DENSITIES AT T = 0.119989E+01
MEAN POWER DENSITY = 0.734631E-03

Y = 9	5.972E-01	5.945E-01	6.369E-01	7.598E-01	9.484E-01	1.101E+00	1.050E+00	0.0	0.0
Y = 8	9.531E-01	8.748E-01	9.048E-01	1.100E+00	1.479E+00	1.958E+00	2.119E+00	1.972E+00	0.0
Y = 7	1.064E+00	7.797E-01	7.489E-01	9.360E-01	1.427E+00	2.458E+00	2.952E+00	2.784E+00	1.641E+00
Y = 6	8.851E-01	6.359E-01	6.072E-01	7.758E-01	1.233E+00	2.223E+00	2.799E+00	2.848E+00	1.812E+00
Y = 5	5.057E-01	4.561E-01	4.761E-01	6.099E-01	8.933E-01	1.324E+00	1.701E+00	1.979E+00	1.361E+00
Y = 4	3.270E-01	3.311E-01	3.698E-01	4.708E-01	6.447E-01	8.727E-01	1.129E+00	1.404E+00	1.003E+00
Y = 3	2.587E-01	2.675E-01	3.046E-01	3.886E-01	5.258E-01	7.021E-01	9.024E-01	1.123E+00	8.035E-01
Y = 2	2.669E-01	2.534E-01	2.783E-01	3.614E-01	5.193E-01	7.462E-01	9.352E-01	1.065E+00	7.305E-01
Y = 1	3.638E-01	2.718E-01	2.746E-01	3.639E-01	5.841E-01	1.044E+00	1.272E+00	1.151E+00	7.254E-01
X =	1	2	3	4	5	6	7	8	9

Figure A6-1a. 2-D LRA BWR transient problem.

NORMALIZED NODAL POWER DENSITIES AT T = 0.139978E+01
MEAN POWER DENSITY = 0.720297E+03

Y = 9	5.411E-01	5.461E-01	5.999E-01	7.355E-01	9.397E-01	1.112E+00	1.077E+00	0.0	0.0
Y = 8	8.633E-01	8.036E-01	8.536E-01	1.069E+00	1.473E+00	1.989E+00	2.197E+00	2.092E+00	0.0
Y = 7	9.622E-01	7.160E-01	7.081E-01	9.134E-01	1.429E+00	2.509E+00	3.088E+00	3.036E+00	1.826E+00
Y = 6	8.011E-01	5.844E-01	5.751E-01	7.588E-01	1.237E+00	2.273E+00	2.932E+00	3.104E+00	2.008E+00
Y = 5	4.592E-01	4.202E-01	4.509E-01	5.948E-01	8.922E-01	1.348E+00	1.765E+00	2.089E+00	1.449E+00
Y = 4	2.975E-01	3.052E-01	3.488E-01	4.550E-01	6.355E-01	8.739E-01	1.145E+00	1.435E+00	1.030E+00
Y = 3	2.347E-01	2.455E-01	2.848E-01	3.701E-01	5.077E-01	6.848E-01	8.872E-01	1.109E+00	7.955E-01
Y = 2	2.405E-01	2.307E-01	2.574E-01	3.391E-01	4.911E-01	7.088E-01	8.922E-01	1.021E+00	7.014E-01
Y = 1	3.259E-01	2.458E-01	2.523E-01	3.385E-01	5.464E-01	9.784E-01	1.195E+00	1.085E+00	6.852E-01
X =	1	2	3	4	5	6	7	8	9

Figure A6-1a. 2-D LRA BWR transient problem.

NORMALIZED NODAL POWER DENSITIES AT T = 0.199964E+01
MEAN POWER DENSITY = 0.798027E+03

Y = 9	4.631E-01	4.733E-01	5.321E-01	6.705E-01	8.819E-01	1.079E+00	1.093E+00	0.0	0.0
Y = 8	7.350E-01	6.929E-01	7.541E-01	9.720E-01	1.383E+00	1.942E+00	2.271E+00	2.335E+00	0.0
Y = 7	8.203E-01	6.167E-01	6.262E-01	8.338E-01	1.352E+00	2.480E+00	3.271E+00	3.648E+00	2.356E+00
Y = 6	6.865E-01	5.063E-01	5.119E-01	6.978E-01	1.179E+00	2.259E+00	3.118E+00	3.723E+00	2.552E+00
Y = 5	3.973E-01	3.683E-01	4.051E-01	5.497E-01	8.496E-01	1.330E+00	1.833E+00	2.294E+00	1.654E+00
Y = 4	2.619E-01	2.716E-01	3.159E-01	4.206E-01	5.999E-01	8.458E-01	1.142E+00	1.472E+00	1.080E+00
Y = 3	2.106E-01	2.214E-01	2.591E-01	3.398E-01	4.705E-01	6.420E-01	8.447E-01	1.073E+00	7.812E-01
Y = 2	2.191E-01	2.100E-01	2.342E-01	3.080E-01	4.453E-01	6.429E-01	8.137E-01	9.408E-01	6.542E-01
Y = 1	2.994E-01	2.247E-01	2.292E-01	3.052E-01	4.893E-01	8.744E-01	1.069E+00	9.747E-01	6.217E-01
X =	1	2	3	4	5	6	7	8	9

Figure A6-1a. 2-D LRA BWR transient problem.

NORMALIZED NODAL POWER DENSITIES AT T = 0.299957E+01
MEAN POWER DENSITY = 0.974213E+02

Y = 9	5.045E-01	5.082E-01	5.560E-01	6.811E-01	8.762E-01	1.058E+00	1.062E+00	0.0	0.0
Y = 8	8.015E-01	7.439E-01	7.872E-01	9.837E-01	1.368E+00	1.893E+00	2.196E+00	2.248E+00	0.0
Y = 7	8.959E-01	6.636E-01	6.529E-01	8.417E-01	1.332E+00	2.411E+00	3.154E+00	3.503E+00	2.261E+00
Y = 6	7.516E-01	5.458E-01	5.348E-01	7.045E-01	1.162E+00	2.197E+00	3.010E+00	3.577E+00	2.453E+00
Y = 5	4.359E-01	3.983E-01	4.251E-01	5.591E-01	8.433E-01	1.302E+00	1.778E+00	2.220E+00	1.600E+00
Y = 4	2.894E-01	2.957E-01	3.351E-01	4.335E-01	6.051E-01	8.406E-01	1.126E+00	1.446E+00	1.062E+00
Y = 3	2.357E-01	2.443E-01	2.789E-01	3.570E-01	4.851E-01	6.540E-01	8.533E-01	1.081E+00	7.859E-01
Y = 2	2.488E-01	2.350E-01	2.561E-01	3.292E-01	4.688E-01	6.706E-01	8.436E-01	9.708E-01	6.744E-01
Y = 1	3.427E-01	2.540E-01	2.528E-01	3.292E-01	5.202E-01	9.233E-01	1.122E+00	1.020E+00	6.497E-01
	X = 1	2	3	4	5	6	7	8	9

Figure A6-1b. 2-D LRA BWR transient problem.

NODE AVERAGED FUEL TEMPERATURES AT T = 0.139978E+01
REACTOR AVERAGE FUEL TEMPERATURE = 0.309592E+03

Y = 9	3.052E+02	3.052E+02	3.058E+02	3.071E+02	3.090E+02	3.107E+02	3.103E+02	3.000E+02	3.000E+02
Y = 8	3.083E+02	3.077E+02	3.082E+02	3.103E+02	3.142E+02	3.191E+02	3.211E+02	3.201E+02	3.000E+02
Y = 7	3.093E+02	3.069E+02	3.068E+02	3.088E+02	3.137E+02	3.241E+02	3.297E+02	3.291E+02	3.175E+02
Y = 6	3.077E+02	3.056E+02	3.055E+02	3.073E+02	3.119E+02	3.218E+02	3.281E+02	3.297E+02	3.192E+02
Y = 5	3.044E+02	3.040E+02	3.043E+02	3.057E+02	3.086E+02	3.129E+02	3.169E+02	3.200E+02	3.139E+02
Y = 4	3.028E+02	3.029E+02	3.033E+02	3.044E+02	3.061E+02	3.084E+02	3.110E+02	3.138E+02	3.099E+02
Y = 3	3.022E+02	3.023E+02	3.027E+02	3.035E+02	3.049E+02	3.066E+02	3.085E+02	3.106E+02	3.076E+02
Y = 2	3.023E+02	3.022E+02	3.025E+02	3.032E+02	3.047E+02	3.068E+02	3.086E+02	3.098E+02	3.067E+02
Y = 1	3.031E+02	3.023E+02	3.024E+02	3.032E+02	3.052E+02	3.094E+02	3.115E+02	3.104E+02	3.066E+02
X =	1	2	3	4	5	6	7	8	9

Figure A6-1b. 2-D LRA BWR transient problem.

NODE AVERAGED FUEL TEMPERATURES AT T = 0.199964E+01
REACTOR AVERAGE FUEL TEMPERATURE = 0.854850E+03

Y = 9	5.983E+02	5.998E+02	6.268E+02	6.979E+02	8.073E+02	9.029E+02	8.918E+02	3.000E+02	3.000E+02
Y = 8	7.748E+02	7.399E+02	7.634E+02	8.758E+02	1.092E+03	1.377E+03	1.510E+03	1.486E+03	3.000E+02
Y = 7	8.302E+02	6.919E+02	6.839E+02	7.914E+02	1.069E+03	1.663E+03	2.014E+03	2.065E+03	1.394E+03
Y = 6	7.425E+02	6.207E+02	6.126E+02	7.093E+02	9.672E+02	1.537E+03	1.930E+03	2.104E+03	1.496E+03
Y = 5	5.544E+02	5.317E+02	5.465E+02	6.227E+02	7.829E+02	1.034E+03	1.275E+03	1.478E+03	1.131E+03
Y = 4	4.663E+02	4.698E+02	4.923E+02	5.488E+02	6.460E+02	7.766E+02	9.289E+02	1.097E+03	8.772E+02
Y = 3	4.330E+02	4.382E+02	4.586E+02	5.041E+02	5.783E+02	6.746E+02	7.864E+02	9.112E+02	7.413E+02
Y = 2	4.383E+02	4.315E+02	4.447E+02	4.882E+02	5.704E+02	6.889E+02	7.891E+02	8.608E+02	6.872E+02
Y = 1	4.893E+02	4.412E+02	4.425E+02	4.885E+02	6.015E+02	8.385E+02	9.561E+02	8.955E+02	6.775E+02
	X = 1	2	3	4	5	6	7	8	9

Figure A6-1b. 2-D LRA BWR transient problem.

NODE AVERAGED FUEL TEMPERATURES AT T = 0.299957E+01
REACTOR AVERAGE FUEL TEMPERATURE = 0.111056E+04

Y = 9	7.220E+02	7.253E+02	7.659E+02	8.707E+02	1.032E+03	1.176E+03	1.167E+03	3.000E+02	3.000E+02
Y = 8	9.713E+02	9.236E+02	9.604E+02	1.126E+03	1.444E+03	1.867E+03	2.081E+03	2.072E+03	3.000E+02
Y = 7	1.050E+03	8.555E+02	8.474E+02	1.006E+03	1.412E+03	2.288E+03	2.835E+03	2.980E+03	1.985E+03
Y = 6	9.264E+02	7.552E+02	7.464E+02	8.886E+02	1.266E+03	2.107E+03	2.714E+03	3.037E+03	2.136E+03
Y = 5	6.609E+02	6.297E+02	6.526E+02	7.644E+02	9.993E+02	1.370E+03	1.737E+03	2.055E+03	1.547E+03
Y = 4	5.367E+02	5.422E+02	5.755E+02	6.579E+02	8.000E+02	9.921E+02	1.219E+03	1.470E+03	1.151E+03
Y = 3	4.900E+02	4.977E+02	5.274E+02	5.931E+02	7.004E+02	8.402E+02	1.003E+03	1.186E+03	9.416E+02
Y = 2	4.980E+02	4.883E+02	5.073E+02	5.696E+02	6.872E+02	8.568E+02	1.001E+03	1.105E+03	8.571E+02
Y = 1	5.713E+02	5.023E+02	5.041E+02	5.695E+02	7.306E+02	1.068E+03	1.236E+03	1.151E+03	8.401E+02
X =	1	2	3	4	5	6	7	8	9

Figure A6-2a. 3-D LRA BWR (quarter-core) transient problem.

NORMALIZED ASSEMBLY POWER DENSITIES AT T = 0.0

MEAN POWER DENSITY = 0.100000E-05

Y = 7	0.0	0.0	0.0	0.0	0.0	0.0	0.0
Y = 6	9.275E-01	8.424E-01	8.890E-01	9.142E-01	0.0	0.0	0.0
Y = 5	1.500E+00	1.215E+00	1.317E+00	1.674E+00	1.328E+00	0.0	0.0
Y = 4	1.522E+00	9.550E-01	1.084E+00	2.048E+00	1.674E+00	9.142E-01	0.0
Y = 3	6.409E-01	5.677E-01	6.970E-01	1.084E+00	1.317E+00	8.890E-01	0.0
Y = 2	4.233E-01	4.063E-01	5.677E-01	9.550E-01	1.215E+00	8.424E-01	0.0
Y = 1	6.047E-01	4.233E-01	6.409E-01	1.522E+00	1.500E+00	9.275E-01	0.0
X =	1	2	3	4	5	6	7

Figure A6-2a. 3-D LRA BWR (quarter-core) transient problem.

NORMALIZED ASSEMBLY POWER DENSITIES AT T = 0.400000E+00

MEAN POWER DENSITY = 0.119211E-05

Y = 7	0.0	0.0	0.0	0.0	0.0	0.0	0.0
Y = 6	8.706E-01	7.990E-01	8.769E-01	9.398E-01	0.0	0.0	0.0
Y = 5	1.407E+00	1.153E+00	1.304E+00	1.738E+00	1.461E+00	0.0	0.0
Y = 4	1.424E+00	9.058E-01	1.079E+00	2.140E+00	1.917E+00	1.086E+00	0.0
Y = 3	6.008E-01	5.384E-01	6.867E-01	1.111E+00	1.390E+00	9.469E-01	0.0
Y = 2	3.955E-01	3.827E-01	5.453E-01	9.279E-01	1.189E+00	8.262E-01	0.0
Y = 1	5.635E-01	3.971E-01	6.102E-01	1.455E+00	1.442E+00	8.933E-01	0.0
X =	1	2	3	4	5	6	7

Figure A6-2a. 3-D LRA BWR (quarter-core) transient problem.

NORMALIZED ASSEMBLY POWER DENSITIES AT T = 0.799997E+00
MEAN POWER DENSITY = 0.798657E-01

Y = 7	0.0	0.0	0.0	0.0	0.0	0.0	0.0
Y = 6	5.127E-01	5.424E-01	8.198E-01	1.107E+00	0.0	0.0	0.0
Y = 5	8.261E-01	7.821E-01	1.248E+00	2.145E+00	2.175E+00	0.0	0.0
Y = 4	8.349E-01	6.183E-01	1.067E+00	2.769E+00	3.280E+00	2.067E+00	0.0
Y = 3	3.541E-01	3.661E-01	6.389E-01	1.288E+00	1.789E+00	1.262E+00	0.0
Y = 2	2.231E-01	2.411E-01	4.136E-01	7.684E-01	1.024E+00	7.234E-01	0.0
Y = 1	3.033E-01	2.347E-01	4.165E-01	1.040E+00	1.054E+00	6.613E-01	0.0
X =	1	2	3	4	5	6	7

Figure A6-2a. 3-D LRA BWR (quarter-core) transient problem.

NORMALIZED ASSEMBLY POWER DENSITIES AT T = 0.999995E+00

MEAN POWER DENSITY = 0.112932E+03

Y = 7	0.0	0.0	0.0	0.0	0.0	0.0	0.0
Y = 6	5.727E-01	5.803E-01	8.101E-01	1.059E+00	0.0	0.0	0.0
Y = 5	9.211E-01	8.342E-01	1.222E+00	2.032E+00	2.083E+00	0.0	0.0
Y = 4	9.319E-01	6.589E-01	1.039E+00	2.615E+00	3.148E+00	2.011E+00	0.0
Y = 3	4.001E-01	3.960E-01	6.375E-01	1.244E+00	1.736E+00	1.236E+00	0.0
Y = 2	2.633E-01	2.730E-01	4.391E-01	7.951E-01	1.056E+00	7.473E-01	0.0
Y = 1	3.693E-01	2.739E-01	4.567E-01	1.116E+00	1.127E+00	7.080E-01	0.0
X =	1	2	3	4	5	6	7

Figure A6-2a. 3-D LRA BWR (quarter-core) transient problem.

NORMALIZED ASSEMBLY POWER DENSITIES AT T = 0.199997E+01
MEAN POWER DENSITY = 0.236073E+03

Y = 7	0.0	0.0	0.0	0.0	0.0	0.0	0.0
Y = 6	4.603E-01	4.909E-01	7.651E-01	1.091E+00	0.0	0.0	0.0
Y = 5	7.381E-01	7.048E-01	1.162E+00	2.130E+00	2.369E+00	0.0	0.0
Y = 4	7.482E-01	5.599E-01	1.003E+00	2.798E+00	3.761E+00	2.488E+00	0.0
Y = 3	3.238E-01	3.379E-01	6.060E-01	1.286E+00	1.883E+00	1.365E+00	0.0
Y = 2	2.132E-01	2.288E-01	3.896E-01	7.280E-01	9.849E-01	7.042E-01	0.0
Y = 1	2.964E-01	2.253E-01	3.887E-01	9.628E-01	9.813E-01	6.216E-01	0.0
X =	1	2	3	4	5	6	7

Figure A6-2a. 3-D LRA BWR (quarter-core) transient problem.

NORMALIZED ASSEMBLY POWER DENSITIES AT T = 0.299996E+01
MEAN POWER DENSITY = 0.712415E+02

Y = 7	0.0	0.0	0.0	0.0	0.0	0.0	0.0
Y = 6	4.937E-01	5.154E-01	7.692E-01	1.072E+00	0.0	0.0	0.0
Y = 5	7.921E-01	7.397E-01	1.164E+00	2.082E+00	2.290E+00	0.0	0.0
Y = 4	8.044E-01	5.872E-01	1.000E+00	2.733E+00	3.639E+00	2.405E+00	0.0
Y = 3	3.495E-01	3.561E-01	6.104E-01	1.266E+00	1.840E+00	1.333E+00	0.0
Y = 2	2.340E-01	2.459E-01	4.045E-01	7.439E-01	1.000E+00	7.141E-01	0.0
Y = 1	3.291E-01	2.454E-01	4.103E-01	1.005E+00	1.019E+00	6.442E-01	0.0
X =	1	2	3	4	5	6	7

Figure A6-2b. 3-D LRA BWR (quarter-core) transient problem.

NORMALIZED NODAL POWER DENSITIES AT T = 0.0
PLANE # 4

Y = 7	0.0	0.0	0.0	0.0	0.0	0.0	0.0
Y = 6	1.169E+00	1.062E+00	1.121E+00	1.152E+00	0.0	0.0	0.0
Y = 5	1.890E+00	1.532E+00	1.660E+00	2.110E+00	1.672E+00	0.0	0.0
Y = 4	1.919E+00	1.204E+00	1.367E+00	2.582E+00	2.110E+00	1.152E+00	0.0
Y = 3	8.082E-01	7.160E-01	8.789E-01	1.367E+00	1.660E+00	1.121E+00	0.0
Y = 2	5.339E-01	5.124E-01	7.160E-01	1.204E+00	1.532E+00	1.062E+00	0.0
Y = 1	7.626E-01	5.339E-01	8.082E-01	1.919E+00	1.890E+00	1.169E+00	0.0
X =	1	2	3	4	5	6	7

Figure A6-2b. 3-D LRA BWR (quarter-core) transient problem.

NORMALIZED NODAL POWER DENSITIES AT T = 0.400000E+00
PLANE # 4

Y = 7	0.0	0.0	0.0	0.0	0.0	0.0	0.0
Y = 6	1.137E+00	1.050E+00	1.170E+00	1.261E+00	0.0	0.0	0.0
Y = 5	1.839E+00	1.513E+00	1.742E+00	2.322E+00	1.917E+00	0.0	0.0
Y = 4	1.857E+00	1.190E+00	1.439E+00	2.848E+00	2.456E+00	1.375E+00	0.0
Y = 3	7.847E-01	7.068E-01	9.155E-01	1.485E+00	1.846E+00	1.253E+00	0.0
Y = 2	5.150E-01	5.012E-01	7.203E-01	1.231E+00	1.576E+00	1.098E+00	0.0
Y = 1	7.333E-01	5.183E-01	8.033E-01	1.916E+00	1.906E+00	1.180E+00	0.0
X =	1	2	3	4	5	6	7

Figure A6-2b. 3-D LRA BWR (quarter-core) transient problem.

NORMALIZED NODAL POWER DENSITIES AT T = 0.799997E+00
PLANE # 4

Y = 7	0.0	0.0	0.0	0.0	0.0	0.0	0.0
Y = 6	8.819E-01	9.657E-01	1.568E+00	2.242E+00	0.0	0.0	0.0
Y = 5	1.420E+00	1.393E+00	2.403E+00	4.408E+00	4.749E+00	0.0	0.0
Y = 4	1.432E+00	1.102E+00	2.072E+00	5.777E+00	7.529E+00	4.861E+00	0.0
Y = 3	6.053E-01	6.486E-01	1.220E+00	2.606E+00	3.751E+00	2.677E+00	0.0
Y = 2	3.753E-01	4.170E-01	7.489E-01	1.429E+00	1.934E+00	1.373E+00	0.0
Y = 1	5.044E-01	3.988E-01	7.337E-01	1.861E+00	1.904E+00	1.199E+00	0.0
X =	1	2	3	4	5	6	7

Figure A6-2b. 3-D LRA BWR (quarter-core) transient problem.

NORMALIZED NODAL POWER DENSITIES AT T = 0.999995E+00

PLANE # 4

Y = 7	0.0	0.0	0.0	0.0	0.C	0.0	0.0
Y = 6	8.737E-01	9.139E-01	1.374E+00	1.920E+00	0.0	0.0	0.0
Y = 5	1.404E+00	1.313E+00	2.085E+00	3.743E+00	4.117E+00	0.0	0.0
Y = 4	1.418E+00	1.039E+00	1.789E+00	4.900E+00	6.531E+00	4.303E+00	0.0
Y = 3	6.096E-01	6.232E-01	1.082E+00	2.260E+00	3.290E+00	2.377E+00	0.0
Y = 2	3.976E-01	4.219E-01	7.075E-01	1.315E+00	1.772E+00	1.263E+00	0.0
Y = 1	5.534E-01	4.174E-01	7.161E-01	1.771E+00	1.806E+00	1.139E+00	0.0
X =	1	2	3	4	5	6	7

Figure A6-2b. 3-D LRA BWR (quarter-core) transient problem.

NORMALIZED NODAL POWER DENSITIES AT T = 0.199997E+01

PLANE # 4

Y = 7	0.0	0.0	0.0	0.0	0.0	0.0	0.0
Y = 6	4.827E-01	5.050E-01	7.454E-01	1.031E+00	0.0	0.0	0.0
Y = 5	7.745E-01	7.232E-01	1.128E+00	1.993E+00	2.172E+00	0.0	0.0
Y = 4	7.881E-01	5.749E-01	9.686E-01	2.616E+00	3.449E+00	2.281E+00	0.0
Y = 3	3.433E-01	3.497E-01	5.953E-01	1.220E+00	1.760E+00	1.273E+00	0.0
Y = 2	2.301E-01	2.423E-01	3.975E-01	7.273E-01	9.749E-01	6.973E-01	0.0
Y = 1	3.231E-01	2.415E-01	4.037E-01	9.852E-01	9.958E-01	6.293E-01	0.0
X =	1	2	3	4	5	6	7

Figure A6-2b. 3-D LRA BWR (quarter-core) transient problem.

NORMALIZED NODAL POWER DENSITIES AT T = 0.299996E+01
PLANE # 4

Y = 7	0.0	0.0	0.0	0.0	0.0	0.0	0.0
Y = 6	5.647E-01	5.837E-01	8.405E-01	1.151E+00	0.0	0.0	0.0
Y = 5	9.068E-01	8.355E-01	1.270E+00	2.221E+00	2.419E+00	0.0	0.0
Y = 4	9.225E-01	6.636E-01	1.089E+00	2.908E+00	3.832E+00	2.536E+00	0.0
Y = 3	4.028E-01	4.049E-01	6.720E-01	1.363E+00	1.967E+00	1.422E+00	0.0
Y = 2	2.728E-01	2.835E-01	4.561E-01	8.278E-01	1.107E+00	7.917E-01	0.0
Y = 1	3.860E-01	2.851E-01	4.675E-01	1.133E+00	1.145E+00	7.226E-01	0.0
X =	1	2	3	4	5	6	7

Figure A6-2c. 3-D LRA BWR (quarter-core) transient problem.

NODE AVERAGED FUEL TEMPERATURES AT T = 0.999995E+00
REACTOR AVERAGE FUEL TEMPERATURE = 0.556622E+03

PLANE # 4

Y = 7	3.000E+02	3.000E+02	3.000E+02	3.000E+02	3.000E+02	3.000E+02	0.0
Y = 6	5.258E+02	5.415E+02	6.752E+02	8.273E+02	3.000E+02	3.000E+02	3.000E+02
Y = 5	6.629E+02	6.474E+02	8.708E+02	1.331E+03	1.415E+03	3.000E+02	3.000E+02
Y = 4	6.687E+02	5.745E+02	7.895E+02	1.657E+03	2.077E+03	1.460E+03	3.000E+02
Y = 3	4.560E+02	4.628E+02	5.925E+02	9.152E+02	1.187E+03	9.374E+02	3.000E+02
Y = 2	3.993E+02	4.074E+02	4.859E+02	6.493E+02	7.718E+02	6.356E+02	3.000E+02
Y = 1	4.361E+02	4.047E+02	4.852E+02	7.663E+02	7.724E+02	5.981E+02	3.000E+02
X =	1	2	3	4	5	6	7

Figure A6-2c. 3-D LRA BWR (quarter-core) transient problem.

```
NODE AVERAGED FUEL TEMPERATURES AT T =     0.199997E+01
REACTOR AVERAGE FUEL TEMPERATURE =     0.897433E+03

PLANE #   4
Y =  7   3.000E+02   3.000E+02   3.000E+02   3.000E+02   3.000E+02   3.000E+02   0.0

Y =  6   7.330E+02   7.605E+02   1.008E+03   1.292E+03   3.000E+02   3.000E+02   3.000E+02

Y =  5   9.951E+02   9.618E+02   1.375E+03   2.235E+03   2.404E+03   3.000E+02   3.000E+02

Y =  4   1.006E+03   8.237E+02   1.223E+03   2.844E+03   3.649E+03   2.496E+03   3.000E+02

Y =  3   6.020E+02   6.135E+02   8.562E+02   1.464E+03   1.983E+03   1.514E+03   3.000E+02

Y =  2   4.956E+02   5.100E+02   6.583E+02   9.683E+02   1.202E+03   9.425E+02   3.000E+02

Y =  1   5.702E+02   5.061E+02   6.585E+02   1.194E+03   1.206E+03   8.723E+02   3.000E+02

       X =    1           2           3           4           5           6           7
```

Figure A6-2c. 3-D LRA BWR (quarter-core) transient problem.

```
NODE AVERAGED FUEL TEMPERATURES AT T =     0.299996E+01
REACTOR AVERAGE FUEL TEMPERATURE =     0.103252E+04

PLANE #   4
Y =  7   3.000E+02   3.000E+02   3.000E+02   3.000E+02   3.000E+02   3.000E+02   0.0

Y =  6   8.050E+02   8.350E+02   1.117E+03   1.442E+03   3.000E+02   3.000E+02   3.000E+02

Y =  5   1.111E+03   1.069E+03   1.539E+03   2.524E+03   2.719E+03   3.000E+02   3.000E+02

Y =  4   1.124E+03   9.086E+02   1.364E+03   3.222E+03   4.148E+03   2.826E+03   3.000E+02

Y =  3   6.532E+02   6.653E+02   9.430E+02   1.641E+03   2.239E+03   1.699E+03   3.000E+02

Y =  2   5.301E+02   5.461E+02   7.168E+02   1.075E+03   1.344E+03   1.044E+03   3.000E+02

Y =  1   6.189E+02   5.423E+02   7.183E+02   1.339E+03   1.353E+03   9.652E+02   3.000E+02

       X =    1           2           3           4           5           6           7
```

Figure A6-3a. 3-D LRA BWR (full-core) transient problem.

NORMALIZED ASSEMBLY POWER DENSITIES AT T = 0.0

MEAN POWER DENSITY = 0.100007E-05

Y = 11	0.0	0.0	9.099E-01	8.877E-01	8.435E-01	9.274E-01	8.435E-01	8.877E-01	9.099E-01	0.0	0.0
Y = 10	0.0	1.321E+00	1.666E+00	1.314E+00	1.217E+00	1.503E+00	1.217E+00	1.314E+00	1.666E+00	1.321E+00	0.0
Y = 9	9.099E-01	1.666E+00	2.039E+00	1.079E+00	9.571E-01	1.536E+00	9.571E-01	1.079E+00	2.039E+00	1.666E+00	9.099E-01
Y = 8	8.877E-01	1.314E+00	1.079E+00	6.974E-01	5.702E-01	6.417E-01	5.702E-01	6.974E-01	1.079E+00	1.314E+00	8.877E-01
Y = 7	8.435E-01	1.217E+00	9.571E-01	5.702E-01	4.087E-01	4.250E-01	4.087E-01	5.702E-01	9.571E-01	1.217E+00	8.435E-01
Y = 6	9.274E-01	1.503E+00	1.536E+00	6.417E-01	4.250E-01	6.185E-01	4.250E-01	6.417E-01	1.536E+00	1.503E+00	9.274E-01
Y = 5	8.435E-01	1.217E+00	9.571E-01	5.702E-01	4.087E-01	4.250E-01	4.087E-01	5.702E-01	9.571E-01	1.217E+00	8.435E-01
Y = 4	8.877E-01	1.314E+00	1.079E+00	6.974E-01	5.702E-01	6.417E-01	5.702E-01	6.974E-01	1.079E+00	1.314E+00	8.877E-01
Y = 3	9.099E-01	1.666E+00	2.039E+00	1.079E+00	9.571E-01	1.536E+00	9.571E-01	1.079E+00	2.039E+00	1.666E+00	9.099E-01
Y = 2	0.0	1.321E+00	1.666E+00	1.314E+00	1.217E+00	1.503E+00	1.217E+00	1.314E+00	1.666E+00	1.321E+00	0.0
Y = 1	0.0	0.0	9.099E-01	8.877E-01	8.435E-01	9.274E-01	8.435E-01	8.877E-01	9.099E-01	0.0	0.0
X =	1	2	3	4	5	6	7	8	9	10	11

Figure A6-3a. 3-D LRA BWR (full-core) transient problem.

NORMALIZED ASSEMBLY POWER DENSITIES AT T = 0.400000E+00

MEAN POWER DENSITY = 0.105439E-05

Y = 11	0.0	0.0	8.761E-01	8.606E-01	8.315E-01	9.318E-01	8.763E-01	9.789E-01	1.057E+00	0.0	0.0
Y = 10	0.0	1.270E+00	1.603E+00	1.273E+00	1.200E+00	1.510E+00	1.264E+00	1.455E+00	1.956E+00	1.649E+00	0.0
Y = 9	8.734E-01	1.600E+00	1.961E+00	1.044E+00	9.438E-01	1.541E+00	9.927E-01	1.202E+00	2.416E+00	2.174E+00	1.237E+00
Y = 8	8.508E-01	1.260E+00	1.036E+00	6.734E-01	5.601E-01	6.425E-01	5.898E-01	7.634E-01	1.240E+00	1.555E+00	1.061E+00
Y = 7	8.064E-01	1.164E+00	9.157E-01	5.480E-01	3.979E-01	4.205E-01	4.148E-01	5.958E-01	1.013E+00	1.299E+00	9.029E-01
Y = 6	8.851E-01	1.435E+00	1.467E+00	6.143E-01	4.109E-01	6.043E-01	4.219E-01	6.087E-01	1.561E+00	1.532E+00	9.461E-01
Y = 5	8.040E-01	1.160E+00	9.127E-01	5.447E-01	3.925E-01	4.112E-01	3.991E-01	5.639E-01	9.520E-01	1.211E+00	8.392E-01
Y = 4	8.452E-01	1.251E+00	1.028E+00	6.647E-01	5.449E-01	6.149E-01	5.491E-01	6.758E-01	1.049E+00	1.279E+00	8.647E-01
Y = 3	8.659E-01	1.585E+00	1.941E+00	1.028E+00	9.132E-01	1.468E+00	9.170E-01	1.038E+00	1.966E+00	1.608E+00	8.789E-01
Y = 2	0.0	1.257E+00	1.585E+00	1.251E+00	1.161E+00	1.436E+00	1.165E+00	1.262E+00	1.604E+00	1.273E+00	0.0
Y = 1	0.0	0.0	8.659E-01	8.453E-01	8.045E-01	8.859E-01	8.075E-01	8.525E-01	8.754E-01	0.0	0.0
X =	1	2	3	4	5	6	7	8	9	10	11

Figure A6-3a. 3-D LRA BWR (full-core) transient problem.

NORMALIZED ASSEMBLY POWER DENSITIES AT T = 0.799990E+00

MEAN POWER DENSITY = 0.115577E-02

Y = 11	0.0	0.0	2.041E-01	3.096E-01	5.627E-01	9.726E-01	1.493E+00	2.785E+00	3.967E+00	0.0	0.0
Y = 10	0.0	2.472E-01	3.587E-01	4.433E-01	8.217E-01	1.568E+00	2.137E+00	4.254E+00	7.706E+00	7.945E+00	0.0
Y = 9	1.533E-01	2.939E-01	4.102E-01	3.428E-01	6.493E-01	1.581E+00	1.668E+00	3.632E+00	9.931E+00	1.199E+01	7.592E+00
Y = 8	1.293E-01	2.000E-01	1.900E-01	1.977E-01	3.446E-01	6.354E-01	9.626E-01	2.082E+00	4.432E+00	6.244E+00	4.419E+00
Y = 7	9.028E-02	1.329E-01	1.172E-01	1.143E-01	1.802E-01	3.220E-01	5.284E-01	1.093E+00	2.107E+00	2.879E+00	2.057E+00
Y = 6	7.510E-02	1.244E-01	1.383E-01	8.567E-02	1.332E-01	3.213E-01	3.519E-01	7.679E-01	2.006E+00	2.035E+00	1.276E+00
Y = 5	5.267E-02	7.816E-02	6.721E-02	5.540E-02	7.988E-02	1.407E-01	2.066E-01	4.241E-01	8.222E-01	1.051E+00	7.219E-01
Y = 4	3.941E-02	5.851E-02	5.064E-02	4.358E-02	5.955E-02	9.673E-02	1.356E-01	2.447E-01	4.314E-01	5.610E-01	3.925E-01
Y = 3	3.391E-02	6.236E-02	7.957E-02	5.305E-02	7.566E-02	1.610E-01	1.408E-01	2.354E-01	5.133E-01	4.503E-01	2.565E-01
Y = 2	0.0	4.777E-02	6.337E-02	6.229E-02	8.871E-02	1.457E-01	1.603E-01	2.475E-01	3.670E-01	3.095E-01	0.0
Y = 1	0.0	0.0	3.470E-02	4.220E-02	5.985E-02	8.814E-02	1.090E-01	1.599E-01	1.912E-01	0.0	0.0
X =	1	2	3	4	5	6	7	8	9	10	11

Figure A6-3a. 3-D LRA BWR (full-core) transient problem.

NORMALIZED ASSEMBLY POWER DENSITIES AT T = 0.119996E+01

MEAN POWER DENSITY = 0.485979E+02

Y = 11	0.0	0.0	3.049E-01	4.070E-01	6.412E-01	1.016E+00	1.427E+00	2.482E+00	3.474E+00	0.0	0.0
Y = 10	0.0	3.929E-01	5.418E-01	5.862E-01	9.325E-01	1.638E+00	2.040E+00	3.767E+00	6.719E+00	7.089E+00	0.0
Y = 9	2.510E-01	4.732E-01	6.316E-01	4.576E-01	7.328E-01	1.658E+00	1.591E+00	3.200E+00	8.696E+00	1.085E+01	6.995E+00
Y = 8	2.196E-01	3.341E-01	3.009E-01	2.699E-01	3.975E-01	6.713E-01	9.320E-01	1.882E+00	3.942E+00	5.631E+00	4.027E+00
Y = 7	1.657E-01	2.416E-01	2.029E-01	1.681E-01	2.209E-01	3.588E-01	5.393E-01	1.057E+00	2.004E+00	2.737E+00	1.959E+00
Y = 6	1.492E-01	2.447E-01	2.630E-01	1.404E-01	1.758E-01	3.884E-01	3.896E-01	8.031E-01	2.074E+00	2.094E+00	1.313E+00
Y = 5	1.133E-01	1.661E-01	1.374E-01	9.969E-02	1.172E-01	1.848E-01	2.502E-01	4.811E-01	9.107E-01	1.169E+00	8.060E-01
Y = 4	9.535E-02	1.411E-01	1.190E-01	9.130E-02	1.060E-01	1.561E-01	1.952E-01	3.258E-01	5.607E-01	7.221E-01	5.023E-01
Y = 3	8.786E-02	1.612E-01	2.024E-01	1.230E-01	1.509E-01	2.980E-01	2.366E-01	3.614E-01	7.658E-01	6.593E-01	3.717E-01
Y = 2	0.0	1.257E-01	1.629E-01	1.475E-01	1.833E-01	2.783E-01	2.821E-01	4.003E-01	5.720E-01	4.762E-01	0.0
Y = 1	0.0	0.0	8.923E-02	1.001E-01	1.251E-01	1.698E-01	1.937E-01	2.627E-01	3.030E-01	0.0	0.0
	X = 1	2	3	4	5	6	7	8	9	10	11

Figure A6-3a. 3-D LRA BWR (full-core) transient problem.

NORMALIZED ASSEMBLY POWER DENSITIES AT T = 0.139995E+01

MEAN POWER DENSITY = 0.851563E+02

Y = 11	0.0	0.0	2.803E-01	3.799E-01	6.116E-01	9.862E-01	1.413E+00	2.509E+00	3.568E+00	0.0	0.0
Y = 10	0.0	3.581E-01	4.972E-01	5.465E-01	8.894E-01	1.588E+00	2.018E+00	3.811E+00	6.912E+00	7.379E+00	0.0
Y = 9	2.284E-01	4.312E-01	5.787E-01	4.267E-01	7.012E-01	1.609E+00	1.579E+00	3.257E+00	8.975E+00	1.137E+01	7.377E+00
Y = 8	1.988E-01	3.029E-01	2.748E-01	2.511E-01	3.795E-01	6.525E-01	9.247E-01	1.908E+00	4.055E+00	5.826E+00	4.181E+00
Y = 7	1.492E-01	2.176E-01	1.839E-01	1.554E-01	2.101E-01	3.477E-01	5.321E-01	1.057E+00	2.020E+00	2.765E+00	1.984E+00
Y = 6	1.337E-01	2.195E-01	2.369E-01	1.287E-01	1.664E-01	3.734E-01	3.799E-01	7.909E-01	2.048E+00	2.069E+00	1.299E+00
Y = 5	1.008E-01	1.480E-01	1.230E-01	9.049E-02	1.094E-01	1.755E-01	2.402E-01	4.661E-01	8.862E-01	1.135E+00	7.829E-01
Y = 4	8.416E-02	1.246E-01	1.054E-01	8.174E-02	9.665E-02	1.441E-01	1.825E-01	3.075E-01	5.313E-01	6.842E-01	4.768E-01
Y = 3	7.735E-02	1.419E-01	1.784E-01	1.093E-01	1.361E-01	2.709E-01	2.170E-01	3.347E-01	7.121E-01	6.141E-01	3.469E-01
Y = 2	0.0	1.104E-01	1.436E-01	1.307E-01	1.646E-01	2.519E-01	2.571E-01	3.678E-01	5.285E-01	4.404E-01	0.0
Y = 1	0.0	0.0	7.866E-02	8.870E-02	1.122E-01	1.536E-01	1.764E-01	2.411E-01	2.796E-01	0.0	0.0
	X = 1	2	3	4	5	6	7	8	9	10	11

Figure A6-3a. 3-D LRA BWR (full-core) transient problem.

NORMALIZED ASSEMBLY POWER DENSITIES AT T = 0.199991E+01

MEAN POWER DENSITY = 0.606043E+02

Y = 11	0.0	0.0	2.676E-01	3.586E-01	5.712E-01	9.222E-01	1.340E+00	2.443E+00	3.588E+00	0.0	0.0
Y = 10	0.0	3.439E-01	4.750E-01	5.162E-01	8.302E-01	1.484E+00	1.915E+00	3.719E+00	7.007E+00	7.794E+00	0.0
Y = 9	2.203E-01	4.150E-01	5.531E-01	4.041E-01	6.553E-01	1.502E+00	1.503E+00	3.203E+00	9.181E+00	1.233E+01	8.143E+00
Y = 8	1.934E-01	2.940E-01	2.653E-01	2.393E-01	3.569E-01	6.141E-01	8.841E-01	1.873E+00	4.114E+00	6.055E+00	4.388E+00
Y = 7	1.479E-01	2.156E-01	1.815E-01	1.509E-01	2.006E-01	3.313E-01	5.099E-01	1.024E+00	1.978E+00	2.728E+00	1.966E+00
Y = 6	1.349E-01	2.213E-01	2.375E-01	1.276E-01	1.612E-01	3.582E-01	3.638E-01	7.547E-01	1.949E+00	1.981E+00	1.248E+00
Y = 5	1.033E-01	1.514E-01	1.254E-01	9.112E-02	1.076E-01	1.703E-01	2.305E-01	4.432E-01	8.404E-01	1.076E+00	7.431E-01
Y = 4	8.800E-02	1.302E-01	1.100E-01	8.412E-02	9.718E-02	1.427E-01	1.774E-01	2.945E-01	5.062E-01	6.510E-01	4.536E-01
Y = 3	8.172E-02	1.498E-01	1.876E-01	1.138E-01	1.382E-01	2.706E-01	2.136E-01	3.231E-01	6.811E-01	5.877E-01	3.319E-01
Y = 2	0.0	1.169E-01	1.515E-01	1.363E-01	1.677E-01	2.530E-01	2.539E-01	3.564E-01	5.084E-01	4.229E-01	0.0
Y = 1	0.0	0.0	8.303E-02	9.248E-02	1.145E-01	1.544E-01	1.743E-01	2.340E-01	2.695E-01	0.0	0.0
X =	1	2	3	4	5	6	7	8	9	10	11

Figure A6-3a. 3-D LRA BWR (full-core) transient problem.

NORMALIZED ASSEMBLY POWER DENSITIES AT T = 0.299989E+01
MEAN POWER DENSITY = 0.225659E+02

Y = 11	0.0	0.0	3.299E-01	4.183E-01	6.200E-01	9.556E-01	1.319E+00	2.303E+00	3.323E+00	0.0	0.0
Y = 10	0.0	4.338E-01	5.885E-01	6.042E-01	8.999E-01	1.538E+00	1.884E+00	3.495E+00	6.469E+00	7.146E+00	0.0
Y = 9	2.817E-01	5.273E-01	6.917E-01	4.760E-01	7.098E-01	1.561E+00	1.480E+00	3.000E+00	8.479E+00	1.133E+01	7.492E+00
Y = 8	2.513E-01	3.800E-01	3.364E-01	2.853E-01	3.909E-01	6.403E-01	8.744E-01	1.772E+00	3.823E+00	5.596E+00	4.056E+00
Y = 7	1.989E-01	2.891E-01	2.396E-01	1.866E-01	2.267E-01	3.544E-01	5.172E-01	1.002E+00	1.909E+00	2.618E+00	1.883E+00
Y = 6	1.872E-01	3.060E-01	3.251E-01	1.654E-01	1.886E-01	3.986E-01	3.851E-01	7.707E-01	1.974E+00	1.994E+00	1.254E+00
Y = 5	1.476E-01	2.155E-01	1.764E-01	1.227E-01	1.325E-01	1.978E-01	2.559E-01	4.731E-01	8.841E-01	1.131E+00	7.819E-01
Y = 4	1.306E-01	1.932E-01	1.620E-01	1.195E-01	1.295E-01	1.819E-01	2.142E-01	3.408E-01	5.776E-01	7.376E-01	5.121E-01
Y = 3	1.237E-01	2.266E-01	2.826E-01	1.664E-01	1.910E-01	3.624E-01	2.745E-01	3.973E-01	8.253E-01	7.051E-01	3.962E-01
Y = 2	0.0	1.774E-01	2.286E-01	2.003E-01	2.342E-01	3.419E-01	3.312E-01	4.469E-01	6.261E-01	5.168E-01	0.0
Y = 1	0.0	0.0	1.252E-01	1.359E-01	1.604E-01	2.092E-01	2.281E-01	2.951E-01	3.339E-01	0.0	0.0
	X = 1	2	3	4	5	6	7	8	9	10	11

Figure A6-3b. 3-D LRA BWR (full-core) transient problem.

NORMALIZED NODAL POWER DENSITIES AT T = 0.0
PLANE # 4

Y = 11	0.0	0.0	1.147E+00	1.119E+00	1.063E+00	1.169E+00	1.063E+00	1.119E+00	1.147E+00	0.0	0.0
Y = 10	0.0	1.664E+00	2.099E+00	1.656E+00	1.535E+00	1.895E+00	1.535E+00	1.656E+00	2.099E+00	1.664E+00	0.0
Y = 9	1.147E+00	2.099E+00	2.570E+00	1.360E+00	1.207E+00	1.937E+00	1.207E+00	1.360E+00	2.570E+00	2.099E+00	1.147E+00
Y = 8	1.119E+00	1.656E+00	1.360E+00	8.794E-01	7.191E-01	8.092E-01	7.191E-01	8.794E-01	1.360E+00	1.656E+00	1.119E+00
Y = 7	1.063E+00	1.535E+00	1.207E+00	7.191E-01	5.154E-01	5.359E-01	5.154E-01	7.191E-01	1.207E+00	1.535E+00	1.063E+00
Y = 6	1.169E+00	1.895E+00	1.937E+00	8.092E-01	5.359E-01	7.799E-01	5.359E-01	8.092E-01	1.937E+00	1.895E+00	1.169E+00
Y = 5	1.063E+00	1.535E+00	1.207E+00	7.191E-01	5.154E-01	5.359E-01	5.154E-01	7.191E-01	1.207E+00	1.535E+00	1.063E+00
Y = 4	1.119E+00	1.656E+00	1.360E+00	8.794E-01	7.191E-01	8.092E-01	7.191E-01	8.794E-01	1.360E+00	1.656E+00	1.119E+00
Y = 3	1.147E+00	2.099E+00	2.570E+00	1.360E+00	1.207E+00	1.937E+00	1.207E+00	1.360E+00	2.570E+00	2.099E+00	1.147E+00
Y = 2	0.0	1.664E+00	2.099E+00	1.656E+00	1.535E+00	1.895E+00	1.535E+00	1.656E+00	2.099E+00	1.664E+00	0.0
Y = 1	0.0	0.0	1.147E+00	1.119E+00	1.063E+00	1.169E+00	1.063E+00	1.119E+00	1.147E+00	0.0	0.0
X =	1	2	3	4	5	6	7	8	9	10	11

Figure A6-3b. 3-D LRA BWR (full-core) transient problem.

NORMALIZED NODAL POWER DENSITIES AT T = 0.400000E+00

PLANE # 4

Y = 11	0.0	0.0	1.107E+00	1.091E+00	1.061E+00	1.199E+00	1.146E+00	1.311E+00	1.426E+00	0.0	0.0
Y = 10	0.0	1.603E+00	2.026E+00	1.613E+00	1.532E+00	1.942E+00	1.651E+00	1.951E+00	2.627E+00	2.161E+00	0.0
Y = 9	1.103E+00	2.020E+00	2.477E+00	1.323E+00	1.205E+00	1.981E+00	1.297E+00	1.609E+00	3.228E+00	2.753E+00	1.537E+00
Y = 8	1.074E+00	1.591E+00	1.309E+00	8.527E-01	7.138E-01	8.258E-01	7.697E-01	1.019E+00	1.661E+00	2.065E+00	1.401E+00
Y = 7	1.018E+00	1.469E+00	1.156E+00	6.929E-01	5.055E-01	5.378E-01	5.372E-01	7.812E-01	1.334E+00	1.711E+00	1.192E+00
Y = 6	1.117E+00	1.810E+00	1.851E+00	7.758E-01	5.207E-01	7.690E-01	5.406E-01	8.380E-01	2.019E+00	1.984E+00	1.225E+00
Y = 5	1.014E+00	1.464E+00	1.151E+00	6.876E-01	4.964E-01	5.214E-01	5.080E-01	7.211E-01	1.221E+00	1.553E+00	1.077E+00
Y = 4	1.066E+00	1.577E+00	1.296E+00	8.386E-01	6.879E-01	7.768E-01	6.948E-01	8.570E-01	1.331E+00	1.624E+00	1.098E+00
Y = 3	1.092E+00	1.998E+00	2.447E+00	1.296E+00	1.152E+00	1.853E+00	1.158E+00	1.313E+00	2.486E+00	2.034E+00	1.113E+00
Y = 2	0.0	1.584E+00	1.998E+00	1.578E+00	1.465E+00	1.812E+00	1.471E+00	1.595E+00	2.027E+00	1.609E+00	0.0
Y = 1	0.0	0.0	1.092E+00	1.066E+00	1.015E+00	1.118E+00	1.020E+00	1.077E+00	1.106E+00	0.0	0.0
	X = 1	2	3	4	5	6	7	8	9	10	11

Figure A6-3b. 3-D LRA BWR (full-core) transient problem.

NORMALIZED NODAL POWER DENSITIES AT T = 0.799990E+00

PLANE # 4

Y = 11	0.0	0.0	3.063E-01	4.863E-01	9.329E-01	1.684E+00	2.747E+00	5.448E+00	8.107E+00	0.0	0.0
Y = 10	0.0	3.637E-01	5.363E-01	6.947E-01	1.364E+00	2.713E+00	3.933E+00	8.366E+00	1.594E+01	1.722E+01	0.0
Y = 9	2.233E-01	4.301E-01	6.096E-01	5.350E-01	1.078E+00	2.732E+00	3.074E+00	7.207E+00	2.079E+01	2.702E+01	1.742E+01
Y = 8	1.867E-01	2.900E-01	2.800E-01	3.069E-01	5.686E-01	1.095E+00	1.768E+00	4.078E+00	9.087E+00	1.316E+01	9.396E+00
Y = 7	1.284E-01	1.897E-01	1.697E-01	1.745E-01	2.925E-01	5.465E-01	9.471E-01	2.044E+00	4.038E+00	5.601E+00	4.021E+00
Y = 6	1.055E-01	1.751E-01	1.969E-01	1.276E-01	2.123E-01	5.304E-01	6.052E-01	1.362E+00	3.603E+00	3.685E+00	2.319E+00
Y = 5	7.307E-02	1.087E-01	9.443E-02	8.089E-02	1.237E-01	2.256E-01	3.418E-01	7.217E-01	1.417E+00	1.815E+00	1.247E+00
Y = 4	5.371E-02	7.980E-02	6.948E-02	6.151E-02	8.739E-02	1.457E-01	2.113E-01	3.904E-01	6.948E-01	9.086E-01	6.378E-01
Y = 3	4.573E-02	8.413E-02	1.078E-01	7.311E-02	1.073E-01	2.322E-01	2.077E-01	3.553E-01	7.827E-01	6.918E-01	3.959E-01
Y = 2	0.0	6.439E-02	8.562E-02	8.544E-02	1.247E-01	2.079E-01	2.328E-01	3.669E-01	5.499E-01	4.666E-01	0.0
Y = 1	0.0	0.0	4.689E-02	5.786E-02	8.390E-02	1.254E-01	1.579E-01	2.359E-01	2.850E-01	0.0	0.0
	X = 1	2	3	4	5	6	7	8	9	10	11

Figure A6-3b. 3-D LRA BWR (full-core) transient problem.

NORMALIZED NODAL POWER DENSITIES AT T = 0.119996E+01

PLANE # 4

Y = 11	0.0	0.0	4.109E-01	5.621E-01	9.124E-01	1.489E+00	2.180E+00	4.000E+00	5.836E+00	0.0	0.0
Y = 10	0.0	5.244E-01	7.298E-01	8.071E-01	1.329E+00	2.394E+00	3.119E+00	6.088E+00	1.141E+01	1.259E+01	0.0
Y = 9	3.340E-01	6.316E-	8.475E-01	6.292E-01	1.044E+00	2.425E+00	2.436E+00	5.211E+00	1.494E+01	1.994E+01	1.313E+01
Y = 8	2.915E-01	4.438E-01	4.026E-01	3.699E-01	5.656E-01	9.822E-01	1.429E+00	3.046E+00	6.675E+00	9.792E+00	7.085E+00
Y = 7	2.184E-01	3.190E-01	2.691E-01	2.287E-01	3.116E-01	5.215E-01	8.140E-01	1.651E+00	3.188E+00	4.412E+00	3.172E+00
Y = 6	1.956E-01	3.209E-01	3.466E-01	1.885E-01	2.455E-01	5.549E-01	5.720E-01	1.202E+00	3.131E+00	3.177E+00	2.002E+00
Y = 5	1.477E-01	2.169E-01	1.798E-01	1.326E-01	1.608E-01	2.592E-01	3.575E-01	7.000E-01	1.334E+00	1.716E+00	1.182E+00
Y = 4	1.234E-01	1.826E-01	1.543E-01	1.196E-01	1.415E-01	2.109E-01	2.687E-01	4.544E-01	7.863E-01	1.015E+00	7.091E-01
Y = 3	1.133E-01	2.079E-01	2.613E-01	1.598E-01	1.984E-01	3.953E-01	3.169E-01	4.899E-01	1.043E+00	9.017E-01	5.089E-01
Y = 2	0.0	1.617E-01	2.103E-01	1.913E-01	2.406E-01	3.672E-01	3.758E-01	5.379E-01	7.733E-01	6.444E-01	0.0
Y = 1	0.0	0.0	1.151E-01	1.300E-01	1.638E-01	2.242E-01	2.575E-01	3.527E-01	4.082E-01	0.0	0.0
	X = 1	2	3	4	5	6	7	8	9	10	11

Figure A6-3b. 3-D LRA BWR (full-core) transient problem.

NORMALIZED NODAL POWER DENSITIES AT T = 0.139995E+01

PLANE # 4											
Y = 11	0.0	0.0	3.633E-01	4.982E-01	8.103E-01	1.325E+00	1.934E+00	3.538E+00	5.155E+00	0.0	0.0
Y = 10	0.0	4.621E-01	6.444E-01	7.149E-01	1.180E+00	2.130E+00	2.766E+00	5.375E+00	1.006E+01	1.108E+01	0.0
Y = 9	2.944E-01	5.567E-01	7.491E-01	5.581E-01	9.305E-01	2.160E+00	2.168E+00	4.619E+00	1.317E+01	1.757E+01	1.158E+01
Y = 8	2.565E-01	3.906E-01	3.555E-01	3.282E-01	5.040E-01	8.776E-01	1.274E+00	2.704E+00	5.911E+00	8.651E+00	6.271E+00
Y = 7	1.918E-01	2.801E-01	2.373E-01	2.028E-01	2.786E-01	4.677E-01	7.291E-01	1.474E+00	2.845E+00	3.924E+00	2.822E+00
Y = 6	1.716E-01	2.817E-01	3.048E-01	1.671E-01	2.200E-01	4.988E-01	5.142E-01	1.079E+00	2.802E+00	2.838E+00	1.791E+00
Y = 5	1.292E-01	1.896E-01	1.578E-01	1.171E-01	1.436E-01	2.327E-01	3.209E-01	6.274E-01	1.195E+00	1.533E+00	1.056E+00
Y = 4	1.074E-01	1.590E-01	1.347E-01	1.050E-01	1 252E-01	1.878E-01	2.398E-01	4.060E-01	7.028E-01	9.060E-01	6.332E-01
Y = 3	9.862E-02	1.809E-01	2.275E-01	1.398E-01	1.751E-01	3.499E-01	2.814E-01	4.360E-01	9.291E-01	8.028E-01	4.536E-01
Y = 2	0.0	1.405E-01	1.831E-01	1.671E-01	2.115E-01	3.245E-01	3.325E-01	4.772E-01	6.873E-01	5.725E-01	0.0
Y = 1	0.0	0.0	1.002E-01	1.135E-01	1.440E-01	1.979E-01	2.281E-01	3.125E-01	3.632E-01	0.0	0.0
X =	1	2	3	4	5	6	7	8	9	10	11

Figure A6-3b. 3-D LRA BWR (full-core) transient problem.

NORMALIZED NODAL POWER DENSITIES AT T = 0.199991E+01

PLANE # 4

Y = 11	0.0	0.0	3.211E-01	4.211E-01	6.480E-01	1.016E+00	1.413E+00	2.458E+00	3.516E+00	0.0	0.0
Y = 10	0.0	4.162E-01	5.705E-01	6.071E-01	9.405E-01	1.635E+00	2.017E+00	3.725E+00	6.815E+00	7.495E+00	0.0
Y = 9	2.676E-01	5.027E-01	6.668E-01	4.761E-01	7.430E-01	1.657E+00	1.585E+00	3.196E+00	8.917E+00	1.183E+01	7.820E+00
Y = 8	2.360E-01	3.582E-01	3.211E-01	2.833E-01	4.072E-01	6.808E-01	9.384E-01	1.896E+00	4.052E+00	5.909E+00	4.282E+00
Y = 7	1.816E-01	2.643E-01	2.217E-01	1.805E-01	2.325E-01	3.734E-01	5.542E-01	1.076E+00	2.045E+00	2.797E+00	2.013E+00
Y = 6	1.666E-01	2.730E-01	2.919E-01	1.546E-01	1.893E-01	4.123E-01	4.074E-01	8.246E-01	2.107E+00	2.131E+00	1.340E+00
Y = 5	1.281E-01	1.874E-01	1.549E-01	1.114E-01	1.285E-01	1.995E-01	2.649E-01	4.984E-01	9.356E-01	1.196E+00	8.265E-01
Y = 4	1.096E-01	1.622E-01	1.368E-01	1.040E-01	1.186E-01	1.724E-01	2.107E-01	3.447E-01	5.885E-01	7.547E-01	5.249E-01
Y = 3	1.021E-01	1.869E-01	2.340E-01	1.414E-01	1.704E-01	3.315E-01	2.594E-01	3.877E-01	8.134E-01	6.986E-01	3.941E-01
Y = 2	0.0	1.460E-01	1.889E-01	1.696E-01	2.071E-01	3.109E-01	3.097E-01	4.309E-01	6.108E-01	5.073E-01	0.0
Y = 1	0.0	0.0	1.037E-01	1.149E-01	1.417E-01	1.897E-01	2.132E-01	2.832E-01	3.250E-01	0.0	0.0
	X = 1	2	3	4	5	6	7	8	9	10	11

Figure A6-3b. 3-D LRA BWR (full-core) transient problem.

NORMALIZED NODAL POWER DENSITIES AT T = 0.299989E+01

PLANE # 4

Y = 11	0.0	0.0	4.053E-01	5.085E-01	7.366E-01	1.115E+00	1.492E+00	2.521E+00	3.562E+00	0.0	0.0
Y = 10	0.0	5.352E-01	7.237E-01	7.344E-01	1.069E+00	1.793E+00	2.132E+00	3.811E+00	6.897E+00	7.552E+00	0.0
Y = 9	3.483E-01	6.516E-01	8.523E-01	5.793E-01	8.434E-01	1.822E+00	1.675E+00	3.263E+00	9.024E+00	1.194E+01	7.891E+00
Y = 8	3.121E-01	4.711E-01	4.157E-01	3.484E-01	4.667E-01	7.500E-01	9.949E-01	1.948E+00	4.115E+00	5.984E+00	4.341E+
Y = 7	2.475E-01	3.598E-01	2.976E-01	2.294E-01	2.734E-01	4.201E-01	5.983E-01	1.132E+00	2.131E+00	2.905E+00	2.087E+00
Y = 6	2.339E-01	3.820E-01	4.052E-01	2.048E-01	2.295E-01	4.789E-01	4.545E-01	8.939E-01	2.272E+00	2.288E+00	1.439E+00
Y = 5	1.846E-01	2.696E-01	2.204E-01	1.526E-01	1.628E-01	2.404E-01	3.070E-01	5.595E-01	1.038E+00	1.327E+00	9.169E-01
Y = 4	1.640E-01	2.424E-01	2.031E-01	1.494E-01	1.609E-01	2.247E-01	2.622E-01	4.133E-01	6.973E-01	8.887E-01	6.169E-01
Y = 3	1.552E-01	2.844E-01	3.546E-01	2.085E-01	2.384E-01	4.509E-01	3.400E-01	4.885E-01	1.011E+00	8.619E-01	4.837E-01
Y = 2	0.0	2.226E-01	2.869E-01	2.510E-01	2.927E-01	4.259E-01	4.112E-01	5.516E-01	7.699E-01	6.344E-01	0.0
Y = 1	0.0	0.0	1.573E-01	1.702E-01	2.007E-01	2.605E-01	2.836E-01	3.644E-01	4.116E-01	0.0	0.0
X =	1	2	3	4	5	6	7	8	9	10	11

Figure A6-3c. 3-D LRA BWR (full-core) transient problem.

NODE AVERAGED FUEL TEMPERATURES AT T = 0.119996E+01
REACTOR AVERAGE FUEL TEMPERATURE = 0.376054E+03

PLANE # 4

Y = 11	3.000E+02	3.000E+02	3.297E+02	3.426E+02	3.734E+02	4.245E+02	4.894E+02	6.579E+02	8.291E+02	3.000E+02	3.000E+02
Y = 10	3.000E+02	3.371E+02	3.525E+02	3.610E+02	4.070E+02	5.004E+02	5.707E+02	8.467E+02	1.337E+03	1.440E+03	3.000E+02
Y = 9	3.233E+02	3.444E+02	3.606E+02	3.474E+02	3.844E+02	5.023E+02	5.117E+02	7.701E+02	1.657E+03	2.103E+03	1.480E+03
Y = 8	3.200E+02	3.306E+02	3.284E+02	3.275E+02	3.450E+02	3.814E+02	4.227E+02	5.701E+02	8.988E+02	1.176E+03	9.314E+02
Y = 7	3.145E+02	3.213E+02	3.183E+02	3.164E+02	3.241E+02	3.420E+02	3.680E+02	4.416E+02	5.773E+02	6.839E+02	5.762E+02
Y = 6	3.126E+02	3.208E+02	3.227E+02	3.130E+02	3.184E+02	3.431E+02	3.462E+02	4.001E+02	5.631E+02	5.680E+02	4.687E+02
Y = 5	3.093E+02	3.136E+02	3.115E+02	3.088E+02	3.115E+02	3.194E+02	3.278E+02	3.562E+02	4.088E+02	4.395E+02	3.961E+02
Y = 4	3.074E+02	3.110E+02	3.094E+02	3.075E+02	3.094E+02	3.146E+02	3.195E+02	3.342E+02	3.600E+02	3.778E+02	3.544E+02
Y = 3	3.067E+02	3.123E+02	3.155E+02	3.098E+02	3.128E+02	3.262E+02	3.218E+02	3.350E+02	3.756E+02	3.659E+02	3.374E+02
Y = 2	3.000E+02	3.095E+02	3.125E+02	3.116E+02	3.153E+02	3.241E+02	3.254E+02	3.377E+02	3.551E+02	3.463E+02	3.000E+02
Y = 1	3.000E+02	3.000E+02	3.068E+02	3.079E+02	3.104E+02	3.147E+02	3.174E+02	3.246E+02	3.290E+02	3.000E+02	3.000E+02
X =	1	2	3	4	5	6	7	8	9	10	11

Figure A6-3c. 3-D LRA BWR (full-core) transient problem.

NODE AVERAGED FUEL TEMPERATURES AT T = 0.139995E+01
REACTOR AVERAGE FUEL TEMPERATURE = 0.394161E+03
PLANE # 4

Y = 11	3.000E+02	3.000E+02	3.365E+02	3.518E+02	3.887E+02	4.494E+02	5.262E+02	7.255E+02	9.281E+02	3.000E+02	3.000E+02
Y = 10	3.000E+02	3.456E+02	3.645E+02	3.744E+02	4.291E+02	5.405E+02	6.233E+02	9.496E+02	1.530E+03	1.653E+03	3.000E+02
Y = 9	3.288E+02	3.547E+02	3.744E+02	3.578E+02	4.018E+02	5.430E+02	5.529E+02	8.585E+02	1.910E+03	2.440E+03	1.703E+03
Y = 8	3.247E+02	3.378E+02	3.349E+02	3.336E+02	3.544E+02	3.979E+02	4.468E+02	6.217E+02	1.012E+03	1.342E+03	1.052E+03
Y = 7	3.180E+02	3.264E+02	3.226E+02	3.202E+02	3.292E+02	3.507E+02	3.818E+02	4.696E+02	6.314E+02	7.586E+02	6.300E+02
Y = 6	3.158E+02	3.260E+02	3.283E+02	3.161E+02	3.224E+02	3.524E+02	3.558E+02	4.205E+02	6.160E+02	6.216E+02	5.025E+02
Y = 5	3.116E+02	3.171E+02	3.143E+02	3.109E+02	3.142E+02	3.238E+02	3.338E+02	3.679E+02	4.312E+02	4.683E+02	4.160E+02
Y = 4	3.094E+02	3.139E+02	3.118E+02	3.094E+02	3.117E+02	3.181E+02	3.239E+02	3.417E+02	3.731E+02	3.947E+02	3.662E+02
Y = 3	3.085E+02	3.156E+02	3.196E+02	3.123E+02	3.160E+02	3.326E+02	3.270E+02	3.431E+02	3.928E+02	3.807E+02	3.458E+02
Y = 2	3.000E+02	3.121E+02	3.158E+02	3.146E+02	3.192E+02	3.301E+02	3.315E+02	3.465E+02	3.678E+02	3.568E+02	3.000E+02
Y = 1	3.000E+02	3.000E+02	3.086E+02	3.099E+02	3.130E+02	3.183E+02	3.216E+02	3.303E+02	3.357E+02	3.000E+02	3.000E+02
X =	1	2	3	4	5	6	7	8	9	10	11

Figure A6-3c. 3-D LRA BWR (full-core) transient problem.

NODE AVERAGED FUEL TEMPERATURES AT T = 0.199991E+01
REACTOR AVERAGE FUEL TEMPERATURE = 0.459973E+03

PLANE # 4

Y = 11	3.000E+02	3.000E+02	3.578E+02	3.806E+02	4.346E+02	5.232E+02	6.319E+02	9.146E+02	1.202E+03	3.000E+02	3.000E+02
Y = 10	3.000E+02	3.729E+02	4.022E+02	4.157E+02	4.958E+02	6.592E+02	7.743E+02	1.237E+03	2.061E+03	2.238E+03	3.000E+02
Y = 9	3.462E+02	3.875E+02	4.184E+02	3.901E+02	4.545E+02	6.634E+02	6.714E+02	1.105E+03	2.607E+03	3.367E+03	2.315E+03
Y = 8	3.399E+02	3.610E+02	3.559E+02	3.527E+02	3.831E+02	4.471E+02	5.167E+02	7.671E+02	1.326E+03	1.801E+03	1.384E+03
Y = 7	3.295E+02	3.432E+02	3.368E+02	3.321E+02	3.453E+02	3.773E+02	4.224E+02	5.503E+02	7.859E+02	9.708E+02	7.828E+02
Y = 6	3.261E+02	3.430E+02	3.466E+02	3.260E+02	3.353E+02	3.811E+02	3.849E+02	4.806E+02	7.710E+02	7.785E+02	6.013E+02
Y = 5	3.195E+02	3.286E+02	3.239E+02	3.180E+02	3.226E+02	3.373E+02	3.522E+02	4.034E+02	4.984E+02	5.544E+02	4.754E+02
Y = 4	3.160E+02	3.237E+02	3.201E+02	3.158E+02	3.192E+02	3.293E+02	3.380E+02	3.653E+02	4.136E+02	4.468E+02	4.025E+02
Y = 3	3.145E+02	3.267E+02	3.336E+02	3.209E+02	3.266E+02	3.536E+02	3.437E+02	3.687E+02	4.471E+02	4.276E+02	3.723E+02
Y = 2	3.000E+02	3.207E+02	3.270E+02	3.249E+02	3.320E+02	3.496E+02	3.514E+02	3.747E+02	4.082E+02	3.905E+02	3.000E+02
Y = 1	3.000E+02	3.000E+02	3.148E+02	3.169E+02	3.218E+02	3.302E+02	3.352E+02	3.488E+02	3.570E+02	3.000E+02	3.000E+02
X =	1	2	3	4	5	6	7	8	9	10	11

Figure A6-3c. 3-D LRA BWR (full-core) transient problem.

NODE AVERAGED FUEL TEMPERATURES AT T = 0.299989E+01
REACTOR AVERAGE FUEL TEMPERATURE = 0.502935E+03

PLANE # 4

Y = 11	3.000E+02	3.000E+02	3.733E+02	4.004E+02	4.642E+02	5.688E+02	6.942E+02	1.021E+03	1.353E+03	3.000E+02	3.000E+02
Y = 10	3.000E+02	3.932E+02	4.299E+02	4.444E+02	5.389E+02	7.326E+02	8.632E+02	1.398E+03	2.356E+03	2.561E+03	3.000E+02
Y = 9	3.593E+02	4.121E+02	4.509E+02	4.126E+02	4.884E+02	7.380E+02	7.412E+02	1.243E+03	2.992E+03	3.877E+03	2.652E+03
Y = 8	3.516E+02	3.787E+02	3.716E+02	3.662E+02	4.018E+02	4.777E+02	5.581E+02	8.494E+02	1.501E+03	2.056E+03	1.569E+03
Y = 7	3.387E+02	3.565E+02	3.479E+02	3.408E+02	3.561E+02	3.942E+02	4.471E+02	5.976E+02	8.753E+02	1.093E+03	8.707E+02
Y = 6	3.347E+02	3.569E+02	3.615E+02	3.337E+02	3.442E+02	4.002E+02	4.034E+02	5.174E+02	8.650E+02	8.731E+02	6.608E+02
Y = 5	3.261E+02	3.383E+02	3.319E+02	3.236E+02	3.288E+02	3.467E+02	3.644E+02	4.261E+02	5.407E+02	6.084E+02	5.127E+02
Y = 4	3.218E+02	3.322E+02	3.273E+02	3.212E+02	3.252E+02	3.377E+02	3.481E+02	3.815E+02	4.411E+02	4.820E+02	4.269E+02
Y = 3	3.200E+02	3.367E+02	3.461E+02	3.283E+02	3.353E+02	3.703E+02	3.565E+02	3.874E+02	4.862E+02	4.610E+02	3.910E+02
Y = 2	3.000E+02	3.285E+02	3.371E+02	3.338E+02	3.426E+02	3.653E+02	3.668E+02	3.957E+02	4.378E+02	4.149E+02	3.000E+02
Y = 1	3.000E+02	3.000E+02	3.203E+02	3.229E+02	3.290E+02	3.398E+02	3.458E+02	3.627E+02	3.728E+02	3.000E+02	3.000E+02
X =	1	2	3	4	5	6	7	8	9	10	11